### **Springer Theses**Recognizing Outstanding Ph.D. Research

Hyungjun Kim

# Multiscale and Multiphysics Computational Frameworks for Nano- and Bio-Systems



#### Springer Theses

Recognizing Outstanding Ph.D. Research

For further volumes: http://www.springer.com/series/8790

#### **Aims and Scope**

The series "Springer Theses" brings together a selection of the very best Ph.D. theses from around the world and across the physical sciences. Nominated and endorsed by two recognized specialists, each published volume has been selected for its scientific excellence and the high impact of its contents for the pertinent field of research. For greater accessibility to non-specialists, the published versions include an extended introduction, as well as a foreword by the student's supervisor explaining the special relevance of the work for the field. As a whole, the series will provide a valuable resource both for newcomers to the research fields described, and for other scientists seeking detailed background information on special questions. Finally, it provides an accredited documentation of the valuable contributions made by today's younger generation of scientists.

#### Theses are accepted into the series by invited nomination only and must fulfill all of the following criteria

- They must be written in good English.
- The topic of should fall within the confines of Chemistry, Physics and related interdisciplinary fields such as Materials, Nanoscience, Chemical Engineering, Complex Systems and Biophysics.
- The work reported in the thesis must represent a significant scientific advance.
- If the thesis includes previously published material, permission to reproduce this must be gained from the respective copyright holder.
- They must have been examined and passed during the 12 months prior to nomination.
- Each thesis should include a foreword by the supervisor outlining the significance
  of its content.
- The theses should have a clearly defined structure including an introduction accessible to scientists not expert in that particular field.

#### Hyungjun Kim

#### Multiscale and Multiphysics Computational Frameworks for Nano- and Bio-Systems

Doctoral Thesis accepted by The California Institute of Technology, Pasadena, California, USA



Author Hvungiun Kim Center for Materials Simulations & Design Korea Advanced Institute of Science and Technology Daejeon, Republic of Korea Materials and Process Simulation Center

California Institute of Technology Pasadena, USA

Supervisor William A. Goddard III Charles and Mary Ferkel Professor of Chemistry, Material Science. and Applied Physics California Institute of Technology 316 Beckman Insitute 1200 East California Blvd. Pasadena, California USA wag@wag.caltech.edu

ISSN 2190-5053 e-ISSN 2190-5061 ISBN 978-1-4419-7600-0 e-ISBN 978-1-4419-7601-7 DOI 10.1007/978-1-4419-7601-7 Springer New York Dordrecht Heidelberg London

#### © Springer Science+Business Media, LLC 2011

All rights reserved. This work may not be translated or copied in whole or in part without the written permission of the publisher (Springer Science+Business Media, LLC, 233 Spring Street, New York, NY 10013, USA), except for brief excerpts in connection with reviews or scholarly analysis. Use in connection with any form of information storage and retrieval, electronic adaptation, computer software, or by similar or dissimilar methodology now known or hereafter developed is forbidden. The use in this publication of trade names, trademarks, service marks, and similar terms, even if they are not identified as such, is not to be taken as an expression of opinion as to whether or not they are subject to proprietary rights.

Printed on acid-free paper

Springer is part of Springer Science+Business Media (www.springer.com)



#### **Foreword**

Multiscale and multiphysics simulation strategy is important to investigate complex problems in nature because it provides a systematic method to understand underpinning physics of the systems depending on the size. In this thesis, we discuss how such multiscale and multiphysics simulation framework can explain and rationalize the experimental observations in several nano- and bio-systems. Furthermore, we exhibit the computational simulation methods that play major roles to rationally design novel materials with desired properties in next generation nano electronic devices, alternative energy materials, life science, and so on.

Chapter 1 reviews the significance of multiscale and multiphysics simulation strategy. In this chapter, we briefly discuss the multiscale and multiphysics natures in nano- and bio-systems, and detailed examples are contained in the next chapters. Chapter 2 introduces an electric field induced conformational change mechanism, which is responsible for the unique current-voltage (I-V) behavior of nano device, negative differential resistance (NDR). In Chapter 3, the on/off kinetics of the Stoddart-Heath rotaxane-based programmable molecular electronic switch is discussed in terms of the free energy quantities. Chapter 4 explores sodium diffusion through the aluminum-doped zeolite BEA system, and the effect of water uptake amount is thoroughly discussed. This has importance for the application of zeolite to proton exchange membranes for fuel cells (PEMFC). In Chapters 5 and 6, the ion mobilities of tertiary and quaternary ammonium cations (precursors for lipids), and phosphatidylcholine (PC) lipid cations are investigated, respectively. In order to compute the ion mobilities of the precursors and entire lipids, we develop a modified trajectory (TJ) method dealing with the complicated integrals of interaction terms. QM and MD simulations are performed to determine the structures and charge distributions. In Chapter 7, we study how the model lung system of lipid monolayer with surfactant protein B (SP-B) responds to ozone introduction. In parallel with the field induced droplet ionization (FIDI) mass spectrometry study, MD simulations identify the distinct ozone reaction mechanism at the interface, and the role of SP-B at the pulmonary surfactant (PS) system on the oxidative stresses. From these studies, we suggest various multiscale and multiphysics modeling approaches depending on the characteristics of systems and objectives. These efforts allow us

viii Foreword

to overcome the limited time- and length-scales of the monoscale simulations. In addition, we expect that an establishment of such multiscale modeling procedures will invoke interdisciplinary studies by tightly combining the developments occurring independently across fields.

#### Acknowledgments

I would like to express my gratitude to Prof. Bill Goddard, who guided me to become an independent researcher during my PhD journey. He allowed me the freedom to spend my time on many different projects, trained me to solve various problems, and let me have a broad scientific scope with sharp instinct and creative ideas. His wide range of research interests and enthusiasm for science always provided plenty of insights and thoughts, which, I believe will be a great asset to me as I continue my research life. It is also a great chance and honor for me that I can continue to work with Bill and get many fresh ideas from Bill in Korea through the world class university (WCU) program of Korea government.

Prof. Seung Soon Jang, at Georgia Institute of Technology, taught me a lot of simulation techniques and tips, along with his systematic way of thinking to tackle scientific problems, during his days at Caltech. Even after he moved to Gatech, he continues to be my mentor about science and non-science, and I really appreciate his invaluable advice.

I also appreciate Prof. Eok Kyun Lee, who was my undergraduate advisor. He introduced me to computational and theoretical chemistry, and furthermore, he first taught me how to figure out and solve science problems. I am always indebted to him for his warm encouragement and support.

My committee members, Prof. Vincent McKoy, Prof. Mark Davis, Prof. Jack Beauchamp, and Prof. Jim Heath, have provided useful insights and guidance through the candidacy, proposal, and thesis defense. Moreover, it has been an honor for me to work on several projects with them.

I also thank Dr. Isik Kanik and Dr. Luther Beegle at Jet Propulsion Laboratory (JPL) for supporting me during the IMS project. Their fruitful discussions helped me successfully complete our project. It was a great thrill for me to be involved in a Mars project of NASA.

While working at the MSC, it was a pleasure to have many friends and colleagues who shared a similar interest. I want to thank all MSC members, especially, Sergey Zybin and Julius Su who helped me a lot on the energetic material project and the eFF project with their kind advice. I would also like to thank my friend, Mu-Jeng Cheng, for engaging in scientific discussions as well as listening to my random complaints. I owe a lot of coffees to Jiyoung Heo, Sang Soo Han and Soo-Kyung Kim, too.

x Acknowledgments

I also thank to group members in Center for Materials Simulations & Design (CMSD) in KAIST; Dr. Tod A. Pascal, my truly friend (he is almost my brother) from the days in Caltech, and Ms. Jiwon Jeon, a super smart graduate student. Thanks also to Ms. Heejung Kim for proofing the text, and thanks to Yeon Jung Joo for her whole-hearted support.

Finally, I wish to thank Prof. Hugh I Kim in Postech and Young Shik Shin, who gave me many insights on the experiments while conducting our lipid projects. And last but not least, I am truly grateful for all the scientific, mental, and sometimes physical help from all other friends at KAIST and Caltech.

#### **Contents**

1	Intro	oduction	1	1
2	_		fferential Resistance of Oligo (Phenylene Ethynylene) led Monolayer Systems: The Electric Field Induced	
	Con	formatio	onal Change Mechanism	9
	2.1	Introdu	iction	g
	2.2		tion Details	10
		2.2.1	Computational Details of QM Calculations	10
		2.2.2	Conductivities of P and T Conformations (NEGF	
			Calculations)	11
		2.2.3	Coarse-Grained NN Interacting Hamiltonian	11
		2.2.4	Extracting NN Model Parameters from QM/FF Energies	11
		2.2.5	Coarse-Grained MC Simulations	13
	2.3	Results	and Discussion	14
		2.3.1	Two Conformations of AN-OPE	14
		2.3.2	Electrical Conductivities of P and T	16
		2.3.3	Response to Constant External Field	18
		2.3.4	NDR for Time Dependent Electric Field	23
	2.4	Conclu	sions	25
	Bibli	iography	,	25
3	Free	Energy	Barrier for Molecular Motions in Bistable [2]Rotaxane	
,			Electronic Devices	27
	3.1		action.	27
	3.2		tion Details	29
	3.2	3.2.1	Potential of Mean Force from Constrained Molecular	
		3.2.1	Dynamics Simulation	29
		3.2.2	Constrained Molecular Dynamics Simulation	31
		3.2.3	Force Field and MD Parameters	
	3.3		and Discussion	
		3.3.1	Charge Scheme: Adiabatic Approximation	
		3.3.2	Free Energy Profiles from PMF Calculations	

xii Contents

	3.4		isions	
	DIUI	iograpiiy	/	42
4			fusion Through Aluminum-Doped Zeolite BEA System:	
	<b>Effe</b>	ct of Wa	ater Solvation	47
	4.1	Introdu	uction	47
	4.2	Simula	ation Details	48
		4.2.1	Force Field	48
		4.2.2	Grand Canonical Monte Carlo (GCMC) Method	
			and Molecular Dynamics (MD) Simulation	50
		4.2.3	Construction of Models and Calculation of Properties	50
	4.3	Result	s and Discussion	51
		4.3.1	Water Absorption	51
		4.3.2	Structure of Water in Zeolite	53
		4.3.3	Effect of Water Contents on Sodium Diffusion	54
		4.3.4	Effect of Temperature on Sodium Diffusion	57
	4.4	Conclu	asions	61
	Bibli	iography	/	62
			rrelation Between Mass and Ion Mobility for Choline Ammonium Cations in N <sub>2</sub>	65
	5.1		uction	65
	5.2		mental Section	68
	3.2	5.2.1	Chemicals and Reagents	68
		5.2.2	Electrospray Ionization Ion Mobility Spectrometer	68
		5.2.3	Computational Modeling	69
	5.3		S	70
		5.3.1	Mass-Mobility Correlation of Ammonium Cations	70
		5.3.2	Tertiary and Quaternary Ammonium Cations with Similar	
			Molecular Weights	72
		5.3.3	Functional Group Isomers of Ammonium Cations	73
		5.3.4	Collision Cross-Sections of Ions in N <sub>2</sub> via the Trajectory	
			Method	74
	5.4	Discus	ssion	75
		5.4.1	Classical Ion-Neutral Collision Model	75
		5.4.2	Computational Trajectory Method	76
		5.4.3	Ion-Quadrupole Potential	76
		5.4.4		
			Ion-Induced Dipole Potential	78
		5.4.5	Van der Waals Potential	78 79
	5.5	5.4.5 5.4.6 Conclu	Van der Waals Potential	79

Contents xiii

		• •	
	_		85
			85
6.2			87
			87
	6.2.2		
			88
	6.2.3		89
			89
6.3	Results		90
	6.3.1		90
	6.3.2	Unsaturated Phosphatidylcholine Cations	91
	6.3.3	Sodiated Phosphatidylcholine Cations	91
	6.3.4	Estimated Collision Cross-Sections of Ions Using T-Wave	
		Calibration	93
	6.3.5	Determination of Collision Cross-Sections of Ions	93
	6.3.6	Calculated Collision Cross-Sections of Ions Using	
			96
6.4	Discus	·	97
	6.4.1		97
	6.4.2		
			98
	6.4.3		
	01110	•	100
	644		100
	0.1.1		102
6.5	Conclu	·	
DIUL	iograpity	· · · · · · · · · · · · · · · · · · ·	104
Into	rfacial I	Pagetions of Ozona with Linids	
			107
		· · · · · · · · · · · · · · · · · · ·	
1.2			
			111
	1.2.2		111
	7.0.0		
7.3			
7.4			
Bibl	iography	<i>I</i>	122
	6.1 6.2 6.3 6.4 6.5 Bibl Inte and 7.1 7.2	## Conclusion	6.2.1 Chemicals and Reagents 6.2.2 Electrospray Ionization Traveling Wave Ion Mobility Mass Spectrometer 6.2.3 Collision Cross-Section Calibration 6.2.4 Computational Modeling 6.3 Results 6.3.1 Saturated Phosphatidylcholine Cations 6.3.2 Unsaturated Phosphatidylcholine Cations 6.3.3 Sodiated Phosphatidylcholine Cations 6.3.4 Estimated Collision Cross-Sections of Ions Using T-Wave Calibration 6.3.5 Determination of Collision Cross-Sections of Ions Using the Trajectory Method 6.4.1 Effect of Drift Gas on Ion Mobility 6.4.2 Geometrical Effect on the Collision Cross-Sections of Phosphatidyl-choline Cations 6.4.3 Mass-Mobility Correlations of Phophatidylcholine Cations 6.4.4 Characterizing Unsaturated Phosphatidylcholine Cations 6.4.5 Conclusions Bibliography  Interfacial Reactions of Ozone with Lipids and Proteins in a Model Lung Surfactant System 7.1 Introduction 7.2 Methods 7.2.1 Chemicals and Reagents 7.2.2 Online FIDI-MS Technique and Heterogeneous Oxidation by O3 7.2.3 Molecular Dynamic Simulations 7.3 Results and Discussion 7.3.1 Interfacial Reaction of POPG with O3 7.3.2 Interfacial Oxidation of SP-B1-25 in POG Monolayer by O3 7.3.4 Interactions of SP-B1-25 in POG Monolayer

xiv Contents

ength- .1.1 .1.2 ppend onduc ppend .3.1 .3.2 ppend nd Bias ppend 2/Rota	ix A: Discussions on Coarse-Graining of Time- and Scale in Monte Carlo Simulations for AN-OPE SA Time-Scale Length-Scale ix B: Effect of Molecular Fluctuations on the Electricity of AN-OPE SAM ix C: NDR in Other OPE-derivative Systems Bare OPE Nitro OPE ix D: Conversion Factor Between External Electric is Voltage ix E: Mulliken Charge Distributions of Bistable is an employed and the state of	M 12
.1.1 .1.2 ppend onduc ppend .3.1 .3.2 ppend nd Bias ppend 2/Rota	Time-Scale Length-Scale ix B: Effect of Molecular Fluctuations on the Electricity of AN-OPE SAM ix C: NDR in Other OPE-derivative Systems Bare OPE Nitro OPE ix D: Conversion Factor Between External Electric is Voltage ix E: Mulliken Charge Distributions of Bistable	
.1.2 ppend onduc ppend .3.1 .3.2 ppend nd Bias ppend 2/Rota	Length-Scale ix B: Effect of Molecular Fluctuations on the Elect ivity of AN-OPE SAM ix C: NDR in Other OPE-derivative Systems Bare OPE Nitro OPE ix D: Conversion Factor Between External Electric is Voltage ix E: Mulliken Charge Distributions of Bistable	
ppend onduc ppend .3.1 .3.2 ppend nd Bias ppend 2/Rota	ix B: Effect of Molecular Fluctuations on the Electrivity of AN-OPE SAM ix C: NDR in Other OPE-derivative Systems Bare OPE Nitro OPE ix D: Conversion Factor Between External Electric Systems ix E: Mulliken Charge Distributions of Bistable	trical
onduc ppend .3.1 .3.2 ppend nd Bias ppend 2/Rota	ivity of AN-OPE SAM  x C: NDR in Other OPE-derivative Systems  Bare OPE  Nitro OPE  ix D: Conversion Factor Between External Electric Voltage  ix E: Mulliken Charge Distributions of Bistable	
ppend .3.1 .3.2 .ppend nd Bias .ppend 2/Rota	x C: NDR in Other OPE-derivative Systems Bare OPE Nitro OPE x D: Conversion Factor Between External Electric Voltage ix E: Mulliken Charge Distributions of Bistable	
.3.1 .3.2 ppend nd Bias append 2/Rota	Bare OPE	
.3.2 ppend nd Bias append 2/Rota	Nitro OPE  ix D: Conversion Factor Between External Electric voltage ix E: Mulliken Charge Distributions of Bistable	Field 13
ppend nd Bias append 2/Rota	x D: Conversion Factor Between External Electrics Voltage	Field 13
nd Bias append 2/Rota	s Voltageix E: Mulliken Charge Distributions of Bistable	13
append 2]Rota	ix E: Mulliken Charge Distributions of Bistable	
2]Rota		
	wone Melecular Switch Depending on CDDOT4+ D	
	xane Molecular Switch Depending on CBPQ1 11 R	Ring's
osition		13
ppend	ix F: Consideration of Metric Effect on the Bistab	le
2]Rota	xane Molecule During the Constant MD Simulation	ons
sing F	ixman's Theorem	16
ppend	x G: Time for Consumption of POPG	16
.8.1	Methods	16
.8.2	Results and Discussion	16
raphy		16
	sing From ppending 8.1 8.2	sing Fixman's Theorem

#### **List of Figures**

1.1	Multiscale and Multiphysics paradigm simulation strategy	2
1.2	Multiscale and Multiphysics characteristics in nano electronic systems. At electron size scale, electrical conductivity depends on the	
	quantum states of the molecules. At molecular size scale, classical	
	interactions determine the molecular conformation, which affects	
	its quantum state. At device size scale, hundreds of molecules are	
	assembled to build a mesoscale junction and these are packaged into a	
	device component. Courtesy of Dr. Jang Wook Choi; Korea Advanced	
	Institute of Science and Technology (scanning electron microscope	
	image of the nano electronic system in the bottom-middle panel)	3
1.3	Multiscale and Multiphysics characteristics in bio systems. At electron	
	size scale, chemical reactions, which are governed by huge QM effects	
	(e.g. electron/proton transfer), regulate the molecular architecture of	
	the protein for an effective functionality. At molecular scale, CM	
	describes the interactions, such as hydrophobic interaction, among	
	the bio components of proteins, lipids, etc. Large scale motion of	
	the membrane, such as endo- or exo-vesiculation, is in the regime of	
	hydrodynamic descriptions, and this affects the dynamics of a cell. Courtesy of Dr. Tod A. Pascal; California Institute of Technology	
	(trans-membrane protein figure in the <i>top-right panel</i> ). Optical	
	microscope image of the cells (bottom-left panel) is obtained from the	
	National Institutes of Health (NIH) image bank	4
2.1	(a) Energies of various conformations of AN-OPE relative to the	
	AP conformation computed with a 1.2 V/Å external field from FF	
	calculations (black histograms) and NN model calculations (orange	
	histograms). (b) Energies of various conformations of AN-OPE	
	relative to the AP conformation computed with no external field from	
	FF calculations (black histograms), NN model calculations (orange	
		12
2.2	Torsional strain energy $E_i^{torsion}$ as a function of twisting angle $\chi$	
	from QM (PBE) on the isolated molecule. The energy at $\chi=4^{\circ}$	
	(corresponding to P) is 0.01 kcal/mol higher than the ground state	
	energy at $\chi = 0^{\circ}$ . The energy at $\chi = 160^{\circ}$ (which corresponds to	

xvi List of Figures

	0.22 kcal/mol higher $E_i^{torsion}$ of T compared to $E_i^{torsion}$ of P	13
2.3	(a) Optimized geometry for the low field structure (P) of AN-OPE	13
2.5	SAM. Here [0001] is the surface normal and the views are along	
	z-axis (upper middle), y-axis (lower middle), and x-axis (lower	
	right). The left picture is a perspective along the axis of one plane	
	of molecules. The hydrogen bonding network is aligned along the	
	$[11\overline{2}0]$ direction. (b) Optimized geometry for the high field structure	
	(T) of AN-OPE SAM. Here [0001] is the surface normal and the	
	views are along z-axis ( <i>upper middle</i> ), y-axis ( <i>lower middle</i> ), and	
	x-axis (lower right). The left picture is a perspective along the axis of	
	one plane of molecules. The hydrogen bonding network is aligned	
	along the [1010] direction	15
2.4	Density of state (DOS) and transmission function $T(E)$ of P structure	10
2	(a) and T structure (b). The <i>top</i> electrode is located $12 \text{ Å}$ above from	
	the bottom electrode	16
2.5	(a) Current through P conformation, $I_P$ and current through T	
	conformation, $I_T$ versus the bias voltage $V$ determined from the NEGF	
	calculations using the DOS and T(E) of Fig. 2.4. (b) Conductivity of P	
	conformation, $\sigma_P$ and conductivity of T conformation, $\sigma_T$ versus the	
	bias voltage V determined. The top electrode is located 12 Å above	
	from the <i>bottom</i> electrode. $\sigma_P$ is $\sim 10$ times larger than $\sigma_T$	17
2.6	Density of state (DOS) and transmission function $T(E)$ of P structure	
	(a) and T structure (b). The <i>top</i> electrode is located 20 Å above from	
	the <i>bottom</i> electrode	18
2.7	(a) Current through P conformation, $I_P$ and current through T	
	conformation, $I_T$ versus the bias voltage $V$ determined from the NEGF	
	calculations using the DOS and T(E) of Fig. 2.6. (b) Conductivity of P	
	conformation, $\sigma_P$ and conductivity of T conformation, $\sigma_T$ versus the	
	bias voltage V determined. The <i>top</i> electrode is located 20 Å above	
	from the <i>bottom</i> electrode. $\sigma_P$ is $\sim 163$ times larger than $\sigma_T$	19
2.8	Conductivities depending on the twisting angle are extracted	
	from the previous study [36], which are the results from NEGF	
	calculations. (a) Semi-log plots of $I$ - $V$ curves shows that the	
	slope decrease as the twist angle approaches to 90°, which	
	means that the tunneling barrier from the <i>bottom</i> electrode to	
	top electrode, $\Phi_B$ increases as the $\pi$ - $\pi$ orbital overlap decreases.	
	(b) Since the conductivity is dominated by the $\pi$ - $\pi$ orbital	
	overlap, we assumed that the conductivity between two phenyl	
	rings, $\sigma_i = 1/R_i$ is proportional to $\cos^4(\chi_i)$ . From simple calculation leads the total conductivity $\sigma_{\text{tot}}$ to be proportional to	
	the $\cos^4(\chi_1)\cos^4(\chi_2)/(\cos^4(\chi_1)+\cos^4(\chi_i))$ , which shows good	
	agreement with the NEGF results	20
2.9	(a) Snapshots during P-to-T transition from MC simulation with	20
۷.)	1.2 V/Å external field. The first nucleation is occurred at 55,184 MCS,	

List of Figures xvii

	then, the [1120] line propagates until 55,214 MCS. More nucleation	
	and propagation along [1120] are taken place, and finally, the full	
	system is transformed by 1,008,706 MCS. We note that increased bias	
	voltage yields a faster P-to-T transition. (b) Time dependence of P and	
	T populations and electrical conductivity through the SAM during	
	P-to-T transition. (c) Snapshots during T-to-P transition from MC	
	simulation without an external field. The first nucleation is occurred at 486,389 MCS, then, the [1120] line propagates until 486,410 MCS.	
	More nucleation and propagation along $\begin{bmatrix} 11\bar{2}0 \end{bmatrix}$ are taken place, and finally, the full system is transformed by 2,377,335 MCS. (d) Time	
	dependence of P and T populations and electrical conductivity through	
	the SAM during T-to-P transition	21
2.10	(a) P-to-T transition; (b) T-to-P transition; <i>Top panels</i> show the	
	temperature dependence of the propagation rate along [11 $\bar{2}0$ ], $k_{[11}\bar{2}0]$ .	
	<i>Middle panels</i> show the probability, $P(t)$ of exhibiting no nucleation	
	by time, $t$ for the case when the nucleation is initiated next to another	
	[11 $\bar{2}$ 0] line. The <i>dotted lines</i> is an exponential fit of $P(t)$ . This leads	
	to a nucleation rate of $\tau = 5,583$ MCS for the P-to-T transition and	
	$\tau = 72,926$ MCS for the T-to-P transition. <i>Bottom panels</i> show	
	the probability, $P(t)$ of exhibiting no nucleation by time, $t$ for the	
	case when the nucleation is initiated in the absence of next [1120]	
	line. The exponential fit leads to a nucleation rate of $\tau_0 = 274,193$	
	MCS for the P-to-T transition and $\tau_0 = 357,135$ MCS for the T-to-P	
	transition	22
2.11	(a) Current-voltage ( <i>I-V</i> ) curves calculated at 300 K from MC	22
2.11	simulations combined with the $I-V$ results of the Green's function	
	calculations. Results for three sweeping rates are shown: S (blue line):	
	$1 \times 10^{-8}$ V/MCS, M (red line): $4 \times 10^{-8}$ V/MCS, and F (black line):	
	$2 \times 10^{-7}$ V/MCS. Inset is the experimental <i>I-V</i> curves from the	
	reference [9] with 3 different sweeping rates: S (blue line): 21 mV/s,	
	M (red line): 83 mV/s, and F (black line): 415 mV/s. (b) The sweep	
	rate dependence of the integral of the current from the peak to the	
	valley during NDR, $Q_F$ from current simulation ( <i>left panel</i> ) and	
	experiment [9] (right panel)	23
3.1	Structural formula of the two co-conformations of a bistable	
	[2]rotaxane fragment used in this study	28
3.2	(a) Backbone of the rotaxane molecule simulated in this study. (b)	
	CBPQT <sup>4+</sup> ring positions along the backbone (unit: Å)	30
3.3	Charges for the initial nine structures obtained from QM with	
	Mulliken analysis. In addition, we included two more structures	
	beyond each station of the TTF and the DNP, using charges identical	
	to those for the equilibrium CBPQT <sup>4+</sup> @TTF and CBPQT <sup>4+</sup> @DNP	
	cases, respectively. Ten more structures were generated on the basis of	
	these eleven structures. The position of the CBPOT <sup>4+</sup> ring for each	

xviii List of Figures

	two adjacent cases from the eleven structures. The charges were also averaged	31
3.4	Probability density function of kinetic energy KE $(=mv^2/2)$ is	01
	from the MD simulation of the CBPQT <sup>4+</sup> ring@TTF (blue line)	
	at 300 K. Here the time step was 0.01 fs and the total simulation	
	time was 3 ns after 500 ps of equilibration. The <i>black dashed line</i> compares with the Maxwell-Boltzmann distribution of the energy,	
	2 $\left(\text{KE}/\pi (k_B T)^3\right)^{1/2} \exp\left(-\text{KE}/k_B T\right)$ , for $T = 300 \text{ K}$	22
3.5	$2\left(\text{KE}/\pi \left(k_B I\right)^2\right) = \exp\left(-\text{KE}/k_B I\right)$ , for $I = 300 \text{ K}$	33
	$KE_y \left(=mv_y^2/2; green line\right)$ , and $KE_z \left(=mv_z^2/2; red line\right)$ are	
	computed from the MD simulation of the CBPQT <sup>4+</sup> ring@TTF	
	(blue line), which are identical to each other. These are compared	
	with the Maxwell-Boltzmann distribution of $KE_i$ , $\sqrt{1/(\pi KE_i k_B T)}$	
	$\exp(-KE_i/k_BT)$ at 300 K. $(i \in \{x, y, z\}; black dashed line)$	33
3.6	Change of mean force as a function of simulation time. In each	
	case this follows 500 ps of equilibration time. This plot shows	
	two representative cases: the CBPQT <sup>4+</sup> ring@TTF (TTF) and the	34
3.7	CBPQT <sup>4+</sup> ring@DNP (DNP)	34
3.1	along the backbone. The <i>blue curve</i> allows the charge to change	
	adiabatically as the ring moves along the dumbbell, which is the	
	reliable result. The other two <i>curves</i> show the error obtained when	
	the charges are fixed: the <i>green curve</i> uses fixed charges from the	
	ring@TTF; the <i>red curve</i> uses a fixed charge from the ring@DNP	35
3.8	(a) Change of the mean force as a function of ring position along the	
	backbone. (b) Change of the potential of mean force as a function of	
	ring position along the backbone. The <i>green vertical lines</i> denote the	
2.0	ring@TTF (8.90 Å) and ring@DNP (47.70 Å)	36
3.9	Change of Coulombic interaction energy as a function of the ring position: (a) neutral state; (b) oxidation state $+1$ ; (c) oxidation	
	state $+2$	40
3.10	Change of van der Waals interaction energy as a function of the	70
3.10	ring position: (a) neutral state; (b) oxidation state +1; (c) oxidation	
	state +2	41
3.11	Variations in the total charge on the ring as a function of the ring	
	position for the neutral case	41
4.1	Atomistic structure for the primitive periodic cell with composition	
	of Na <sub>8</sub> Al <sub>8</sub> Si <sub>248</sub> O <sub>512</sub> . This shows <i>green</i> balls are aluminum and	
	magenta balls are sodium. (a) Minimized aluminosilicate zeolite	
	BEA structures without $H_2O$ , (b) snapshot of zeolite BEA structures	
	after the GCMC simulation for 298.15 K and 101.3250 kPa, and (c)	

List of Figures xix

	snapshot of zeolite BEA structures after 4 ns NPT MD simulation at 298.15 K and 101.3250 kPa	49
4.2	Dashed line is the least-squares fitted to $f(x) = a \tanh(bx)$ , where $a = 46.19$ mole/ unit cell and $b = 0.753$ (1/kPa). We obtain a vapor	
	pressure of 3.578 kPa for the point at which the water uptake reaches	
	to 99% of the maximum loading uptake	51
4.3	Predicted temperature-dependence of water uptake at 101.3250 kPa	<i>J</i> 1
	when the zeolite BEA has no aluminum doping (red curve) and	
	Si/Al = 30 (blue curve). The presence of aluminum-doped sites as	
	well as sodium ions enhance the water uptake amount especially in	
	the high temperature	52
4.4	(a) Probability of finding additional water molecules at a specific	
	distance from each water molecule. This is obtained as the product of	
	pair correlation functions of water oxygens, $\rho g_{O(water)-O(water)}$ with	
	water density $\rho$ and $4\pi r^2$ . (b) Water coordination number (CN) of	
	water molecule as a function of pressure. The CN of water molecule is	
	obtained from the integration of curve a up to first minimum, which is	
	at 3.7 Å. The saturated value of CN of the absorbed phase ( $\sim$ 3.8) is	
4.5	smaller than the CN of the bulk phase (4.5)	53
4.3	water molecule. This is obtained as the product of pair correlation	
	functions of sodium atoms and water oxygen, $\rho g_{Na-O(water)}$ with	
	water density $\rho$ and $4\pi r^2$ . (b) Water coordination number (CN) of	
	sodium ions as a function of pressure. The CN of water molecule is	
	obtained from the integration of curve a up to first minimum, which is	
	at 3.5 Å. The saturated value of CN of the absorbed phase ( $\sim$ 5.0) is	
	same to the CN of the bulk phase	55
4.6	Log-log plot of mean square displacements (MSD) vs time at	
	298.15 K and 101.3250 kPa based on a trajectory of 12 ns. Initially the	
	MSD shows MSD $\propto t^{1/2}$ up to $t = \sim 20$ ps, but the times $> \sim 2$ ns,	
	we see normal 3D Fickian behavior (MSD $\propto t$ ). The Fickian regime	- /
4.7	leads to a diffusion coefficient of $D = 1.233 \times 10^{-7} \text{ cm}^2/\text{s} \dots$	56
4.7	Dependence of diffusion coefficient of sodium ion on water coordination number (CN) of sodium ion. The diffusion coefficients	
	were calculated from three partitioned trajectories of 12 ns NPT	
	simulations (each partition has 4 ns length), and the error bars were	
	evaluated from the diffusion coefficients obtained from the three	
	partitioned trajectories. This represents pressures from 0.1013 to	
	$101.3250$ kPa at 298.15 K. At a pressure of $\sim$ 2.0 kPa, we find an	
	abrupt change in the water CN. When the sodium ion is solvated by	
	>4.5 water molecules, its diffusion coefficient increases abruptly by a	
	factor of 3.5. The <i>dashed line</i> is to guide the eye	56
4.8	Time dependence of the distances of one sodium ion to all 8 aluminum	
	atoms of the zeolite membrane. The distance to each aluminum atom	
	is shown with a different color. (a) Vapor pressure is 101.3250 kPa	

xx List of Figures

	the Na to hop from a position 4.8 Å from the <i>purple</i> Al to a position 7.5 Å from the <i>black</i> Al. Here a distance of 4.8 Å indicates one water shell between the Na and the Al, while 7.5 Å indicates separate water shells around each; ( <b>b</b> ) vapor pressure is 0.1013 kPa (poor solvation regime) at 298.15 K. In this case the Na remains at 4 Å from the Al which indicates that the Na remains coordinated to the O of the Al	58
4.9	Dependence of the sodium diffusion coefficient on the temperature for a vapor pressure of 101.3250 kPa. The diffusion coefficients were calculated from three partitioned trajectories of 12 ns NPT simulations (each partition has 4 ns length), and the error bars were evaluated from the diffusion coefficients obtained from the three partitioned trajectories. Up to 373.15 K, the diffusion coefficient increases with increasing temperature, whereas it decreases beyond 373.15 K due to the depletion of the water solvation	59
4.10	Arrhenius plots of diffusion coefficient from each solvation regime: the <i>red squares</i> are for the poor solvation regime and the <i>blue diamond</i> is for the good solvation regime. The <i>solid black line</i> is a linear fitting of each regime. This leads to $D_{300K} = 3.762 \times 10^{-8}$ cm <sup>2</sup> /s and $E_{act} = 3.810$ kcal/mol for the poor solvation regime and $D_{300K} = 1.512 \times 10^{-7}$ cm <sup>2</sup> /s and $E_{act} = 3.540$ kcal/mol for the good solvation regime, and the equation of each fitted line and R2 value are <i>inset</i> in the figure	60
5.1	Examples of the ion mobility spectra taken in this study. Shown are two spectra taken in 730 Torr $N_2$ . The electric field strength and the temperature of the drift tube were 292 V/cm and 473 K, respectively. The <i>dash curve</i> is a spectrum taken with pure solvent being introduced to the electrospray needle while the <i>solid curve</i> is a spectrum of solvent and 300 $\mu$ M $N$ , $N$ -dimethylammoniumethanol. The two spectra were smoothed (10 point adjacent averaging) and shifted in intensity by an additive constant to avoid overlap. The $N$ , $N$ -dimethylammoniumethanol feature is indicated in the figure. The unlabeled features correspond to ionized solvent (water, methanol, acetic acid) and atmospheric constituents ionized through proton transfer (due to the open nature of	71
5.2	the ESI-IMS instrument)	
	are indicated with dashed lines	73

List of Figures xxi

5.3	of abiotic amino acid cations [14] and carboxylic acid anions [15] in N <sub>2</sub> versus theoretically determined $\Omega_D$ using the modified TJ	
	method for $N_2$ drift gas. Abiotic amino acid cation data are shown	
	as <i>solid squares</i> and carboxylic acid anion data are shown as <i>empty</i>	
	circles. The solid line is $y = x$ . (b) Plot of experimentally determined	
	collision cross-sections ( $\Omega_D$ ) of 3° and 4° ammonium cations in N <sub>2</sub>	
	versus theoretically determined $\Omega_D$ using the modified TJ method for	
	N <sub>2</sub> drift gas. 3° ammonium cation data are shown as <i>asterisks</i> and	
	4° ammonium cation data are shown as <i>solid squares</i> . Each ion is	
	labeled with the appropriate identifying number and alphabet shown	
	in Fig. 5.1. The <i>solid line</i> is $y = x$	74
5.4	Plots of theoretically determined collision cross-sections $(\Omega_D)$ (a) with	
	potential from van der Waals and ion-induced dipole $(VDW + IID)$	
	interactions over the theoretical $\Omega_D$ with original pairwise	
	potential, van der Waals + ion-induced dipole + ion-quadrupole	
	(VDW + IID + IQ) interactions, and (b) with potential from van der	
	Waals potential ( $VDW$ ) over the theoretical $\Omega_D$ with potential from	
	van der Waals and ion-induced dipole ( $VDW + IID$ ) interactions of 3°	
	and 4° ammonium cations, abiotic amino acid cations, and carboxylic	
	acid anions in $N_2$ versus ion mass. The ammonium cation data, the	
	abiotic amino acid cation, and carboxylic acid anion data are shown as	77
<i></i>	solid squares, empty circles, and asterisks, respectively	77
5.5	Plots of theoretically determined collision cross-sections ( $\Omega_D$ ) of 3° and 4° ammonium actions, shiptic amino acid actions, and aerhovelic	
	and 4° ammonium cations, abiotic amino acid cations, and carboxylic acid anions in $N_2$ versus ion mass. The calculated $\Omega_D$ of the molecular	
	ions only with van der Waals ( $VDW$ ) interaction with $N_2$ are shown as	
	empty squares (left y-axis). The calculated $\Omega_D$ of the molecular ions	
	with original pairwise potential, van der Waals + ion-induced dipole +	
	ion-quadrupole ( $VDW + IID + IQ$ ) interactions, with N <sub>2</sub> are shown	
	as solid circles (right y-axis)	78
5.6	Plot of the total shape asymmetry (AS) of the ammonium cations	, -
	versus ion mass. The ammonium cations with no oxygen atom are	
	shown as solid squares. The ions containing one oxygen atom and	
	two oxygen atoms are shown as empty triangles and empty circles,	
	respectively. The DFT optimized structure of each numerically or	
	alphabetically labeled ion is shown in Fig. 5.2	81
6.1	(a) Plot of drift time of saturated phosphatidylcholine (PC) cations	
	in traveling wave ion mobility spectrometer versus ion mass.	
	Experimentally determined data for symmetric PC and asymmetric	
	PC cations are shown as <i>solid squares</i> and <i>empty circles</i> , respectively.	
	The black dash and red solid lines are the linear fit to the symmetric	
	PC cation data set and to both symmetric and asymmetric PC cation	
	data set, respectively. (b) Plot of drift time of PC cations spanning	
	mass range $700 - 800$ Da in traveling wave ion mobility spectrometer	

xxii List of Figures

	unsaturated PC cations are shown as <i>solid squares</i> and <i>empty circles</i> , respectively. The <i>black dash</i> and <i>red solid lines</i> are the linear fit to the saturated PC cation data set and to both saturated and unsaturated PC cation data set, respectively. (c) Plot of drift time of protonated and sodiated PC cations in traveling wave ion mobility spectrometer versus ion mass. Experimentally determined data for protonated PC and sodiated PC cations are shown as <i>solid squares</i> and <i>empty circles</i> , respectively. The <i>black dash</i> and <i>red solid lines</i> are the linear fit to the	
6.2	protonated PC cation data set and to both protonated and sodiated PC cation data set, respectively	92
6.3	and PC the singly charged cation is used. Linear trend and power trend lines are shown as <i>solid</i> and <i>dash lines</i> , respectively. (b) A plot of the estimated cross-sections versus the ion mass for PC cations investigated in this study. The estimated collision cross-sections from linear trend and power trend are shown as <i>solid squares</i> and <i>empty circles</i> , respectively	94
6.4	molecular dynamics simulation. The fluctuation is ranging from $\sim 5$ Å to $\sim 25$ Å with the time period of 5–20 ps. Approximately 17 times of fluctuation is observed from this trajectory. (b) Plot of experimentally determined collision cross-sections $(\Omega_D)$ of phosphatidylcholine (PC) cations in N <sub>2</sub> against theoretically determined $\Omega_D$ using the modified TJ method for N <sub>2</sub> drift gas. The theoretical $\Omega_D$ is obtained by averaging $\Omega_D$ for 200 structures from MD simulations. The <i>solid line</i> is $y = x$ . (c) Plot of theoretical $\Omega_D$ in He over theoretical $\Omega_D$ in N <sub>2</sub> versus mass of PC cations	96
6.5	ion mass. The calculated average $\Omega_D$ of the 200 ion conformations are shown as <i>solid squares</i> (left <i>y</i> -axis). The calculated surface areas of PC cations in N <sub>2</sub> at 300 K are shown as <i>empty circles</i> (right <i>y</i> -axis). (b) Plots of experimentally evaluated $\Omega_D$ and surface areas of phosphatidylcholine (PC) cations in N <sub>2</sub> versus ion mass. The $\Omega_D$ of PC cations are shown as <i>solid squares</i> (left <i>y</i> -axis). The calculated surface areas of PC cations in N <sub>2</sub> at 300 and 400 K are shown as <i>empty circles</i> and <i>empty triangle</i> , respectively (right <i>y</i> -axis)	99

List of Figures xxiii

	cations in $N_2$ against theoretically determined $\Omega_D$ at $E_0$ and $E^*$ using
	the modified TJ method for $N_2$ drift gas. The <i>solid line</i> is $y = x \dots 101$
6.6	MD simulated structures of unsaturated phosphatidylcholine cations
	at minimum energy state $(E_0)$ are shown. The structures of the
	closest $\Omega_D$ to the experimental values are also shown along with
	corresponding relative energy values $(E^*)$ . Unsaturated acyl chain is
	colored in <i>yellow</i>
7.1	Illustration of FIDI-MS methodology for studies of
	interfacial reactions. (a) A quiescent hanging droplet of
	analyte-containing solution is formed on the end of a
	capillary. All electrical components remain at ground as the
	droplet is formed and reacts in a field-free environment.
	(b) The droplet is exposed to gas-phase reactants for a variable
	period of time to allow for heterogeneous reactions between
	gas-phase and solution-phase species. (c) After a reaciton period,
	a pulsed electric field stretches the neutral droplet until it emits stream
	of positively and negatively charged submicron droplets in opposite
	directions. Ionized reactants and products from heterogeneous
	reactions enter the capillary inlet of the mass analyzer. Either positive
	or negative ions can be sampled
7.2	Structures of POPG, POG, and SP- $B_{1-25}$ investigated in this study 110
7.3	(a) Heterogeneous reaction of POPG with O <sub>3</sub> as a function
	of time. In the absence of ozone, the negative ion FIDI-MS
	spectrum of POPG is dominated by the singly deprotonated
	POPG peak at m/z 748. POPG is depleted after 15 s of the
	exposure and oxidation products are dominated by deprotonated
	hydroxyhydroperoxide (HHP) at m/z 672. The aldehyde, carboxylic
	acid, and methoxyhydroperoxide products are observed at m/z 638,
	m/z 654, and m/z 686, respectively. The secondary ozonide (SOZ)
	and sodiated alcohol products show up in the spectra at
	m/z 796 and m/z 662, respectively. (b) Summary
	of heterogeneous oxidation of POPG with O <sub>3</sub> at the
	air-liquid interface. R' is H for water and CH <sub>3</sub> for
	methanol
7.4	(a) Air-liquid interfacial oxidation of SP- $B_{1-25}$ by $O_3$ as a function
	of time. In the absence of ozone, the positive ion FIDI-MS spectrum
	of $SP-B_{1-25}$ is dominated by the doubly protonated $SP-B_{1-25}$ peak
	at m/z 1,465. The products at m/z 1,481 and m/z 1,489 correspond to
	doubly protonated SP- $B_{1-25}$ with two oxygen atoms and with three
	oxygen atoms, respectively, appear after the droplet is exposed to
	O <sub>3</sub> for 5 s. The triply oxygenated product at m/z 1,489 dominates
	the FIDI-MS spectrum after exposing the droplet to O <sub>3</sub> for 10 s. No
	further oxidation of the peptide is observed up to 30 s of exposure.
	(b) FIDI-MS <sup>2</sup> of doubly charged triply oxygenated SP-B <sub>1-25</sub>
	product from heterogeneous oxidation yields an exclusive fragment

xxiv List of Figures

	at m/z 1,457 resulting from the elimination of hydrosulfinylmethane (CH <sub>4</sub> SO). (c) The oxidation mechanisms of Trp by ozonolysis and hydrolysis with hydrolysis mechanism of Met in peptide. (d) Air-liquid interfacial oxidation of SP-B <sub>1-25</sub> by O <sub>3</sub> in the POG monolayer as a function of time. Doubly protonated SP-B <sub>1-25</sub> products with two oxygen atoms and with three oxygen atoms appear after the droplet is exposed to O <sub>3</sub> for 10 s. The triply oxygenated product dominates the FIDI-MS spectrum after exposing the droplet to O <sub>3</sub> for 15 s and no further oxidation of the peptide is observed up to
7.5	30 s of exposure
7.6	the lipid layer. The lipid surface densities are ( <b>a</b> ) 55 Å <sup>2</sup> /lipid, ( <b>b</b> ) 60 Å <sup>2</sup> /lipid, ( <b>c</b> ) 65 Å <sup>2</sup> /lipid, and ( <b>d</b> ) 70 Å <sup>2</sup> /lipid. <i>Blue lines</i> denote the density profiles of oxygen atoms of water molecules, <i>black lines</i> denote that of saturated carbons of lipid acyl chains, and <i>red lines</i> denote that of unsaturated carbons of lipid acyl chains
	POG monolayer at 60 Å <sup>2</sup> /lipid. The peptide is shown in <i>rainbow</i> color (C-terminal: <i>red</i> , N-terminal: <i>blue</i> ). Lipids, water molecules, and chloride are shown in <i>purple</i> , <i>cyan</i> , and <i>red</i> , respectively. (b) AA hydrophobicities [46] ( <i>top</i> ) and $\Delta z$ of $C_{\alpha}$ of each residue averaged during the last 0.5 ns of a 2.0 ns duration MD simulation ( <i>bottom</i> ) are plotted as a function of amino acid residue number. The air/water interface is located near $\Delta z = 0$ . (c) Atomic density profiles of
	SP-B <sub>1-25</sub> in POG monolayer at $60 \text{ Å}^2$ /lipid as a function of $\Delta z$ during the last 0.5 ns of the 2.0 ns MD simulation. <i>Blue dash line</i> denotes the density profiles of oxygen atoms of water molecules. <i>Black</i> and <i>red dash lines</i> denote those of separately summed saturated and unsaturated carbons of lipid acyl chains, respectively. <i>Wine, magenta, cyan,</i> and <i>olive solid lines</i> denote the 100 times scaled density profiles of the $C_\alpha$ carbon of Cys <sub>8</sub> , Trp <sub>9</sub> , Cys <sub>11</sub> , Met <sub>21</sub> residues, respectively 118
7.7	(a) The $xy$ -projected density profiles of saturated carbon atoms of lipid acyl chains from MD simulations is shown with colors and the averaged positions of $C_{\alpha}$ carbons of $SP-B_{1-25}$ in the POG monolayer is shown with a <i>black line</i> (each residue is shown with cross). (b) Top view of final snapshot after 2.0 ns of MD simulation of $SP-B_{1-25}$ in
	a POG monolayer at 60 Å <sup>2</sup> /lipid. The peptide is shown in <i>rainbow color</i> (C-terminal: <i>red</i> , N-terminal: <i>blue</i> ). Lipids and water molecules are shown in <i>gray</i> and <i>cyan</i> , respectively. <i>Black spheres</i> denote unsaturated carbon atoms of lipid acyl chains, and <i>orange spheres</i>
	denote hydroxyl oxygen atoms

List of Figures xxv

7.8	(a) Final snapshot after 2.0 ns MD simulation of SP-B <sub>1-25</sub> in POPG
	monolayer at 60 Å <sup>2</sup> /lipid is shown at <i>top panel</i> . The peptide is shown in <i>rainbow color</i> (C-terminal: <i>red</i> , N-terminal: <i>blue</i> ), lipids in
	gray, water molecules in cyan, and chloride ions in red. Lower left
	and right show that Arg residues and Lys residues (displayed with
	sticks) are interacting with phosphate groups of lipids, respectively.
	(Phosphorous atoms are in <i>magenta</i> .) ( <b>b</b> ) AA index for hydrophobicity
	scale [46] (top) and $\Delta z$ of $C\alpha$ of each residue averaged during the
	last 0.5 ns trajectory of 2.0 ns duration MD simulations (bottom) are
	plotted as a function of amino acid residue number. The air/water interface is located near $\Delta z = 0$ . (c) Atomic density profiles of
	SP-B <sub>1-25</sub> in POG monolayer at 60 Å <sup>2</sup> /lipid as a function of $\Delta z$ during the last 0.5 ns of the 2.0 ns MD simulation. <i>Blue dash line</i> denotes the
	density profiles of oxygen atoms of water molecules. <i>Black and red</i>
	dash lines denote those of saturated and unsaturated carbons of lipid
	acyl chains, respectively. Wine, magenta, cyan, and olive solid lines
	denote the 100 times scaled density profiles of the $C_{\alpha}$ carbon of Cys <sub>8</sub> ,
	Trp <sub>9</sub> , Cys <sub>11</sub> , and Met <sub>21</sub> residues, respectively
7.9	The xy-projected density profiles of saturated carbon atoms of lipid
	acyl chains is shown with colors and the averaged positions of $C_{\alpha}$
	carbons of SP-B <sub>1-25</sub> in the POPG monolayer is shown with a <i>black</i>
0 1	line (each residue is shown with cross)
8.1	Total time taken for the complete P-to-T transition, $t_{P-to-T}$ by varying the area of the periodic simulation cell as $10 \times 10 = 100$ ,
	$30 \times 30 = 900, 40 \times 40 = 1600, 50 \times 50 = 2500, \text{ and } 60 \times 60 = 3600.$
	Black line denotes the change of $t_{P-to-T}$ under the external field of
	$F = 1.2 \text{ V/Å}$ , red line denotes the change of $t_{\text{P-to-T}}$ scaled by 10 under
	the external field of $F = 1.0 \text{ V/Å}$ , and blue line denotes the change
	of $t_{\text{P-to-T}}$ scaled by 15 under the external field of $F = 0.95 \text{ V/Å}$ . The
	$t_{\text{P-to-T}}$ value is converged at the area of 900–1600 and 2500–3600
	when $F = 1.2 \text{ V/Å}$ and $1.0 \text{ V/Å}$ , respectively. When $F = 0.95 \text{ V/Å}$ ,
	the $t_{P-to-T}$ value is not converged until the area of 3600. This infers that
	we need much larger simulation cell to get the right converged value
	of $t_{P-to-T}$ as the $F$ approaches to the critical field, $F_c = 0.56 \text{ V/Å}$ . Otherwise, we will get the overestimated value of $t_{P-to-T}$ near $F_c \dots 126$
8.2	(top panel) Electrical conductivity through the AN-OPE is estimated
0.2	based on the twisting angles from MD simulations with $(10 \times 10)$ unit
	cell. (bottom panels) The final snapshot after each step is shown with
	the populations of $\chi_1$ and $\chi_2$ , which are averaged during the last 0.5
	ns dynamics
8.3	(a) Optimized geometry for the low field structure (P) of N-OPE
	SAM. Here [0001] is the surface normal and the views are along
	z-axis (upper middle), y-axis (lower middle), and x-axis (lower
	right). The left picture is a perspective along the axis of one plane of

xxvi List of Figures

	molecules. The weak hydrogen bonding network is aligned along the	
	$[11\bar{2}0]$ direction. (b) Optimized geometry for the high field structure	
	(T) of N-OPE SAM. Here [0001] is the surface normal and the views	
	are along z-axis (upper middle), y-axis (lower middle), and x-axis	
	(lower right). The left picture is a perspective along the axis of one	
	plane of molecules. The weak hydrogen bonding network is aligned	
	along the [1010] direction	130
8.4	(a) Energies of various conformations of N-OPE relative to the	
	AP conformation computed with a 0.6 V/Å external field from FF	
	calculations (black histograms). (b) Energies of various conformations	
	of N-OPE relative to the AP conformation computed with no external	
	field from FF calculations (black histograms), and QM calculations	
	(green histograms)	131
8.5	Structures of (a) backbone part and (b) CBPQT <sup>4+</sup> ring part with	
	numbered atoms. The assigned numbers on the atoms are associated	
	with the partial charge distribution data shown in Table 8.1, 8.2,	
	and 8.3	132
8.6	(a) Quadruply charged SP- $B_{1-25}$ and oxidized products from (b)	
	the bulk-phase O <sub>3</sub> reaction and (c) the Fenton reaction with intact	
	SP- $B_{1-25}$ . (d) Triply charged SP- $B_{1-25}$ and oxidized products from	
	(e) the bulk-phase O <sub>3</sub> reaction and (f) the Fenton reaction are also	
	shown	162
8.7	(a) The ESI mass spectrum of the trypsin digests of $SP-B_{1-25}$ in	
	positive mode. (b) The ESI mass spectrum of the trypsin digests of the	
	oxidized SP- $B_{1-25}$ from the bulk-phase $O_3$ reaction in positive mode.	
	(c) The negative mode ESI mass spectrum of the trypsin digests of the	
	oxidized SP-B <sub>1-25</sub> from the bulk-phase O <sub>3</sub> reaction	164
8.8	(a) The CID spectrum of cationic IQAMIPK $+$ 30 at m/z 817 from	
	the tryptic digest of the oxidized SP- $B_{1-25}$ . (b) The CID of cationic	
	FPIPLPYCWLCR $+$ 8O at m/z 1,636 from the tryptic digest of the	
	oxidized SP-B <sub>1-25</sub> . (c) The CID of anionic FPIPLPYCWLCR $+$ 80	
	at m/z 1,634 from the tryptic digest of the oxidized SP- $B_{1-25}$	165
8.9	ESI-MS <sup>2</sup> of triply oxygenated products of quadruply protonated	
	$SP-B_{1-25}$ from (a) bulk-phase $O_3$ application, and from (b) the	
	Fenton reaction. M denotes a parent ion, which is triply oxygenated	
	SP-B <sub>1-25</sub>	166

#### **List of Tables**

2.1	AN-OPE interaction energies, $U_{ij}$ , for Monte Carlo (MC) calculations	13
3.1	Free energy barriers, rate constants, and relaxation half-lives from	13
	DNP toward TTF (DNP $\rightarrow$ TTF) at 298 K (all simulation results from	
	this work)	37
4.1	Vapor pressures, water uptake/cell, water coordination numbers of the water molecule (up to 3.7 Å cutoff), water coordination numbers of the sodium ion (up to 3.5 Å cutoff), and diffusion coefficients from NPT MD at temperature of 298.15 K	59
4.2	Temperature, water uptake/cell, and diffusion coefficients at constant	33
7.2	pressure condition of 101.3250 kPa	59
5.1	Drift times, reduced mobilities, and collision cross-sections of	
	ammonium cations in N <sub>2</sub> drift gas	71
5.2	Critical impact parameter, $b^*$ , Langevin capture cross-section, $\Omega_L$ , and mean relative kinetic energies, KE, during the experiments with	
	experimentally determined hard-sphere collision radius, $R_c$ for each	70
5.3	ammonium cation	76
	ammonium cations	80
6.1	Mass, drift time, and corrected drift time of ion molecule used in this	
	study	88
6.2	Optimized partial charge distribution of protonated phosphate from the DFT calculation of protonated dimethyl phosphate (the partial	
	charges with atom types for CHARMM force field are tabulated.)	90
6.3	Collision cross-sections of phosphatidylcholine cations in N <sub>2</sub> drift gas estimated and evaluated using empiric calibration method	
	and equations from Shavartsburg and Smith [27], respectively.	
	Theoretically determined collision cross-sections in N <sub>2</sub> and He are	
	also listed	95
6.4	Theoretically determined collision cross-sections $(\Omega_D)$ of	
	phosphatidylcholine cations at minimum energy state $(E_0)$ . The	
	differences of $\Omega_D$ ( $\Delta\Omega_D$ ) and potential energy ( $\Delta E$ ) from the PC	
	structure at $E_0$ to experimentally determined $\Omega_D$	102

xxviii List of Tables

Partial charge distribution of neutral rotaxane when the center of	
mass of the CBPQT <sup>4+</sup> ring moves from $z = 10.92 \text{Å}$ (TTF side) to	
$z = 44.83 \text{Å}  (DNP  \text{side})  \dots $	133
Partial charge distribution of $+1$ oxidized rotaxane when the center	
of mass of the CBPQT <sup>4+</sup> ring moves from $z = 10.92 \text{Å}$ (TTF side) to	
$z = 44.83 \text{Å}  (DNP  \text{side})  \dots $	142
Partial charge distribution of $+2$ oxidized rotaxane when the center	
of mass of the CBPQT <sup>4+</sup> ring moves from $z = 10.92 \text{Å}$ (TTF side) to	
$z = 44.83 \text{ Å (DNP side)} \dots$	151
	mass of the CBPQT <sup>4+</sup> ring moves from $z=10.92\text{Å}$ (TTF side) to $z=44.83\text{Å}$ (DNP side)

#### Chapter 1 Introduction

Abstract Many chemical and physical problems in complex systems such as nanoand bio-systems have multiscale and multiphysics characteristics. To understand these systems, we developed multiscale and multiphysics simulation methods by overcoming the limitations of time- and length-scales. Here the key issue is to extend current computational simulation methods to be useful for providing microscopic understanding of complex experimental systems. We discussed the multiscale simulation approaches in nanoscale metal-insulator-metal junction, molecular memory, ionic transport in zeolite systems, dynamics of biomolecules such as lipids, and model lung system. Based on the cases discussed here, we expect that multiscale modeling procedures will be an interdisciplinary tool that can combine the developments occurring independently across fields.

Generally, a great number of chemical and physical problems in real-life have multiscale and multiphysics features. Many observable physical quantities originate from multiple physical phenomena working cooperatively at different time- and length-scale. Interestingly, it is well known that different regimes are interpreted in terms of the different physics, which are inter-connected to each other through the "coarse-graining of the scale." Exemplifying, quantum mechanics (QM) governs the physics between nuclei and electrons. Classical mechanics (CM) governs the atomic or molecular dynamics on the complex energy surface, which is the outcome of the quantum mechanical interactions. The material flow is described by rheology, which coarse grains the particles into a continuum. Here, the governing parameters of such rheology are determined by the inter-molecular interactions.

Computational simulation methods, along with statistical mechanics, have been employed as a useful tool to expand our knowledge of microscale events and connect them into macroscopic observances. Thanks to the development of many simulation methods at various scales and the combination of these methods within a multiscale and multiphysics simulation paradigm (Fig. 1.1), computational simulation is now regarded as an indispensable tool for the new advancement in science and engineering. In a good number of cases, computer simulations efficiently supplement experiments in interpreting observations, otherwise research would be too expensive or dangerous. On the contrary, in many others, computer simulations are the only

1

2 1 Introduction

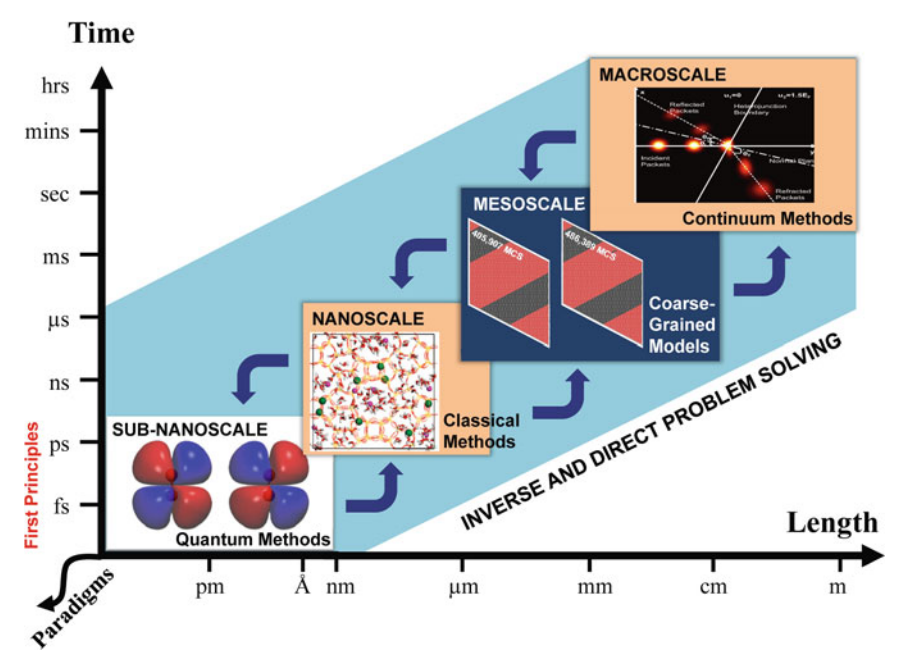


Fig. 1.1 Multiscale and Multiphysics paradigm simulation strategy

possible choice to probe the complicated phenomena. In this context, the tremendous quest for ever-higher levels of detail and realism in such simulations, contribute to the inexorable demand for new theory, methods, and computational tools.

Currently, an enormous amount of research is focused on nano- and bio-systems. Research on nano-systems is most often centered on predicting nanoscaled transport properties such as electron, thermo, and mass transportations for the application of next-generation electronic devices or alternative energy materials. Research on biosystems has significant potential in life science and medical applications. In particular, such nano- or bio-systems have a strong multiscale and multiphysical nature within them, intriguing the quest for the development of an elaborated methodology to understand the scale-dependent physics. Specifically, in nano-systems (Fig. 1.2), electron transport through a molecule is strongly dependent on the energy eigen states of the molecule (QM regime), which are affected by the molecular/ atomic conformations and motions (CM regime). When we design an engineering process for manufacturing electronic device such as ultimate complementary metal-oxide-semiconductor (CMOS) electronics using novel materials, continuum level theory and simulations are important. In bio-systems (Fig. 1.3), lipid layers encapsulate cells and control fluidity and surface tensions, which are macroscopic/hydrodynamic regime quantities. These macroscopic changes are yielded by the inter-molecular interactions at the interface (CM region). In the lower scale, such molecular interactions are often tuned by chemical reactions such as a proton transfer, which has a strong QM effect.

1 Introduction 3

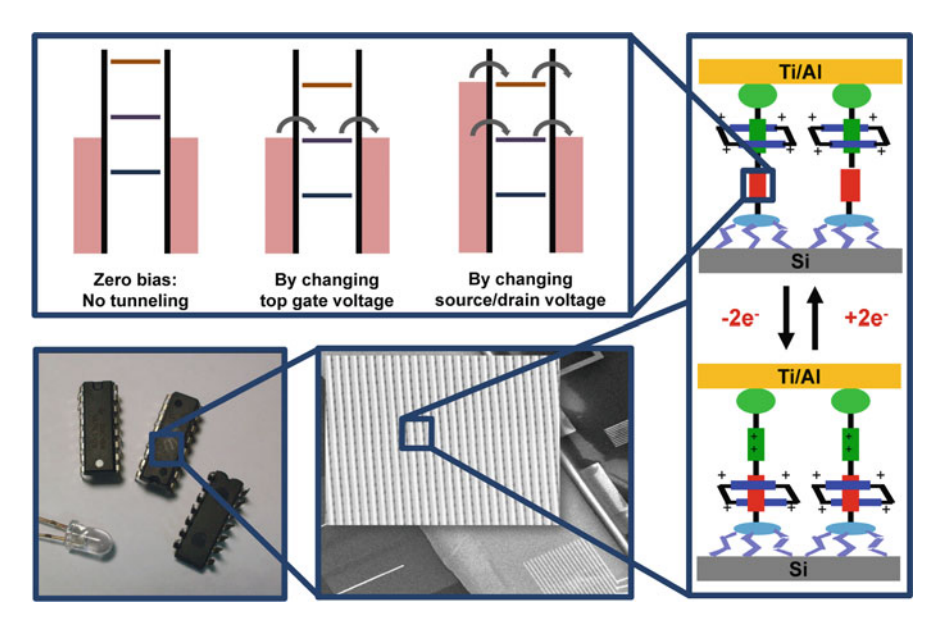


Fig. 1.2 Multiscale and Multiphysics characteristics in nano electronic systems. At electron size scale, electrical conductivity depends on the quantum states of the molecules. At molecular size scale, classical interactions determine the molecular conformation, which affects its quantum state. At device size scale, hundreds of molecules are assembled to build a mesoscale junction and these are packaged into a device component. Courtesy of Dr. Jang Wook Choi; Korea Advanced Institute of Science and Technology (scanning electron microscope image of the nano electronic system in the bottom-middle panel)

Within contemporary computing power, direct use of first principle computational methods is limited by an order of  $\sim 1,000$  atoms and an order of pico to nano seconds. Thus, for managing many practical issues in using computational simulation methods which often involve a large length- and long time-span, we need to overcome the limitations in simulation scales. In this thesis, several cases of nanoand bio-systems are presented; (1) we understand them by capturing fundamental nanoscale intrinsic and extensive properties, then, (2) we define the macroscopic behavior observed from experiments based on the microscopic understandings.

The first half (Chapters 2–4) discusses the multiscale and multiphysics simulation approaches for nano-systems.

In Chapter 2, we investigate a negative differential resistance (NDR) effect observed from a metal/molecular SAM/metal junction. Amino- and nitrosubstituted oligo-phenylene ethynelene (OPE) molecules in the self-assembled monolayer (SAM) have a large molecular dipole moment, which responds to the external electric field. Hence, applying the bias voltage induces the conformational changes of the individual molecules and thereby yield a structural transition of the SAM. Such a conformational change is in the regime where the molecular dynamics (MD) simulation is useful. However, the kinetics during the structural relaxation of the SAM requires larger scale simulation methods. On the other hand, electrical

4 1 Introduction

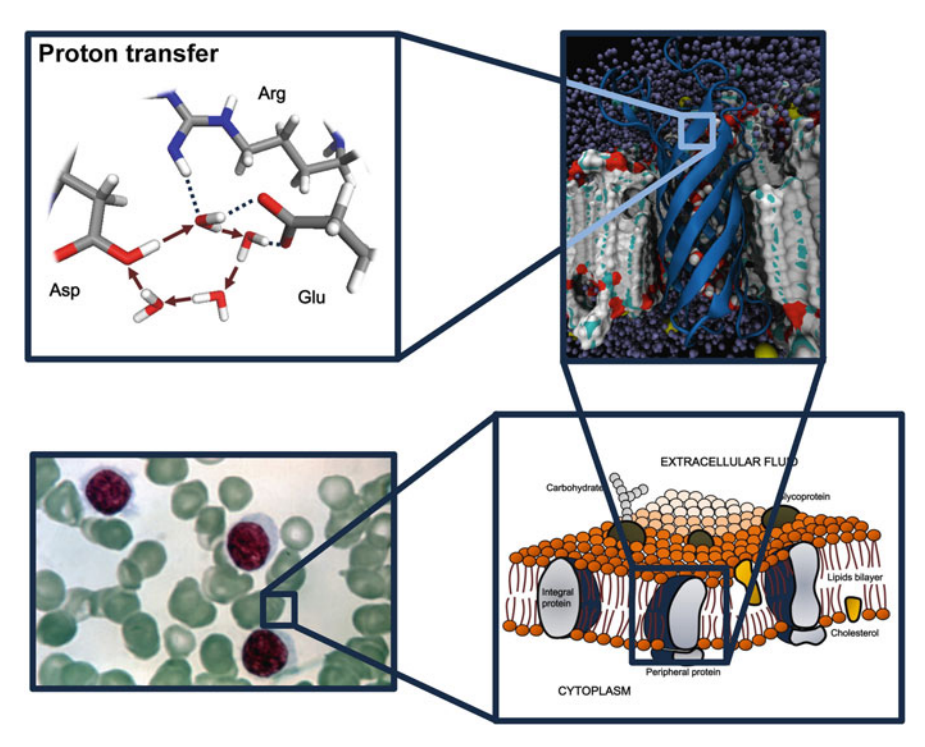


**Fig. 1.3** Multiscale and Multiphysics characteristics in bio systems. At electron size scale, chemical reactions, which are governed by huge QM effects (e.g. electron/proton transfer), regulate the molecular architecture of the protein for an effective functionality. At molecular scale, CM describes the interactions, such as hydrophobic interaction, among the bio components of proteins, lipids, etc. Large scale motion of the membrane, such as endo- or exo-vesiculation, is in the regime of hydrodynamic descriptions, and this affects the dynamics of a cell. Courtesy of Dr. Tod A. Pascal; California Institute of Technology (trans-membrane protein figure in the *top-right panel*). Optical microscope image of the cells (*bottom-left panel*) is obtained from the National Institutes of Health (NIH) image bank

conductivities on the total I-V curve are rooted in QM. In order to manage such a complicated problem, we design a nearest neighbor (NN) model with lattice Monte Carlo (MC) simulation, whose parameters are obtained by coarse-graining QM and MD simulation results. The electrical conductivities depending on the conformations are parameterized using non-equilibrium Green function theory combined with QM.

In Chapter 3, on/off kinetics of the molecular switch, bistable [2]rotaxane is discussed. The rotaxane has been intensively studied because of its interesting properties, which are attributed to the molecular recognition between charge donor and acceptor. The shuttling motion of electron accepting cyclobis-(paraquat-p-phenylene) (CBPQT<sup>4+</sup>) between the charge donating stations such as tetrathiafulvalene (TTF) and 1,5-dioxynaphthalene (DNP) moieties, has brought many applications such as molecular switch in nanoelectronics and artificial muscle in

1 Introduction 5

nanomechanics. Therefore, comprehensive understanding of the free energy barrier required for this shuttling motion is essential. In addition, the fine control of the free energy barrier can open an application of the rotaxane system toward non-volatile flash memory devices, which has not yet achieved. Since the ring and backbone form a charge transfer complex, the local charge distribution (OM effect) strongly determines the free energy profiles for the rings shuttling. However, the time scale for the shuttling is order of µs, which is beyond the available time scale of atomistic simulations. To handle such difficulties, we perform a "blue moon sampling technique" with MD simulations, which allows an effective sampling using a series of constraint MD simulations. The change of potential energy surface depending on the charge transfer amount is reflected on the MD simulations using various Mulliken charge populations from QM calculations according to the ring's location. The free energy barrier from the TTF station to the DNP station is evaluated as 19 kcal/mol when the system is neutral and 8-9 kcal/mol for the oxidation states +1 and +2, and the free energy barrier from the DNP station to the TTF station is 18 kcal/mol, 22–23 kcal/mol, and 32–33 kcal/mol for the neutral and the oxidation states +1 and +2, respectively. These values are quite comparable to the values that were obtained from various prior experiments, and greatly explain the microscopic ground for the on/off switching kinetics of the molecular switch.

In Chapter 4, the diffusion process of sodium ion in the aluminum-doped zeolite BEA system is studied. Understanding the ionic diffusion through a percolated pore of the zeolite is important for the application of the zeolite to proton exchange membranes for fuel cells (PEMFC). Especially, investigating the role of the confined water is vital because it provides a medium for transport of the ions. The amount of water swelled into the PEMFC depends on the macroscopic variables, such as pressure and temperature, where the PEMFC is working. Thus, combining the grand canonical Monte Carlo (GCMC) simulations (for the study of water uptake amount) with MD simulations (for the study of confined water structure), we investigate the effect of water on the sodium diffusion. We observe a first-order-like transition from the absorption isotherm, inferring that zeolite provides a hydrophobic environment. From MD trajectories, we observe the sodium ions diffused via a hopping mechanism among aluminum-doped sites (which are Brönsted acid sites). We figure out that, above 15 wt.% hydration (good solvation regime), the solvation cage is easily formed, and dramatically increases sodium diffusion by reducing the hopping energy barrier by 25% from the value of 3.8 kcal/mol observed in the poor solvation regime.

The second half (Chapters 5–7) discusses the multiscale and multiphysics simulation approaches for bio-systems. In particular, we scrutinize lipid systems, which have critical roles in cell structure, energy storage and metabolic control, using computational methods in collaboration with gas-phase experiments.

In Chapter 5, we study the ion mobility of a number of tertiary amine and quaternary ammonium cations in gas-phase. These tertiary amine and quaternary ammonium cations are related to the choline and its derivatives, which are precursors for lipids such as a phosphatidylcholine and sphingomyelin. For example, choline is oxidized to betaine, which is readily demethylated to yield *N*, *N*-dimethylglycine.

6 1 Introduction

Decomposition of choline yields trimethylamine and dimethylamine. Ion mobility in gas phase is determined by the collision of the ion with drift gas molecules. Utilizing the kinetic theory under the assumption of binary collision, the ion mobility in gas-phase is formulated as a complex integration of interaction terms between the ion and the drift gas molecule. We develop a methodology (referred to as modified trajectory (TJ) method) for the numerical integrations of complex interaction terms for the case where the ion drifts within the N2 buffer gas. Since the interaction terms depend on the electron distribution and molecular conformation, the gas phase structures and the charge distributions are investigated using QM calculations. Then, ion mobilities are calculated using the modified TJ method. The calculated ion mobility is in agreement with the experimental value, and it well explains the observed mass-mobility correlation of tertiary amine and quaternary ammonium cations, in terms of the asymmetry of the shape. In addition, computational numerical study allows us to identify the role of each interaction term (van der Waals interaction, ion-induced dipole interaction, ion-quadrupole interaction, charge-charge interaction) on the ion mobility at the border-line regime, which lies between the regime where the long-range interactions are dominant (small ion size) and the regime where the short-range interactions are dominant (large ion size).

In Chapter 6, we expand the ion mobility study of lipid precursors in Chapter 5 into the study of the intact lipids of phophatidycholines (PC). Since the PC contains a flexible acyl chain, the molecular fluctuation changes the mobility of the PC cation. Taking the molecular fluctuation effect into account, 200 conformations are sampled from the MD simulations, then, the average collision cross-section is computed using the modified TJ method for the calculation of ion mobility. Here, for the experimental section, a commercial traveling wave ion mobility spectrometry (TWIMS) has been employed. Our simulation results exhibit a good agreement with the experimental values. In particular, we reveal that the traveling wave applied in the experiments excites the ions. Since this excitation yields a less compact form of saturated PCs, while unsaturated PCs can not form such a stretched conformation due to the rigid double bonds, we observe distinct mass-mobility correlation lines for the saturated PC cations and for the unsaturated PC cations.

In Chapter 7, a model lung surfactant system composed of lipid monolayer with surfactant protein B (SP-B) is examined. Lung disease is the third leading cause of death in United States, and concerns about chronic respiratory tract disease increase significantly as the level of air pollution increases. Thus, chemical and physical comprehensions about the response of pulmonary surfactant (PS) system to ozone (O<sub>3</sub>), one of the most common air pollutants, are required. Due to the interfacial characteristic of PS, the ozonolysis of PS can undergo different pathways according to the reaction environment, especially, depending on whether or not the reaction occurs under water-rich conditions. From the multiscale/multiphysics point of view, the ozonolysis is the result of the QM effect, but the reaction environment is determined by the location of each component, which is the outcome of the CM interactions among the molecules. In addition, the change of physical properties of PS (e.g. surface tension) is in the regime of larger-scale physics such as

1 Introduction 7

hydrodynamics. In this chapter, a complete study on the response of lipid monolayer to  $O_3$  is achieved at the air–liquid interface when  $O_3$  is introduced from the air. The chemical composition changes during the heterogeneous  $O_3$  reaction are analyzed using field induced droplet ionization (FIDI) mass spectrometry, which exhibits quite a different reaction pathway to the bulk-phase ozone reaction. Our MD simulation provides molecular level understanding and rationalization for the observed distinct reaction pathways.

Depending on the characteristics of systems and the objectives that we want to figure out, as exemplified in this thesis, distinct approaches are required to explain the actual observations from experiments. Based on the cases discussed here, we suggest various systematic strategies to overcome the limitations in time-and length-scales of the traditional monoscale approaches. In addition, due to the nature of multiscale and mutiphysics phenomena, we expect that a concrete establishment of the fundamental multiscale modeling procedures will invoke interdisciplinary studies by tightly combining the developments occurring independently across fields.

## Chapter 2 Negative Differential Resistance of Oligo (Phenylene Ethynylene) Self-Assembled Monolayer Systems: The Electric Field Induced Conformational Change Mechanism

**Abstract** We investigate here a possible mechanism for the room temperature Negative Differential Resistance (NDR) in the Au/AN-OPE/RS/Hg self-assembled monolayer (SAM) system, where AN-OPE = 2'-amino, 5'-nitro oligo (phenylene ethynylene) and RS is a C14 alkyl thiolate. Kiehl and co-workers showed that this molecular system leads to NDR with hysteresis and sweep-rate-dependent position and amplitude in the NDR peak. To investigate a molecular basis for this interesting behavior, we combine first principles quantum mechanics (QM) and meso-scale lattice Monte Carlo (MC) methods to simulate the switching as a function of voltage and voltage rate, leading to results consistent with experimental observations. This simulation shows how the structural changes at the microscopic level lead to the NDR and sweep-rate dependent macroscopic *I-V* curve observed experimentally, suggesting a microscopic model that might aid in designing improved NDR systems.

#### 2.1 Introduction

Esaki's discovery of the negative differential resistance (NDR) in Ge *p-n* diodes opened a new phase in semiconductor devices [1]. Since the NDR devices enable faster and more efficient circuits by reducing the number of transistors required, they have many applications such as high-speed integrated circuits and low-power memories. As the scale of electronic devices is reduced toward nano-scale sizes, it would be useful to demonstrate NDR in molecular electronic systems [2–13].

Derivatives of oligo (phenylene ethynylene) (OPE) have been identified as a good candidate for the molecular junctions due to its rigid and good conducting (fully conjugated) characteristics [9, 11–19]. Chen et al. reported that a SAM of aminonitro substituted OPE (AN-OPE) between two Au electrodes exhibits NDR at 60 K with an applied voltage of  $\sim$ 2 V. The current-voltage (I-V) curve is fully reversible, but the NDR peak decays as the temperature increases. This NDR has been rationalized by the electrochemical oxidation/reduction or resonant-tunneling mechanism [15–17]. Support for this oxidation/reduction mechanism was the correspondence

between the threshold potential for the electrical conductance (2.09 V) and the electrochemical potential (1.67 V) [15, 19].

The device showing NDR at room temperature (RT) is important for many practical applications [20, 21]. However, the poor reproducibility in device construction and the limited device stability have hampered extensive study on NDR. Kiehl and co-workers showed that a SAM of AN-OPE deposited on an Au electrode coupled to a Hg electrode covered with a tetradecane-thiolate (RS) leads to a well-defined and stable NDR at RT [9]. In this system, a distinct sweeping-rate-dependency in the NDR hysteresis loop was observed for a bias voltage near  $\sim 0.6$  V. The presence of hysteresis rules out the resonant tunneling mechanism [5–8, 10]. Based on the observed hysteresis and a variety of detailed features of the characteristics, they proposed a charge capture (QC) mechanism to explain the macroscopic I-V behavior. However, an atomistic level analysis of a charge capture process and other possible mechanisms has not yet been established.

Several studies suggest that the conformational change would be a plausible mechanism to explain hysteretic *I-V* curve [14, 22], and the external electric field can induce conformational change of the molecule in the junction [14, 23–26]. Especially, Donhauser et al. reported STM studies in which isolated AN-OPE molecules contained in a dodecane-thiolate SAM on the Au substrate show at least two states having different conductances [14]. They showed that the transition from the high-conductance state to the low-conductance state is switched by applying external electric field. However no detailed atomic level description of the mechanism was provided.

In this chapter, we use first principle theory to analyze the sweeping-ratedependent hysteresis of NDR observed in Kiehl's system, focusing on the possibility of electric field based conformational changes. We find that this system has two states:

- a high-conductance phase stable at low field (planar structure) and
- a low-conductance phase stable at high field (twisted structure).

The transition between the two phases is driven by the interaction between the external field and the molecular dipole moment of the middle phenylene ring in AN-OPE. This leads to consistent results with the charge capturing mechanism of Kiehl. Using coarse-grained Monte Carlo simulations, we investigated how such a molecular conformational change results in a sweep-rate-dependent hysteresis in the NDR as well as the detailed kinetics of transition.

#### 2.2 Simulation Details

# 2.2.1 Computational Details of QM Calculations

To obtain the structures and energies of planar (P) and twisted (T) structures, we carried out QM calculations for a  $(1 \times 1)$  periodic unit cell. We employed the Perdew-Burke-Ernzerhof (PBE) generalized gradient approximation exchange-correlation density-functional with a plane wave basis set (540 eV cutoff), using the Vienna

2.2 Simulation Details 11

Ab initio Simulation Package (VASP) [27]. Only the gamma point is sampled in reciprocal space to reduce computational cost for this large system (67 atoms per periodic cell). For the electrodes, we used 3-layer of Au (111) surface with all gold atoms fixed at their bulk value ( $a=2.8838\,\text{Å}$ ) during the geometry optimization steps. The OPE molecules were anchored on the  $3\times3$  Au (111) surface through sulfur atoms with hexagonal packing.

To understand the local electronic structure and local interactions of the AN-OPE part, we performed non-periodic QM calculations of the isolated OPE with 3 connected Au atoms, using Jaguar package [28] with PBE exchange-correlation functional and LACVP\*\* basis set. Using the geometries from VASP calculations, we carried out the single point calculations.

# 2.2.2 Conductivities of P and T Conformations (NEGF Calculations)

The *I-V* performance of each conformation is calculated by combining Green's function theory with the DFT Hamiltonian that are determined from the SeqQuest calculation with PBE functional [29, 30]. The current is calculated using following equation:

$$I(v) = \frac{2e}{h} \int_{-\infty}^{\infty} T(E, V) \left[ f_1(E, V) - f_2(E, V_2) \right] dE,$$
 (2.1)

where T(E, V) is the transmission function for the AN-OPE SAM part.

# 2.2.3 Coarse-Grained NN Interacting Hamiltonian

The NN interacting Hamiltonian which describes the AN-OPE SAM is

$$H = \sum_{i=1}^{N} \left( E_i^{torsion} \left( \chi \right) - D_i F \right) + \sum_{NN} U_{ij}, \tag{2.2}$$

where  $E_i^{torsion}(\chi)$  is the internal torsional energy of the *i*-th AN-OPE molecule due to twisting the AN-OPE by an angle  $\chi$ ,  $D_i$  is the [0001] component of the dipole moment of the *i*-th AN-OPE, F is the [0001] component of the external electric field,  $U_{ij}$  is the intermolecular interaction energy between *i*-th and *j*-th AN-OPE, and summation over NN denotes that the summation is over nearest neighbors. There are two interactions each for three directions: [10 $\bar{1}0$ ], [01 $\bar{1}0$ ], and [11 $\bar{2}0$ ]. To avoid double counting, however, we used just one interaction per direction.

# 2.2.4 Extracting NN Model Parameters from QM/FF Energies

The  $U_{ij}$  terms when  $\{i, j\} \subset P$  or  $\{i, j\} \subset T$  were determined from the Jaguar calculations (*vide infra*). In order to extract  $U_{ij}$  when  $\{i \in P, j \in T\}$  or  $\{i \in T, j \in P\}$ ,

we need to investigate inter-OPE interaction in the packed system from a larger simulation cell containing more than one OPE. Since this is too expensive for QM calculations (268 atoms), we used a simple DREIDING Force Field [31] (FF) in which the charges are based on QM. We considered six possible packings within a  $(2 \times 2)$  unit cell:

- AP: all P's,
- AT: all T's,
- P3T1: 3 P's and 1 T,
- $P2T2_{10\bar{1}0}$ : 2 P's and 2 T's aligned along [10 $\bar{1}0$ ],
- $P2T2_{01\overline{1}0}$ : 2 P's and 2 T's aligned along  $[01\overline{1}0]$ ,
- P2T2<sub>11 $\bar{2}0$ </sub>: 2 P's and 2 T's aligned along [11 $\bar{2}0$ ],
- P1T3: 1 P and 3 T's.

The FF energies are shown at Fig. 2.1a, b for when no external electric field and 1.2 V/Å external electric field is applied, respectively. Using FF energies under

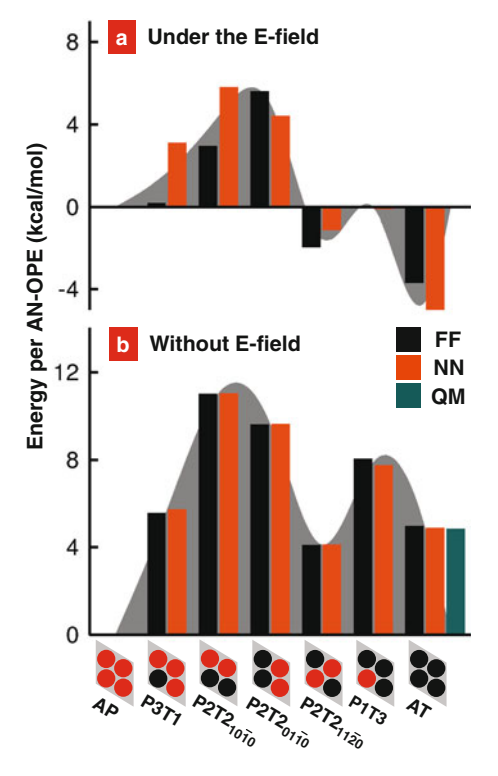


**Fig. 2.1** (a) Energies of various conformations of AN-OPE relative to the AP conformation computed with a 1.2 V/Å external field from FF calculations (*black histograms*) and NN model calculations (*orange histograms*). (b) Energies of various conformations of AN-OPE relative to the AP conformation computed with no external field from FF calculations (*black histograms*), NN model calculations (*orange histograms*), and QM calculations (*green histograms*)

2.2 Simulation Details 13

	[1010] Pair	[0110] Pair	[1120] Pair
$\{i,j\}\subset P$	-3.95	-5.00	-7.19
$\{i,j\}\subset T$	-7.66	-3.12	-0.61
$\{i \in P, j \in T\} \text{ or } \{i \in T, j \in P\}$	-5.70	-2.56	3.13

**Table 2.1** AN-OPE interaction energies,  $U_{ij}$ , for Monte Carlo (MC) calculations

All energy values are in kcal/mol.

zero external field, the  $U_{ij}$  terms when  $\{i \in P, j \in T\}$  or  $\{i \in T, j \in P\}$  were fitted. Values are in Table 2.1.

The torsional energy,  $E_i^{torsion}$  is estimated from the energy versus twisting angle  $\chi$  curve (Fig. 2.2), leading the 0.01 kcal/mol per AN-OPE when  $i \in P$ , and 0.23 kcal/mol when  $i \in T$ . The  $D_i$  values were optimized to fit the energies from Hamiltonian in Eq. 2.2 to FF energies under 1.2 V/Å external field. The fitted values are  $D_i = 5.48$  debye per AN-OPE for P and 7.30 Debye for T, which are quite comparable to the dipoles from Mulliken charge analysis,  $D_i = 5.74$  Debye per AN-OPE for P and 7.03 debye for T.

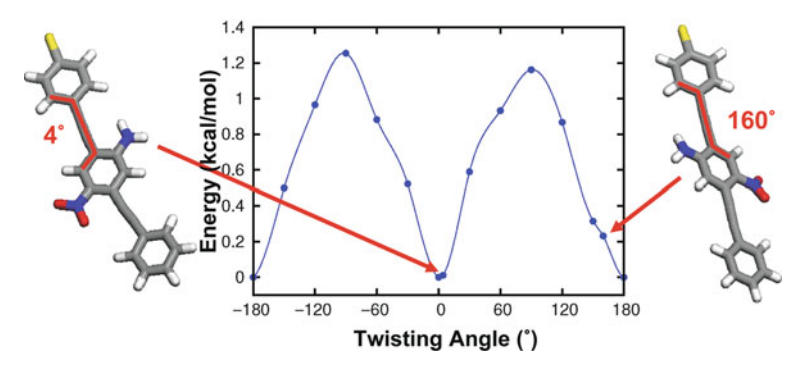


**Fig. 2.2** Torsional strain energy  $E_i^{torsion}$  as a function of twisting angle  $\chi$  from QM (PBE) on the isolated molecule. The energy at  $\chi=4^\circ$  (corresponding to P) is 0.01 kcal/mol higher than the ground state energy at  $\chi=0^\circ$ . The energy at  $\chi=160^\circ$  (which corresponds to T) is 0.23 kcal/mol higher than the energy at  $\chi=0^\circ$ , leading the 0.22 kcal/mol higher  $E_i^{torsion}$  of T compared to  $E_i^{torsion}$  of P

All MD simulations with DREIDING FF were performed using LAMMPS (large-scale atomic/molecular massively parallel simulator) MD code from Plimpton at Sandia [32, 33]. The equations of motion were integrated using the velocity-Verlet algorithm [34], with a time step of 1.0 fs.

#### 2.2.5 Coarse-Grained MC Simulations

The 2-dimensional rhombic MC simulation cell containing ( $50 \times 50$ ) lattice points with periodic boundary conditions. The MC simulations used the Metropolis

algorithm (our own code). Each Monte Carlo Step (MCS) is defined as 2,500 MC trials with a fixed external field applied in the *z*-direction. Our MC simulations are similar to the study of an Ising model in a time-dependent magnetic field [35].

#### 2.3 Results and Discussion

#### 2.3.1 Two Conformations of AN-OPE

Figure 2.3a shows the minimized conformation of AN-OPE determined from the periodic DFT calculation. The three phenylene rings are coplanar, forming a well-conjugated structure, which we label as P (for planar). Here the lowest ring is connected to the Au electrode via a thiolate group. The middle ring (containing the functional groups) has a twist angle of  $\chi=4^\circ$  with respect to the bottom ring ( $\chi=0^\circ$  for the isolated OPE). This structure packs on the Au surface as (3 × 3), with the axis of the molecule along the  $\begin{bmatrix} 1\bar{1}00 \end{bmatrix}$  direction, and a tilt angle  $\theta=66^\circ$  from the z-axis. The adjacent amino and nitro groups form hydrogen bonding (HB) networks along the  $\begin{bmatrix} 11\bar{2}0 \end{bmatrix}$  direction.

To understand the local electronic structure and local interactions of the organic molecular part, we performed a single point non-periodic QM calculation of an isolated OPE. The polar amino and nitro groups lead to a large dipole moment of 9.24 (7.22) debye with the z-axis component ([0001]) of 5.74 (3.55) debye, the component along  $\begin{bmatrix} 1\bar{1}00 \end{bmatrix}$  (tilt direction) of 4.44 (3.35) debye, and the component along  $\begin{bmatrix} 11\bar{2}0 \end{bmatrix}$  (HB direction) of 5.72 (5.32) debye. These dipole moments were determined from the analysis of Mulliken charges, while the values in parenthesis are from quantum mechanical wave-functions.

The inter AN-OPE interaction energies on the SAM,  $U_{ij}$  are determined from the difference between dimer energy and doubled monomer energy:

$$U_{ij} = E_{2 \times (AN - OPE \ w/\ 3Au)} - 2 \times E_{AN - OPE \ w/\ 3Au}, \tag{2.3}$$

where we included three Au atoms connected to the sulfur atom.

The value of  $U_{ij}$  between two P's are shown at Table 2.1, especially,  $U_{ij}$  along [11 $\overline{2}$ 0] direction shows the largest stabilization energy of -7.19 kcal/mol, due to the HB interaction.

Figure 2.3b shows the T (for twisted) conformation, which is 4.85 kcal/mol less stable than P. The middle and terminal phenyl rings are rotated from the bottom one by  $\chi=160^\circ$ . Although we note that this twist angle is not stable for the isolated AN-OPE, it becomes meta-stable in the packed system (Fig. 2.2). The rotation of the middle ring changes the direction of amino/nitro groups along  $[10\bar{1}0]$  from  $[11\bar{2}0]$ , leading the hydrogen bond network to be aligned along  $[10\bar{1}0]$ . The axis of the molecule is at  $\theta=71^\circ$  from the z-axis, which makes the T lies more down than the P. The height of the terminal phenyl ring of T is 7.60 Å while that of P is 8.73 Å from the Au surface. The lower height of T is comparable to the Don-

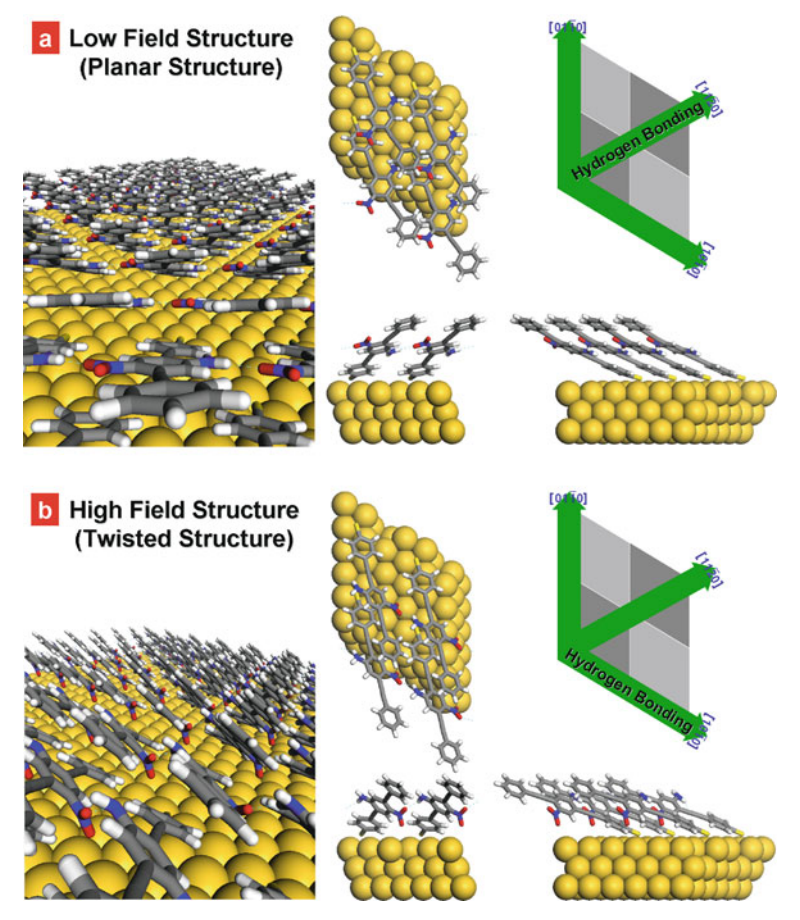


Fig. 2.3 (a) Optimized geometry for the low field structure (P) of AN-OPE SAM. Here [0001] is the surface normal and the views are along z-axis ( $upper\ middle$ ), y-axis ( $lower\ middle$ ), and x-axis ( $lower\ right$ ). The left picture is a perspective along the axis of one plane of molecules. The hydrogen bonding network is aligned along the  $[11\bar{2}0]$  direction. (b) Optimized geometry for the high field structure (T) of AN-OPE SAM. Here [0001] is the surface normal and the views are along z-axis ( $upper\ middle$ ), y-axis ( $upper\ middle$ ),  $upper\ middle$ ), and u-axis ( $upper\ middle$ ). The left picture is a perspective along the axis of one plane of molecules. The hydrogen bonding network is aligned along the  $[10\bar{1}0]$  direction

hauser's observations from the STM experiment that exhibits  $\sim$ 3 Å lower height of low conductance phase to higher conductance phase [14].

The dipole moment of T is 8.71 (6.88) debye with the component along [0001] of 7.04 (4.62) debye, a component along  $[1\bar{1}00]$  (tilt direction) of -3.32 (-3.40) debye and a component along  $[\bar{1}010]$  (HB direction) of 5.12 (5.10) debye.

The value of  $U_{ij}$  between two T's shown at Table 2.1. For T conformation,  $U_{ij}$  along the [1010] direction (HB network direction) is the most stable with the value of -7.66 kcal/mol.

#### 2.3.2 Electrical Conductivities of P and T

The electrical conductivity,  $\sigma$ , was predicted using non-equilibrium Green's function (NEGF) theory for P and T structures with QM on the  $(1 \times 1)$  unit cell. These calculations partition the tunneling Hamiltonian using the Gaussian basis function representation. The semi-infinite electrode is calculated interactively using 3 explicit layers of Au [29].

The experiments use a top Hg electrode covered with a tetradecane-thiolate (RS), the atomic structure of which is not certain due to the amorphous character of the Hg electrode and the fluctuations in the alkyl thiol at room temperature. Instead, our calculations use a second 3-layer of Au (111) surface 12 Å above the bottom electrode. We also tested placing the top electrode in contact with the OPE, which 20 Å above the bottom electrode.

The density of states (DOS) with the transmission function T(E) were computed (Figs. 2.4 and 2.6), and these are used to obtain the I-V curve and the  $\sigma$ -V curve (Figs. 2.5 and 2.7). Over the range of 0–1.5 V, we see that the average ratio of  $\sigma_P$  to  $\sigma_T$  is 10 for the thickness of 12 Å, and 163 for the thickness of 20 Å. Since the experimental value is  $\sim$ 13 fold larger  $\sigma_P$  than  $\sigma_T$ , we adopted the case of 12 Å.

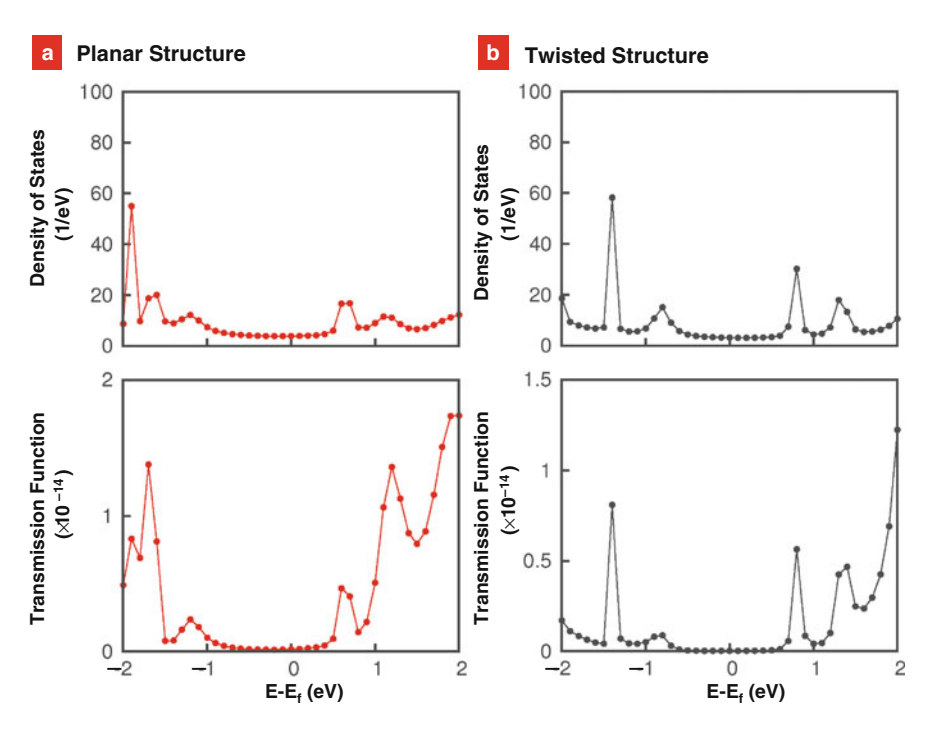


Fig. 2.4 Density of state (DOS) and transmission function T(E) of P structure (a) and T structure (b). The *top* electrode is located 12 Å above from the *bottom* electrode

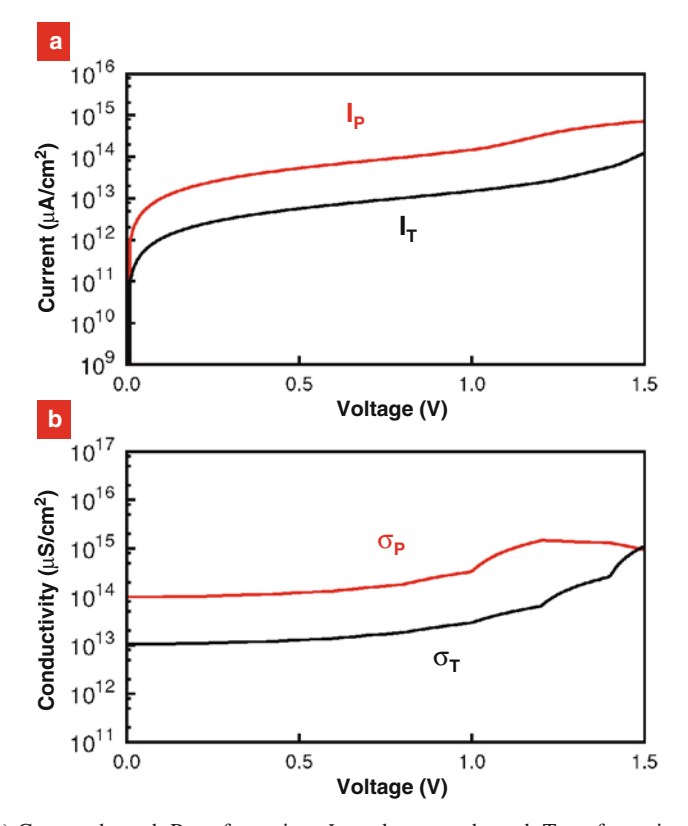


Fig. 2.5 (a) Current through P conformation,  $I_P$  and current through T conformation,  $I_T$  versus the bias voltage V determined from the NEGF calculations using the DOS and T(E) of Fig. 2.4. (b) Conductivity of P conformation,  $\sigma_P$  and conductivity of T conformation,  $\sigma_T$  versus the bias voltage V determined. The top electrode is located 12 Å above from the bottom electrode.  $\sigma_P$  is  $\sim$ 10 times larger than  $\sigma_T$ 

The calculated I-V curves lead correctly to a smaller  $\sigma$  for the high field stable phase. The difference in  $\sigma$  is explained by two factors:

- 1. the loss of  $\pi$ - $\pi$  orbital overlap due to the rotation of the middle phenyl ring (which contributes to the conductivity through the molecules) and
- 2. the increase of vacuum distance due to the lower height of T phase.

Previous studies showed that the rotation of the ring by  $\chi$  reduces the conductivity by factor of  $\cos^4 \chi$  (Fig. 2.8) [36]. Thus, using the QM minimized structures, which are twisted by 4° and 160°, yield an average ratio of  $\sigma_P$  to  $\sigma_T$  by  $\sim$ 1.3 times. However, considering the distribution of angles from the MD, we find an average ratio of  $\sigma_P$  to  $\sigma_T$  of  $\sim$ 3.5 times. (Details are discussed in Section 8.2.)

The minimized structures for P and T lead semi-log plots of I-V curves (Fig. 2.5) to show similar slopes for both phases, in disagreement with experiment showing a slope ratio of  $\sim$ 3.2. From previous study [36], we found that the slope of the

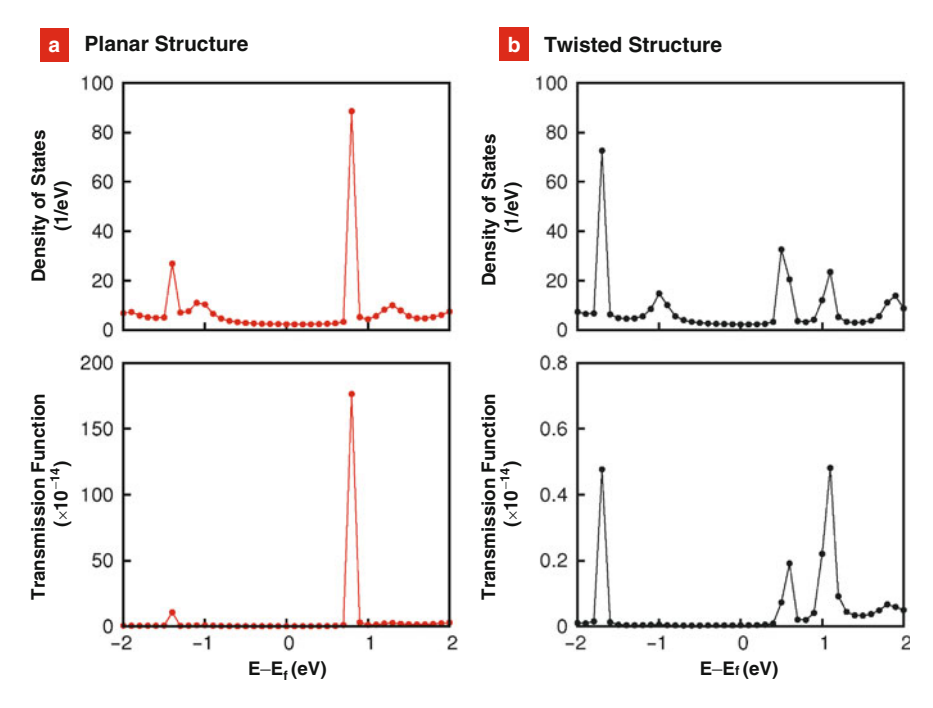


Fig. 2.6 Density of state (DOS) and transmission function T(E) of P structure (a) and T structure (b). The *top* electrode is located 20 Å above from the *bottom* electrode

semi-log plot of I-V curve strongly depends on the  $\chi$ , and it decreases until almost zero when the molecule twisted with  $\chi=90^\circ$  (Fig. 2.8a). This is a reasonable result since the slope of semi-log plot is related to the height of tunneling barrier,  $\Phi_B$  which highly depends on the  $\pi$ - $\pi$  orbital overlap. Therefore, consideration of the twisted structure from MD simulations, which has a significant population near  $90^\circ$ , well explains the distinct difference between the slopes of semi-log I-V plots for both structures observed in the experiment.

# 2.3.3 Response to Constant External Field

In order to describe the structural rearrangement process of the AN-OPE SAM, we use a  $(50 \times 50)$  unit cell containing 2,500 AN-OPE molecules. To describe the dynamics of such a large simulation cell, we developed a simplified nearest neighbor (NN) interaction Hamiltonian with the model parameters extracted from QM and Force Field (FF) energies (Fig. 2.1). Important feature of the NN model is that the energetically favorable state changes from P to T as the external electric field increases, due to the higher dipole moment along [0001] of the T phase. In this model, the critical field for which the energies of both states are same is  $F_c = 0.56 \, \text{V/Å}$ .

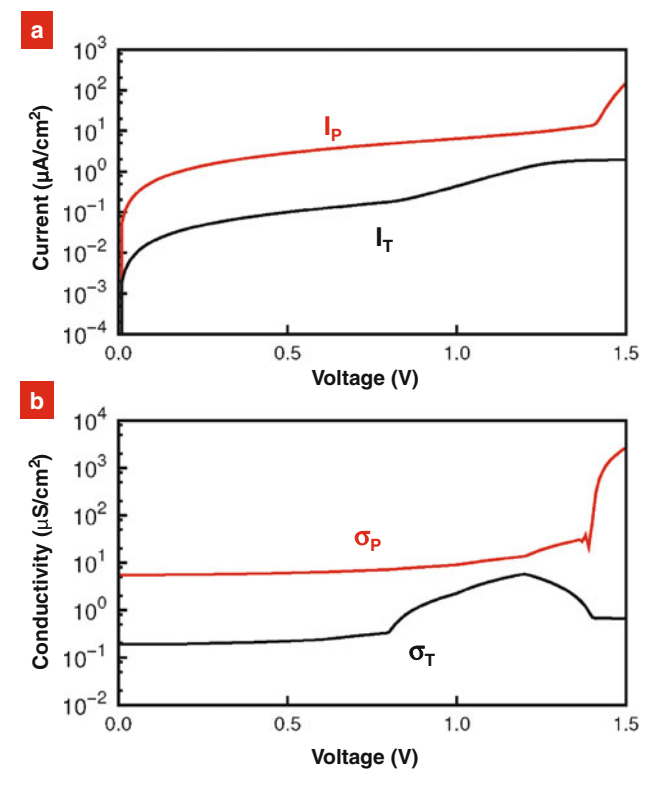


Fig. 2.7 (a) Current through P conformation,  $I_P$  and current through T conformation,  $I_T$  versus the bias voltage V determined from the NEGF calculations using the DOS and T(E) of Fig. 2.6. (b) Conductivity of P conformation,  $\sigma_P$  and conductivity of T conformation,  $\sigma_T$  versus the bias voltage V determined. The *top* electrode is located 20 Å above from the *bottom* electrode.  $\sigma_P$  is  $\sim 163$  times larger than  $\sigma_T$ .

We simulated the response of the SAM of the P's to the  $1.2\,\text{V/Å}$  external field during  $1.2\times10^6$  Monte Carlo steps (MCS) at  $T=300\,\text{K}$ . Figure 2.9a, b show the time evolution of the system starting with all P's and ending with all T's and the population change with the electrical conductivity change during this P-to-T transition, respectively. There were no T states until just before 55,184 MCS, but within the next 15 steps, half of the neighbors along [11 $\bar{2}0$ ] have transformed, and after another 15 steps the entire [11 $\bar{2}0$ ] line is transformed to the T. Then, by 405,907 MCS, totally 19 [11 $\bar{2}0$ ] lines have transformed, which are all neighbors to the original one. Then, at 486,389 MCS, we see that a second [11 $\bar{2}0$ ] swath has nucleated. By 697,272 MCS, these two have grown to 28 and 7 adjacent lines but still just two swathes, and from 697,273 MCS, they are merged into one swath. Finally, by 1,008,706 MCS the full system is transformed to T. Along with the decrease of the P population, the total conductivity through the SAM also decreases.

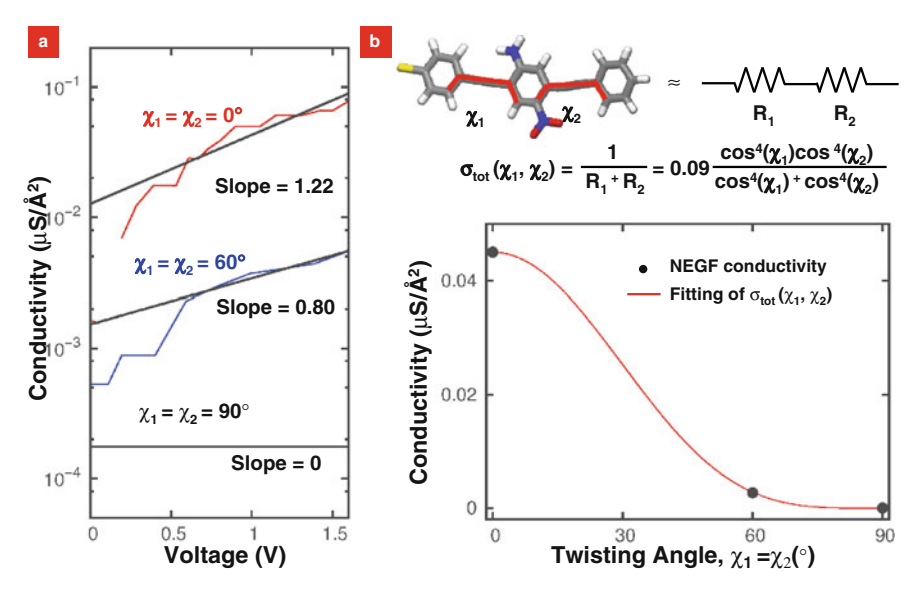
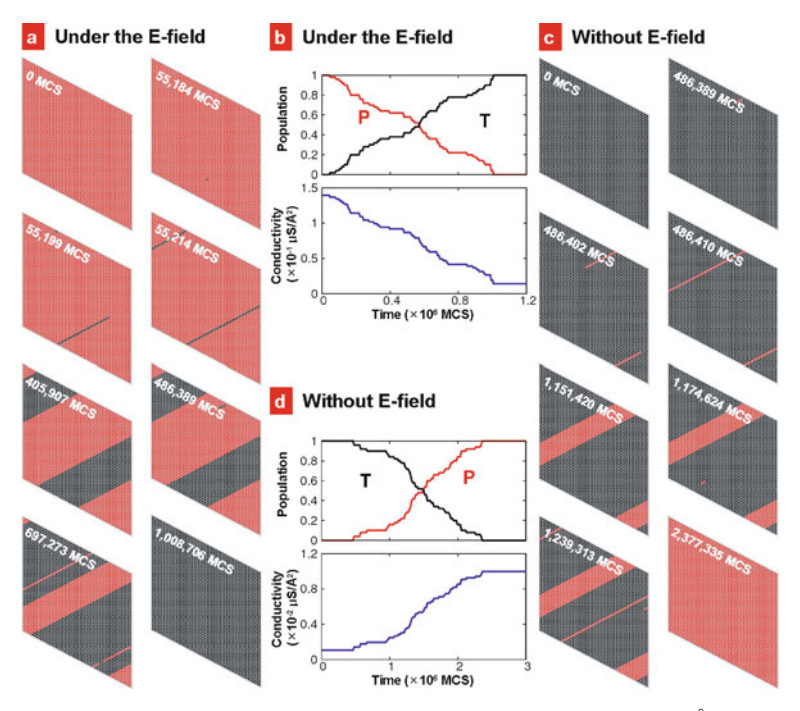


Fig. 2.8 Conductivities depending on the twisting angle are extracted from the previous study [36], which are the results from NEGF calculations. (a) Semi-log plots of I-V curves shows that the slope decrease as the twist angle approaches to  $90^{\circ}$ , which means that the tunneling barrier from the *bottom* electrode to *top* electrode,  $\Phi_B$  increases as the  $\pi$ - $\pi$  orbital overlap decreases. (b) Since the conductivity is dominated by the  $\pi$ - $\pi$  orbital overlap, we assumed that the conductivity between two phenyl rings,  $\sigma_i = 1/R_i$  is proportional to  $\cos^4(\chi_i)$ . From simple calculation leads the total conductivity  $\sigma_{tot}$  to be proportional to the  $\cos^4(\chi_1)\cos^4(\chi_2)/(\cos^4(\chi_1)+\cos^4(\chi_i))$ , which shows good agreement with the NEGF results

The analysis of the snapshots demonstrates that the time to complete the transformation of each line in  $[11\bar{2}0]$  after initiation is 26.32 MCS, leading to the rate constant of propagation,  $k_{[11\bar{2}0]} = 5.48$  Å/MCS. The  $k_{[11\bar{2}0]}$  shows almost no dependence on the temperature (Fig. 2.10a, top), which infers that the energy barrier for the propagation is zero or quite negligible. Thus, once one AN-OPE is switched as a nucleation, the transformation propagates quickly along the  $[11\bar{2}0]$  line, which is quite reasonable in terms of the energetic stability of  $P2T2_{11\bar{2}0}$  (Fig. 2.1). Then, another nucleation occurs for subsequent transformation of another  $[11\bar{2}0]$  line. Typically this subsequent transformation takes place right next to the precedent transformed line in the  $[1\bar{1}00]$  direction.

Therefore, the nucleation is the key step governing the time scale of the transition. The middle panel of Fig. 2.10a shows the probability, P(t) of exhibiting no nucleation until time t. To obtain the nucleation time  $(\tau)$  when we have a transformed  $\begin{bmatrix} 11\bar{2}0 \end{bmatrix}$  line already, the nucleation events initiated next to  $\begin{bmatrix} 11\bar{2}0 \end{bmatrix}$  line are analyzed among the snapshots. The nucleation process is found to be a Poisson process, in which P(t) decays exponentially with time. The value of  $\tau$  was obtained as 5,583 MCS by fitting of P(t).



**Fig. 2.9** (a) Snapshots during P-to-T transition from MC simulation with 1.2 V/Å external field. The first nucleation is occurred at 55,184 MCS, then, the [1120] line propagates until 55,214 MCS. More nucleation and propagation along [1120] are taken place, and finally, the full system is transformed by 1,008,706 MCS. We note that increased bias voltage yields a faster P-to-T transition. (b) Time dependence of P and T populations and electrical conductivity through the SAM during P-to-T transition. (c) Snapshots during T-to-P transition from MC simulation without an external field. The first nucleation is occurred at 486,389 MCS, then, the [1120] line propagates until 486,410 MCS. More nucleation and propagation along [1120] are taken place, and finally, the full system is transformed by 2,377,335 MCS. (d) Time dependence of P and T populations and electrical conductivity through the SAM during T-to-P transition

To obtain the nucleation time  $(\tau_0)$  in the absence of  $[11\bar{2}0]$  line, we carried out additional 50 simulations to find when the first P transforms to the T, showing that this process proceeds as a Poisson process with  $\tau_0 = 274,193$  MCS that is  $\sim 50$  time larger than  $\tau$  (Fig. 2.10a, bottom panel).

Figure 2.9c, d show the time evolution of the system with no external field starting with all T's and ending with all P's and the population change with the electrical conductivity change during this T-to-P transition, respectively. The overall process is quite similar to that of P-to-T transition except for the detailed numbers. The first nucleation occurred at 486,389 MCS, and then, the neighbors along  $\begin{bmatrix} 11\bar{2}0 \end{bmatrix}$  showed fast transition to P within 21 MCS. While this swath is growing along  $\begin{bmatrix} 1\bar{1}00 \end{bmatrix}$  direction, the second and the third nucleation without next transformed line occurred at 1,174,624 MCS and 1,239,313 MCS, respectively. Finally, the full system is

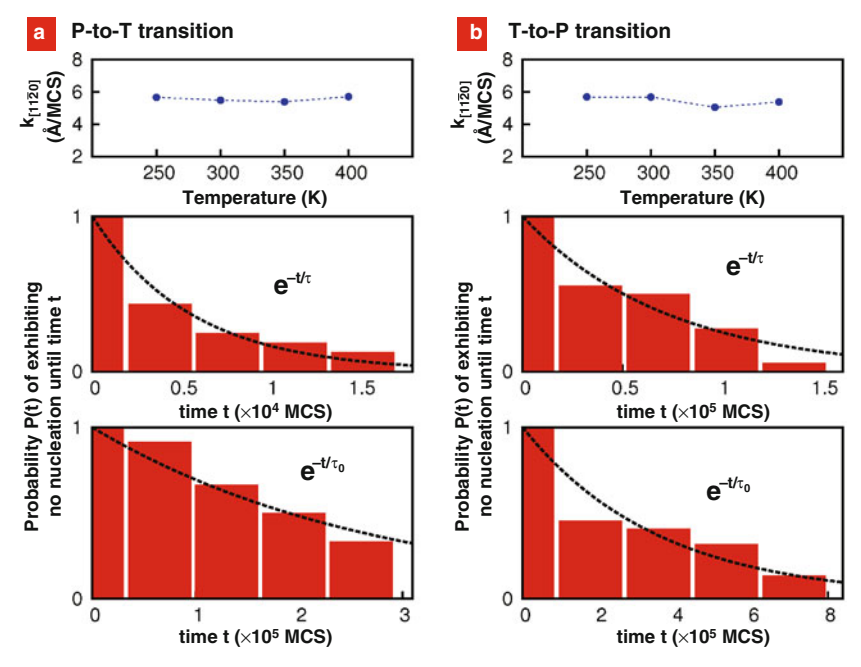


Fig. 2.10 (a) P-to-T transition; (b) T-to-P transition; *Top panels* show the temperature dependence of the propagation rate along  $\begin{bmatrix} 11\bar{2}0 \end{bmatrix}$ ,  $k_{\begin{bmatrix} 11\bar{2}0 \end{bmatrix}}$ . *Middle panels* show the probability, P(t) of exhibiting no nucleation by time, t for the case when the nucleation is initiated next to another  $\begin{bmatrix} 11\bar{2}0 \end{bmatrix}$  line. The *dotted lines* is an exponential fit of P(t). This leads to a nucleation rate of  $\tau=5,583$  MCS for the P-to-T transition and  $\tau=72,926$  MCS for the T-to-P transition. *Bottom panels* show the probability, P(t) of exhibiting no nucleation by time, t for the case when the nucleation is initiated in the absence of next  $\begin{bmatrix} 11\bar{2}0 \end{bmatrix}$  line. The exponential fit leads to a nucleation rate of  $\tau_0=274,193$  MCS for the P-to-T transition and  $\tau_0=357,135$  MCS for the T-to-P transition

transformed to P by 2,377,335 MCS. During the transition, the total conductivity through the SAM increases along with the decrease of the P population.

During T-to-P transition, the average time to complete each line of  $[11\bar{2}0]$  growth is 25.38 MCS, leading to  $k_{[11\bar{2}0]} = 5.68$  Å/MCS with no temperature dependency (Fig. 2.10b, top panel).

The nucleation times are studied in the same manner with the P-to-T transition. The nucleation process follows Poisson process with the  $\tau=72,926$  MCS and  $\tau_0=357,135$  MCS in the presence and the absence of the next transformed  $\begin{bmatrix}11\bar{2}0\end{bmatrix}$  line, respectively (Fig. 2.10b, middle and bottom panels).

The interaction between P-T is smaller than the interaction between P-P or T-T by  $\sim$ 8.6 kcal/mol in average (Table 2.1), due to the loss of HB or less-favorable van der Waals interaction caused by the packing of two different conformations. This infers that the boundary of [1120] line is energetically less stable, leading a fast transformation at the boundary. This well explains the smaller  $\tau$  than  $\tau_0$ .

We also found  $\tau$  during P-to-T transition is smaller than  $\tau$  during T-to-P transition (which is responsible to that NDR is not shown during the backward sweep). This is because the formation of T-T HB network is accompanied with the expansion of  $\begin{bmatrix} 11\bar{2}0 \end{bmatrix}$  swath along  $\begin{bmatrix} 1\bar{1}00 \end{bmatrix}$  during the P-to-T transition, while the loss of T-T HB network is accompanied during the T-to-P transition.

#### 2.3.4 NDR for Time Dependent Electric Field

Applying a time dependent external field, we calculated the response of the system to voltage sweeps at various sweep rates. For each sweep, the magnitude of the external field was increased linearly until F = 1.4 V/Å (corresponding to 1.5 V bias voltage in forward sweep) and then it was decreased at the same rate until the field was 0 V/Å (corresponding to 0 V bias voltage in backward sweep). (Section 8.4 discusses the conversion factor between the external electric field and the bias voltage.) The sweep rates were  $1 \times 10^{-8}$ ,  $4^{-8}$ , and  $2 \times 10^{-7} \text{ V/MCS}$ . The resultant I-V curves are shown in Fig. 2.11a. Although the current drops dramatically at sufficiently high voltage, similar for all cases, we found that faster sweep let the systems stay in

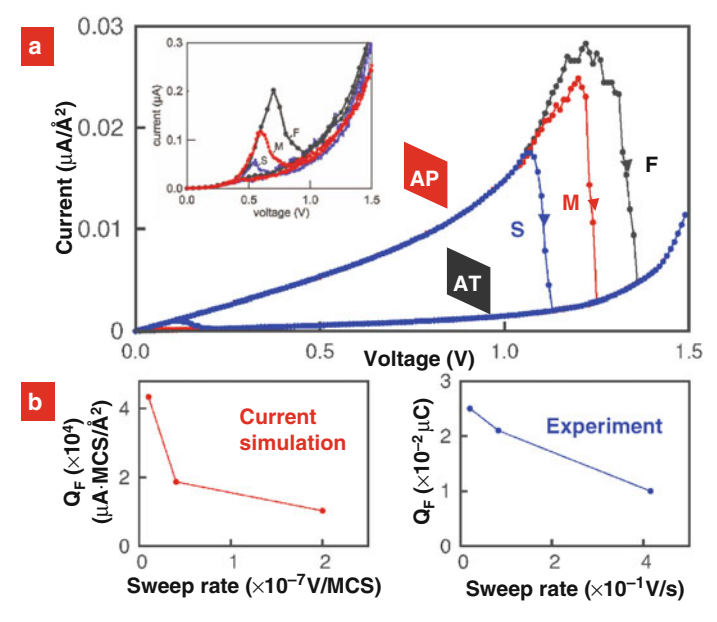


Fig. 2.11 (a) Current-voltage (I-V) curves calculated at 300 K from MC simulations combined with the I-V results of the Green's function calculations. Results for three sweeping rates are shown: S (blue line):  $1 \times 10^{-8}$  V/MCS, M (red line):  $4 \times 10^{-8}$  V/MCS, and F (black line):  $2 \times 10^{-7}$  V/MCS. Inset is the experimental I-V curves from the reference [9] with 3 different sweeping rates: S (blue line):  $2 \times 10^{-7}$  V/MCS, M (red line):  $2 \times 10^{-7}$  V/MCS, and F (black line):  $2 \times 10^{-7}$  V/MCS, M (red line):  $2 \times 10^{-7}$  V/MCS, and F (black line):  $2 \times 10^{-7}$  V/MCS,  $2 \times 10^{-7}$  V/MCS, and F (black line):  $2 \times 10^{-7}$  V/MCS,  $2 \times 10^{-7}$  V/MCS, and F (black line):  $2 \times 10^{-7}$  V/MCS, and F (black li

the P phase at higher voltage, which is in a good agreement with the experimental observation. Clearly, the simulations show both the NDR phenomena and hysteretic behavior with sweep rate dependence as observed experimentally.

We found that the P-to-T transition voltage is located at 1.1-1.4 V, depending on sweep rate. This can be compared to the experimental results in which the transition is completed by 0.6-1.0 V. During the backward sweep, the simulations found that the T state transforms back to P at  $\sim 0.2$  V bias voltage with slower sweep rates.

To determine the total charge associated with the NDR region, we integrated the current from the peak to the valley in Fig. 2.11a. This amount of charge  $(Q_F)$  flowing through the junction during NDR, is an important physical quantity that characterizes the QC model [9]. The calculated  $Q_F$  values are

- $Q_F = 4.34 \times 10^4 \ \mu\text{A·MCS/Å}^2 \ (\sim 1.76 \times 10^6 \ \text{e/AN-OPE})$ , for sweep rates of  $1 \times 10^{-8} \ \text{V/MCS}$ .
- $Q_F = 1.87 \times 10^4 \ \mu \text{A·MCS/Å}^2 \ (\sim 7.57 \times 10^5 \text{ e/AN-OPE})$ , for sweep rates of  $4 \times 10^{-8} \text{ V/MCS}$ , and
- $Q_F = 1.03 \times 10^4 \ \mu \text{A·MCS/Å}^2 \ (\sim 4.17 \times 10^5 \ \text{e/AN-OPE})$ , for sweep rates of  $2 \times 10^{-7} \ \text{V/MCS}$ .

Figure 2.11b shows the sweep rate versus  $Q_F$  plots from the simulation (left panel) and from the experiment (right panel). The simulations reproduce the experimental observation that  $Q_F$  decreases with increasing sweep rate. Additionally, we find that changing the sweep rate by 20 times only changes the  $Q_F$  by 4.2 times, which is comparable to the experimental observation that the  $Q_F$  varies 2.5 times while the sweep rate changes by  $\sim$ 20 times [9].

The NDR peak from the MC simulations leads to a voltage range of  $\sim 0.15$  V while the experimental NDR range is  $\sim 0.25$  V. One issue is the time scale. Our MC sweep frequency was  $\sim 10^{-7}$  V/MCS whereas experimental sweep frequency is  $\sim 10^{-1}$  V/s. To convert from MCS to second, we compared the initial nucleation rate expressed in MCS to that expected from the transition state theory using the predicted barrier in kcal/mol. The result is 1 MCS equals  $\sim 10^{-13}$  s (see Section 8.1.), indicating the theoretical sweep frequency  $\sim 10^6$  times the experimental sweep frequency. This faster sweep should decrease the NDR range. In addition, the small size of our periodic cell, 1,620 nm², compared to the experiment of  $O(\text{cm}^2)$  would also tend to decrease the NDR range.

A limitation in our MC simulations is that we idealized the degrees of freedom for the molecules into two states, which consider as the perfectly crystallized phases where an infinite AN-OPEs are connected through the HB network. In order to investigate the effect of molecular fluctuations, we performed a series of MD simulations with a  $(10 \times 10)$  unit cell (100) independent AN-OPE molecules). The MD simulations account for two aspects missing from the MC simulations:

 The AN-OPE is allowed to have a distribution of conformations, accounting for the much lower current for χ near 90° while losing the HB network at high fields. This distribution in χ leads to decreased current at a given voltage, leading to a lower slope in the higher-field due to the larger ΔΦ<sub>B</sub>. Bibliography 25

2. The AN-OPE forms a partially disordered phase with some HB along [1010] in the low field (Section 8.2). The loss of the HB network at high field decreases the hysteresis during the backward sweep since the loss of HB in the high field decreases the T-to-P transition barrier.

In addition, we found that once a disordered area is developed, it does not easily recover the P phase; hence, the development of a disordered part on the SAM yields less dramatic changes in conductivity. The experimental observation of slight current decrease with successive sweeps may result from the expansion of the disordered area during the sweep cycles.

In order to validate the suggested mechanism for NDR for AN-OPE, we investigated the possibility of NDR from the system N-OPE which contains no NH<sub>2</sub> group and the bare B-OPE containing no functional group. We found that the N-OPE system shows NDR behavior very similar to AN-OPE, in agreement with experiment [37]. However, we found no NDR behavior for B-OPE, also in agreement with experiment (Section 8.3).

#### 2.4 Conclusions

Summarizing, we find that a coarse-grained model based on parameters from first principles calculations leads to a mechanism for room temperature hysteretic NDR that is in qualitative agreement with experiments on AN-OPE, N-OPE, and B-OPE. This provide a plausible mechanism for understanding this phenomena which maybe useful in developing new NDR systems.

**Acknowledgments** The computational work was initiated with support by the National Science Foundation (NIRT, WAG). The collaboration was supported by the Microelectronics Advanced Research Corporation (MARCO, WAG and RAK) and its Focus Centers on Functional Engineered NanoArchitectonics (FENA). The facilities of the MSC (WAG) were supported by ONR-DURIP, ARO-DURIP and the facilities of the CNBT lab (SSJ) were supported by the start-up from the MSE in Georgia Tech.

# **Bibliography**

- 1. Esaki, L. Phys. Rev. 1958, 109, 603-604.
- Xue, Y. Q.; Datta, S.; Hong, S.; Reifenberger, R.; Henderson, J. I.; Kubiak, C. P. Phys. Rev. B 1999, 59, R7852–R7855.
- 3. Tao, N. J. Nat. Nanotechnol. 2006, 1, 173-181.
- 4. Chen, J.; Reed, M. A.; Rawlett, A. M.; Tour, J. M. Science 1999, 286, 1550–1552.
- 5. Selzer, Y.; Salomon, A.; Ghabboun, J.; Cahen, D. Angew. Chem. Int. Ed. 2002, 41, 827.
- 6. Pitters, J. L.; Wolkow, R. A. Nano Lett. 2006, 6, 390-397.
- 7. He, J.; Lindsay, S. M. J. Am. Chem. Soc. 2005, 127, 11932–11933.
- Salomon, A.; Arad-Yellin, R.; Shanzer, A.; Karton, A.; Cahen, D. J. Am. Chem. Soc. 2004, 126, 11648–11657.
- 9. Kiehl, R. A.; Le, J. D.; Candra, P.; Hoye, R. C.; Hoye, T. R. Appl. Phys. Lett. 2006, 88, 172102.

- Guisinger, N. P.; Yoder, N. L.; Hersam, M. C. Proc. Natl. Acad. Sci. USA. 2005, 102, 8838–8843.
- Kratochvilova, I.; Kocirik, M.; Zambova, A.; Mbindyo, J.; Mallouk, T. E.; Mayers, T. S. J. Mater. Chem. 2002, 12, 2927–2930.
- Rawlett, A. M.; Hopson, T. J.; Nagahara, L. A.; Tsui, R. K.; Ramachandran, G. K.; Lindsay, S. M. Appl. Phys. Lett. 2002, 81, 3043–3045.
- Amlani, I.; Rawlett, A. M.; Nagahara, L. A.; Tsui, R. K. Appl. Phys. Lett. 2002, 80, 2761–2763.
- Donhauser, Z. J.; Mantooth, B. A.; Kelly, K. F.; Bumm, L. A.; Monnell, J. D.; Stapleton, J. J.;
   Price, D. W.; Rawlett, A. M.; Allara, D. L.; Tour, J. M.; Weiss, P. S. Science 2001, 292, 2303–2307.
- Fan, F. R. F.; Lai, R. Y.; Cornil, J.; Karzazi, Y.; Bredas, J. L.; Cai, L. T.; Cheng, L.; Yao, Y. X.;
   Price, D. W.; Dirk, S. M.; Tour, J. M.; Bard, A. J. J. Am. Chem. Soc. 2004, 126, 2568–2573.
- 16. Seminario, J. M.; Zacarias, A. G.; Tour, J. M. J. Am. Chem. Soc. 2000, 122, 3015-3020.
- Xiao, X. Y.; Nagahara, L. A.; Rawlett, A. M.; Tao, N. J. J. Am. Chem. Soc. 2005, 127, 9235–9240.
- Reed, M. A.; Chen, J.; Rawlett, A. M.; Price, D. W.; Tour, J. M. Appl. Phys. Lett. 2001, 78, 3735–3737.
- Chen, J.; Wang, W.; Reed, M. A.; Rawlett, A. M.; Price, D. W.; Tour, J. M. Appl. Phys. Lett. 2000, 77, 1224–1226.
- Sollner, T. C. L. G.; Goodhue, W. D.; Tannenwald, P. E.; Parker, C. D.; Peck, D. D. Appl. Phys. Lett. 1983, 43, 588–590.
- 21. Tsuchiya, M.; Sakaki, H.; Yoshino, J. Jpn. J. Appl. Phys., Part 2-Letters 1985, 24, L466-L468.
- 22. Oiu, X. H.; Nazin, G. V.; Ho, W. Phys. Rev. Lett. 2004, 93, 4.
- 23. Akdim, B.; Pachter, R. J. Phys. Chem. C 2008, 112, 3170–3174.
- 24. Troisi, A.; Ratner, M. A. Nano Lett. 2004, 4, 591-595.
- 25. Emberly, E. G.; Kirczenow, G. Phys. Rev. B 2001, 64, 125318.
- 26. Galperin, M.; Ratner, M. A.; Nitzan, A. Nano Lett. 2005, 5, 125-130.
- 27. Kresse, G.: Furthmuller, J. Phys. Rev. B 1996, 54, 11169–11186.
- 28. Jaguar, V. 6.5 ed.; Schrödinger Inc.: Portland, 2005.
- 29. Kim, Y. H.; Jang, S. S.; Jang, Y. H.; Goddard, W. A. Phys. Rev. Lett. 2005, 94, 156801.
- 30. Schultz, P., SeqQuest Project; Sandia National Laboratories: Albuquerque, NM, 2003.
- 31. Mayo, S. L.; Olafson, B. D.; Goddard, W. A. J. Phys. Chem. 1990, 94, 8897-8909.
- 32. Plimpton, S. J. J. Comput. Phys. 1995, 117, 1-19.
- 33. Plimpton, S. J.; Pollock, R.; Stevens, M. The Eighth SIAM Conference on Parallel Processing for Scientific Computing Minneapolis; 1997.
- Swope, W. C.; Andersen, H. C.; Berens, P. H.; Wilson, K. R. J. Chem. Phys. 1982, 76, 637–649.
- 35. Lo, W. S.; Pelcovits, R. A. Phys. Rev. A 1990, 42, 7471-7474.
- 36. Stokbro, K.; Taylor, J.; Brandbyge, M.; Ordejón, P.; Ann. N Y. Acad. Sci. 2003, 1006, 212-216.
- 37. Candra, P. M.S. Dissertations, University of Minnesota, 2006.

# Chapter 3 Free Energy Barrier for Molecular Motions in Bistable [2]Rotaxane Molecular Electronic Devices

Reprinted with permission from Kim, H; Goddard, W. A.; Jang S. S.; Dichtel, W. R.; Heath, J. R.; Stoddart J. F. J. Phys. Chem. A 2009, 113 (10), 2136-2143. Copyright 2009 American Chemical Society.

**Abstract** Donor-acceptor binding of the  $\pi$ -electron-poor cyclophane cyclobis (paraquat-p-phenylene) (CBPQT<sup>4+</sup>) with the  $\pi$ -electron-rich tetrathiafulvalene (TTF) and 1,5-dioxynaphthalene (DNP) stations provides the basis for electrochemically switchable, bistable [2] rotaxanes, which have been incorporated and operated within solid state devices to form ultradense memory circuits [1, 2] and nanoelectromechanical systems. The rate of CBPQT<sup>4+</sup> shuttling at each oxidation state of the [2] rotaxane dictates critical write-and-retention time parameters within the devices, which can be tuned through chemical synthesis. To validate how well computational chemistry methods can estimate these rates for use in designing new devices, we used molecular dynamics simulations to calculate the free energy barrier for the shuttling of the CBPQT<sup>4+</sup> ring between the TTF and the DNP. The approach used here was to calculate the potential of mean force along the switching pathway. from which we calculated free energy barriers. These calculations find a turn-on time after the rotaxane is doubly oxidized of  $\sim 10^{-7}$  s (suggesting that the much longer experimental turn-on time is determined by the time scale of oxidization). The return barrier from the DNP to the TTF leads to a predicted lifetime of 2.1 s, which is compatible with experiments.

#### 3.1 Introduction

The electrochemically switchable, bistable [2]rotaxanes [1] (Fig. 3.1) developed in recent years by Stoddart and co-workers exhibit two distinct co-conformations [3, 4, 5, 6, 7]: the ground-state co-conformation, in which the cyclobis(paraquat-p-phenylene) (CBPQT<sup>4+</sup>) encircles the tetrathiafulvalene (TTF) station, and the metastable state co-conformation, in which the CBPQT<sup>4+</sup> encircles the 1,5-dioxynaphthalene (DNP) station [2, 8, 9, 10, 11, 12, 13, 14, 15]. The population of the two co-conformations may be shifted away from equilibrium by temporarily

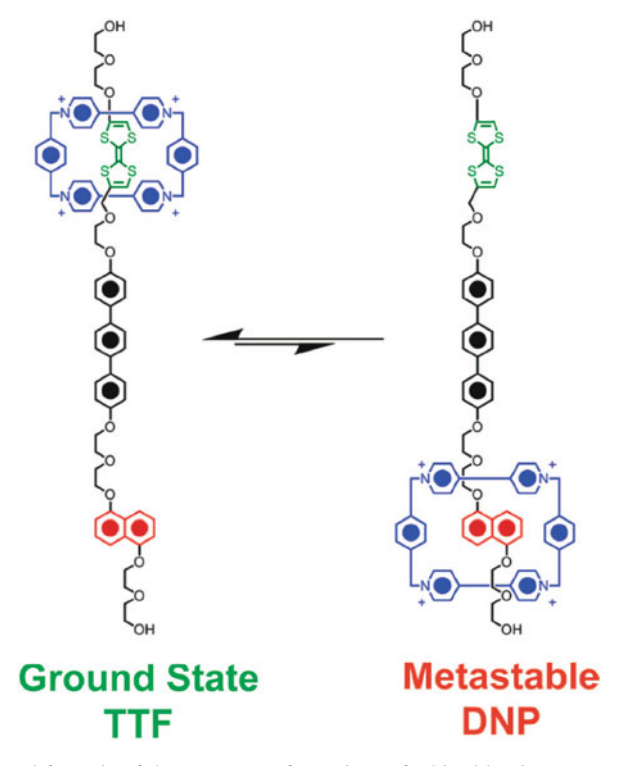


Fig. 3.1 Structural formula of the two co-conformations of a bistable [2]rotaxane fragment used in this study

oxidizing one or two electrons from the TTF units. This switching process forms the basis of using these compounds as storage elements in molecular electronic devices. Consequently, significant experimental efforts have been made to investigate the switching behavior of molecular switches [5, 6, 16, 17, 18, 19, 20, 21, 22, 23] and molecular machines [24, 25, 26, 27, 28, 29] in various environments, such as solution [5, 6, 30, 31, 32, 33, 34, 35, 36, 37], polymer electrolyte gels [38], metal surfaces [39, 40, 41] and devices [7, 16, 17]. Important experimental evidence [15] for molecular switching in these devices was the correlation of the kinetics of relaxation from the DNP to the TTF, across each of these environments. However, the rate of this process is also a function of the molecular structure, suggesting that longer storage times, or even nonvolatile memory, might be possible with the appropriate molecular design.

Computation chemistry calculations could provide an effective approach for optimizing the performance of such molecular switches, but such applications require that the accuracy of the theory be validated by comparing to well-documented experimental results. The purpose of this paper is to provide such validation. Previously, we investigated these compounds using a multiscale first principles approach combining quantum mechanics (QM) and atomistic force field (FF)

3.2 Simulation Details 29

methods [42, 43, 44, 45, 46, 47]. First we considered the molecules as individual species, and then we examined self-assembled monolayers bound to gold surfaces or compressed into Langmuir monolayers at the air-water interface. These studies successfully predicted a number of phenomena that were confirmed later experimentally, including the higher conductivity [47] of the DNP relative to the TTF, and the increased stability of the TTF relative to the DNP (by 2.0 kcal/mol from QM, 2.3 kcal/mol from the FF, and 1.4 – 1.6 kcal/mol from experiment) [15, 43]. In addition, on the basis of the predicted footprint of the 115 Å<sup>2</sup>/molecule for the self-assembled structure, we predicted that the surface tension of the TTF is 32% lower than that of the DNP, an observation that was confirmed in subsequent experiments [43, 44].

In this study, we evaluated the free energy profile of the shuttling motion of the CBPQT<sup>4+</sup> ring between the TTF and the DNP stations to determine how the nature of the rotaxane affects the switching and relaxation rates. These rates have been determined experimentally in various environments [15, 35, 40, 48], and we now want to understand the structural contributions to these rates. We seek to find a level for theoretical calculations of these rates that is both accurate and fast so that we can use theory to optimize the structural characteristics to achieve desired rates.

Rather than finding the energy barrier for a minimized reaction path connecting the two states, we used potential of mean force (PMF) to evaluate the change of free energy along the shuttling pathway of the CBPQT<sup>4+</sup> ring between the TTF and the DNP so that we can determine the rates at the experimental temperature. We carried out these calculations for three oxidation states of the molecule relevant to the switching and thermally activated relaxation process.

#### 3.2 Simulation Details

# 3.2.1 Potential of Mean Force from Constrained Molecular Dynamics Simulation

The experimental time scale for the ring to relax back from the DNP to the TTF is  $10^{-1}-10^3$  seconds [15, 34, 49], suggesting that simple molecular dynamics (MD) simulation of a few hundred nanoseconds might not be sufficiently ergodic to provide an accurate transition rate. Hence, we adopted the "Blue Moon sampling" technique [50, 51] of constrained MD simulations using holonomic constraints that fix the systems along the reaction coordinate. To determine the free energy barrier, we used the reaction-coordinate (R)-dependent potential of mean force (PMF),  $F_{\rm rxn}$  (R) defined as the integration of the mean force (MF) along the reaction coordinate,  $-dF_{\rm rxn}$  (R) dR [52],

$$F_{\text{rxn}}(R) = F_{\text{rxn}}(\infty) + \int_{-\infty}^{R} \frac{\mathrm{d}F_{\text{rxn}}(R')}{\mathrm{d}R'} \mathrm{d}R'. \tag{3.1}$$

Here, the MF is a measurable quantity from our simulations. To calculate the MF, we assumed that the CBPQT<sup>4+</sup> ring moves between the TTF and the DNP along the backbone of the rotaxane (Fig. 3.2a), which we assume to be in an extended conformation but with the minimized structure. This extended conformation should provide the fastest shuttling motion of the CBPQT<sup>4+</sup> ring, being governed mainly by its interaction with the backbone. This MF does not account for the presence of folded chain conformations, so that the PMF may lack some contributions from conformational entropy.

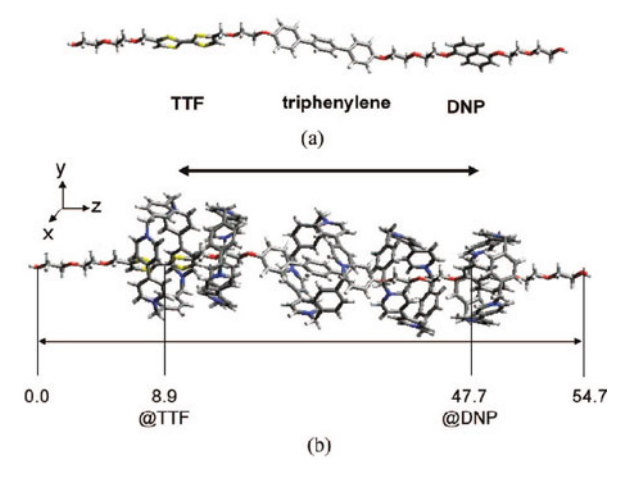


**Fig. 3.2** (a) Backbone of the rotaxane molecule simulated in this study. (b) CBPQT<sup>4+</sup> ring positions along the backbone (unit: Å)

First, we prepared the extended rotaxane backbone without the CBPQT<sup>4+</sup> ring using quantum mechanical geometry optimization at the level of B3LYP/6-31G\* (Fig. 3.2a). Then, we added and optimized the CBPQT<sup>4+</sup> ring at various fixed points on the fixed extended backbone (Fig. 3.2b) using quantum mechanics. Thus, the atomic partial charges of all atoms are allowed to readjust, depending on the relative position of the charge acceptor (CBPQT<sup>4+</sup>) with respect to the charge donor (TTF and DNP).

To obtain the change of the PMF during the shuttling process, we first evaluated the MF as a function of the position of the CBPQT<sup>4+</sup> ring. Because the length of the backbone is 54.7 Å and the distance between the TTF and the DNP is 36.9 Å, we chose to the dynamics for nine independent samples, each of which has the *z*-coordinate (along the backbone) of the center of mass (COM) of the CBPQT<sup>4+</sup> ring at a different position along the extended backbone, as schematically presented in Fig. 3.3. Using quantum mechanics, the geometry and atomic charges were obtained from each of these nine cases.

After preparing these nine initial structures, we prepared two more structures beyond each station of the TTF and the DNP with identical charges to the CBPQT<sup>4+</sup>@TTF case and the CBPQT<sup>4+</sup>@DNP case, respectively. In addition,

3.2 Simulation Details 31

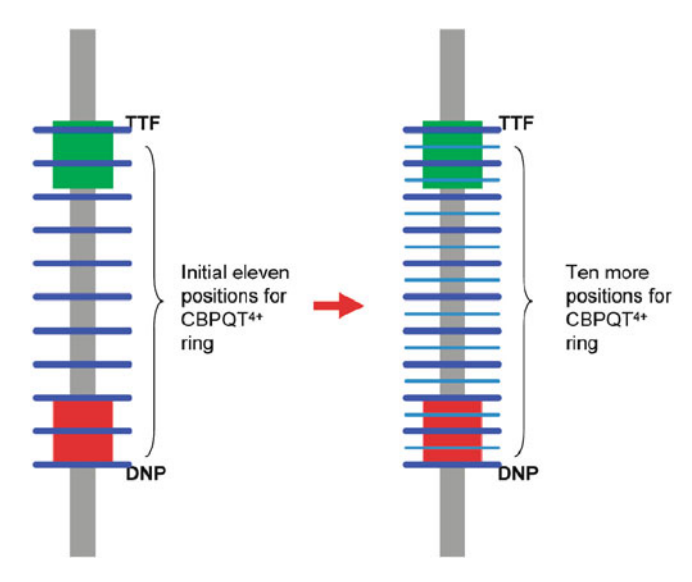


**Fig. 3.3** Charges for the initial nine structures obtained from QM with Mulliken analysis. In addition, we included two more structures beyond each station of the TTF and the DNP, using charges identical to those for the equilibrium CBPQT<sup>4+</sup>@TTF and CBPQT<sup>4+</sup>@DNP cases, respectively. Ten more structures were generated on the basis of these eleven structures. The position of the CBPQT<sup>4+</sup> ring for each additional structure was obtained using the arithmetic average of the two adjacent cases from the eleven structures. The charges were also averaged

we constructed another ten structures in which the position and charges of the CBPQT<sup>4+</sup> ring were calculated by arithmetically averaging the coordinates and charges of two consecutive structures in the eleven structures. Thus, a total of 21 structures were prepared for simulations.

Then, to simulate both the turning on and turning off the rotaxane switch, we investigated the effect of oxidation of rotaxane molecule on the free energy profile, for three different oxidation states: the neutral state, the +1 oxidation state, and the +2 oxidation state.

The QM calculations of the charges for the nine different structures were repeated for each of the three oxidation states: 0, +1, and +2. The atomic partial charge distributions are tabulated in the Section 8.5 (Tables 8.5.1, 8.5.2, and 8.5.3).

All quantum mechanical computations in this study were performed using Jaguar [53].

# 3.2.2 Constrained Molecular Dynamics Simulation

Next, we carried out a constrained NVT MD simulation at 300 K for 500 ps to equilibrate each system. This MD was then continued for an additional 3 ns at 300 K (constrained NVT MD) to compute the MF. The constraint was introduced using Gauss' principle of least constraints [54] to fix only the z-component of the

center of mass (COM) of the CBPQT<sup>4+</sup> ring parallel to the molecular axis direction (z-axis direction as in Fig. 3.2b). To ensure that our constrained dynamics produces the correct equilibrium averages without bias due to ensemble sampling, we used Fixman's theorem [55] to evaluate the metric effect originating from the holonomic constraints. We determined that the metric effect only adds a constant scalar value to the absolute free energy values, which has no influence on the relative energetics. (Details are in the Section 8.6.)

We also fixed the position of the last oxygen atom at each end of the backbone to retain the extended conformation. This restricts the conformational flexibility of the system, which suppresses conformational entropic contributions to the free energy. The mean force was sampled from such constrained MD simulations.

#### 3.2.3 Force Field and MD Parameters

We used the generic DREIDING force field [56], which was found to lead to accurate results in our previous studies on rotaxane systems [43, 44, 45]. It was also successful in our studies on various other molecular systems, such as the hydrated polymer electrolyte membranes [57, 58, 59] and the surfactant-mediated air-water interface [60, 61].

The force field has the form

$$E_{\text{total}} = E_{\text{vdW}} + E_{\text{Q}} + E_{\text{bond}} + E_{\text{angle}} + E_{\text{torsion}} + E_{\text{inversion}},$$
 (3.2)

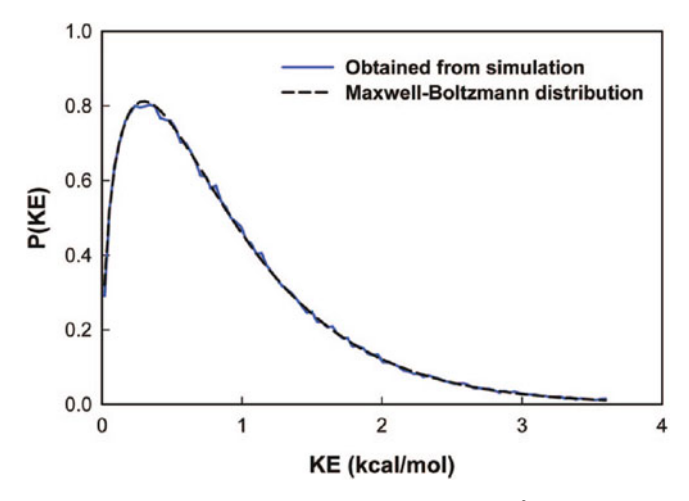
where  $E_{\text{total}}$ ,  $E_{\text{vdW}}$ ,  $E_{\text{Q}}$ ,  $E_{\text{bond}}$ ,  $E_{\text{angle}}$ ,  $E_{\text{torsion}}$ , and  $E_{\text{inversion}}$  are the total energies, the van der Waals, electrostatic, bond stretching, angle bending, torsion, and inversion energy components, respectively, and the force field parameters are described in the original papers [56]. The atomic charges were obtained from a QM Mulliken population analysis as indicated above.

All MD simulations were performed using LAMMPS (large-scale atomic/molecular massively parallel simulator) MD code from Plimpton at Sandia [62, 63]. The equations of motion were integrated using the velocity-Verlet algorithm [64], with a time step of 0.01 fs. This unusually small time step was to ensure high quality sampling of phase space by avoiding abrupt changes in atomic positions.

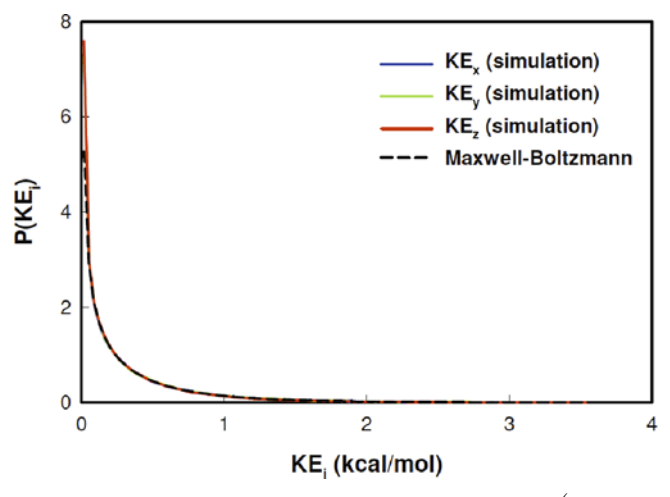
The temperature was kept constant during the MD using the Berendsen thermostat with temperature damping time of 0.01 fs. To demonstrate that our MD leads to a proper canonical ensemble, the probability distribution function (PDF) of kinetic energy KE (=  $mv^2/2$ ) is shown in Fig. 3.4. The PDF is quite close to the Maxwell-Boltzmann distribution of energy at T=300 K, indicating that the simulation describes a proper canonical ensemble. Furthermore, the PDF for each component of velocity is the same and the system obeys the equipartition theorem (Fig. 3.5).

Figure 3.6 shows the typical behavior of the MF as a function of simulation time for two representative systems: one is the ground state, CBPQT<sup>4+</sup>@TTF, green

3.2 Simulation Details 33



**Fig. 3.4** Probability density function of kinetic energy KE (=  $mv^2/2$ ) is from the MD simulation of the CBPQT<sup>4+</sup> ring@TTF (*blue line*) at 300 K. Here the time step was 0.01 fs and the total simulation time was 3 ns after 500 ps of equilibration. The *black dashed line* compares with the Maxwell-Boltzmann distribution of the energy,  $2 \left( \text{KE}/\pi \left( k_B T \right)^3 \right)^{1/2} \exp \left( -\text{KE}/k_B T \right)$ , for T = 300 K



**Fig. 3.5** Probability density function of  $KE_x (= mv_x^2/2; blue line)$ ,  $KE_y (= mv_y^2/2; green line)$ , and  $KE_z (= mv_z^2/2; red line)$  are computed from the MD simulation of the CBPQT<sup>4+</sup> ring@TTF (blue line), which are identical to each other. These are compared with the Maxwell-Boltzmann distribution of  $KE_i$ ,  $\sqrt{1/(\pi KE_i k_B T)}$  exp  $(-KE_i/k_B T)$  at 300 K.  $(i \in \{x, y, z\}; black dashed line)$ 

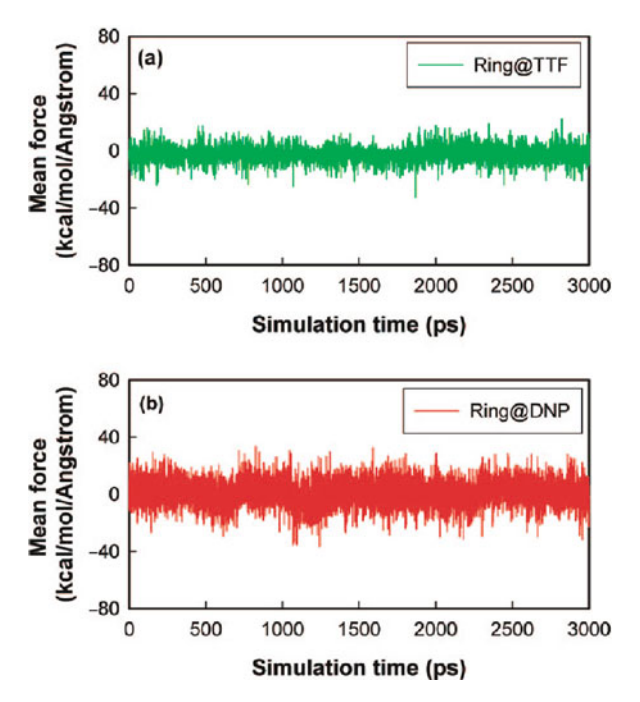


**Fig. 3.6** Change of mean force as a function of simulation time. In each case this follows 500 ps of equilibration time. This plot shows two representative cases: the CBPQT $^{4+}$  ring@TTF (TTF) and the CBPQT $^{4+}$  ring@DNP (DNP)

color, denoted as TTF and the other is the metastable state, the CBPQT<sup>4+</sup> ring on the DNP, red color, denoted as DNP. This shows that the mean force was well equilibrated for both cases.

The weakness of this blue moon sampling method is that the error in each MF measurement is integrated to obtain the PMF profile along the reaction coordinate. From block averages, we estimate the uncertainty of the MF values to be 0.04 kcal/mol/Å for CBPQT<sup>4+</sup>@TTF and 0.22 kcal/mol/Å for CBPQT<sup>4+</sup>@DNP. Assuming that these errors are random and that the average value is 0.13 kcal/mol/Å, we estimate that the error of the free energy difference between two stations is  $38.8\times0.13/(20)^{1/2}=1.13$  kcal/mol from integrating over the 38.8 Å distance. Similarly the error of the barrier from the DNP toward the TTF is  $25.5\times0.13/(14)^{1/2}=0.89$  kcal/mol from the integration over the 25.5 Å distance. Hence, the small errors in the MF values can lead to substantial errors in the PMF value. However, previous studies that carefully compare various PMF calculation methods show that constraint-biased sampling to determine mean forces is one of the best methods to obtain reasonable PMF values, even though, statistically, they contain large error bars [52].

#### 3.3 Results and Discussion

### 3.3.1 Charge Scheme: Adiabatic Approximation

We expected that no set of fixed charges scheme would be adequate enough to describe the electrostatic interactions as the highly charged ring is moved along the backbone. Thus, as described in Section 3.2.1, we obtained atomic charges from independent QM at each position as the ring is moved along the backbone.

This assumption of adiabatically adjusted charges assumes that charge redistribution is much faster than the time for the ring to travel along the backbone. To test the effect of these charge re-adjustments on the PMF, Fig. 3.7 shows the PMF based on three different charge schemes for the neutral rotaxane system: the green curve was obtained using the fixed charges from the ring@TTF, the red curve was obtained using the fixed charges from the ring@DNP, and the blue curve was obtained using adiabatic charges.

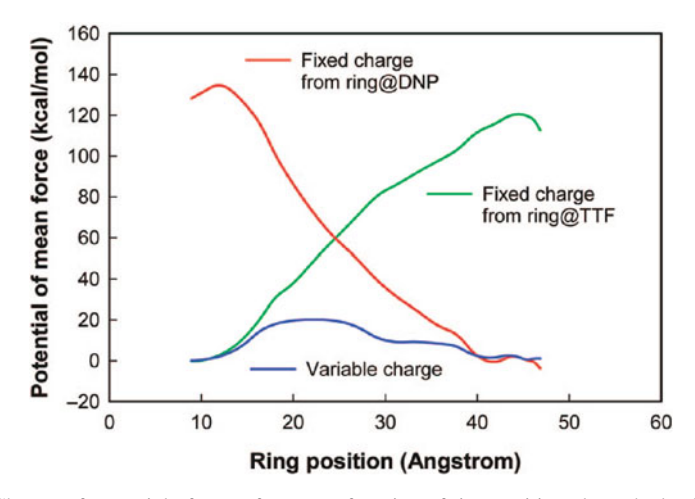


**Fig. 3.7** Change of potential of mean force as a function of ring position along the backbone. The *blue curve* allows the charge to change adiabatically as the ring moves along the dumbbell, which is the reliable result. The other two *curves* show the error obtained when the charges are fixed: the *green curve* uses fixed charges from the ring@TTF; the *red curve* uses a fixed charge from the ring@DNP

Clearly, the green and red curves are biased to have a minimum PMF at the position for which the charge was calculated, leading to very bad estimates of the barrier. In contrast, the energy barrier between the TTF and the DNP sites, based on the adiabatic charges, is consistent with experimental observations. Thus, we used the adiabatic charges for all oxidation states from the neutral state to the +2 state.

## 3.3.2 Free Energy Profiles from PMF Calculations

Sampling the MFs from the constrained MD simulations (Fig. 3.8a) and integrating them along the ring position, we calculated the profile of the PMF for the shuttling motion of the CBPQT<sup>4+</sup> ring (Fig. 3.8b). We found that each oxidation state (neutral state (0), oxidized states (+1 and +2)), leads to significantly different profiles.

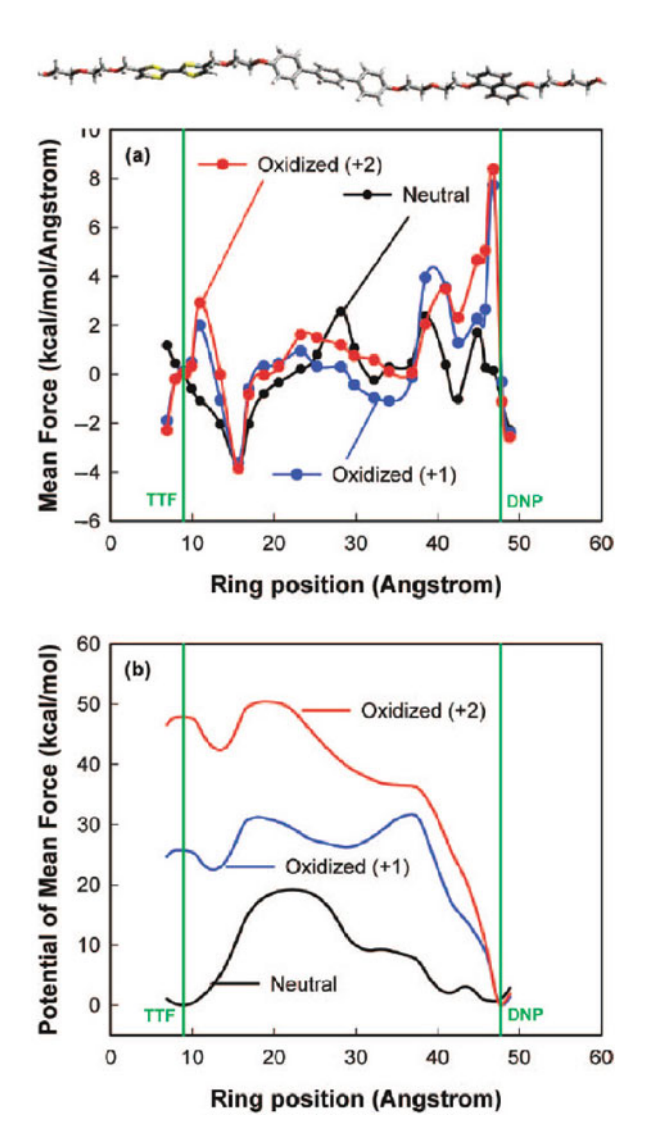


**Fig. 3.8** (a) Change of the mean force as a function of ring position along the backbone. (b) Change of the potential of mean force as a function of ring position along the backbone. The *green vertical lines* denote the ring@TTF (8.90 Å) and ring@DNP (47.70 Å)

#### 3.3.2.1 $\Delta G_{T2D}$

We calculated that the most stable complex for the neutral state (black) is CBPQT<sup>4+</sup>@TTF (ring at 8.9 Å) whereas the CBPQT<sup>4+</sup>@DNP state (ring at 47.7 Å) is less stable than the TTF by  $\Delta G_{\rm T2D} = 1.0\,\rm kcal/mol$ . This agrees with various experiments, which lead to  $\Delta G_{\rm T2D} = 1.4 - 1.6\,\rm kcal/mol$  [15, 65, 66, 67, 68] on the basis of the difference in the binding free energies of the individual components of the rotaxane in the MeCN solvent. In addition, this calculation agrees with our previous computations from QM ( $\Delta G_{\rm T2D} = 2.0\,\rm kcal/mol$ ) [43] and Hessian-based FF calculations ( $\Delta G_{\rm T2D} = 2.3\,\rm kcal/mol$ ) [43]. We emphasize here that all previous experimental and theoretical studies studied  $\Delta G_{\rm T2D}$  by comparing the binding free energy of the TTF derivatives with the CBPQT<sup>4+</sup> ring and the binding free energy of the DNP derivatives with the CBPQT<sup>4+</sup> ring. Thus, our current calculation is the first direct measurement of the  $\Delta G_{\rm T2D}$  on a complete rotaxane.

# 3.3.2.2 $\Delta G_{\mathrm{T2D}}^{\ddagger}$ and $\Delta G_{\mathrm{D2T}}^{\ddagger}$ for Neutral Case

We calculate that the free energy barrier is  $\Delta G_{\rm T2D}^{\ddagger}=19.03$  kcal/mol from the TTF toward the DNP, and  $\Delta G_{\rm D2T}^{\ddagger}=18.03$  kcal/mol in the opposite direction. The relaxation barrier in the neutral state was measured for a similar bistable [2]rotaxane in which the triphenylene spacer was missing, leading to [15] (see Table 3.1)

Table 3.1 Free energy barriers, rate constants, and relaxation half-lives from DNP toward TT	F
$(DNP \rightarrow TTF)$ at 298 K (all simulation results from this work)	

$\Delta G$ (kcal/mol)	$ak (s^{-1})$	$^{a}\tau_{1/2}$ (s)	condition
18.03 ± 1.5 (simul.)	$0.33 \pm 0.83$	$2.1 \pm 5.4$	gas phase (neutral)
$16.2 \pm 0.3$ (exp.[34])	$7.3 \pm 3.7$	$0.095 \pm 0.048$	(CH <sub>3</sub> CN) (neutral)
$18.1 \pm 0.2$ (exp.[15, 34, 71])	$0.3 \pm 0.10$	$2.4 \pm 0.082$	<sup>b</sup> polymer matrix (neutral)
$22.21 \pm 0.04$ (exp.[15, 34, 71])	$(2.7 \pm 0.19) \times 10^{-4}$	$(2.5 \pm 0.18) \times 10^3$	molecular-switch junction (neutral)
31.22 (simul.)	$6.3 \times 10^{-11}$	$1.1 \times 10^{10}$	gas phase (oxidation +1)
50.43 (simul.)	$4.5 \times 10^{-25}$	$1.5 \times 10^{24}$	gas phase (oxidation +2)
65	_	_	<sup>c</sup> SAM on SiO <sub>2</sub> wafers
$(\exp. + \text{simul.}[72])$			(oxidation +2)

<sup>&</sup>lt;sup>a</sup> Values are calculated using the Eyring equation,  $1/\tau = (k_B T/h) \exp(-\Delta G^{\ddagger}/RT)$ . <sup>b</sup>Weight ratio 70:7:20:3 for CH<sub>3</sub>CN/poly(methylmethacrylate)/propylene carbonate/LiClO<sub>4</sub>. <sup>c</sup>The modified AFM tip is attached to the CBPQT<sup>4+</sup> ring.

- $\Delta G_{\rm D2T}^{\ddagger} = 16.2 \, {\rm kcal/mol} \; (\tau \sim 0.095 \, {\rm s}) \; {\rm in \; MeCN \; solvent},$
- $\Delta G_{\mathrm{D2T}}^{\ddagger}=18.1$  kcal/mol ( $\tau\sim2.4$  s) in a MeCN/polymethylmethacrylate/ propylene carbonate/LiClO<sub>4</sub> polymer matrix containing weight ratios of 70:7:20:3, and

•  $\Delta G_{\rm D2T}^{\ddagger}$  = 22.21 kcal/mol ( $\tau \sim$  2.5 × 10<sup>3</sup> s) in the molecular switch tunnel junction.

In addition, the devices fabricated with this derivative containing the triphenylene spacer exhibit a relaxation half-life of  $\tau \sim 90$  min [2] ( $\Delta G_{\rm D2T}^{\ddagger} = 22.66$  kcal/mol).

In addition, our free energy barrier is quite comparable to the barriers to circumrotation of [2]catenanes. Leigh and co-workers used NMR to determine  $\Delta G^{\ddagger}$  of interlocked catenane molecules as 11-20 kcal/mol for various solvents and calculated the free energy barrier as 10-20 kcal/mol using force-field based Hessians [69, 70, 71].

Although our simulations were performed in the gas phase, the  $\Delta G_{\rm D2T}^{\ddagger}$  of 18 kcal/mol agrees well with the experimental barriers (17 – 22 kcal/mol) [15, 34, 49] for a variety of environments. This suggests that the energy barrier does not depend strongly on environment.

We did not include the counterions in this study because preliminary calculations showed that the charges would sometimes change in erratic ways due to the floppy energy landscape for the countercharges. Indeed, the good agreement with experiment for the barriers suggests that the instantaneous changes in the potential due to counterions can be neglected.

# 3.3.2.3 $\Delta G_{\mathrm{T2D}}^{\ddagger}$ and $\Delta G_{\mathrm{D2T}}^{\ddagger}$ for Oxidized Cases

Although the neutral state prefers to have the CBPQT<sup>4+</sup> ring at the TTF, we find that the +1 and +2 oxidized states lead to a completely different energy profile (Fig. 3.8b). In both cases, the DNP becomes the global minimum with the TTF destabilized by  $\Delta G = 25.75 \, \text{kcal/mol}$  for the +1 oxidation state and  $\Delta G = 47.78 \, \text{kcal/mol}$  for the +2 oxidation state.

Starting with the ring at the TTF site and oxidizing, we find that the ring moves first by  $\sim 5$  Å to a local minimum on the ethylene oxide linker (with an energy decrease by  $\Delta G = 3.25$  kcal/mol for the +1 and  $\Delta G = 5.49$  kcal/mol for the +2). Then, it has a free energy barrier of  $\Delta G = 8.70$  kcal/mol (+1 state) or 8.02 kcal/mol (+2 state) to continue past the triphenylene spacer and toward the DNP for oxidation states.

Using the Eyring rate equation  $\left[1/\tau = (k_BT/h)\exp\left(-\Delta G^{\ddagger}/RT\right)\right]$ , the time required to overcome this barrier to move onto the DNP is  $2.9 \times 10^{-7}$  s for the +1 oxidation state and  $9.0 \times 10^{-8}$  s for the +2 oxidation state. It would be interesting to design an experiment to probe for this predicted barrier. It has been assumed that the huge Coulomb potential of the +4 ring with the +2 TTF would preclude a barrier. The origin of this barrier in the oxidized state is discussed below, which we find arises from the triphenylene spacer. We expect that there would be no barrier without this spacer.

Relative to the final state of the ring at the DNP site, the energy at the ethylene oxide linker (EO) near the TTF site is  $22.52 \,\text{kcal/mol}$  higher (+1 oxidation), leading to a Boltzmann population of  $10^{-17}$ . For the +2 oxidation state, the energy is  $42.41 \,\text{kcal/mol}$  higher, leading to a population of  $10^{-32}$ . Thus, for oxidation states

+1 and +2, we expect the CBPQT<sup>4+</sup> ring to stay on the DNP site until the system is reduced.

Indeed, there is an experimental estimate of this reverse barrier. Using a modified AFM with the ring attached, Brough *et al.* [72] measured the force exerted on the ring shuttling from the DNP to the TTF in the +2 oxidized system as 145 pN. Combining this experimental data with results from molecular mechanics simulations, they estimated the energy barrier to be 65 kcal/mol. This can be compared to our calculated barrier of 50.4 kcal/mol energy, validating the accuracy of the experiment. The maximum force measured in our simulation during the ring shuttling is 583 pN, which is similar to the experimental value of 145 pN.

#### 3.3.2.4 Effect of Coulombic Energy and van der Waals Energy

To understand why the PMF profiles are so different between the neutral, +1, and +2 oxidation states, we calculated the change in the Coulombic interaction energy and the van der Waals (vdW) interaction energy as a function of ring position along the backbone, for these three oxidation states (Figs. 3.9 and 3.10).

For the neutral state, we find that the Coulombic energy increases by  $60\,\mathrm{kcal/mol}$  as the ring moves from the TTF to the triphenylene spacer (barrier) and then drops by  $45\,\mathrm{kcal/mol}$  as it moves to the DNP. On the other hand, the vdW energy changes, within a range of  $\pm 4\,\mathrm{kcal/mol}$ , while the ring travels from the TTF to the DNP.

This indicates that the barrier is dominated by the differential Coulombic interactions with a peak of 443 kcal/mol at z = 28 Å (over the spacer). We were quite surprised because we expected the barrier to be dominated by vdW repulsions due to the bulky size of the triphenylene. To understand why Coulombic interactions are so important, we plot in Fig. 3.11 the total charge on the ring along the pathway, in the neutral case. We see that at the TTF or the DNP positions there is strong delocalization from the ring onto the backbone, but as the ring passes over the triphenylene spacer (at z = 28 Å), this charge localizes back onto the ring. Thus, we conclude that localization of the ring charge increases the Coulombic repulsion and dominates the free energy barrier. This suggests that the barrier can be modified dramatically by changing the polarity of the spacer.

We also found that as the system is oxidized, the magnitude of Coulombic repulsion increases from  $380-445\,\mathrm{kcal/mol}$  for the neutral state, to  $520-545\,\mathrm{kcal/mol}$  for the +1 oxidation state, and finally, to  $670-700\,\mathrm{kcal/mol}$  for the +2 oxidation state. In contrast, the vdW energy changes from 165-173 to 165-172 to  $164-171\,\mathrm{kcal/mol}$  as the system is oxidized. This implies that the driving force inducing the mechanical movement of the ring is the increased Coulombic repulsion due to oxidization of the rotaxane. This confirms our view since the beginning of our experiments.

However, the PMF profile (Fig. 3.7b) still differs substantially from the Coulombic energy profile (Fig. 3.9). For instance, in the neutral case, the Coulombic energy difference between two stations is 12.03 kcal/mol, which is  $\sim$  12 times larger than  $\Delta G_{\rm T2D} = 1.0$  kcal/mol, and the Coulombic energy barrier for the shuttling from the DNP to the TTF is 46.75 kcal/mol, which is  $\sim$  2.6 times larger than

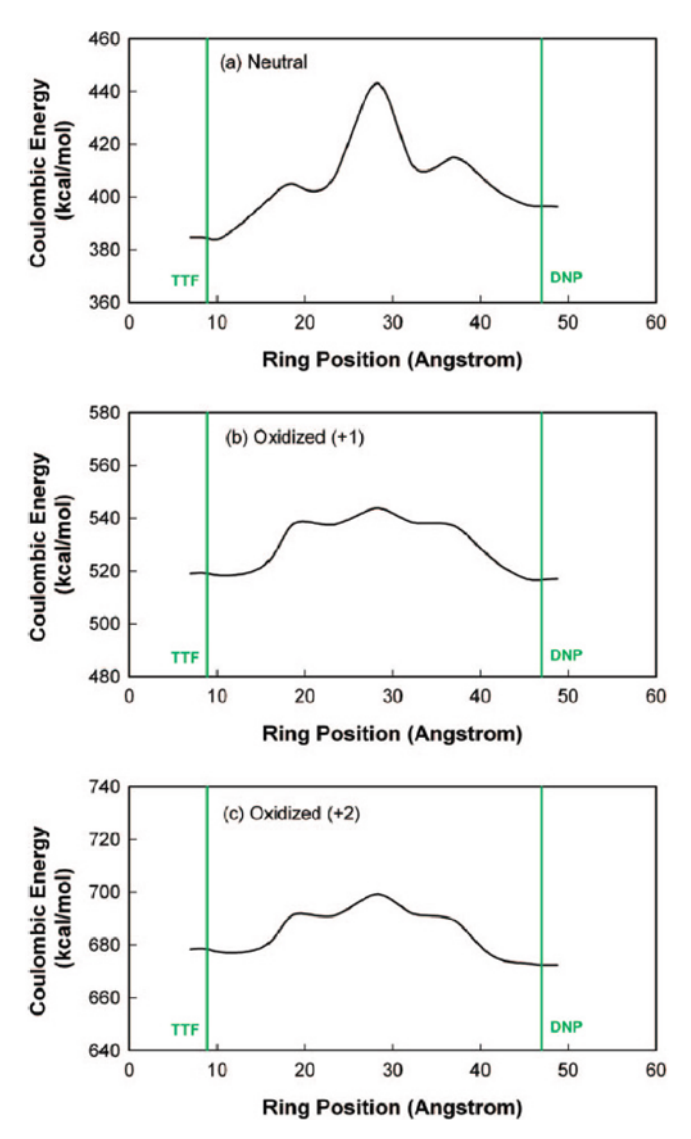


Fig. 3.9 Change of Coulombic interaction energy as a function of the ring position: (a) neutral state; (b) oxidation state +1; (c) oxidation state +2

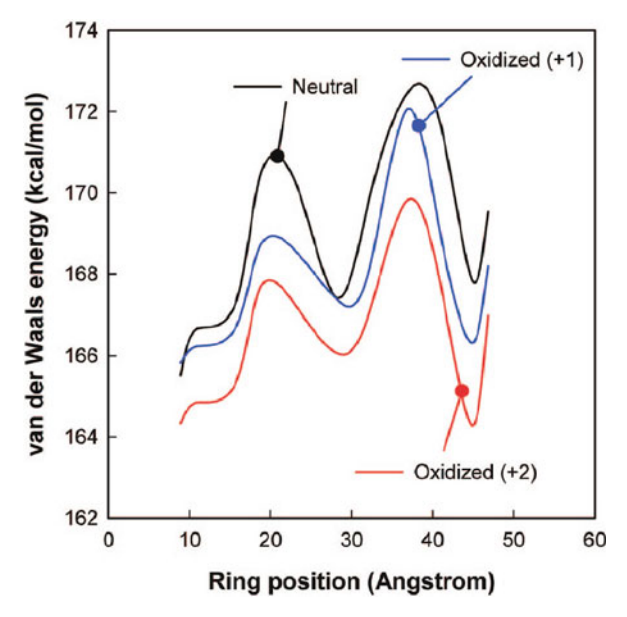


Fig. 3.10 Change of van der Waals interaction energy as a function of the ring position: (a) neutral state; (b) oxidation state +1; (c) oxidation state +2

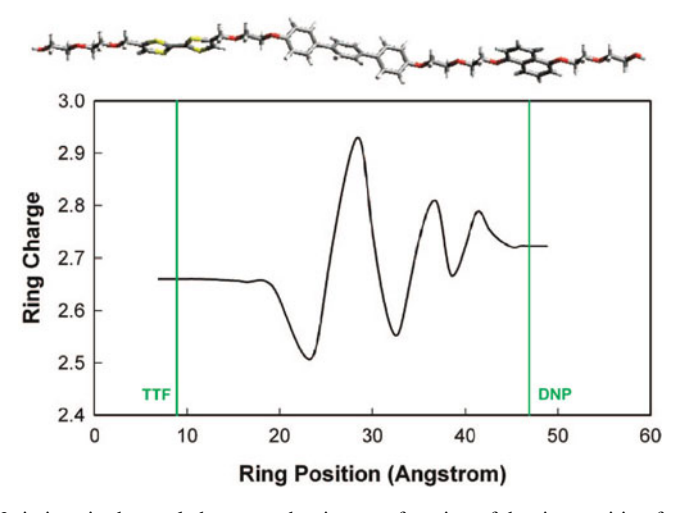


Fig. 3.11 Variations in the total charge on the ring as a function of the ring position for the neutral case

 $\Delta G_{\mathrm{D2T}}^{\ddagger} = 18.03\,\mathrm{kcal/mol}$ . Thus, the key features of the PMF profile are not fully explained in terms of the Coulombic energy alone. Another possible contributor to the free energy is vibrational entropy, which can be investigated directly from the MD simulation trajectory [73, 74].

#### 3.4 Conclusions

We used constrained MD simulations to calculate the free energy profile at 300 K for the shuttling of the CBPQT<sup>4+</sup> ring between the TTF and the DNP in the rotaxane molecule. This free energy profile was derived by calculating and integrating the MF acting on the ring as it is moved from one position to another position along the backbone. We found that it is particularly important to allow the charges to adjust adiabatically as the ring moves. Indeed, we find that the Coulomb interactions dominate the barriers for these systems.

We found that the free energy barrier from the DNP to the TTF is 18.03 kcal/mol for the neutral system, which agrees well with experimental values of 17-22 kcal/mol for various environments. We calculate that the  $\Delta G$  between the TTF and the DNP positions is 1.0 kcal/mol, which compares well with experimental results of 1.4-1.6 kcal/mol obtained from binding energies of separate DNP and TTF systems with the CBPQT<sup>4+</sup> ring.

These results validate the accuracy of our computational procedure. Thus, we can now use this validated technique for estimating the switching kinetics for new designs of molecular architectures.

Acknowledgments The computational work was initiated with support by the National Science Foundation (NIRT, W.A.G.). The collaboration was supported by the Microelectronics Advanced Research Corporation (MARCO; W.A.G. and J.F.S.) and its Focus Centers on Functional Engineered NanoArchitectonics (FENA) and Materials Structures and Devices, the Molectronics Program of the Defense Advanced Research Projects Agency (DARPA; J.F.S. and J.R.H.), the Center for Nanoscale Innovation for Defense (CNID; J.F.S.), and the MARCO Materials Structures and Devices Focus Center (J.R.H.). In addition, the facilities of the MSC (W.A.G.) were supported by ONR-DURIP and ARO-DURIP.

# **Bibliography**

- Luo, Y.; Collier, C. P.; Jeppesen, J. O.; Nielsen, K. A.; Delonno, E.; Ho, G.; Perkins, J.; Tseng, H. R.; Yamamoto, T.; Stoddart, J. F.; Heath, J. R. ChemPhysChem 2002, 3, 519–525.
- Green, J. E.; Choi, J. W.; Boukai, A.; Bunimovich, Y.; Johnston-Halperin, E.; DeIonno, E.; Luo, Y.; Sheriff, B. A.; Xu, K.; Shin, Y. S.; Tseng, H.-R.; Stoddart, J. F.; Heath, J. R. *Nature* 2007, 445, 414–417.
- 3. Anelli, P. L.; Spencer, N.; Stoddart, J. F. J. Am. Chem. Soc. 1991, 113, 5131–5133.
- 4. Bissell, R. A.; Cordova, E.; Kaifer, A. E.; Stoddart, J. F. Nature 1994, 369, 133–137.
- Asakawa, M.; Ashton, P. R.; Balzani, V.; Credi, A.; Hamers, C.; Mattersteig, G.; Montalti, M.; Shipway, A. N.; Spencer, N.; Stoddart, J. F.; Tolley, M. S.; Venturi, M.; White, A. J. P.; Williams, D. J. Angew. Chem. Int. Ed. 1998, 37, 333–337.

Bibliography 43

 Balzani, V.; Credi, A.; Mattersteig, G.; Matthews, O. A.; Raymo, F. M.; Stoddart, J. F.; Venturi, M.; White, A. J. P.; Williams, D. J. J. Org. Chem. 2000, 65, 1924–1936.

- Collier, C. P.; Mattersteig, G.; Wong, E. W.; Luo, Y.; Beverly, K.; Sampaio, J.; Raymo, F. M.; Stoddart, J. F.; Heath, J. R. Science 2000, 289, 1172–1175.
- 8. Barboiu, M.; Lehn, J.-M. Proc. Natl. Acad. Sci. U.S.A. 2002, 99, 5201–5206.
- Hogg, L.; Leigh, D. A.; Lusby, P. J.; Morelli, A.; Parsons, S.; Wong, J. K. Y. Angew. Chem., Int. Ed. 2004, 43, 1218–1221.
- Zheng, X.; Mulcahy, M. E.; Horinek, D.; Galeotti, F.; Magnera, T. F.; Michl, J. J. Am. Chem. Soc. 2004, 126, 4540–4542.
- Hawthorne, M. F.; Zink, J. I.; Skelton, J. M.; Bayer, M. J.; Liu, C.; Livshits, E.; Baer, R.; Neuhauser, D. Science 2004, 303, 1849–1851.
- de Jong, J. J. D.; Lucas, L. N.; Kellogg, R. M.; van Esch, J. H.; Reringa, B. L. Science 2004, 304, 278–281.
- Turberfield, A. J.; Mitchell, J. C.; Yurke, B.; Mills, A. P.; Blakey, M. I.; Simmel, F. C. *Phys. Rev. Lett.* 2003, 90, art. no.118102.
- Liu, H. Q.; Schmidt, J. J.; Bachand, G. D.; Rizk, S. S.; Looger, L. L.; Hellinga, H. W.; Montemagno, C. D. Nat. Mater. 2002, 1, 173–177.
- Choi, J. W.; Flood, A.; Steuerman, D. W.; Nygaard, S.; Braunschweig, A.; Moonen, N.; Laursen, B.; Luo, Y.; DeIonno, E.; Peters, A. J.; Jeppesen, J. O.; Stoddart, J. F.; Heath, J. R. Chem. Eur. J. 2006, 12, 261–279.
- Collier, C. P.; Jeppesen, J. O.; Luo, Y.; Perkins, J.; Wong, E. W.; Heath, J. R.; Stoddart, J. F. J. Am. Chem. Soc. 2001, 123, 12632–12641.
- Diehl, M. R.; Steuerman, D. W.; Tseng, H. R.; Vignon, S. A.; Star, A.; Celestre, P. C.; Stoddart, J. F.; Heath, J. R. *ChemPhysChem* 2003, 4, 1335–1339.
- Credi, A.; Balzani, V.; Langford, S. J.; Stoddart, J. F. J. Am. Chem. Soc. 1997, 119, 2679–2681.
- Collier, C. P.; Wong, E. W.; Belohradsky, M.; Raymo, F. M.; Stoddart, J. F.; Kuekes, P. J.;
   Williams, R. S.; Heath, J. R. Science 1999, 285, 391–394.
- 20. Elizarov, A. M.; Chiu, S. H.; Stoddart, J. F. J. Org. Chem. 2002, 67, 9175-9181.
- 21. Carroll, R. L.; Gorman, C. B. Angew. Chem. Int. Ed. 2002, 41, 4379–4400.
- Yu, H. B.; Luo, Y.; Beverly, K.; Stoddart, J. F.; Tseng, H. R.; Heath, J. R. Angew. Chem. Int. Ed. 2003, 42, 5706–5711.
- 23. Heath, J. R.; Ratner, M. A. Phys. Today 2003, 56, 43-49.
- 24. Balzani, V.; Gomez-Lopez, M.; Stoddart, J. F. Acc. Chem. Res. 1998, 31, 405-414.
- Balzani, V.; Credi, A.; Raymo, F. M.; Stoddart, J. F. Angew. Chem. Int. Ed. 2000, 39, 3349–3391.
- 26. Chia, S. Y.; Cao, J. G.; Stoddart, J. F.; Zink, J. I. Angew. Chem. Int. Ed. 2001, 40, 2447–2451.
- Belohradsky, M.; Elizarov, A. M.; Stoddart, J. F. Collect. Czech. Chem. Commun. 2002, 67, 1719–1728.
- Hernandez, R.; Tseng, H. R.; Wong, J. W.; Stoddart, J. F.; Zink, J. I. J. Am. Chem. Soc. 2004, 126, 3370–3371.
- 29. Badjic, J. D.; Balzani, V.; Credi, A.; Silvi, S.; Stoddart, J. F. Science 2004, 303, 1845–1849.
- 30. Tseng, H. R.; Vignon, S. A.; Stoddart, J. F. Angew. Chem., Int. Ed. 2003, 42, 1491–1495.
- 31. Jeppesen, J. O.; Perkins, J.; Becher, J.; Stoddart, J. F. Angew. Chem. Int. Ed. 2001, 40, 1216–1221.
- 32. Jeppesen, J. O.; Nielsen, K. A.; Perkins, J.; Vignon, S. A.; Di Fabio, A.; Ballardini, R.; Gandolfi, M. T.; Venturi, M.; Balzani, V.; Becher, J.; Stoddart, J. F. *Chem. Eur. J.* **2003**, 9, 2982–3007.
- 33. Yamamoto, T.; Tseng, H. R.; Stoddart, J. F.; Balzani, V.; Credi, A.; Marchioni, F.; Venturi, M. Collect. Czech. Chem. Commun. 2003, 68, 1488–1514.
- Tseng, H. R.; Vignon, S. A.; Celestre, P. C.; Perkins, J.; Jeppesen, J. O.; Di Fabio, A.; Ballardini, R.; Gandolfi, M. T.; Venturi, M.; Balzani, V.; Stoddart, J. F. Chem. Eur. J. 2004, 10, 155–172.

- 35. Kang, S. S.; Vignon, S. A.; Tseng, H. R.; Stoddart, J. F. Chem. Eur. J. 2004, 10, 2555–2564.
- 36. Livoreil, A.; Dietrichbuchecker, C. O.; Sauvage, J. P. J. Am. Chem. Soc. 1994, 116, 9399–9400.
- Flood, A. H.; Peters, A. J.; Vignon, S. A.; Steuerman, D. W.; Tseng, H.-R.; Kang, S.; Heath, J. R.; Stoddart, J. F. Chem. Eur. J. 2004, 24, 6558–6561.
- Steuerman, D. W.; Tseng, H.-R.; Peters, A. J.; Flood, A. H.; Jeppesen, J. O.; Nielsen, K. A.;
   Stoddart, J. F.; Heath, J. R. Angew. Chem. Int. Ed. 2004, 43, 6486–6491.
- Lee, I. C.; Frank, C. W.; Yamamoto, T.; Tseng, H.-R.; Flood, A. H.; Stoddart, J. F.; Jeppesen,
   J. O. Langmuir 2004, 20, 5809–5828.
- 40. Tseng, H. R.; Wu, D. M.; Fang, N. X. L.; Zhang, X.; Stoddart, J. F. *ChemPhysChem* **2004**, 5, 111–116.
- Raehm, L.; Kern, J. M.; Sauvage, J. P.; Hamann, C.; Palacin, S.; Bourgoin, J. P. Chem. Eur. J. 2002, 8, 2153–2162.
- 42. Jang, Y. H.; Kim, Y. H.; Jang, S. S.; Hwang, S. G.; Goddard, W. A., III *Abstr. Pap., Am. Chem. Soc.* **2004**, 227, U850–U850.
- Jang, S. S.; Jang, Y. H.; Kim, Y.-H.; Goddard, W. A., III; Flood, A. H.; Laursen, B. W.; Tseng, H.-R.; Stoddart, J. F.; Jeppesen, J. O.; Choi, J. W.; Steuerman, D. W.; DeIonno, E.; Heath, J. R. J. Am. Chem. Soc. 2005, 127, 1563–1575.
- 44. Jang, S. S.; Jang, Y. H.; Kim, Y. H.; Goddard, W. A., III; Choi, J. W.; Heath, J. R.; Laursen, B. W.; Flood, A. H.; Stoddart, J. F.; Norgaard, K.; Bjornholm, T. J. Am. Chem. Soc. 2005, 127, 14804–14816.
- 45. Jang, Y. H.; Jang, S. S.; Goddard, W. A., III J. Am. Chem. Soc. 2005, 127, 4959–4964.
- 46. Jang, Y. H.; Goddard, W. A., III J. Phys. Chem. B 2006, 110, 7660-7665.
- 47. Kim, Y.-H.; Goddard, W. A., III *J. Phys. Chem. C* **2007**, 111, 4831–4837.
- 48. Jeppesen, J. O.; Nygaard, S.; Vignon, S. A.; Stoddart, J. F. Eur. J. Org. Chem. 2004, 196, 220.
- Dichtel, W. R.; Heath, J. R.; Stoddart, J. F. Philos. Trans. R. Soc. A, Math. Phys. Eng. Sci. 2007, 365, 1607–1625.
- 50. Carter, E. A.; Ciccotti, G.; Hynes, J. T.; Kapral, R. Chem. Phys. Lett. 1989, 156, 472–477.
- 51. Sprik, M.; Ciccotti, G. J. Chem. Phys. 1998, 109, 7737-7744.
- 52. Trzesniak, D.; Kunz, A. P. E.; van Gunsteren, W. F. ChemPhysChem 2007, 8, 162–169.
- 53. Jaguar, V. 5.0 ed.; Schrödinger Inc.: Portland, 2003.
- 54. Evans, D. J.; Morriss, G. P. Statistical Mechanics of Nonequilibrium Liquids; Academic Press: London, 1990.
- 55. Fixman, M. Proc. Natl. Acad. Sci. U.S.A. 1974, 71, 3050-3053.
- 56. Mayo, S. L.; Olafson, B. D.; Goddard, W. A., III J. Phys. Chem. 1990, 94, 8897–8909.
- Jang, S. S.; Molinero, V.; Cagin, T.; Goddard, W. A., III J. Phys. Chem. B 2004, 108, 3149–3157.
- Jang, S. S.; Lin, S.-T.; Cagin, T.; Molinero, V.; Goddard, W. A., III J. Phys. Chem. B 2005, 109, 10154–10167.
- 59. Jang, S. S.; Goddard, W. A. J. Phys. Chem. C 2007, 111, 2759-2769.
- Jang, S. S.; Lin, S.-T.; Maiti, P. K.; Blanco, M.; Goddard, W. A., III; Shuler, P.; Tang, Y. J. Phys. Chem. B 2004, 108, 12130–12140.
- 61. Jang, S. S.; Goddard, W. A. J. Phys. Chem. B 2006, 110, 7992–8001.
- 62. Plimpton, S. J. J. Comput. Phys. 1995, 117, 1-19.
- 63. Plimpton, S. J.; Pollock, R.; Stevens, M. The Eighth SIAM Conference on Parallel Processing for Scientific Computing Minneapolis; 1997.
- Swope, W. C.; Andersen, H. C.; Berens, P. H.; Wilson, K. R. J. Chem. Phys. 1982, 76, 637–649.
- 65. Castro, R.; Nixon, K. R.; Evanseck, J. D.; Kaifer, A. E. J. Org. Chem. 1996, 61, 7298-7303.
- Ashton, P. R.; Balzani, V.; Becher, J.; Credi, A.; Fyfe, M. C. T.; Mattersteig, G.; Menzer, S.;
   Nielsen, M. B.; Raymo, F. M.; Stoddart, J. F.; Venturi, M.; Williams, D. J. J. Am. Chem. Soc. 1999, 121, 3951–3957.
- Bryce, M. R.; Cooke, G.; Duclairoir, F. M. A.; Rotello, V. M. Tetrahedron Lett. 2001, 42, 1143–1145.

Bibliography 45

68. Nielsen, M. B.; Jeppesen, J. O.; Lau, J.; Lomholt, C.; Damgaard, D.; Jacobsen, J. P.; Becher, J.; Stoddart, J. F. *J. Org. Chem.* **2001**, 66, 3559–3563.

- Leigh, D. A.; Murphy, A.; Smart, J. P.; Deleuze, M. S.; Zerbetto, F. J. Am. Chem. Soc. 1998, 120, 6458–6467.
- 70. Leigh, D. A.; Troisi, A.; Zerbetto, F. Chem. Eur. J. 2001, 7, 1450-1454.
- 71. Deleuze, M. S.; Leigh, D. A.; Zerbetto, F. J. Am. Chem. Soc. 1999, 121, 2364–2379.
- Brough, B.; Northrop, B. H.; Schmidt, J. J.; Tseng, H. R.; Houk, K. N.; Stoddart, J. F.;
   Ho, C. M. Proc. Natl. Acad. Sci. U.S.A. 2006, 103, 8583–8588.
- 73. Lin, S. T.; Blanco, M.; Goddard, W. A. J. Chem. Phys. 2003, 119, 11792–11805.
- 74. Lin, S. T.; Jang, S. S.; Cagin, T.; Goddard, W. A. J. Phys. Chem. B 2004, 108, 10041–10052.

## Chapter 4 Sodium Diffusion Through Aluminum-Doped Zeolite BEA System: Effect of Water Solvation

Reprinted with permission from Kim, H; Deng, W.-Q.; Goddard, W. A.; Jang S. S.; Davis M. E.; Yan Y. J. Phys. Chem. C 2009, 113 (3), 819-826. Copyright 2009 American Chemical Society.

**Abstract** To investigate the effect of hydration on the diffusion of sodium ions through the aluminum-doped zeolite BEA system (Si/Al = 30), we used the grand canonical Monte Carlo (GCMC) method to predict the water absorption into aluminosilicate zeolite structure under various conditions of vapor pressure and temperature, followed by molecular dynamics (MD) simulations to investigate how the sodium diffusion depends on the concentration of water molecules. The predicted absorption isotherm shows first-order-like transition, which is commonly observed in hydrophobic porous systems. The MD trajectories indicate that the sodium ions diffuse through zeolite porous structures via hopping mechanism, as previously discussed for similar solid electrolyte systems. These results show that above 15 wt % hydration (good solvation regime) the formation of the solvation cage dramatically increases sodium diffusion by reducing the hopping energy barrier by 25% from the value of 3.8 kcal/mol observed in the poor solvation regime.

#### 4.1 Introduction

Zeolites constitute a unique class of the porous materials widely used in ion exchange, selective catalysis, and molecular sieve applications [1, 2]. An important property for many of these applications is migration of the absorbed water molecules. It has been observed that water migration in such porous materials proceeds differently than in the bulk water phase under the same temperature and chemical potential conditions [3, 4, 5, 6]; hence, we undertook a study of how nanoscale confinement in zeolites affects such of properties as structure, dynamics, and thermodynamics with absorbed molecules [7, 8, 9, 10, 11, 12, 13, 14, 15, 16, 17, 18].

In aluminosilicate zeolites the aluminum is generally incorporated in the three-dimensional framework in the form of  $AlO_4^-$  surrounded by neighboring  $SiO_4$  while

alkali metals such as Na<sup>+</sup> or K<sup>+</sup> are in the pores, interacting electrostatically with the zeolite framework. These positively charged and Movable cations in various zeolite systems have been studied intensively [7, 8, 19, 20, 21, 22, 23, 24, 25, 26, 27, 28, 29] since they impart many interesting properties to the zeolite systems. In particular, the ionic conductivity of zeolites can be controlled by the level of non-framework ions and their hydration (undoped zeolites are insulators with an electronic band gap of  $\sim$ 7 eV) [9]. The chemical nature, hydrophilicity, and selectivity for binding guest molecules in zeolites can be manipulated as appropriate for many practical applications [10, 11].

One recent interesting application of zeolites is as proton exchange membranes for fuel cells (PEMFC) [12, 13, 14, 15, 16, 17]. Here the molecular sieving capability and tunable acidity/hydrophilicity of zeolites can be incorporated to form a polyelectrolyte-based membrane that could improve the high temperature/low humidity performance of fuel cells [18].

We report here studies of the aluminosilicate zeolite BEA (Si/Al = 30). A distinct structural feature of interest for BEA is its three-dimensional channel structure which is characterized by  $\sim$ 1 nm diameter channels (Fig. 4.1) in which water molecules may form a continuous phase, thereby facilitate ionic transport which makes membranes based on such materials useful as a replacement for polymer electrolyte membranes (PEM) for fuel cell applications. In PEM fuel cell membrane such at Nafion, the protons are transported through two mechanisms: vehicular diffusion of protonated waters and Grotthuss diffusion in which protons hop from water to water, with the relative contributions depending on the water content, counterions, porosity, temperature etc. Of course, diffusion of sodium or potassium cations occurs only through hopping. In this study, we determine how the nanometer scale confinement in the aluminosilicate zeolite BEA (Si/Al = 30) affects sodium diffusion.

First, we used grand canonical Monte Carlo (GCMC) simulations to predict the water absorption of aluminosilicate zeolite BEA system at various conditions, and then we applied the equilibrium molecular dynamics (MD) simulations on the diffusion starting with the hydrated systems obtained from the GCMC simulations. During such MD simulations, we sampled the time evolution of both the sodium diffusion and the water structure associated with the sodium ions.

#### 4.2 Simulation Details

#### 4.2.1 Force Field

To calculate the energy and geometry of the zeolite framework, we employed Burchart force field (FF) [19] developed to describe aluminosilicate structures and the van der Waals interactions with the Na. This FF uses the Lennard-Jones 12–6 form for the van der Waals interactions between all atoms of the framework. To describe the interactions between water molecules, we used the F3C water

4.2 Simulation Details 49

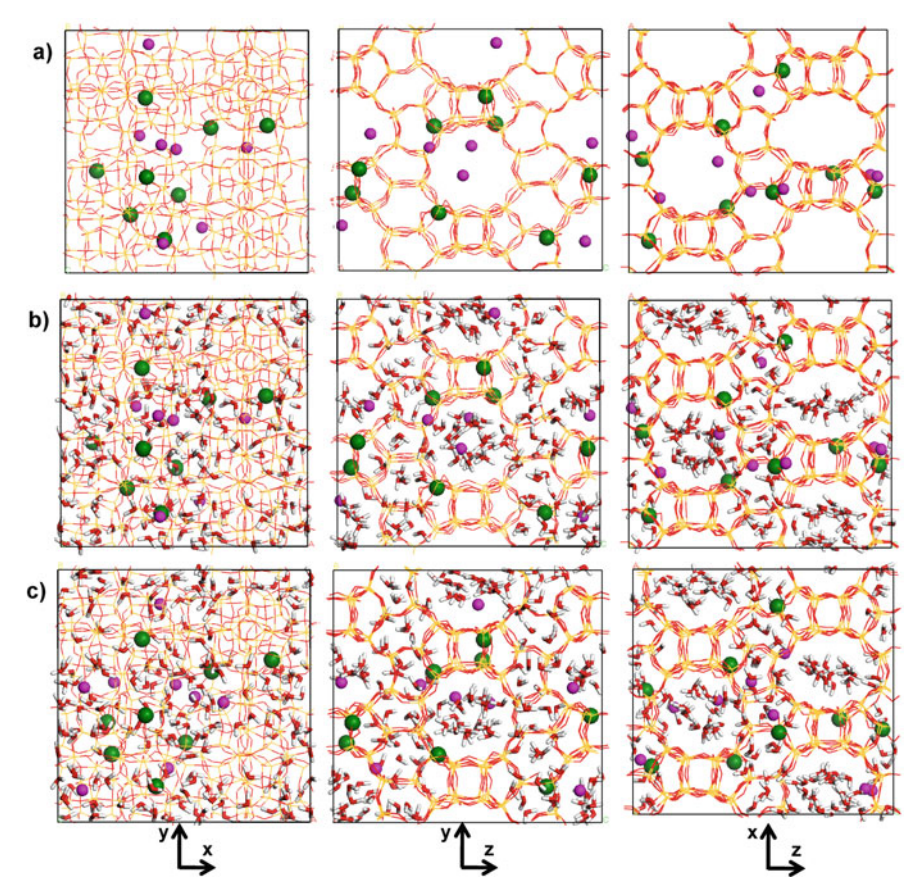


**Fig. 4.1** Atomistic structure for the primitive periodic cell with composition of  $Na_8Al_8Si_{248}O_{512}$ . This shows *green* balls are aluminum and *magenta* balls are sodium. (a) Minimized aluminosilicate zeolite BEA structures without  $H_2O$ , (b) snapshot of zeolite BEA structures after the GCMC simulation for 298.15 K and 101.3250 kPa, and (c) snapshot of zeolite BEA structures after 4 ns NPT MD simulation at 298.15 K and 101.3250 kPa

FF [20]. For the off-diagonal van der Waals interactions between different types of atoms, we used the geometric-mean combination rule. The Lennard-Jones interactions were terminated beyond 18.0 Å, using a cubic spline function starting at 15.0 Å.

The atomic charges of the individual atoms of the zeolite frame were determined using the charge equilibration (QEq) method [21]. Since our simulation cell contains eight  $AlO_4^-$  sites, the total charge of the framework is set by -8. The eight sodium ions each were taken to have +1 charge, leading to charge neutrality of the simulation cell. The atomic charge of the water is from the F3C model [20]. The particle-particle particle-mesh (PPPM) method [22] was employed to compute the electrostatic using an accuracy criterion of  $10^{-5}$ .

## 4.2.2 Grand Canonical Monte Carlo (GCMC) Method and Molecular Dynamics (MD) Simulation

To predict the water absorption in aluminosilicate zeolite BEA framework as a function of partial pressure and temperature, we carried out grand canonical Monte Carlo (GCMC) simulations [23, 24] using the Sorption module of Cerius2 [25]. Since the chemical potential of the adsorbed phase equals the chemical potential of the bulk gas at equilibrium condition, the GCMC simulation makes multiple attempts to add one water molecule according to the probability

$$P_{add} = \min \left[ 1, \frac{V}{(N+1)\Lambda^3} \exp\left( -\frac{\Delta U}{k_B T} \right) \right], \tag{4.1}$$

or subtract one with the following probability

$$P_{sub} = \min \left[ 1, \frac{N\Lambda^3}{V} \exp \left( -\frac{\Delta U}{k_B T} \right) \right], \tag{4.2}$$

where V is the pore volume, N is the number of water molecules in the simulated system,  $\Lambda$  is the thermal de Broglie wavelength, and  $\Delta U$  is the change in potential energy. For each GCMC simulation, we ran  $2 \times 10^8$  Monte Carlo steps (MCS), during which the zeolite framework including sodium ions were fixed and water molecules were moved by the Metropolis sampling rule [26, 27]. Each Monte Carlo step is allowed four different types of operations—translation, rotation, creation, and destructions—of the water molecule with equal probabilities.

All molecular dynamics (MD) simulations were performed using the LAMMPS (large-scale atomic/molecular massively parallel simulator) MD code developed by Plimpton at Sandia [28, 29]. The velocity Verlet algorithm[30] was used to solve the equations of motion with a time step of 1.0 fs. The isobaric-isothermal ensembles (NPT) were generated using Nosé-Hoover thermostat with a temperature damping relaxation time of 0.1 ps and the Andersen-Hoover barostat with a dimensionless cell mass factor of 1.0. A series of MD simulations were conducted at constant temperature of 298.15 K with various pressure conditions from 0.1013 to 101.3250 kPa. To understand the effect of temperature, another set of simulations were performed at constant pressure of 101.3250 kPa with various temperature conditions from 298.15 to 453.15 K.

#### 4.2.3 Construction of Models and Calculation of Properties

We used the  $2 \times 2 \times 1$  superstructure of zeolite BEA (based on the X-ray crystallography database [31]) as the periodic simulation cell for the MD. Then, eight silicon atoms in the channels were randomly chosen and replaced with aluminum atoms to have the lowest energy using substitutional disorder option of Cerius2 [25]. This

leads to a Si/Al ratio of 30, with a simulation cell consisting of  $8 \text{ AlO}_4^-$  and  $248 \text{ SiO}_4$  tetrahedral sites with an overall composition of  $Na_8Al_8Si_{248}O_{512}$ .

The eight sodium ions were initially placed near the aluminum-doped sites, and the full structure of zeolite frame including the sodium ions were energy minimized. Then the water contents were determined from GCMC simulations at various pressure and temperature conditions.

Then we carried out 8–12 ns NPT MD simulations and evaluated such properties as density, pair correlation function, and diffusion coefficients using the full trajectory files.

#### 4.3 Results and Discussion

#### 4.3.1 Water Absorption

Using GCMC, the chemical potential of water in zeolite frame was equilibrated with that of the external reservoir at various vapor pressure conditions ranging from 0.1013 to 101.3250 kPa. The water absorption isotherm at 298.15 K and the temperature dependence of water adsorption at 101.3250 kPa are shown at Figs. 4.2 and 4.3, respectively.

We were unable to locate published water adsorption isotherms for zeolite BEA with Si/Al of 30. Thus the data shown in Figs. 4.2 and 4.3 are from simulation

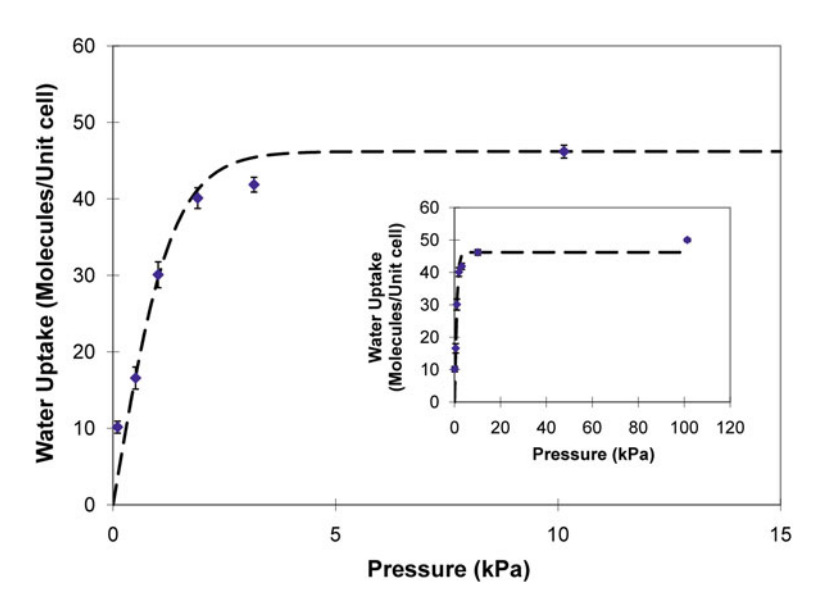


**Fig. 4.2** Dashed line is the least-squares fitted to  $f(x) = a \tanh(bx)$ , where a = 46.19 mole/ unit cell and b = 0.753 (1/kPa). We obtain a vapor pressure of 3.578 kPa for the point at which the water uptake reaches to 99% of the maximum loading uptake

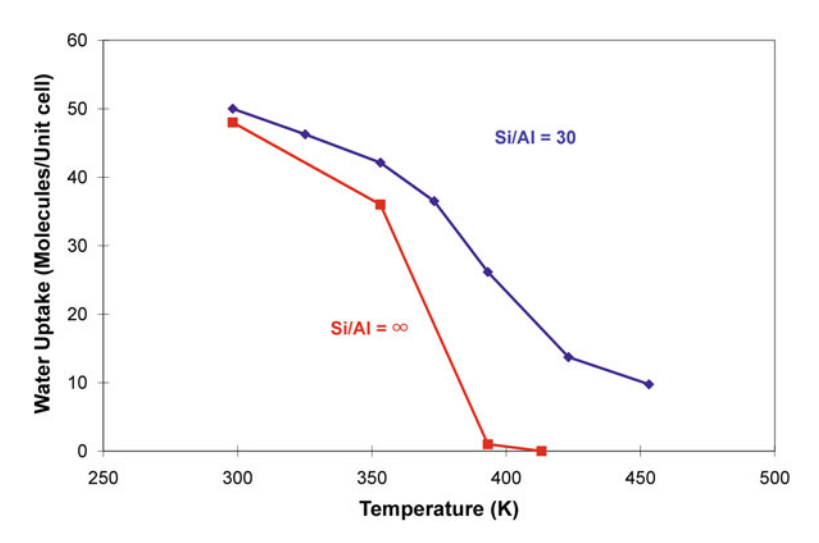


Fig. 4.3 Predicted temperature-dependence of water uptake at  $101.3250 \, \text{kPa}$  when the zeolite BEA has no aluminum doping ( $red \, curve$ ) and  $Si/Al = 30 \, (blue \, curve)$ . The presence of aluminum-doped sites as well as sodium ions enhance the water uptake amount especially in the high temperature

only. We observe a stepwise condensation at 3.5 kPa. The amount of water uptake increases abruptly and then shows fast saturation up to  $\sim$ 50 molecules per crystallographic unit cell, which can be regarded as a maximum loading number at 298.15 K. Previous studies discovered that a spontaneous condensation of water occurs in hydrophobic porous materials such as sodium faujasites of NaY and NaX [32], silicate-1 zeolites [33, 34] and carbon nanotubes [35]. Here, the term "hydrophobic" is used because of the spontaneous condensation behavior: if the surface of the nanopore were hydrophilic, then water absorption would proceed gradually over wide range of pressure through wetting the surface of the nanopore instead of increasing abruptly at a certain narrow pressure range. We expect that the capillary condensation would follow a first-order-like transition since the non-wetting character of the pore prohibits the intrusion of liquid water until a certain hydraulic pressure. This suggests that the aluminosilicate BEA zeolite system may sustain some extent of hydrophobicity even after some of the hydrophobic SiO<sub>4</sub> sites are replaced by hydrophilic AlO<sub>4</sub> sites.

The temperature dependence of water absorption is plotted at Fig. 4.3 at 101.3250 kPa. As the temperature increases, the amount of water uptake in zeolite frame decreases. This type of temperature dependency of water uptake has been observed in the experiments on the zeolite-4A structure [36] and in other simulation studies [32]. Of particular interest is that at 423 K, this BEA aluminosilicate zeolite frame still holds 20% of water absorbed at 300 K. We expect that this capability to retain significant amount of water at high temperature could make these materials useful as a replacement for performance of the PEM for fuel cell operation under high temperature/low humidity condition.

#### 4.3.2 Structure of Water in Zeolite

To characterize the water structure we calculated the density-normalized O(water)-O(water) pair correlation function,  $4\pi r^2 \rho \ g_{O(water)-O(water)}$  where r is the distance and  $\rho$  is the number density of water. Figure 4.4a shows  $4\pi r^2 \rho g_{O(water)-O(water)}$ 

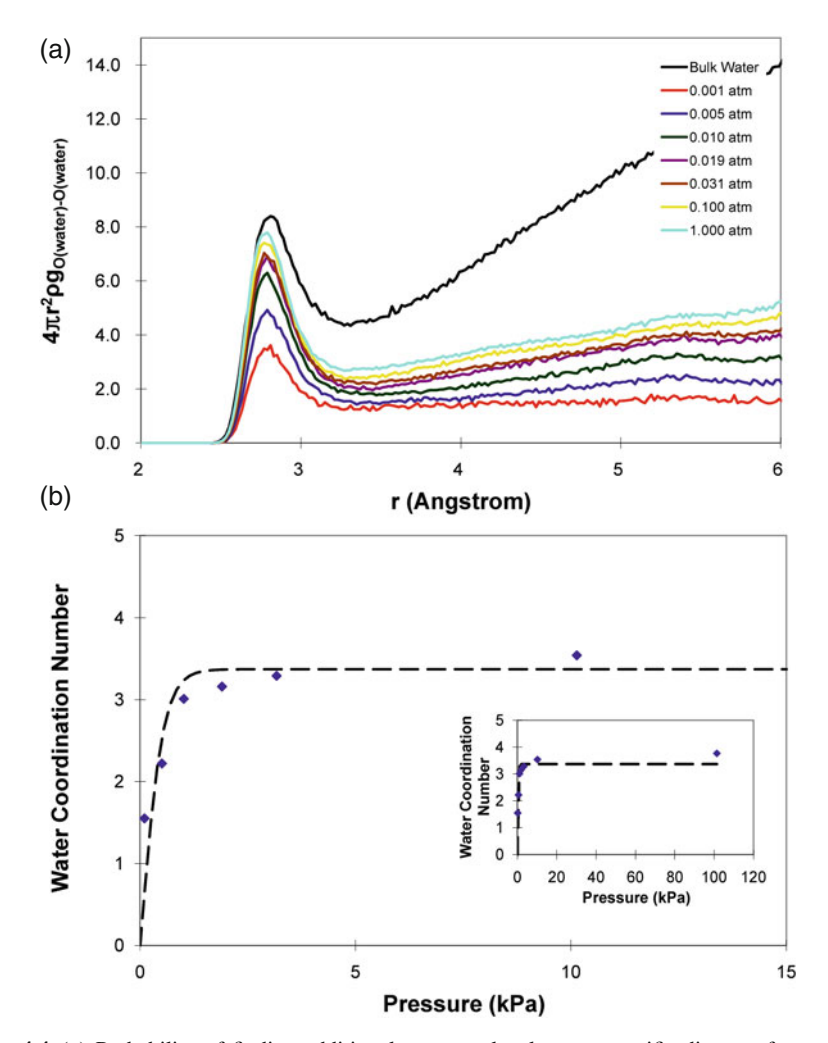


**Fig. 4.4** (a) Probability of finding additional water molecules at a specific distance from each water molecule. This is obtained as the product of pair correlation functions of water oxygens,  $\rho g_{O(water)-O(water)}$  with water density  $\rho$  and  $4\pi r^2$ . (b) Water coordination number (CN) of water molecule as a function of pressure. The CN of water molecule is obtained from the integration of curve a up to first minimum, which is at 3.7 Å. The saturated value of CN of the absorbed phase ( $\sim$ 3.8) is smaller than the CN of the bulk phase (4.5)

plots for water absorbed in various vapor pressure conditions and compares to the values for bulk water. Integrating the first peak in Fig. 4.4a leads to the coordination number CN. For bulk water we obtain CN = 4.59, in good agreement with CN = 4.5, from neutron diffraction experiment [37]. Figure 4.4b summarizes the change of the coordination numbers as a function of pressure, showing a behavior identical with the absorption isotherm in Fig. 4.2. This provides clear evidence for the spontaneous condensation in which all the water molecules absorbed into the system participate in water clusters. Figure 4.4 shows that the structure of the water absorbed in the zeolite framework approaches to that of bulk phase water as the water uptake/pressure is increased to 101.3250 kPa. However, the saturated value of CN of the absorbed phase ( $\sim 3.8$ ) is smaller than the CN of the bulk phase (4.5). This is reasonable because of the huge surface area of  $1362.99 \text{ m}^2/\text{g}$  of the nanopores of the zeolite (cf. activated carbon has  $500-1500 \text{ m}^2/\text{g}$ ). We observed similar behavior for water in Nafion and Dendrion polymer membranes [38, 39, 40].

In order to investigate the effect of the sodium ion on the water structure, we analyzed the density-normalized Na-O(water) pair correlation function,  $4\pi r^2 \rho g_{Na-O(water)}$  and the water coordination number of sodium ion as shown in Fig. 4.5, parts a and b, respectively. Similar to  $4\pi r^2 \rho g_{O(water)-O(water)}$  in Fig. 4.4 we see that  $4\pi r^2 \rho g_{Na-O(water)}$  increases with increasing pressure with a first peak position that does not change with pressure. However, the increase of the first peak intensity of  $4\pi r^2 \rho g_{Na-O(water)}$  up to  $\sim 3.5$  Å was not significant compared to that of  $4\pi r^2 \rho g_{O(water)-O(water)}$ . This indicates that the first water solvation shell for the sodium ion saturates rapidly toward CN =  $\sim 5.0$  (see Fig. 5b inset), which is consistent with the previous indication that water molecules cluster with sodium rather than interact with the surface of the nanopore, (indicating a hydrophobic nature of the nanopore surface). We believe that this is because the strong interaction of the net charge in the sodium ion enhances the development of its solvation structure. This value shows excellent agreement with the experiment which finds 4.82 [41].

#### 4.3.3 Effect of Water Contents on Sodium Diffusion

The diffusion coefficient of the sodium ion was calculated at pressures ranging from 0.1013 to 101.3250 kPa, as summarized at Table 4.1. To characterize the nature of the diffusion, Fig. 4.6 shows the log-log plot of the mean square displacements (MSD) versus time. For times up to ~20 ps, the MSD increases as a function of  $t^{1/2}$  indicating single file diffusion (SFD) behavior. For simulation times longer than 20 ps, the MSD shows a normal Fickian behavior (MSD $\propto$  t). This transition of MSD from SFD to normal Fickian diffusion occurs when the pore confines the particles but still allows the particles to pass by each other [42]. In the long time Fickian regime, we obtained the diffusion coefficient D from the mean square displacements of the sodium ions using Equation 4.3,

$$D = \left\langle (r(t) - r(0))^2 \right\rangle / 6t. \tag{4.3}$$

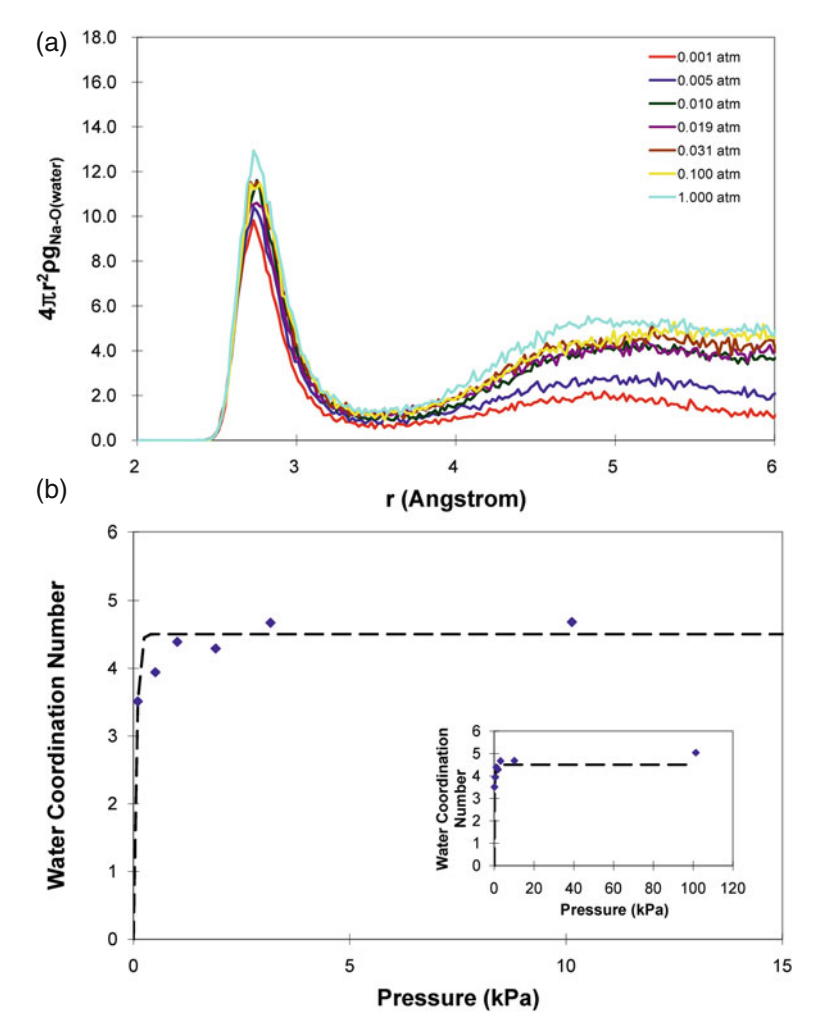


**Fig. 4.5** (a) Probability of finding sodium ions at a specific distance from each water molecule. This is obtained as the product of pair correlation functions of sodium atoms and water oxygen,  $\rho_{SNa-O(water)}$  with water density  $\rho$  and  $4\pi r^2$ . (b) Water coordination number (CN) of sodium ions as a function of pressure. The CN of water molecule is obtained from the integration of curve a up to first minimum, which is at 3.5 Å. The saturated value of CN of the absorbed phase ( $\sim 5.0$ ) is same to the CN of the bulk phase

In order to examine how the dynamics of sodium ion is influenced by its water solvation shell, we analyzed the diffusion coefficient of sodium ion versus water coordination number at 298.15 K. From Fig. 4.7, we observed a dramatic jump at about CN = 4.5 that corresponds to the point of the water uptake saturation in the absorption isotherm (Fig. 4.2). Indeed, Faux and his co-workers [43, 44, 45] reported theoretical studies that the diffusion coefficient of sodium in zeolite-4A

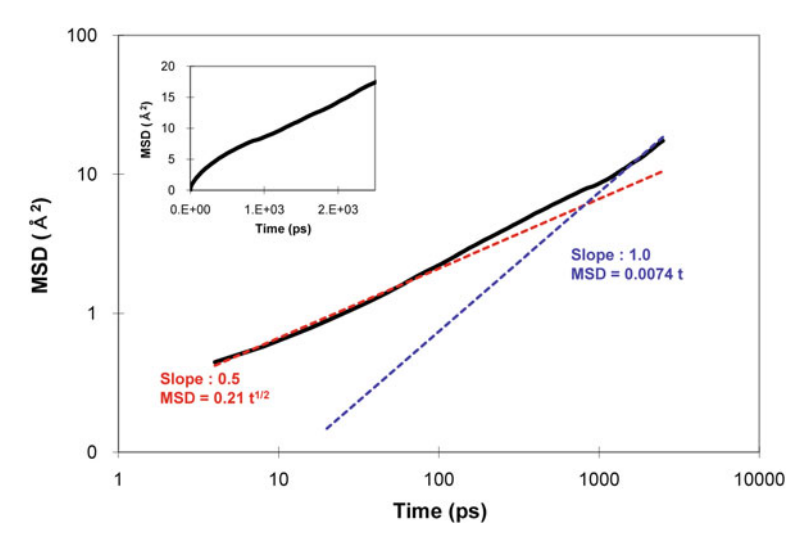


Fig. 4.6 Log-log plot of mean square displacements (MSD) vs time at 298.15 K and 101.3250 kPa based on a trajectory of 12 ns. Initially the MSD shows MSD  $\propto t^{1/2}$  up to  $t=\sim$ 20 ps, but the times  $>\sim$ 2 ns, we see normal 3D Fickian behavior (MSD  $\propto$  t). The Fickian regime leads to a diffusion coefficient of  $D=1.233\times 10^{-7}\,\mathrm{cm}^2/\mathrm{s}$ 

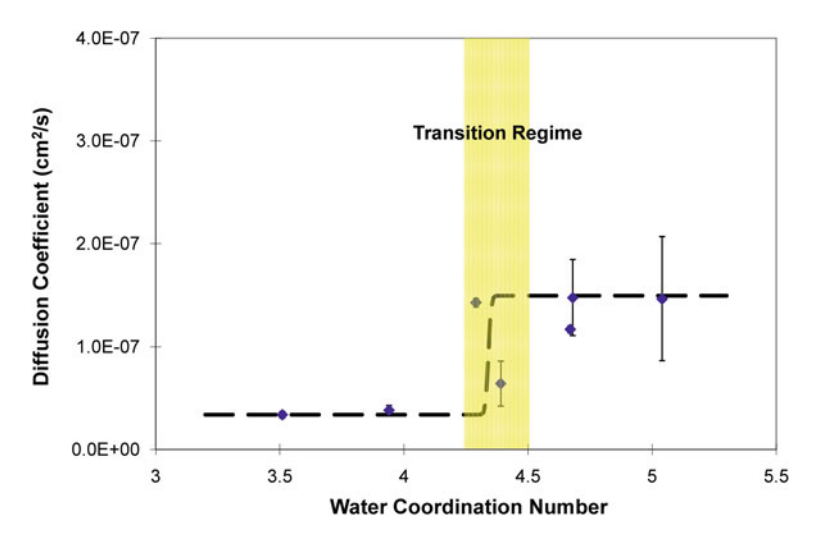
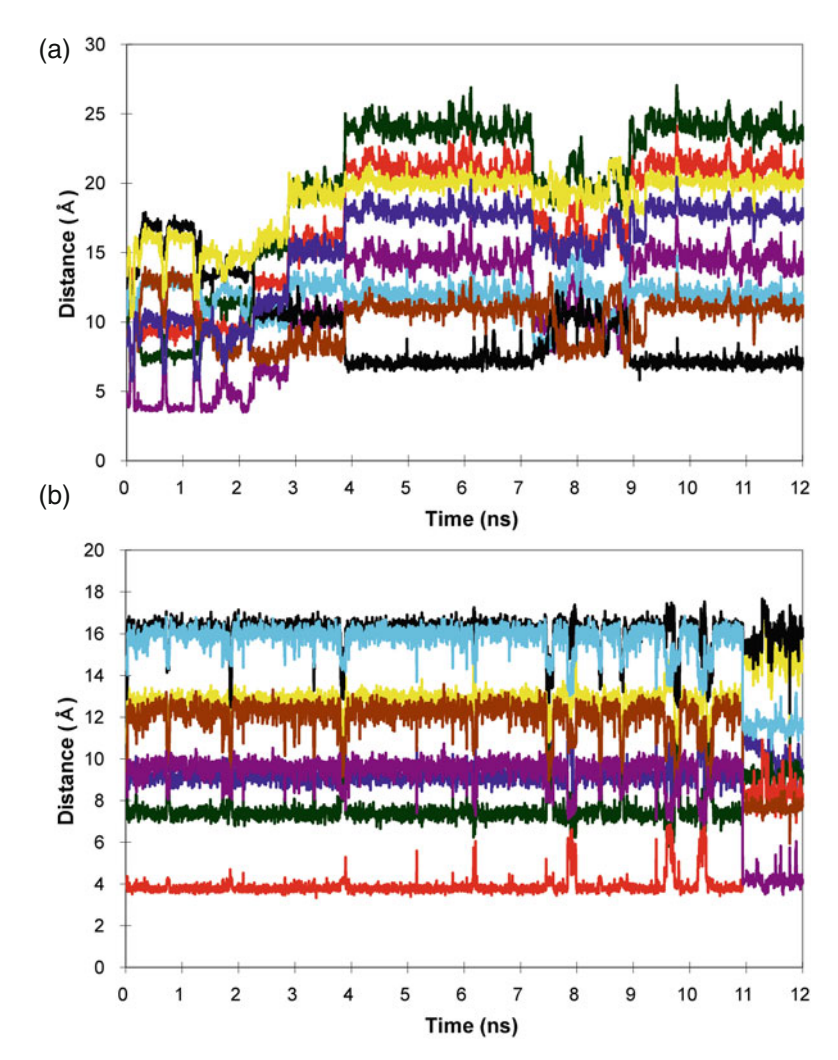


Fig. 4.7 Dependence of diffusion coefficient of sodium ion on water coordination number (CN) of sodium ion. The diffusion coefficients were calculated from three partitioned trajectories of 12 ns NPT simulations (each partition has 4 ns length), and the error bars were evaluated from the diffusion coefficients obtained from the three partitioned trajectories. This represents pressures from 0.1013 to 101.3250 kPa at 298.15 K. At a pressure of  $\sim 2.0$  kPa, we find an abrupt change in the water CN. When the sodium ion is solvated by >4.5 water molecules, its diffusion coefficient increases abruptly by a factor of 3.5. The *dashed line* is to guide the eye

system increases from  $1 \times 10^{-7}$  cm<sup>2</sup>/s to  $10 \times 10^{-7}$  cm<sup>2</sup>/s as the number of water molecules per unit cell increases from 0 to 224 in agreement with the trend and order of magnitude of the diffusion coefficient in our simulations. Furthermore, Faux et al. also observed a sudden jump of the sodium diffusion coefficient between 112 and 168 water molecules per unit cell, but did not explain the origin. We believe that this results directly from the degree of solvation. This spontaneous condensation of water (discussed in Section 4.3.1), leads to two regimes for the ionic diffusion in the presence of water. Detailed analysis of sodium ion trajectories allows us to enunciate why a threshold amount of water uptake is critical to enhance the diffusion of the ion from the microscopic point of view. The doped AlO<sub>4</sub> sites are Brönsted acid sites [46] that bound the nonframework cations via strong Coulomb interaction. Parts a and b of Fig. 4.8 show the time profile of the Al-Na distances for the good solvation regime (vapor pressure = 101.3250 kPa) and the poor solvation regime (vapor pressure = 0.1013 kPa), respectively. This shows clearly that each sodium ion localizes within ~5 Å of one of the aluminum-doped sites and diffuses by hopping from one site to a nearest neighbor aluminum site. Thus, the diffusion of sodium ion occurs through the hopping mechanism between AlO<sub>4</sub> sites (the Brönsted acid sites) with the energy barrier of 3.5-4.0 kcal/mol caused by the electrostatic interaction. Figure 4.8a indicates that the hopping events occur every 2 ns on average in the good solvation regime, whereas Fig. 4.8b shows just 1 hop within 12 ns in the poor solvation regime. This explains why the diffusion coefficient of sodium ion is  $\sim 10$  times larger in the good solvation regime than in the poor solvation regime as in Table 4.1. Sufficient numbers of water molecules are the most critical in creating solvation cage and helping the ionic hopping.

#### 4.3.4 Effect of Temperature on Sodium Diffusion

We calculated the diffusion coefficients of the sodium ions confined in the aluminosilicate zeolite BEA membrane are obtained for various temperatures ranging 298.15 K to 453.15 K. For each temperature, the amount of water uptake was determined using GCMC simulation (Fig. 4.3). The temperature effect on the sodium diffusion was taken from MD simulations based on the hydrated zeolite. These diffusion coefficients are presented in Table 4.2 and Fig. 4.9. Up to 373.15 K, the diffusion coefficient of sodium ion increases with increasing temperature, as expected for a normal activated process. However, we observe from Fig. 4.9 that the diffusion coefficient decreases with increasing temperature from 373.15 K to 453.15 K. This anomaly is a consequence of the less hydration of the zeolite at high temperature as previously discussed in Section 4.3.2. Here, the insufficient water absorption results in a less developed solvation shell, which cannot facilitate the sodium ion hopping events. Thus, the diffusion coefficient decreases at high temperature range with less number of water molecules. Therefore, just as in the discussion about good solvation and poor solvation regimes that depend on the vapor pressure, we consider that the good solvation regime applies up to 373.15 K, while the poor solvation regime applies beyond 400 K (the 393.15 K point lies within the transition regime.)



**Fig. 4.8** Time dependence of the distances of one sodium ion to all 8 aluminum atoms of the zeolite membrane. The distance to each aluminum atom is shown with a different color. (a) Vapor pressure is 101.3250 kPa (good solvation regime) at 298.15 K. This shows that it took 2 ns for the Na to hop from a position 4.8 Å from the *purple* Al to a position 7.5 Å from the *black* Al. Here a distance of 4.8 Å indicates one water shell between the Na and the Al, while 7.5 Å indicates separate water shells around each; (b) vapor pressure is 0.1013 kPa (poor solvation regime) at 298.15 K. In this case the Na remains at 4 Å from the Al which indicates that the Na remains coordinated to the O of the Al

**Table 4.1** Vapor pressures, water uptake/cell, water coordination numbers of the water molecule (up to 3.7 Å cutoff), water coordination numbers of the sodium ion (up to 3.5 Å cutoff), and diffusion coefficients from NPT MD at temperature of 298.15 K

vapor pressure (kPa)	water uptake/Cell	CN water	CN (sodium)	diffusion coefficient (cm <sup>2</sup> /s)
0.1013	10.15	1.55	3.51	$(0.338 \pm 0.033) \times 10^{-7}$
0.5066	16.57	2.22	3.94	$(0.382 \pm 0.048) \times 10^{-7}$
1.0133	30.08	3.01	4.39	$(0.642 \pm 0.219) \times 10^{-7}$
1.9006	40.10	3.16	4.29	$(1.431 \pm 0.041) \times 10^{-7}$
3.1677	41.86	3.29	4.67	$(1.170 \pm 0.035) \times 10^{-7}$
10.1325	46.18	3.54	4.68	$(1.478 \pm 0.368) \times 10^{-7}$
101.3250	50.00	3.77	5.04	$(1.466 \pm 0.601) \times 10^{-7}$

**Table 4.2** Temperature, water uptake/cell, and diffusion coefficients at constant pressure condition of 101 3250 kPa

temperature	water uptake/Cell	CN	CN	diffusion coefficient
(K)		(water)	(sodium)	$(cm^2/s)$
298.15	50.00	3.77	5.04	$(1.466 \pm 0.601) \times 10^{-7}$
325.15	46.25	3.73	4.71	$(2.372 \pm 0.024) \times 10^{-7}$
353.15	42.12	3.72	4.24	$(3.762 \pm 0.822) \times 10^{-7}$
373.15	36.50	3.46	4.39	$(4.806 \pm 0.226) \times 10^{-7}$
393.15	26.17	3.27	4.08	$(3.725 \pm 0.188) \times 10^{-7}$
423.15	13.73	2.45	3.63	$(2.630 \pm 0.459) \times 10^{-7}$
453.15	9.75	1.74	3.42	$(3.042 \pm 0.301) \times 10^{-7}$

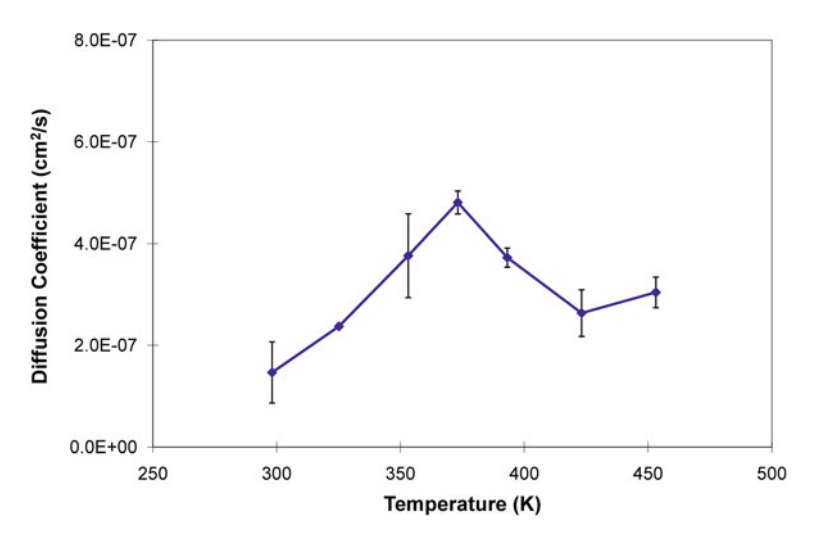


**Fig. 4.9** Dependence of the sodium diffusion coefficient on the temperature for a vapor pressure of 101.3250 kPa. The diffusion coefficients were calculated from three partitioned trajectories of 12 ns NPT simulations (each partition has 4 ns length), and the error bars were evaluated from the diffusion coefficients obtained from the three partitioned trajectories. Up to 373.15 K, the diffusion coefficient increases with increasing temperature, whereas it decreases beyond 373.15 K due to the depletion of the water solvation

Normally, the temperature dependence for diffusion coefficient is written in terms of a standard Arrhenius equation, Equation 4.4.

$$D = A_{diff} \exp\left(-\frac{\Delta E}{k_B T}\right),\tag{4.4}$$

where the  $\Delta E$  implies the energy barrier for the hopping from one site to another site.  $A_{diff} = L^2 k_B T/h \exp(ns/R)$  is the prefactor, a product of frequency factor (activation entropy term) with a hopping-related length (L).  $k_B$  is the Boltzmann constant and T is the absolute temperature. In order to include the solvation effect, we define the stabilization energy  $\Delta E_{solv}$  due to the solvation. This leads to a modified Equation 4.4 where  $A_{diff-solve}$  now includes a correction for solvation.

$$D = A_{diff-solve} \exp\left(-\frac{\Delta E - \Delta E_{solv}}{k_B T}\right). \tag{4.5}$$

We assume that the  $\Delta E_{solv}$  is a step function which is zero for the poor solvation regime and nonzero for the good solvation regime, which implies that the incomplete solvation shell of sodium ion has no effect to stabilization. The Arrhenius plot for each regime is shown in Fig. 4.10 and the curve for each regime is fitted with

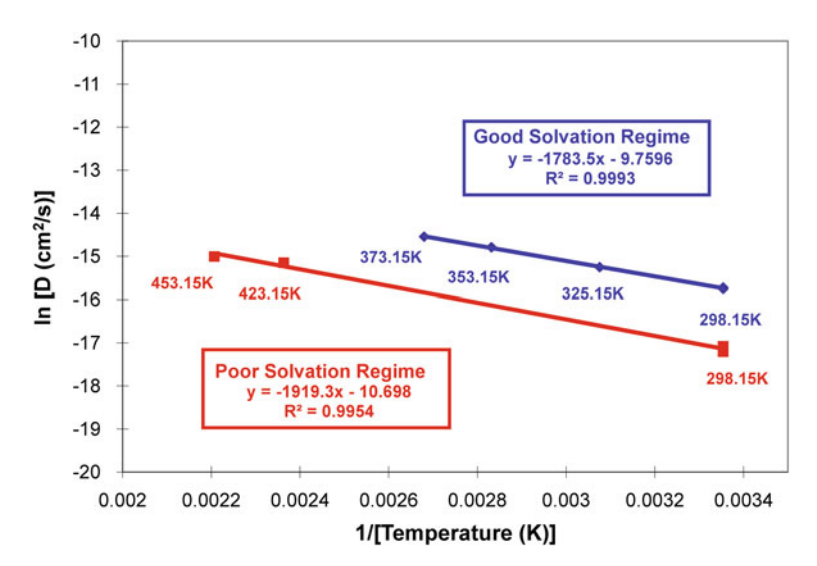


**Fig. 4.10** Arrhenius plots of diffusion coefficient from each solvation regime: the *red squares* are for the poor solvation regime and the *blue diamond* is for the good solvation regime. The *solid black line* is a linear fitting of each regime. This leads to  $D_{300K} = 3.762 \times 10^{-8}$  cm<sup>2</sup>/s and  $E_{act} = 3.810$  kcal/mol for the poor solvation regime and  $D_{300K} = 1.512 \times 10^{-7}$  cm<sup>2</sup>/s and  $E_{act} = 3.540$  kcal/mol for the good solvation regime, and the equation of each fitted line and R2 value are *inset* in the figure

4.4 Conclusions 61

a linear equation using least-squares fitting method. From the slope of the fitted line, we estimate the  $\Delta E = 3.810 \, \text{kcal/mol}$  for the poor solvation regime and the  $\Delta E - \Delta E_{solv} = 3.540$  kcal/mol for the good solvation regime. Thus, the stabilization energy by solvation ( $\Delta E_{solv}$ ) becomes 0.270 kcal/mol. The y-intercepts lead to  $A_{diff} = -10.70 \,\mathrm{cm^2/s}$  and  $A_{diff-solve} = -9.76 \,\mathrm{cm^2/s}$ . The nearly unit value for A suggests that the diffusion mechanism for both regimes is basically identical, supporting the Equation 4.5. Although no experimental data has been reported for the energy barrier of the diffusion of sodium ion, the energy barrier for the diffusion of sodium ion in the  $\beta$  alumina (known as a good ionic conductor) has been measured experimentally [47, 48]. Since the sodium ion in the  $\beta$  alumina is also believed to jump around aluminum oxide sites, these values should be comparable with ours. Kim et al. [47] reported that the barrier as 3.275 kcal/mol from the measurement of ionic conductivity and 3.897 kcal/mol from the measurement of sodium tracer diffusion. Also the values from Whittingham and Huggins [48] obtained values of 3.81 kcal/mol from the tracer diffusion measurement and 3.95 kcal/mol from the dielectric loss measurement. All these values are very comparable to our  $\Delta E$  value of 3.540 kcal/mol, supporting the accuracy of our simulations. On the basis of these comparable values of the energy barrier, we expect that the stabilization energy for the hydrated system would also be reasonable although the effect of hydration in such aluminosilicate system has yet been reported.

#### 4.4 Conclusions

Combining GCMC and MD simulations, we studied the effect of hydration on the sodium dynamics. From the absorption isotherm, we observed that the water absorption in BEA zeolites proceeds with a spontaneous condensation at a pressure of 3.5 kPa and a temperature of 298.15 K even though the internal space of zeolite remains hydrophobic. Below the pressure of 101.3250 kPa, the water uptake of the zeolite decreases monotonically with increasing temperature. From the pair correlation functions, we found that the tetrahedral water solvation structure for water molecule is suppressed by the hydrophobic pore surfaces. In contrast, the water solvation structure surrounding the sodium ion remains ~5.0. This difference is a direct consequence of the strong electrostatic interaction of the positively charged sodium ion with water molecules.

The MD trajectories indicate that the sodium ions are electrostatically bound to the aluminum-doped sites and the diffusion of the sodium ions proceeds via hopping mechanism among these aluminum-doped sites (Fig. 4.8).

On the basis of the spontaneous water condensation process, we found the two regimes: a good solvation regime below 373.15 K and a poor solvation regime above 400 K. The Arrhenius plot of each regime leads to an energy barrier of 3.540 kcal/mol for the diffusion of sodium ion for the good solvation regime and of 3.810 kcal/mol for the poor solvation regime. This leads to an estimate of 0.270 kcal/mol for the stabilization energy due to the solvation of sodium ion.

This study of the sodium diffusion through BEA zeolite shows that the ionic diffusion in the confined geometry depends on the degree of solvation by water which distinguishes it from bulk diffusion. As a next step, we are planning to directly investigate the proton diffusion through the aluminum-doped zeolite BEA system based on results of the current study.

**Acknowledgments** This research was supported in part by the Department of Energy (DE-FG02-05ER15716, William S. Millman). The facilities of the Materials and Process Simulation Center used for these studies were supported by DURIP-ARO, DURIP-ONR.

#### **Bibliography**

- 1. Zones, S. I.; Davis, M. E. Curr. Opin. Solid State Mater. Sci. 1996, 1, 107-117.
- 2. Davis, M. E. Nature 2002, 417, 813-821.
- 3. Truskett, T. M.; Debenedetti, P. G.; Torquato, S. J. Chem. Phys. 2001, 114, 2401–2418.
- 4. Gallo, P.; Ricci, M. A.; Rovere, M. J. Chem. Phys. 2002, 116, 342-346.
- 5. Giaya, A.; Thompson, R. W. J. Chem. Phys. 2002, 117, 3464-3475.
- 6. Brovchenko, I.; Geiger, A.; Oleinikova, A. J. Chem. Phys. 2004, 120, 1958–1972.
- Maurin, G.; Bell, R. G.; Devautour, S.; Henn, F.; Giuntini, J. C. J. Phys. Chem. B 2004, 108, 3739–3745.
- Lee, Y.; Vogt, T.; Hriljac, J. A.; Parise, J. B.; Hanson, J. C.; Kim, S. J. Nature 2002, 420, 485–489.
- 9. Demkov, A. A.; Sankey, O. F. Chem. Mater. 1996, 8, 1793-1806.
- 10. Maurin, G.; Llewellyn, P.; Poyet, T.; Kuchta, B. J. Phys. Chem. B 2005, 109, 125-129.
- Calero, S.; Dubbeldam, D.; Krishna, R.; Smit, B.; Vlugt, T. J. H.; Denayer, J. F. M.; Martens, J. A.; Maesen, T. L. M. J. Am. Chem. Soc. 2004, 126, 11377–11386.
- 12. Carrette, L.; Friedrich, K. A.; Stimming, U. ChemPhysChem 2000, 1, 162–193.
- 13. Kreuer, K. D. J. Membr. Sci. 2001, 185, 29-39.
- 14. Paddison, S. J. Annu. Rev. Mater. Res. 2003, 33, 289–319.
- 15. Li, Q. F.; He, R. H.; Jensen, J. O.; Bjerrum, N. J. Chem. Mater. 2003, 15, 4896–4915.
- 16. Mauritz, K. A.; Moore, R. B. Chem. Rev. 2004, 104, 4535-4585.
- 17. Hickner, M. A.; Pivovar, B. S. Fuel Cells 2005, 5, 213–229.
- Holmberg, B. A.; Hwang, S. J.; Davis, M. E.; Yan, Y. S. *Microporous Mesoporous Mater.* 2005, 80, 347–356.
- 19. Burchart, E. D.; Verheij, V. A.; Vanbekkum, H.; Vandegraaf, B. Zeolites 1992, 12, 183-189.
- Levitt, M.; Hirshberg, M.; Sharon, R.; Laidig, K. E.; Daggett, V. J. Phys. Chem. B 1997, 101, 5051–5061.
- 21. Rappe, A. K.; Goddard, W. A. J. Phys. Chem. 1991, 95, 3358–3363.
- Hockney, R. W.; Eastwood, J. W. Computer simulation using particles; McGraw-Hill: New York, 1981.
- 23. Razmus, D. M.; Hall, C. K. AiChE J. 1991, 37, 769-779.
- Goodbody, S. J.; Watanabe, K.; Macgowan, D.; Walton, J.; Quirke, N. J. Chem. Soc., Faraday Trans. 1991, 87, 1951–1958.
- 25. Accelrys Inc.: San Diego, CA, 1999.
- Allen, M. P.; Tildesley, D. J. Computer Simulation of Liquids; Oxford University Press: Oxford, U.K., 1987.
- 27. Frenkel, D.; Smit, B. *Understanding Molecular Simulations: From Algorithms to Applications*; Academic Press: London, 2002.
- 28. Plimpton, S. J. Comput. Phys. 1995, 117, 1-19.
- 29. Plimpton, S. J.; Pollock, R.; Stevens, M. Minneapolis, MN, 1997.

Bibliography 63

 Swope, W. C.; Andersen, H. C.; Berens, P. H.; Wilson, K. R. J. Chem. Phys. 1982, 76, 637–649.

- 31. Baerlocher, C.; McCusker, L. B. Database of zeolite Structures: http://www.iza-structure.org/databases/.
- 32. Di Lella, A.; Desbiens, N.; Boutin, A.; Demachy, I.; Ungerer, P.; Bellat, J. P.; Fuchs, A. H. *Phys. Chem. Chem. Phys.* **2006**, 8, 5396–5406.
- 33. Desbiens, N.; Demachy, I.; Fuchs, A. H.; Kirsch-Rodeschini, H.; Soulard, M.; Patarin, J. Angew. Chem., Int. Ed. 2005, 44, 5310–5313.
- 34. Desbiens, N.; Boutin, A.; Demachy, I. J. Phys. Chem. B 2005, 109, 24071–24076.
- 35. Hummer, G.; Rasaiah, J. C.; Noworyta, J. P. Nature 2001, 414, 188-190.
- 36. Gorbach, A.; Stegmaier, M.; Eigenberger, G. Ads.-J. Int. Ads. Soc. 2004, 10, 29-46.
- 37. Soper, A. K.; Phillips, M. G. Chem. Phys. 1986, 107, 47-60.
- 38. Jang, S. S.; Goddard, W. A., III J. Phys. Chem. C 2007, 111, 2759-2769.
- Jang, S. S.; Lin, S. T.; Cagin, T.; Molinero, V.; Goddard, W. A., III J. Phys. Chem. B 2005, 109, 10154–10167.
- Jang, S. S.; Molinero, V.; Cagin, T.; Goddard, W. A., III J. Phys. Chem. B 2004, 108, 3149–3157.
- 41. Vaudry, F.; DiRenzo, F.; Espiau, P.; Fajula, F.; Schulz, P. Zeolites 1997, 19, 253–258.
- 42. Keffer, D.; McCormick, A. V.; Davis, H. T. Mol. Phys. 1996, 87, 367-387.
- 43. Faux, D. A.; Smith, W.; Forester, T. R. J. Phys. Chem. B 1997, 101, 1762-1768.
- 44. Faux, D. A. J. Phys. Chem. B 1998, 102, 10658–10662.
- 45. Faux, D. A. J. Phys. Chem. B 1999, 103, 7803-7808.
- 46. Franke, M. E.; Simon, U. Phys. Status Solidi B: Basic Res. 2000, 218, 287–290.
- 47. Kim, K. K.; Mundy, J. N.; Chen, W. K. J. Phys. Chem. Solids 1979, 40, 743-755.
- 48. Whitting, Ms; Huggins, R. A. J. Chem. Phys. 1971, 54, 414.

#### Chapter 5

# Experimental and Theoretical Investigation into the Correlation Between Mass and Ion Mobility for Choline and Other Ammonium Cations in N<sub>2</sub>

Reprinted with permission from Kim, H; Kim, H. I.; Johnson, P. V.; Beegle, L. W.; Beauchamp, J. L.; Goddard, W. A.; Kanik, I. Anal. Chem. 2008, 80 (6), 1928–1936. Copyright 2008 American Chemical Society.

**Abstract** A number of tertiary amine and quaternary ammonium cations spanning a mass range of 60-146 amu (trimethylamine, tetramethylammonium, trimethylethylammonium, N. N-dimethylaminoethanol, choline, N. N-dimethylglycine, betaine, acetylcholine, (3-carboxypropyl)trimethylammonium) were investigated using electrospray ionization ion mobility spectrometry. Measured ion mobilities demonstrate a high correlation between mass and mobility in N<sub>2</sub>. In addition, identical mobilities within experimental uncertainties are observed for structurally dissimilar ions with similar ion masses. For example, dimethylethylammonium (88 amu) cations and protonated N, N-dimethylaminoethanol cations (90 amu) show identical mobilities  $(1.93 \,\mathrm{cm}^2 \,\mathrm{V}^{-1} \,\mathrm{s}^{-1})$  though N, N-dimethylaminoethanol contains a hydroxyl functional group while dimethylethylammonium only contains alkyl groups. Computational analysis was performed using the modified trajectory (TJ) method with nonspherical N<sub>2</sub> molecules as the drift gas. The sensitivity of the ammonium cation collision cross-sections to the details of the ion-neutral interactions was investigated and compared to other classes of organic molecules (carboxylic acids and abiotic amino acids). The specific charge distribution of the molecular ions in the investigated mass range has an insignificant affect on the collision cross-section.

#### 5.1 Introduction

The development of soft ionization methods such as electrospray ionization (ESI) [1] have expanded the application of ion mobility spectrometry (IMS) [2, 3] to structural investigations of nonvolatile biomolecules in the gas phase [4]. ESI allows soft sampling by transferring intact ions directly from the solution phase to the

gas phase. Using this distinctive advantage of ESI, the shapes and sizes of various biomolecular ions from monomeric molecules to macrosize protein complexes have been investigated. The combination of ESI and IMS has facilitated conformational studies of macroions including clusters (oligomers) [5, 6, 7], peptides [8, 9], and proteins [10, 11, 12]. In addition, ion mobilities of organic molecules such as amino acids [13, 14], carboxylic acids [15], and dinucleotides [16], as well as other organic molecules [17, 18], have been reported.

To provide a firm foundation for studies of the shapes of complex organic molecular ions using IMS, many research groups have endeavored to develop theoretical models to predict ion mobilities and related cross-sections of gas-phase molecular ions. Griffin *et al.* [19] have shown that mass and mobility are only correlated on the order of 20% within a collection of structurally unrelated compounds spanning a mass range of  $\sim 70-500$  amu. The correlations are improved up to 2% when only structurally related compounds are considered. Karpas and co-workers have established models to predict the mobility for a number of compound classifications including acetyls, aromatic amines, and aliphatic amines drifting in He, N<sub>2</sub>, air, Ar, CO<sub>2</sub>, and SF<sub>6</sub> [20, 21]. Our laboratory has applied a 12 – 4 potential model in studies of amino acids and carboxylic acids drifting in N<sub>2</sub> and CO<sub>2</sub> [14, 15]. Recently, Steiner *et al.* have reported predictions of mobilities for a series of different classes of amines (primary, secondary, tertiary) in various drift gases, such as He, Ne, Ar, N<sub>2</sub>, and CO<sub>2</sub>, using several theoretical models (rigid-sphere, polarization-limit, 12-6-4, and 12-4 potential model) [22].

Computational modeling related to interpretation of IMS data has been developed by several groups. Efforts toward theoretical ion mobility predictions using computational methods face difficulties associated with complicated collision integrals and the design of functions to accurately describe the ion-neutral interaction potential. Bowers and co-workers have proposed a project approximation method, which is based on a hard-sphere description of the interaction potential [23]. The trajectory (TJ) method, which has been proposed by Jarrold and co-workers, adopts more realistic soft-core interactions [24].

Ion mobility constants (K) can be derived from the collision cross-section using the equation [25]

$$K = \frac{(18\pi)^{1/2}}{16} \frac{1}{\mu^{1/2}} \frac{ze}{(k_B T)^{1/2} \Omega_D} \frac{1}{N},$$
(5.1)

where  $\mu$  is reduced mass, N is the number density of the neutral gas molecule, and z is the charge of the ion. The collision cross-section,  $\Omega_D$ , is given by [24]

$$\Omega_{D} = \frac{1}{8\pi^{2}} \int_{0}^{2\pi} d\theta \int_{0}^{\pi} d\phi \int_{0}^{2\pi} d\gamma \frac{\pi}{8} \left(\frac{\mu}{k_{B}T}\right)^{3}$$
$$\int_{0}^{\infty} dg e^{-\mu/2k_{B}T} g^{5} \int_{0}^{\infty} db 2b \left(1 - \cos\chi \left(\theta, \phi, \gamma, g, b\right)\right)$$
(5.2)

5.1 Introduction 67

and  $\theta$ ,  $\phi$ , and  $\gamma$  are the three-dimensional collision angles, g is the relative velocity, and b is the impact parameter. Because the scattering angle  $\chi$  ( $\theta$ ,  $\phi$ ,  $\gamma$ , g, b) depends on the pairwise potential between the ion and neutral gas molecules, the accuracy of computed cross-section values is determined by the quality of the interaction potential model. The potential employed in the TJ method [24] for a He drift gas is given by

$$\Phi(\theta, \phi, \gamma, b, r) = 4\epsilon \sum_{i}^{n} \left[ \left( \frac{\sigma}{r_i} \right)^{12} - \left( \frac{\sigma}{r_i} \right)^{6} \right] - \frac{\alpha}{2} \left( \frac{ze}{n} \right)^{2}$$

$$\left[ \left( \sum_{i}^{n} \frac{x_i}{r_i^3} \right)^{2} + \left( \sum_{i}^{n} \frac{y_i}{r_i^3} \right)^{2} + \left( \sum_{i}^{n} \frac{z_i}{r_i^3} \right)^{2} \right]. \quad (5.3)$$

The first term is a sum over short-range van der Waals interactions, and the second term represents long-range ion-induced dipole interactions. In the expression,  $\epsilon$  is the depth of the potential well,  $\sigma$  is the value of distance (r) between the centers of mass of the each atom in the ion and neutral gas molecule at the potential minimum, and R is the neutral polarizability. The coordinates,  $r_i$ ,  $x_i$ ,  $y_i$ , and  $z_i$ , are defined by the relative positions of the atoms with respect to the neutral. Utilizing the given ion-neutral interaction potential functions, the integrals in Equation 5.2 can be processed numerically. Monte Carlo integration schemes are used for the integration over  $\theta$ ,  $\phi$ ,  $\gamma$ , and b. The numerical integration over g is performed using a combination of the Runge-Kutta-Gill integration method and the Adams-Moulton predictor corrector integration method.

Choline is a precursor for phosphatidylcholine, sphingomyelin, and other important biological molecules [26]. Further, it is a component of cell membrane lipids in biological systems, and it plays an important role in their repair. Choline can be oxidized to betaine, which is readily demethylated to yield *N*, *N*-dimethylglycine [26]. Decomposition of choline yields trimethylamine and dimethylamine [27]. Searching for lipids and their components (i.e., choline) may be a valuable strategy in the search for evidence of extinct or extant life elsewhere in the cosmos. Under the high oxidizing conditions and significant ultraviolet flux found on the surface of Mars, one would expect decomposition products of lipids to include various alkylamines [28].

In the present study, mobilities have been measured for a number of quaternary and tertiary ammonium cations related to choline and its derivates drifting in  $N_2$ . Of particular interest was the possible dependence of mass-mobility correlations with the heavy atom (C, N, O) complements present in the molecular ion, comparing, for example, alkylated ammonium ions to abiotic amino acids (betaine and N, N-dimethylglycine). A modified TJ method for the ion-neutral interaction, to account for the potential associated with the nonspherical drift gas  $N_2$ , has been applied to predict cross-sections of these polyatomic ammonium cations and to test the sensitivity of collision cross-section to details of the ion-neutral interaction. Comparisons of the results from the ammonium cations to other classes of organic molecules (carboxylic acids and abiotic amino acids) are presented. The

origin of the observed correlation between mass and mobility of ammonium cations is discussed.

#### **5.2 Experimental Section**

#### 5.2.1 Chemicals and Reagents

All the compounds studied in this work were purchased from Sigma Aldrich (St. Louis, MO) and were used without further purification. All solvents (water, methanol, acetic acid) were HPLC grade and were purchased from EMD Chemicals Inc. (Gibbstown, NJ). Quaternary ammonium samples were prepared by dissolving known quantities of ammonium ions in a solvent consisting of 50% water and 50% methanol by volume to give sample concentrations in the range of 100  $\mu$ M. Tertiary amine samples were prepared as 300  $\mu$ M in a solvent of 50:50 water and methanol with 1% acetic acid by volume.

#### 5.2.2 Electrospray Ionization Ion Mobility Spectrometer

The ESI-IMS instrument and the data acquisition system used in this investigation were based on designs previously described by Hill and co-workers [17, 29] and have been described in detail by Johnson *et al.* [14]. The drift length of the ion mobility spectrometer was 13.65 cm and was operated in the positive mode. A drift voltage of 3988 V, corresponding to electric field strength of 292 V/cm, was employed. All measurements were made at local atmospheric pressure ( $\sim$  730 Torr) while a counterflow of the preheated drift gas was introduced at the detection end of the drift region at a flow rate of  $\sim$  800 mL/min. The sample solution was delivered by an Eldex Micropro liquid chromatography pump at a flow rate of 3  $\mu$ L/min into a stainless steel electrospray needle, which was held at a potential 3 – 4 kV above the entrance to the desolvation region of the spectrometer. The gap between the electrospray needle and the entrance electrode was  $\sim$  2 cm.

Ions were introduced into the drift region through the ion gate in 0.2-ms pulses. Signals collected at the Faraday cup were amplified by a factor of  $10^9$  (Stanford Research Systems model SR570 low-noise current preamplifier) and recorded as a function of drift time in 0.02-ms-wide channels. Typically, 1000 individual 0-25-ms scans were averaged to produce the final spectra used in the analysis. Resolution of the instrument was found to be  $\sim 0.43$  ms full width at half-maximum (FWHM) with drift times in the range 12-17 ms for the ions studied and the parameters employed in these experiments.

Throughout this work, it was assumed that ESI of the prepared samples resulted in singly charged ammonium cations. The assumption was confirmed by ESI mass spectrometric analysis using a Finnigan LCQ Deca XP ion trap mass spectrometer. The mass spectra of all nine samples in the present study show singly charged monomeric molecular cations as the major ionic species. Since the experiments were

conducted with the drift cell at 473 K, it was further assumed that there was no significant water cluster formation based on previous IMS-MS studies [18, 30].

Reduced ion mobilities,  $K_0$ , were determined from the recorded spectra and the experimental parameters according to the usual relation,

$$K_0 = \left(\frac{273 \text{ K}}{T}\right) \left(\frac{P}{760 \text{ Torr}}\right) \frac{D^2}{Vt},$$
 (5.4)

where V is the voltage drop across the drift region, D is the drift length, t is the drift time, P is the pressure, and T is the temperature. With the above parameters expressed in units of V, cm, s, Torr, and K, respectively, Equation 5.4 gave the reduced mobility in the typical units of cm<sup>2</sup> V<sup>-1</sup> s<sup>-1</sup>. The experimental uncertainties of the determined  $K_0$  values are estimated to be  $\sim 3\%$  based on the half width at half-maximum (HWHM) of each drift time peak in the averaged ion mobility spectra.

#### 5.2.3 Computational Modeling

More than 500 possible molecular conformations were investigated through dihedral angles of  $-180^{\circ}$  to  $180^{\circ}$  at the PM5 level using CAChe 6.1.12 (Fujitsu, Beaverton, OR). Then, the lowest-energy structures were determined using density functional theory (DFT) with a number of candidate low-energy structures from the previous PM5 calculations. DFT calculations were performed using Jaguar 6.0 (Schrödinger, Inc., Portland, OR) utilizing the Becke three-parameter functional (B3) [31] combined with the correlation functional of Lee, Yang, and Parr (LYP) [32], using the 6-31G\*\* basis set [33]. The optimized structures of ammonium cations investigated in the present study are shown in Fig. 5.2.

The TJ method [24], originally developed by Jarrold and coworkers, was modified to describe the interaction between ions and an N<sub>2</sub> drift gas and expand the applicability of the TJ method beyond cases of ions drifting in He. As shown in Equation 5.3, the potential used in the original TJ method consists of two terms representing van der Waals and ion-induced dipole interactions, which are characterized by the Lennard-Jones parameters  $(\epsilon, \sigma)$  and the neutral polarizability  $(\alpha)$ , respectively. We set the polarizability of N<sub>2</sub> at the experimentally determined value [34] of  $1.710 \times 10^{-24}$  cm<sup>2</sup> and took the Lennard-Jones parameters described in the universal force field [35], which is a general purpose force field optimized for all the elements in the periodic table. Due to the linear geometry of  $N_2$ , two more consequences should be additionally taken into account; the ion-quadrupole interaction and the orientation of the molecule. We mimic the quadrupole moment of N<sub>2</sub>,  $(-4.65 \pm 0.08) \times 10^{-40} \,\mathrm{C} \,\mathrm{cm}^2$  [36], by displacing charges by negative q (0.4825e) to each nitrogen atom and one positive 2q at the center of the nitrogen molecule. Hence, the ion-quadrupole potential can be expressed with simple summations of partial charges as follows:

$$\Phi_{IQ} = \sum_{i=1}^{3} \sum_{i}^{n} \frac{z_i z_j e^2}{r_{ij}},$$
(5.5)

where indexes i and j denote the atoms of the ion, three points of  $N_2$ . j=1 and 3 indicate the two nitrogen atoms, and j=2 indicates the center of mass position of  $N_2$ .

To consider the orientation of the nitrogen molecule rigorously, all possible trajectories with varying molecular orientations were taken into account. It has been widely accepted that the ion field does not exclusively quench the rotational angular momentum of the neutral molecule and only partial locking occurs during the collision process [37, 38]. Thus, we assumed that the interaction potential averaged over the rotational degree of freedom generates an appropriated average impact parameter [39]. The calculated rotation time of a  $N_2$  molecule ( $\sim$  620 ns) implies that approximately three molecular rotations occur during a collision between an ion and  $N_2$  taking place ( $\sim$  2 ps). The orientations of  $N_2$  are sampled along with x, y, and z axes to represent all the three-dimensional rotational space. Then the orientation averaged interaction potential is evaluated using Boltzmann weighting. Using these different weights, the orientation averaged interaction potential is evaluated, and this potential is used to compute the collision cross-section.

For the calculations of collision cross-section of ions, it is assumed that the DFT optimized structures are rigid. To ensure that the assumption is valid for the ammonium cations investigated in the present study, the collision cross-sections of two extreme conformations for the largest two ionic molecules, acetylcholine and (3-carboxypropyl)trimethylammonium, are estimated. The DFT calculated electronic energies reveal that the extended structures of both acetylcholine and (3-carboxypropyl)trimethylammonium are unstable by 4.24 and 0.547 kcal/mol, respectively, compared to cyclic structures shown in Fig. 5.2. The maximum difference between two conformations of (3-carboxypropyl)-trimethylammonium is calculated as  $\sim 7 \mbox{\normalfont{A}}^2$ , which we can set as a maximum error bound originating from the structural uncertainty.

#### 5.3 Results

#### 5.3.1 Mass-Mobility Correlation of Ammonium Cations

IMS spectra were obtained as described above. The drift times of the ammonium cations were determined from the location of the peak maximums. Figure 5.1 shows example spectra taken with pure solvent being introduced to the electrospray needle and with 300  $\mu$ M N, N-dimethylammoniumethanol dissolved in the solvent. These spectra are characteristic of those considered in this work. Measured drift times, reduced ion mobilities (in  $N_2$  drift gas), and determined  $\Omega_D$  for the nine ammonium cations chosen for this study are listed in Table 5.1 along with their respective

5.3 Results 71

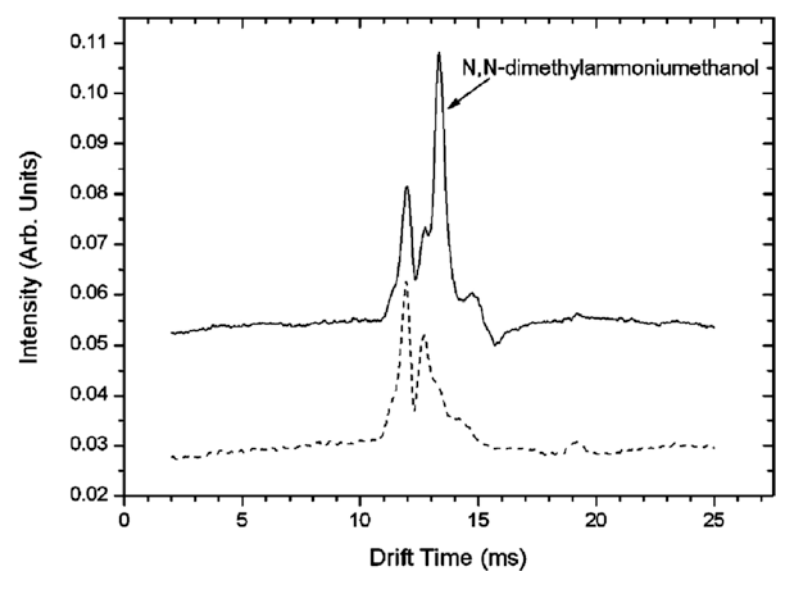


Fig. 5.1 Examples of the ion mobility spectra taken in this study. Shown are two spectra taken in 730 Torr  $N_2$ . The electric field strength and the temperature of the drift tube were 292 V/cm and 473 K, respectively. The *dash curve* is a spectrum taken with pure solvent being introduced to the electrospray needle while the *solid curve* is a spectrum of solvent and 300  $\mu$ M N, N-dimethylammoniumethanol. The two spectra were smoothed (10 point adjacent averaging) and shifted in intensity by an additive constant to avoid overlap. The N, N-dimethylammoniumethanol feature is indicated in the figure. The unlabeled features correspond to ionized solvent (water, methanol, acetic acid) and atmospheric constituents ionized through proton transfer (due to the open nature of the ESI-IMS instrument)

 $\textbf{Table 5.1} \ \ \text{Drift times, reduced mobilities, and collision cross-sections of ammonium cations in } N_2 \\ \text{drift gas}$ 

ammonium cation	$^a { m MW}$	$^b\mathrm{DT}$	$^{c}K_{0}$	$^d\Omega_D$
trimethylammonium	60	12.1	2.15	91.2
tetramethylammonium	74	12.7	2.04	95.3
trimethylethylammonium	88	13.4	1.93	102.2
N, N-dimethylammoniumethanol	90	13.4	1.93	100.9
choline	104	14.1	1.84	104.5
N, N-dimethylglycine	104	14.1	1.84	102.3
betaine	118	14.7	1.76	105.3
acetylcholine	146	16.3	1.59	118.5
(3-carboxypropyl)trimethylammonium	146	16.4	1.58	115.9

<sup>&</sup>lt;sup>a</sup>Molecular weight (amu). <sup>b</sup>Drift time (ms). <sup>c</sup>Reduced mobility (cm<sup>2</sup> V<sup>-1</sup> s<sup>-1</sup>). <sup>d</sup>Collision cross-section ( $\mathring{A}^2$ ).

molecular weights. The 12-4 potential model, which has proven satisfactory to model experimental data [14, 15, 20, 21, 22] has been used for the analysis of the experimentally determined mobilities of ammonium cations. The potential is expressed as

$$\Phi(r) = \frac{\epsilon}{2} \left\{ \left( \frac{\sigma - a}{r - a} \right)^{12} - 3 \left( \frac{\sigma - a}{r - a} \right)^{4} \right\},\tag{5.6}$$

where  $\epsilon$ , r, and  $\sigma$  are defined above and the parameter a is the location of center charge from the center of mass in the ion. Rearrangement of Equation 5.6, along with the substitution of the appropriate constants, yields

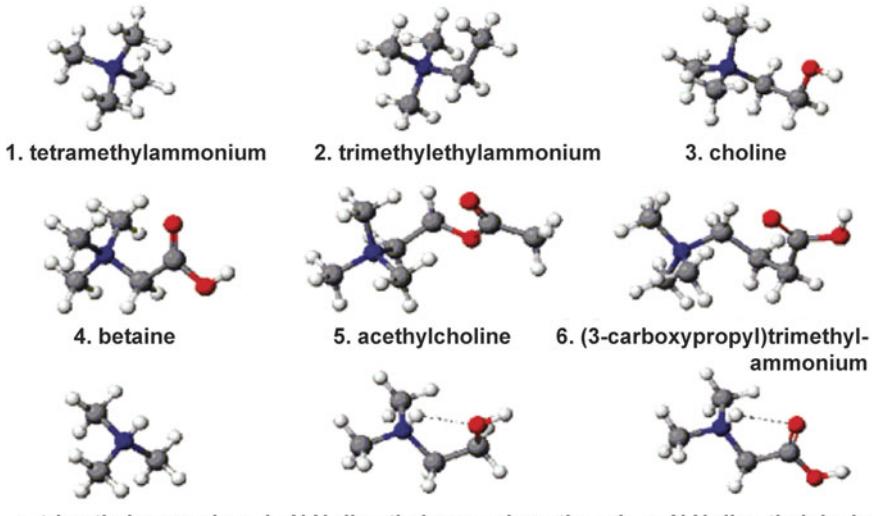
$$K_0^{-1} = \left(1.697 \times 10^{-4}\right) (\mu T)^{1/2} \sigma^2 \Omega^{(1,1)*},\tag{5.7}$$

which gives the reduced ion mobility in terms units of cm<sup>2</sup> V<sup>-1</sup> s<sup>-1</sup>.  $\Omega^{(1,1)*}$  is the dimensionless collision integral, where  $\Omega_D = \pi \sigma^2 \Omega^{(1,1)*}$ . Derivation of Equation 5.7 from Equation 5.6 is well described by Johnson *et al.* [14]. Equation 5.7 was fit to the data set of ammonium ion mobilities in N<sub>2</sub> using a nonlinear least-squares fitting procedure [14]. The plot of  $K_0^{-1}$  versus ion mass for ammonium cations drifting in N<sub>2</sub> is shown in Fig. 5.2 along with the best fit to the data. As seen in Fig. 5.2, all nine ammonium cations investigated in the present study exhibit a good correlation ( $R^2 = 0.99$ ) between mass and mobility of ion. In particular, the two different classes of ammonium cations (tertiary and quaternary) investigated in this study exhibit a common mass-mobility correlation. Further, the heteroatomic complements of the molecular ions do not impact the mass-mobility correlation.

## 5.3.2 Tertiary and Quaternary Ammonium Cations with Similar Molecular Weights

Two sets of cations, which have similar molecular weights but different structures, were chosen to investigate the influence of the composition and structural details of the ion on the mobility. The molecular weights of trimethylethylammonium and N, N-dimethylammnoiumethanol are 88 and 90 amu, respectively. There is a significant structural difference between these two ions in addition to variation in the degree of alkylation to the ammonium groups. Protonated N, Ndimethylammoniumethanol possesses a hydroxyl group at the ethyl group while trimethylethylammonium possesses only alkyl groups. The molecular weights of choline and N, N-dimethylglycine cation are both 104 amu. Protonated N, Ndimethylglycine cations contain a carboxyl group while choline possesses a hydroxyl group. Experimentally determined mobility values of trimethylethylammonium and N, N-dimethylammoniumethanol are identical at  $1.93 \,\mathrm{cm}^2 \,\mathrm{V}^{-1} \,\mathrm{s}^{-1}$ . Mobilities of both choline and N, N-dimethylglycine cation are measured as 1.84 cm<sup>2</sup> V<sup>-1</sup> s<sup>-1</sup>. It is inferred that the contribution of the oxygen atom to the mobility (ion-neutral ion-neutral interaction) is not significantly different from that of a methylene group in the investigated ammonium cations.

5.3 Results 73



a. trimethylammonium b. N,N-dimethylammoniumethanol c. N,N-dimethylglycine

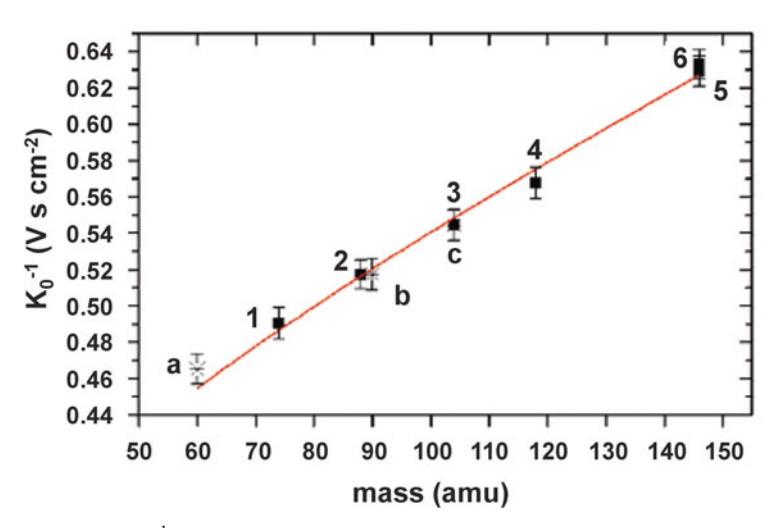


**Fig. 5.2** Plot of  $K_0^{-1}$  for 3° and 4° ammonium cations drifting in N<sub>2</sub> versus ion mass. Experimentally determined data for 3° ammonium and 4° ammonium cations are shown as *asterisks* and *solid squares*, respectively. The *solid line* is the fit of the 12–4 potential model to the ammonium cation data set. DFT optimized structure of each numerically or alphabetically labeled ion is shown above. Optimized geometries are obtained at B3LYP/6-31G\*\* level. The hydrogen bonds are indicated with *dashed lines* 

#### 5.3.3 Functional Group Isomers of Ammonium Cations

Two functional group isomers, acetylcholine and (3-carboxypropyl)-trimethyl-ammonium cation, were examined to study the influence of the location of oxygen atoms on the molecular ion's mobility. As seen in Fig. 5.2, acetylcholine and (3-carboxypropyl)trimethylammonium are not distinguishable based on their mobilities.

### 5.3.4 Collision Cross-Sections of Ions in N<sub>2</sub> via the Trajectory Method

Theoretical  $\Omega_D$  of the ammonium cations investigated in this study were evaluated using the modified TJ method. Prior to application of the modified TJ method to the ammonium cations, we tested the model on previously published experimental data. Figure 5.3a shows the plot of experimentally determined  $\Omega_D$  of carboxylic acid anions [15] and abiotic amino acid cations [14] in N<sub>2</sub> versus those determined

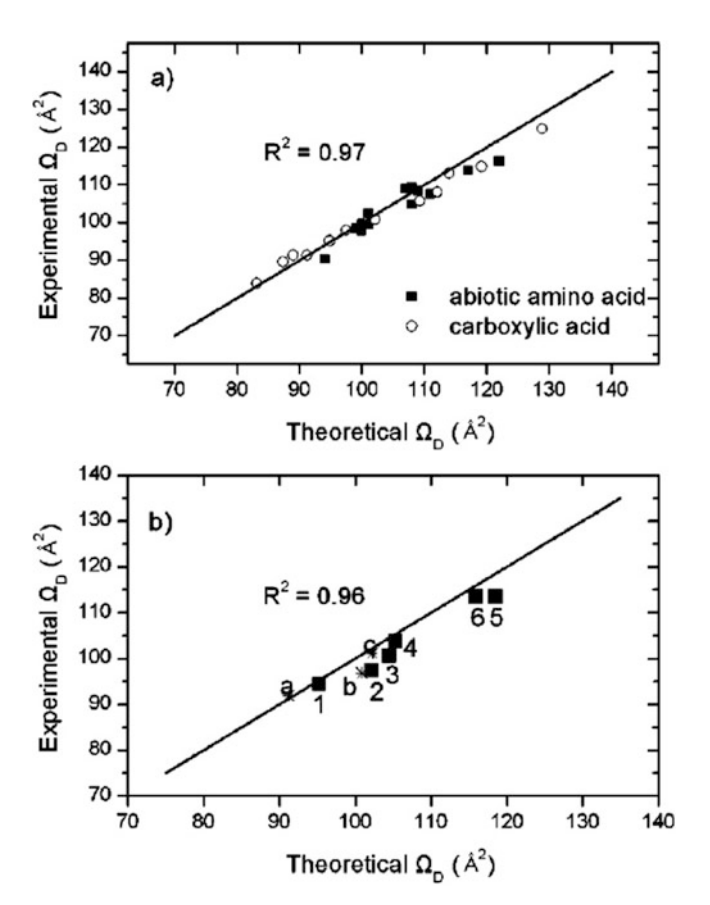


Fig. 5.3 (a) Plot of experimentally determined collision cross-sections  $(\Omega_D)$  of abiotic amino acid cations [14] and carboxylic acid anions [15] in  $N_2$  versus theoretically determined  $\Omega_D$  using the modified TJ method for  $N_2$  drift gas. Abiotic amino acid cation data are shown as *solid squares* and carboxylic acid anion data are shown as *empty circles*. The *solid line* is y=x. (b) Plot of experimentally determined collision cross-sections  $(\Omega_D)$  of 3° and 4° ammonium cations in  $N_2$  versus theoretically determined  $\Omega_D$  using the modified TJ method for  $N_2$  drift gas. 3° ammonium cation data are shown as *asterisks* and 4° ammonium cation data are shown as *solid squares*. Each ion is labeled with the appropriate identifying number and alphabet shown in Fig. 5.1. The *solid line* is y=x

5.4 Discussion 75

theoretically using the modified TJ method following the procedure described in the Experimental Section. Theoretical  $\Omega_D$  of both carboxylic acid anions and abiotic amino acid cations exhibit good agreement with experimental values. The agreement is within 5% in the worst-case deviation with less than 2% deviation on average. Figure 5.3b shows the plot of  $\Omega_D$  of ammonium cations obtained experimentally versus theoretical collision cross-sections calculated using the modified TJ method. The worst observed deviation of the model from the experimental cross-sections is 5% with an average deviation of 2.5%.

#### 5.4 Discussion

#### 5.4.1 Classical Ion-Neutral Collision Model

The cross-section includes the information regarding the ion-neutral interaction. An ion and a neutral interact through the long-range ion-induced dipole potential, which is given by

$$\Phi_{IID} = -\frac{(ze)^2 \alpha}{2r^4},\tag{5.8}$$

where z, R, and r are defined above. The effective potential,  $\Phi_{eff}(r)$ , is expressed as  $\Phi_{IID} + L^2/2\mu r^2$ , where L is angular momentum of the collision partners about the center of mass of the combined system. The critical impact parameter  $b^* = \left(2\alpha e^2/\mathrm{KE}\right)^{1/4}$  is derived by setting KE equal to the maximum effective potential,  $\Phi_{eff}^*(r)$ , which is given by  $1/2(\mathrm{KE})^2b^4/\alpha e^2$ , where KE is the relative kinetic energy. Then the Langevin capture cross-section is

$$\Omega_L = \pi \left( b^* \right)^2 = \pi \sqrt{\frac{2\alpha e^2}{\text{KE}}}.$$
 (5.9)

When the hard-sphere collision radius,  $R_c$ , is greater than  $b^*$ , the Langevin model is no longer appropriate and collisions are dominated by large angle deflections appropriate for a hard-sphere model. In this case, momentum transfer is no longer dominated by long-range interactions. In order to assess the ion-neutral collision under our experimental conditions,  $b^*$  and  $\Omega_L$  are evaluated from the mean relative kinetic energies. The evaluated  $\Omega_L$  and  $b^*$  are then compared to the experimental  $\Omega_D$  and  $R_c$  (Table 5.2). The hard-sphere collision radius  $R_c$  is determined from the experimental  $\Omega_D$  by equating it to  $\pi$   $R_c^2$ . Experimental mean relative kinetic energies can be determined from the Wannier energy formula,

$$KE = \frac{1}{2}\mu g^2 = \frac{3}{2}k_B T + \frac{1}{2}Mv_d^2,$$
 (5.10)

radius, No for each ammonam cation					
	KE	$b^*$	$\Omega_L$	$R_c$	
ammonium cation	(kcal/mol)	(Å)	$(\mathring{A}^2)$	(Å)	
trimethylammonium	1.70	5.08	81.0	5.41	
tetramethylammonium	1.69	5.09	81.3	5.48	
trimethylethylammonium	1.67	5.10	81.7	5.57	
N, N-dimethylammoniumethanol	1.67	5.10	81.7	5.55	
choline	1.65	5.11	82.1	5.66	
N, N-dimethylglycine	1.65	5.11	82.1	5.67	
betaine	1.64	5.12	82.5	5.75	
acetylcholine	1.60	5.15	83.4	6.01	
(3-carboxypropyl)trimethylammonium	1.60	5.15	83.5	6.01	

**Table 5.2** Critical impact parameter,  $b^*$ , Langevin capture cross-section,  $\Omega_L$ , and mean relative kinetic energies, KE, during the experiments with experimentally determined hard-sphere collision radius,  $R_c$  for each ammonium cation

where M is mass of drift gas molecule and  $v_d$  is drift velocity of ion [40]. Under the current experimental conditions described in the Experimental Section,  $b^*$  is calculated on the order of 5 Å. Comparison with  $R_c$  shows that  $b^*$  in our system is on the same order, i.e., less than 1 Å smaller (Table 5.2). It is therefore inferred that the group of molecules studied here are on the borderline between being dominated by long-range versus short-range interactions, favoring some orbiting at lower collision energies, which would then determine the cross-section for momentum transfer and hence the mobility.

#### 5.4.2 Computational Trajectory Method

Ammonium cations investigated in this study exhibit a correlation between mass and mobility (Fig. 5.2). In order to understand and estimate the effect of the each component of the ion-neutral interaction potential in terms of the observed mass-mobility correlation in our experimental system, theoretical calculations were performed using the modified TJ method. The collision cross-sections ( $\Omega_D$ ) were evaluated using molecular ions with restricted interaction potentials and artificial charge distributions. Comparisons of the  $\Omega_D$  of tertiary (3°) and quaternary (4°) ammonium cations, abiotic amino acid cations, and carboxylic acid anions, which are calculated with different interaction potentials, are shown in Figs. 5.4 and 5.5.

#### 5.4.3 Ion-Quadrupole Potential

In order to understand the role of the ion-quadrupole interaction in ion-neutral interactions, the  $\Omega_D$  are computed without ion-quadrupole interactions. The presence of the quadrupole moment elevates the  $\Omega_D$  by 2.8% for the ammonium cations, 2.7% for the abiotic amino acid cations, and 4.2% for carboxylic acid anions (Fig. 5.4a). Overall, it is observed that the addition of the ion-quadrupole potential to the model

5.4 Discussion 77

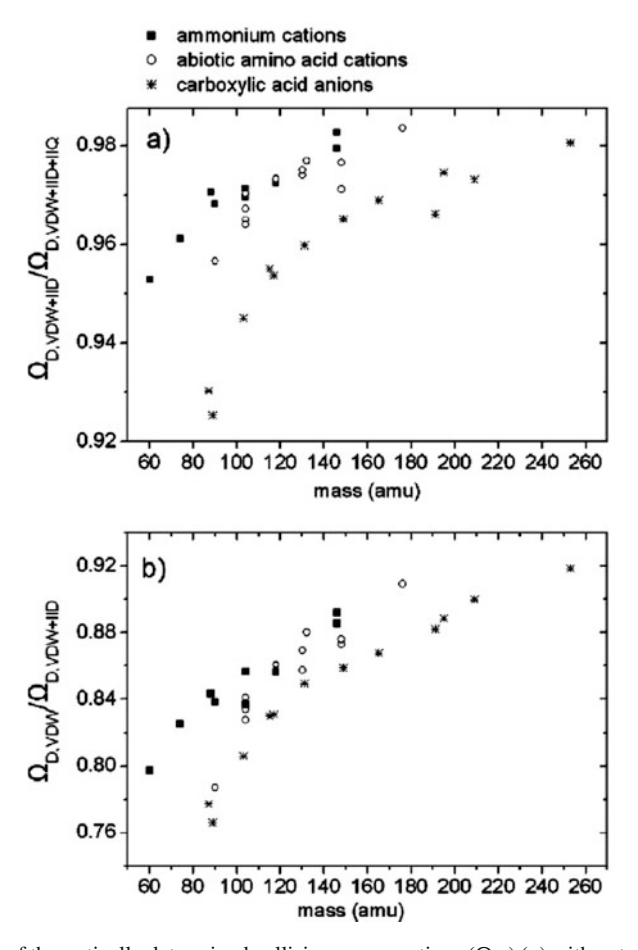


Fig. 5.4 Plots of theoretically determined collision cross-sections ( $\Omega_D$ ) (a) with potential from van der Waals and ion-induced dipole (VDW + IID) interactions over the theoretical  $\Omega_D$  with original pairwise potential, van der Waals + ion-induced dipole + ion-quadrupole (VDW + IID + IQ) interactions, and (b) with potential from van der Waals potential (VDW) over the theoretical  $\Omega_D$  with potential from van der Waals and ion-induced dipole (VDW + IID) interactions of 3° and 4° ammonium cations, abiotic amino acid cations, and carboxylic acid anions in  $N_2$  versus ion mass. The ammonium cation data, the abiotic amino acid cation, and carboxylic acid anion data are shown as *solid squares*, *empty circles*, and *asterisks*, respectively

for ion- $N_2$  interaction improves the agreement between experimental and theoretical  $\Omega_D$  values. Previously, Su and Bowers reported quadrupole effects for molecules with high quadrupole moments using the average quadrupole orientation theory [41]. They demonstrated the significance of quadrupole effects, especially in the case when the ionic charge and quadrupole moment have the same polarity [41]. In analogy, a larger quadrupole effect is observed in carboxylic acid anions versus ammonium and abiotic amino acid cations, since nitrogen has a negative quadrupole moment. During the collision process, therefore, the change of a favorable

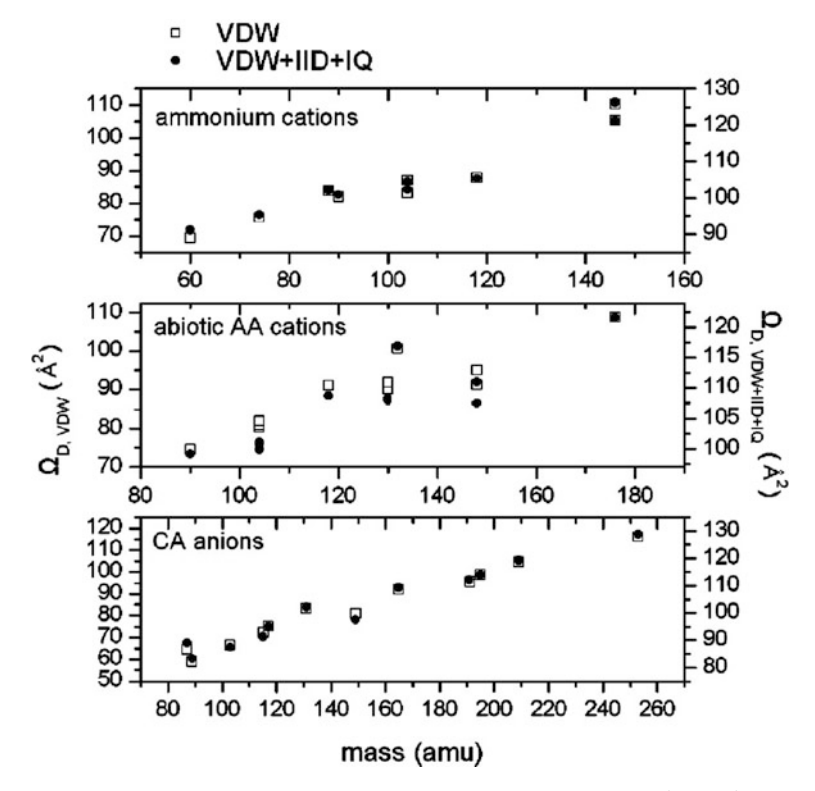


Fig. 5.5 Plots of theoretically determined collision cross-sections ( $\Omega_D$ ) of 3° and 4° ammonium cations, abiotic amino acid cations, and carboxylic acid anions in N<sub>2</sub> versus ion mass. The calculated  $\Omega_D$  of the molecular ions only with van der Waals (VDW) interaction with N<sub>2</sub> are shown as *empty squares* (left y-axis). The calculated  $\Omega_D$  of the molecular ions with original pairwise potential, van der Waals + ion-induced dipole + ion-quadrupole (VDW + IID + IQ) interactions, with N<sub>2</sub> are shown as *solid circles* (right y-axis)

orientation induced by the total ionic charge influences the collision cross-sections via ion-quadrupole interaction. This causes the observed difference of the  $N_2$  drift gas in ion-neutral interactions compared to spherical drift gas (i.e., He).

#### 5.4.4 Ion-Induced Dipole Potential

In order to understand the effect of the long-range ion-induced dipole interactions between ions and neutral  $N_2$  molecules, theoretical collision cross-section with the van der Waals and ion-induced dipole potential ( $\Omega_{D,VDW+IID}$ ) of molecular ions are compared to collision cross-sections computed after assigning the total charge of the ionic molecule as neutral ( $\Omega_{D,VDW}$ ). The calculated  $\Omega_{D,VDW}$  with the van der Waals-only potential are  $\sim$ 8–23% smaller than the calculated  $\Omega_{D,VDW+IID}$ . The observed difference is attributed mainly to the lack of long-range interactions.

5.4 Discussion 79

Figure 5.4b shows plots of theoretically determined  $\Omega_{D,VDW}$  over the theoretical  $\Omega_{D,VDW+IID}$  of 3° and 4° ammonium cations, abiotic amino acid cations, and carboxylic acid anions in N<sub>2</sub> versus ion mass. The agreement between the  $\Omega_{D,VDW}$  of ions and the  $\Omega_{D,VDW+IID}$  increases from 75 to 92% along with the mass of the molecular ion increases (Fig. 5.4b). This is easy to rationalize since the contribution of the van der Waals interaction increases as the size (i.e., number of atoms) of the molecular ion increases. As a result, it can be concluded that the contribution of long-range ion-induced dipole interaction is important for the  $\Omega_D$  of small size molecular ions, while the van der Waals interaction prominently affects to the  $\Omega_D$  in large size molecular ions in this study.

#### 5.4.5 Van der Waals Potential

The plots of the  $\Omega_D$  of 3° and 4° ammonium cations, abiotic amino acid cations, and carboxylic acid anions determined only with the van der Waals potential versus ion mass are shown in Fig. 5.5, providing the comparison with the corresponding  $\Omega_D$  from original pairwise potential, which is the combined potential of van der Waals, ion-induced dipole, and ion-quadrupole interactions. It is notable that the characteristic relative  $\Omega_{D,VDW}$  show high similarity to the relative  $\Omega_D$  from the original theoretical calculations. It is inferred that the distinction between the  $\Omega_D$  for each ion is largely due to the short-range van der Waals interaction between ion and neutral N<sub>2</sub> molecule. The molecular weight and specific geometry of the ions is considered to dominate the short-range van der Waals interaction, which affect the collision cross-section of the ion.

#### 5.4.6 Mass-Mobility Correlation

It has been suggested from the classical ion-neutral collision calculation that our ion-neutral collision occurs at the borderline between systems dominated by either long-range or short-range interactions. This is well supported from the theoretical investigation using the TJ method. The contribution of long-range interaction to the  $\Omega_D$  of ammonium cations is large ( $\sim 30\%$ ) for small ions and decreases to less than 10% as the size of the ion increases.

Previous studies have suggested that charge localization on certain functional groups and the specific structure of the ion play major roles in the interaction between ions and neutral gas molecules in IMS [7, 8, 9]. In order to assess the effect of specific charge distribution in the molecular ion on  $\Omega_D$ , the ionic  $\Omega_D$  were evaluated after assigning the charge of the molecular ion at the center of mass. In general,  $\Omega_D$  of ions, in which a total charge +1 has been assigned at the center of mass in the molecule exhibit insignificant deviations from the  $\Omega_D$  of the ions determined with DFT calculated Mulliken charge distributions. The  $\Omega_D$  of the ammonium cations with the charge at the center of mass show an average deviation

ammonium cation	$^{a}\Omega_{D}$ ( $^{b}$ VDW+ $^{c}$ IID+ $^{d}$ IQ)	$^a\Omega_D$ ( $^b ext{VDW}+$ $^c ext{IID})$	$^{a}\Omega_{D}$ ( $^{b}$ VDW)	$^{a}\Omega_{D}$ ( $^{e}$ center charge)
trimethylammonium	91.2	86.9	69.3	91.3
tetramethylammonium	95.3	91.6	75.6	95.1
trimethylethylammonium	102.2	99.2	83.7	101.0
N, N-dimethylammoniumethanol	100.9	97.7	81.9	100
choline	104.5	101.5	87.0	104
N, N-dimethylglycine	102.3	99.2	83.0	101.7
betaine	105.3	102.4	87.7	105.3
acetylcholine	126.3	123.7	110.3	120.2
(3-carboxypropyl)trimethylammonium	121.1	119.0	105.4	117.8

Table 5.3 Theoretically determined collision cross-sections of 3° and 4° ammonium cations

of 0.7% from the  $\Omega_D$  of ions with Mulliken charge distributions (Table 5.3). The  $\Omega_D$  of the carboxylic acid anions and abiotic amino acid cations exhibit 0.64 and 2.7% deviations, respectively, between the two models. This implies that the influence of the ion charge distribution on  $\Omega_D$  is minimal. The distance of the center of charge from the center of mass was calculated to investigate the specific charge distribution of the molecular ion in the present study. The average distance between the centers of charge from the centers of mass in the molecular ions is 0.7 Å for ammonium cations, and 0.9 Å for abiotic amino acid cations and carboxylic acid anions. It is inferred that the sizes of the molecular ions investigated in this study are too small to expect localization of the charge to a specific site.

In the previous section, we discussed that all potential terms, ion-quadrupole, ion-induced dipole, and van der Waals potential, are important considerations in determining the collision cross-section of the ions. Especially 75–95% of collision cross-section is contributed by van der Waals interactions, which implies that strong mass-mobility correlations are highly affected by the geometries of the ions. This can explain the correlation observed in previous studies such as carboxylic acids and amino acids in terms of their structural similarity [14, 15]. However, it is not able to explain the strong correlation among the ammonium cations. Localization of the charge in molecular ions induces specific gas-phase intramolecular cyclic structures of deprotonated carboxylate anions [15, 42] and protonated abiotic amino acid cations [14]. However, DFT optimized structures of highly alkylated ammonium cations show no significant influence of the localization of the charge on the structures (Fig. 5.2).

To evaluate the pure geometrical effect on the  $\Omega_D$ , we calculated the molecular volume and surface area of ions in  $N_2$ , which are also known as solvent-excluded volume and area [43], using the Maximal Speed Molecular Surface (MSMS) program [44]. The volume and surface area of ion are traced by the inward-facing part of the probe sphere as it rolls over the ion [43]. The radius of the probe sphere is set to be the hard-sphere diameter of  $N_2$  molecule, 3.70 Å. A distinct mass-volume correlation among the ammonium cations with different numbers of oxygen

<sup>&</sup>lt;sup>a</sup>Collision cross-section (Å<sup>2</sup>). <sup>b</sup>Van der Waals potential. <sup>c</sup>Ion-induced dipole interaction. <sup>d</sup>Ion-quadrupole interaction. <sup>e</sup>Ionic charge at center of mass.

5.4 Discussion 81

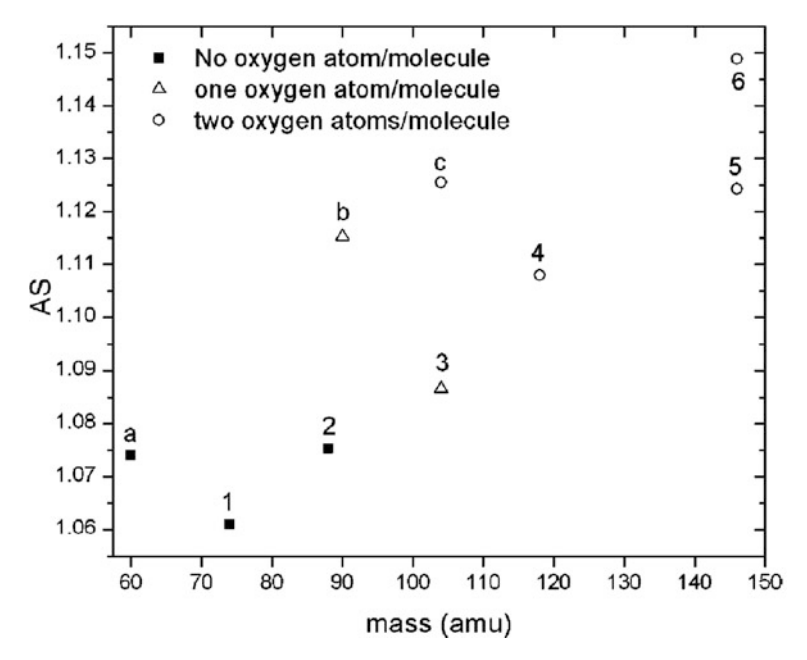


**Fig. 5.6** Plot of the total shape asymmetry (AS) of the ammonium cations versus ion mass. The ammonium cations with no oxygen atom are shown as solid squares. The ions containing one oxygen atom and two oxygen atoms are shown as empty triangles and empty circles, respectively. The DFT optimized structure of each numerically or alphabetically labeled ion is shown in Fig. 5.2

atoms is found. However, the surface area demonstrates a higher correlation with ion mass for the overall mass range. For example, the volume increases 7.6 and 5.6% from trimethylethylammonium (88 amu) to choline (104 amu) and betaine (118 amu) while the surface area increases 6.1 and 6.8%, respectively. Using the obtained molecular volume and surface area, the molecular ion's asymmetry of the total shape is determined (Fig. 5.6). The asymmetry of the total shape (AS) is expressed as

$$AS = \left(\frac{S}{4\pi}\right) \left(\frac{3V}{4\pi}\right)^{-2/3} = \frac{1}{4.836} \left(\frac{S}{V^{2/3}}\right),\tag{5.11}$$

where *S* and *V* are molecular surface area and volume, respectively. When the molecular ion is symmetrical (i.e., spherical) AS becomes unity, with AS increasing from unity as the asymmetry in shape increases. As seen in Fig. 5.6, higher asymmetry is observed as the number of oxygen atoms and the size of the ion increase. Although the larger content of oxygen atom makes for smaller molecular volumes, it increases the asymmetry of the total shape, which increases the surface area of the ion. It is therefore inferred that our observed strong mass-mobility correlation is largely due to geometrical factors. This allows us to comprehend the observed

mass-mobility correlation among two different classes of ammonium cations with the heteroatom complements in the present study.

#### 5.5 Conclusions

A high correlation between mass and mobility in N<sub>2</sub> is observed from a number of tertiary and quaternary ammonium cations. The classical ion-neutral collision calculation implies that the group of molecules studied here are on the borderline between being dominated by long-range versus short-range interactions, favoring some orbiting at lower collision energies, which would then determine the crosssection. Theoretical investigation using a modified trajectory (TJ) method also indicates that all potential terms, ion-quadrupole, ion-induced dipole, and van der Waals potential, are important considerations in determining the collision cross-section of the ions. For the smaller molecular ions, the importance of long-range interaction is emphasized, while short-range interactions dominate the collision cross-sections of the larger molecular ions. The evaluated volume and surface area suggest that shape asymmetry of the ammonium cations plays a small but significant role in determining the observed correlation between mass and mobility. The increase of the asymmetry in the shape of an ion compensates the reduction of the ion's volume, which finally yields similar mobilities of the ammonium cations with similar molecular weight investigated in this study, independent of their heteroatom complement.

Acknowledgments This research was carried out at the Jet Propulsion Laboratory, California Institute of Technology, under a contract with the National Aeronautics and Space Administration (NASA), the Noyes Laboratory of Chemical Physics, California Institute of Technology, and the Material and Process Simulation Center, Beckman Institute, California Institute of Technology. Financial support through NASA's Astrobiology Science and Technology Instrument Development, Planetary Instrument Definition and Development, and Mars Instrument Development programs is gratefully acknowledged. We appreciate the support provided by the Mass Spectrometry Resource Center in the Beckman Institute. The authors greatly appreciate Prof. Martin Jarrold at Indiana University Bloomington for generously allowing us to use and modify the Mobcal program. Hyungjun Kim and Hugh I. Kim contributed equally to this work.

#### **Bibliography**

- Fenn, J. B.; Mann, M.; Meng, C. K.; Wong, S. F.; Whitehouse, C. M. Science 1989, 246, 64-71
- 2. Shumate, C. B.; Hill, H. H. Anal. Chem. 1989, 61, 601-606.
- 3. Wittmer, D.; Luckenbill, B. K.; Hill, H. H.; Chen, Y. H. Anal. Chem. 1994, 66, 2348–2355.
- Creaser, C. S.; Griffiths, J. R.; Bramwell, C. J.; Noreen, S.; Hill, C. A.; Thomas, C. L. P. Analyst 2004, 129, 984–994.
- Gidden, J.; Ferzoco, A.; Baker, E. S.; Bowers, M. T. J. Am. Chem. Soc. 2004, 126, 15132–15140.
- Julian, R. R.; Hodyss, R.; Kinnear, B.; Jarrold, M. F.; Beauchamp, J. L. J. Phys. Chem. B 2002, 106, 1219–1228.

Bibliography 83

- 7. Counterman, A. E.; Clemmer, D. E. J. Phys. Chem. B 2001, 105, 8092–8096.
- 8. Kaleta, D. T.; Jarrold, M. F. J. Phys. Chem. A 2002, 106, 9655-9664.
- 9. Wu, C.; Siems, W. F.; Klasmeier, J.; Hill, H. H. Anal. Chem. 2000, 72, 391–395.
- Shelimov, K. B.; Clemmer, D. E.; Hudgins, R. R.; Jarrold, M. F. J. Am. Chem. Soc. 1997, 119, 2240–2248.
- 11. Hudgins, R. R.; Woenckhaus, J.; Jarrold, M. F. Int. J. Mass Spectrom. 1997, 165, 497-507.
- 12. Clemmer, D. E.; Jarrold, M. F. J. Mass Spectrom. 1997, 32, 577-592.
- 13. Beegle, L. W.; Kanik, I.; Matz, L.; Hill, H. H. Anal. Chem. 2001, 73, 3028-3034.
- 14. Johnson, P. V.; Kim, H. I.; Beegle, L. W.; Kanik, I. J. Phys. Chem. A 2004, 108, 5785-5792.
- Kim, H. I.; Johnson, P. V.; Beegle, L. W.; Beauchamp, J. L.; Kanik, I. J. Phys. Chem. A 2005, 109, 7888–7895.
- 16. Gidden, J.; Bowers, M. T. Eur. Phys. J. D. 2002, 20, 409-419.
- 17. Asbury, G. R.; Klasmeier, J.; Hill, H. H. Talanta 2000, 50, 1291-1298.
- 18. Asbury, G. R.; Wu, C.; Siems, W. F.; Hill, H. H. Anal. Chim. Acta 2000, 404, 273-283.
- Griffin, G. W.; Dzidic, I.; Carroll, D. I.; Stillwel, R. N.; Horning, E. C. Anal. Chem. 1973, 45, 1204–1209.
- 20. Berant, Z.; Karpas, Z. J. Am. Chem. Soc. 1989, 111, 3819-3824.
- 21. Karpas, Z.; Berant, Z. J. Phys. Chem. 1989, 93, 3021–3025.
- 22. Steiner, W. E.; English, W. A.; Hill, H. H. J. Phys. Chem. A 2006, 110, 1836–1844.
- 23. Vonhelden, G.; Hsu, M. T.; Kemper, P. R.; Bowers, M. T. J. Chem. Phys. 1991, 95, 3835–3837.
- Mesleh, M. F.; Hunter, J. M.; Shvartsburg, A. A.; Schatz, G. C.; Jarrold, M. F. J. Phys. Chem. 1996, 100, 16082–16086.
- 25. Mason, E. A.; O'hara, H.; Smith, F. J. J. Phys. B 1972, 5, 169-176.
- 26. Blusztajn, J. K. Science 1998, 281, 794-795.
- 27. Zeisel, S. H.; Dacosta, K. A.; Youssef, M.; Hensey, S. J. Nutr. 1989, 119, 800–804.
- 28. McHowat, J.; Jones, J. H.; Creer, M. H. J. Lipid Res. 1996, 37, 2450-2460.
- 29. Wu, C.; Siems, W. F.; Asbury, G. R.; Hill, H. H. Anal. Chem. 1998, 70, 4929–4938.
- 30. Asbury, G. R.; Hill, H. H. Anal. Chem. 2000, 72, 580-584.
- 31. Becke, A. D. J. Chem. Phys. 1993, 98, 5648-5652.
- 32. Lee, C. T.; Yang, W. T.; Parr, R. G. Phys. Rev. B 1988, 37, 785–789.
- 33. Harihara, P. C.; Pople, J. A. Chem. Phys. Lett. 1972, 16, 217-219.
- 34. Olney, T. N.; Cann, N. M.; Cooper, G.; Brion, C. E. Chem. Phys. 1997, 223, 59–98.
- Rappe, A. K.; Casewit, C. J.; Colwell, K. S.; Goddard, W. A.; Skiff, W. M. J. Am. Chem. Soc. 1992, 114, 10024–10035.
- 36. Graham, C.; Imrie, D. A.; Raab, R. E. Mol. Phys. 1998, 93, 49–56.
- 37. Dugan, J. V.; Palmer, R. W. Chem. Phys. Lett. 1972, 13, 144-149.
- 38. Dugan, J. V.; Magee, J. L. J. Chem. Phys. 1967, 47, 3103-3112.
- 39. Bowers, M. T. Gas Phase Ion Chemistry; Academic Press: New York, 1979; Vol. 1.
- 40. Wannier, G. H. Bell Syst. Tech. J. 1953, 32, 170-254.
- 41. Su, T.; Bowers, M. T. Int. J. Mass Spectrom. Ion Processes 1975, 17, 309–319.
- 42. Woo, H. K.; Wang, X. B.; Lau, K. C.; Wang, L. S. J. Phys. Chem. A 2006, 110, 7801–7805.
- 43. Connolly, M. L. J. Am. Chem. Soc. 1985, 107, 1118–1124.
- 44. Sanner, M. F.; Olson, A. J.; Spehner, J. C. Biopolymers 1996, 38, 305–320.

# Chapter 6 Structural Characterization of Unsaturated Phospholipids Using Traveling Wave Ion Mobility Spectrometry

Reprinted with permission from Kim, H. I.; Kim, H; Pang, E. S.; Ryu, E. K; Beegle, L. W.; Loo, J. A.; Goddard, W. A.; Kanik I. Anal. Chem. 2009, 81 (20), 8289-8297. Copyright 2009 American Chemical Society.

**Abstract** A number of phosphatidylcholine (PC) cations spanning a mass range of 400 to 1000 Da are investigated using electrospray ionization mass spectrometry coupled with traveling wave ion mobility spectrometry (TWIMS). A high correlation between mass and mobility is demonstrated with saturated phosphatidylcholine cations in N<sub>2</sub>. A significant deviation from this mass-mobility correlation line is observed for the unsaturated PC cation. We found that the double bond in the acyl chain causes a 5 % reduction in drift time. The drift time is reduced at a rate of  $\sim 1\%$  for each additional double bond. Theoretical collision cross-sections of PC cations exhibit good agreement with experimentally evaluated values. Collision cross-sections are determined using the recently derived relationship between mobility and drift time in TWIMS stacked ring ion guide (SRIG) and compared to estimate collision cross-sections using empiric calibration method. Computational analysis was performed using the modified trajectory (TJ) method with nonspherical N<sub>2</sub> molecules as the drift gas. The difference between estimated collision crosssections and theoretical collision cross-sections of PC cations is related to the sensitivity of the PC cation collision cross-sections to the details of the ion-neutral interactions. The origin of the observed correlation and deviation between mass and mobility of PC cations is discussed in terms of the structural rigidity of these molecules using molecular dynamics simulations.

### 6.1 Introduction

Lipids are essential biological components and have critical roles for cell structure, energy storage, and metabolic control [1]. Characterizing their structures is an essential part of lipid analysis. In addition, searching for lipid molecules is a valuable strategy for finding traces of extinct or extant life elsewhere in outer space. Lipids and biomembranes can be preserved for a long period; thus, detailed

characterization of these biomarker compositions allows for the assessment of major contributing species [2]. Lipids offer records of modern and ancient life, environmental conditions, and changes in history. However, the variety and *in situ* alteration of lipids also increases complexity, making them difficult to characterize fully [3].

The separation and characterization of phospholipids using tandem ion mobility mass spectrometry (IM-MS) has been investigated by several research groups [4, 5, 6, 7]. Utilizing matrix-assisted laser desorption ionization (MALDI) with IM-MS, phospholipid ions have been separated from other biomolecule ions [4, 8]. Separation can be achieved based on the correlation between mass and ion mobility. Phospholipids in tissue samples have been directly analyzed using MALDI-IM-MS [4, 5]. These studies have reported that phospholipid ions have slower mobility than peptide, carbohydrate, and nucleotide ions with similar masses [4, 7, 8, 9]. In general, peptides, nucleotides, and carbohydrates form globular conformations in the gas phase due to intramolecular Coulombic interactions [10, 11, 12]. However, such interactions are difficult to achieve for phospholipid molecules because their major components are aliphatic acyl chains. Recently, Jackson *et al.* reported the effects of various head and tail groups of phospholipids on mass-mobility correlations using MALDI-IM-MS [6]. They report a slight increase in the mobility of phospholipids as the degree of unsaturation on the acyl chain increases.

The correlation between the mass and mobility of molecular ions has been used to separate and characterize ions related to the mobility of gas phase ion molecules. In the early 1970s, Griffin *et al.* [13] showed that mass and mobility are strongly correlated for structurally related compounds. In the late 1980s, Karpas and Berant demonstrated distinct mass-mobility correlations of acetyls, aromatic amines, and aliphatic amines drifting in various drift gases including He, N<sub>2</sub>, CO<sub>2</sub>, and air [14, 15]. Clemmer and co-workers have demonstrated distinct mass-mobility correlations for peptides with molecular weights of 500 to 2500 Da [16]. Recently, Thalassinos *et al.* characterized phosphorylated peptides as having higher mobilities than their non-phosphorylated counterparts [17].

Our laboratory has investigated the distinct mass-mobility correlations of amino acids and carboxylic acids drifting in  $N_2$  and  $CO_2$  [18, 19]. Recently, we experimentally observed a high correlation between mass and mobility of tertiary and quaternary ammonium cations in  $N_2$  [20]. This observed correlation was investigated using classical ion-neutral collision dynamic theories and computational calculation using a modified trajectory (TJ) method. From these theoretical investigations, the ammonium cations in the mass range from 60 Da to 150 Da are on the borderline between being dominated by long range versus short range interactions with  $N_2$ . In addition, all potential terms, ion-quadrupole, ion-induced dipole, and van der Waals potential are important considerations for determining the collision cross-sections of the ions in  $N_2$ .

In this paper, we measure drift times for a number of phosphatidylcholines (PC) spanning a mass range of 400 to 1000 Da in N<sub>2</sub> using a commercial traveling wave ion mobility spectrometry (TWIMS) coupled with orthogonal acceleration time-of-flight (oa-TOF) mass spectrometry (Waters Synapt HDMS). Of particular interest is the possible dependence of mass-mobility correlations on the symmetry, length,

and degree of saturation of the acyl chains. Despite a wide range of TWIMS applications in various chemistry fields [17, 21, 22, 23, 24, 25], studies have only begun to understand the principal physics behind the TWIMS drift time and ion mobility. A number of studies have employed the empiric calibration method to estimate mobilities and collision cross-sections of analyte ions from the drift times in TWIMS [17, 21, 22, 25, 26]. Recently, Shvartsburg and Smith quantitatively revealed the relationship between drift time and ion mobility in TWIMS [27].

Jarrold and co-workers have proposed a TJ method based on a soft-core ion-neutral interaction potential to interpret collision cross-sections of ion molecules [28]. A modified TJ method for the ion-neutral interaction to account for the potential associated with the non-spherical drift gas N<sub>2</sub> has been applied to predict collision cross-sections of PC cations and to test the sensitivity of these cross-sections in order to detail the structural rigidity of these molecules [20]. Results from the estimated collision-cross sections using empiric calibration are compared with the evaluated relationship between TWIMS drift time and mobility by Shvartsburg and Smith [27]. The origin of the observed correlation and deviation between PC mass and mobility is discussed.

### **6.2 Experimental Section**

### 6.2.1 Chemicals and Reagents

All phosphatidylcholines studied in this work were purchased from Avanti Polar Lipids (Alabaster, AL) and were used without further purification. All solvents (water, methanol, and formic acid) were HPLC grade and were purchased from EMD Chemicals Inc. (Gibbstown, NJ). Calibrant peptides (GGGGGG and AAAAAA), cytochrome C, and trypsin from porcine pancreas were purchased from Sigma-Aldrich (St. Louis, MO). Samples were prepared by dissolving known quantities of molecules in a solvent consisting of 1:1 water and methanol with 0.1 % formic acid by volume to yield sample concentrations in the range of 50  $\mu$ M. Trypsin digest of cytochrome C was prepared by incubating 200  $\mu$ M of cytochrome C with 6  $\mu$ g of trypsin from porcine pancreas in 1 mL of water containing 25 mM ammonium bicarbonate (NH<sub>4</sub>HCO<sub>3</sub>) at 37°C for 4 hours. The trypsin was then removed using a Millipore Microcon centrifugal filter fitted with an Ultracel YM-10 membrane. The sample solution was diluted to an appropriate concentration for ESI with 1:1 water/methanol and 0.1 % formic acid by volume. Phospholipid and peptide ions examined in this study are listed in Table 6.1 along with their respective molecular weights.

Phosphatidylcholines examined in this study are named by their acyl chain length and number of double bonds. For example, 1-steroyl-2-oleoyl-*sn*-phosphatidylcholine (SOPC), which comprises two 18 carbon acyl chains and one double bond, is referred to as 18:0-18:1 PC.

Name	cationization	<sup>c</sup> mass	$t_d$ (ms)	$^{d}t_{d}^{\prime}$ (ms)
<sup>a</sup> 5:0-5:0 PC	H <sup>+</sup>	426	3.58	3.39
3.0 3.0 1 0	Na <sup>+</sup>	448	3.97	3.77
<sup>a</sup> 8:0-8:0 PC	H <sup>+</sup>	510	4.99	4.78
	Na <sup>+</sup>	532	5.50	5.29
<sup>a</sup> 11:0-11:0 PC	$\mathrm{H}^+$	595	6.40	6.18
	Na <sup>+</sup>	617	6.85	6.62
<sup>a</sup> 14:0-16:0 PC	$\mathrm{H}^+$	707	8.06	7.82
	Na <sup>+</sup>	729	8.32	8.07
<sup>a</sup> 16:0-16:0 PC	$\mathrm{H}^+$	735	8.64	8.39
	Na <sup>+</sup>	757	8.77	8.51
<sup>a</sup> 18:0-14:0 PC	$\mathrm{H}^+$	735	8.58	8.33
	Na <sup>+</sup>	757	8.77	8.51
<sup>a,b</sup> 16:0-18:2 PC	$\mathrm{H}^+$	759	8.51	8.26
<sup>a</sup> 18:0-16:0 PC	$\mathrm{H}^+$	763	8.96	8.71
	Na <sup>+</sup>	785	9.15	8.89
<sup>a</sup> 16:0-20:4 PC	$\mathrm{H}^+$	783	8.58	8.32
<sup>a,b</sup> 18:0-18:2 PC	$\mathrm{H}^+$	787	8.90	8.64
<sup>a</sup> 18:0-18:1 PC	$\mathrm{H}^+$	789	8.96	8.70
<sup>a</sup> 18:0-18:0 PC	$\mathrm{H}^+$	791	9.41	9.15
<sup>a</sup> 16:0-22:6 PC	$\mathrm{H}^+$	807	8.83	8.57
<sup>a</sup> 24:0-24:0 PC	$\mathrm{H}^+$	959	12.2	11.9
<sup>b</sup> KK (cytC)	$\mathrm{H}^+$	275	1.86	1.70
<sup>b</sup> HK (cytC)	$\mathrm{H}^+$	284	1.86	1.70
<sup>b</sup> GKK (cytC)	$\mathrm{H}^+$	332	2.37	2.20
<sup>b</sup> GGGGG	$\mathrm{H}^+$	362	2.18	2.00
<sup>b</sup> ATNE (cytC)	$\mathrm{H}^+$	434	3.20	3.01
<sup>b</sup> AAAAA	$\mathrm{H}^+$	446	3.14	2.94
b KATNE (cytC)	$\mathrm{H}^+$	563	4.29	4.07
<sup>b</sup> Ac-GDVEK (cytC)	$\mathrm{H}^+$	590	4.80	4.58
b GITWK (cytC)	$\mathrm{H}^{+}$	605	5.12	4.89
b IFVQK (cytC)	$\mathrm{H}^{+}$	635	5.70	5.46
b YIPGTK (cytC)	H <sup>+</sup>	679	6.02	5.78
1		0,,	0.02	2.70

Table 6.1 Mass, drift time, and corrected drift time of ion molecule used in this study

780

1061

1169

7.36

10.2

11.8

7.10

9.94

11.5

 $H^{+}$ 

 $H^{+}$ 

 $H^{+}$ 

<sup>b</sup> MIFAGIK (cytC)

<sup>b</sup> TGPNLHGLFGR (cytC)

<sup>b</sup> Bradykinin

### 6.2.2 Electrospray Ionization Traveling Wave Ion Mobility Mass Spectrometer

Experiments were performed on a Synapt HDMS traveling wave ion mobility orthogonal acceleration time-of-flight (TW-IM-oa-TOF, Waters, Manchester, U.K.) in positive ion mode. The details of the instrument have been described elsewhere [29, 30]. Source temperature of 100°C, capillary voltage of 3 kV, desolvation temperature of 250°C, and cone voltage of 30 V were set as parameters for ESI. Other parameters of the instrument were optimized to achieve the best separation of

<sup>&</sup>lt;sup>a</sup>Molecules examined in this study. <sup>b</sup>Molecules used as calibrant. <sup>c</sup>All ions are singly charged.

<sup>&</sup>lt;sup>d</sup>Mass dependent corrected drift time.

phospholipids without the roll-over effect [29]. Nitrogen drift gas was introduced to the TWIMS stacked ring ion guide (SRIG) at a 25 mL/min flow rate, which corresponds to 0.39 Torr. The traveling wave (T-wave) height and velocity were optimized as 8 V and 300 m/s, respectively. For each sample, 150 spectra were obtained and averaged for analysis. The drift times of the singly charged phospholipid cations and peptides were determined from the location of the ion mobility peak maxima extracted manually using MassLynx (v 4.1) software (Waters corp. Milford, MA). Resolution of the instrument was found to be  $\sim$  0.8 ms in full width at half maximum (FWHM) with drift times for the ions studied and the parameters employed in this study.

### 6.2.3 Collision Cross-Section Calibration

Previously published collision cross-sections of singly charged peptide hexaglycine, hexaalanine, and tryptic digest of cytochrome C in helium drift gas were used to create a calibration curve [16]. Recently published PC collision cross-sections determined in helium drift gas were also used for the calibration [9]. The calibration procedure was adopted from Thalassinos et al. [17]. The effective drift time  $(t_d'')$  of the calibrant was corrected for mass independent and mass dependent time. The published collision cross-section of the calibrant was scaled by reduced mass in N<sub>2</sub>. The effected drift time was plotted against the corrected published collision cross-section  $(\Omega'_D)$ . The plot was used to fit a linear and power trend. The equation from the fitting result was used to estimate collision cross-sections of phospholipids with reduced mass.

### 6.2.4 Computational Modeling

Collision cross-sections of ions were calculated using the modified TJ method [20], which consists of two potential terms representing van der Waals and ion-induced dipole interactions characterized by Lennard-Jones parameters and neutral polarizability, respectively [28]. The modified TJ method describes the interaction between ions and an  $N_2$  drift gas that expands applicability beyond cases of ions drifting in He (details of this modification can be found elsewhere) [20]. In brief, we set the polarizability of neutral gas for  $N_2$  (1.710 × 10<sup>-24</sup> cm<sup>2</sup>). Due to the linear geometry of  $N_2$ , two more consequences were taken into account: ion-quadrupole interaction and molecule orientation. The ion-quadrupole interaction is expressed in simple summations of partial charges of negative q (0.4825e) to each nitrogen atom and one positive 2q at the center of the nitrogen molecule. The orientations of  $N_2$  are sampled along the x-, y-, and z-axis; the averaged interaction potential is evaluated using Boltzmann weighting.

In order to consider the effect of structural fluctuation on the collision cross-section at room temperature, we performed NVT molecular dynamics (MD) simulations using a Nosé-Hoover thermostat at 300 K. The inter-atom interactions are described with the all-atom CHARMM PARAM27 force field [31] using

the LAMMPS (large-scale atomic/molecular massively parallel simulator) code [32]. We adopted the "sp<sub>2</sub> C-sp<sub>3</sub> C-sp<sub>2</sub> C" angle parameter and the "sp<sub>2</sub> C-sp<sub>2</sub> C-sp<sub>3</sub> C-sp<sub>2</sub> C" dihedral parameters from reference [33], which were optimized using 1, 4-pentadiene. The partial charge distribution of protonated phosphate (O<sub>3</sub>P-O-H) was optimized using Mulliken charge distributions from density functional theory (DFT) calculations (Table 6.2), since the common CHARMM force field only has a partial charge distribution of negatively charged phophate (O<sub>3</sub>P-O<sup>-</sup>). The systems are pre-equilibrated for 100 ps, and the conformations are sampled every one ps from the 200 ps simulations. We note that such a procedure allows for canonical sampling of the conformations at 300 K. We analyzed the collision cross-sections and potential energies of all sampled conformations of PC.

**Table 6.2** Optimized partial charge distribution of protonated phosphate from the DFT calculation of protonated dimethyl phosphate (the partial charges with atom types for CHARMM force field are tabulated.)

	<sup>a</sup> Mulliken Charge	Force Field Charge	Force Field Type
Pa	1.16	1.50	PL
Oa	-0.51	-0.49	OSL
Ob	-0.54	-0.52	OHL
Oc	-0.57	-0.56	O2L
Ha	0.35	0.36	HOL

<sup>&</sup>lt;sup>a</sup>Computed from density functional theory (DFT) calculation using Jaguar 6.0 of Schrödinger company with B3LYP functional and 6-31G\*\* basis set.

#### 6.3 Results

# 6.3.1 Saturated Phosphatidylcholine Cations

The drift times,  $t_d$ , of the PC cations were determined as described above. The drift times were then corrected with the mass dependent flight time, defined as the time that an ion spent in the TOF [17, 26]. Measured and corrected drift times for the PC cations chosen for this study are found in Table 6.1. The corrected drift time from TWIMS was plotted against the mass to charge (m/z) of the ion, and the plot was

6.3 Results 91

used to fit a linear trend. The plot of drift time versus mass for singly protonated PC cations is shown in Fig. 6.1 along with the linear fit to the data. As seen in Fig. 6.1a, all saturated PC cations investigated in this study  $(400 - 1000 \, \text{Da})$  exhibit a good correlation  $(R^2 > 0.999)$  between mass and drift time (i.e., ion mobility). In particular, symmetry of the two acyl chains in the phospholipid does not affect the common mass-mobility correlation of a saturated PC cation.

### 6.3.2 Unsaturated Phosphatidylcholine Cations

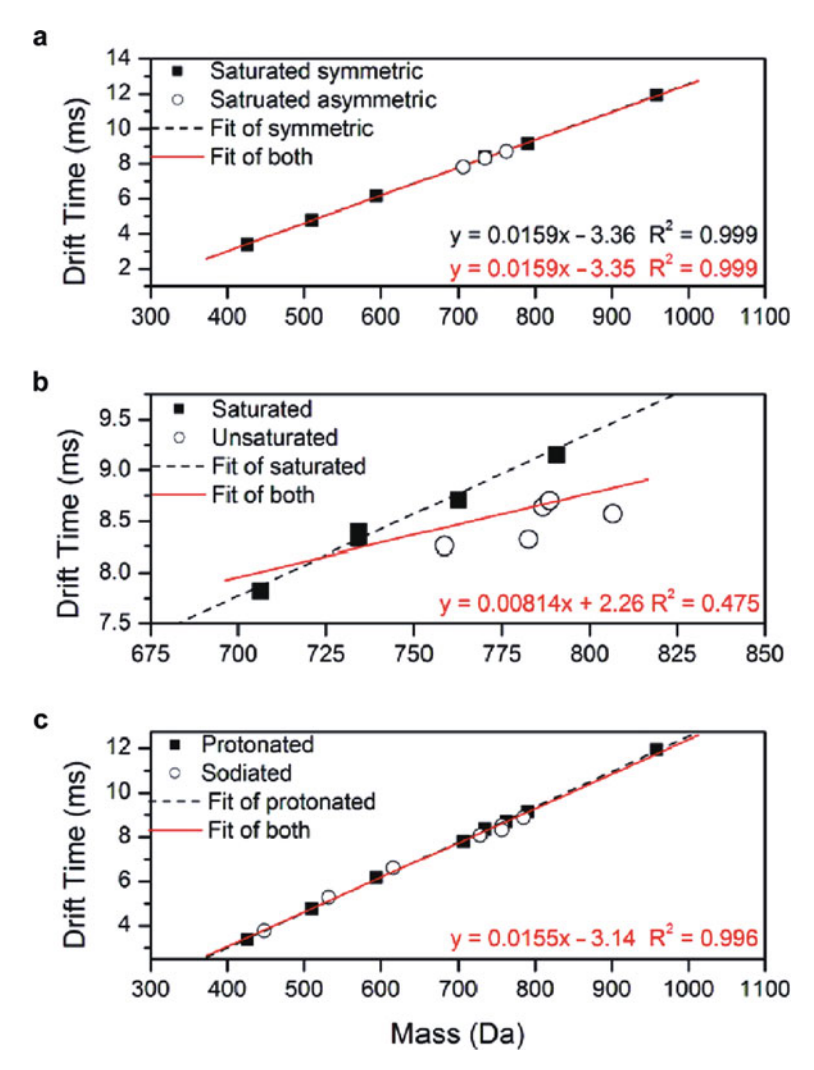
The usual acyl chain length of membrane phospholipids vary from 18 to 20 carbon atoms [34]. Most unsaturated phospholipids contain one acyl chain with one or more *cis*-double bonds and a saturated one as a second acyl chain [34]. We have selected unsaturated PC cations with these characteristics to investigate the dependence of mass-mobility correlations on the presence of double bonds in the acyl chains of membrane phospholipids (Table 6.1).

Figure 6.1b shows a plot of corrected drift time versus mass for PC cations from 700 Da to 810 Da along with the linear fit to the data. A good correlation  $(R^2=0.984)$  is still observed for the saturated PC cations within the mass range. However, a poor correlation between mass and mobility from unsaturated and saturated PC cations is also observed  $(R^2=0.487)$ . Unsaturated PC cations show higher mobilities (i.e., faster drift time) compared to saturated PC cations. Corrected drift times of 16:0-18:2 PC (MW 759) and 16:0-20:4 PC (MW 783) are measured as 8.26 ms and 8.32 ms, respectively. They traveled in the SRIG faster than smaller saturated PC cations such as 16:0-16:0 and 18:0-14:0 (MW 735), which have 8.39 ms and 8.33 ms drift times, respectively. The corrected drift time of 16:0-22:6 PC (MW 807) is measured as 8.57 ms. Compared to the 8.71 ms and 9.15 ms, which are corrected drift times of two smaller saturated PC cations, 18:0-16:0 PC (MW 763) and 18:0-18:0 PC (MW 791), respectively, 16:0-22:6 PC travels across the SRIG faster.

The presence of a *cis*-double bond causes the acyl chain to bend. In addition, a double bond causes a relatively rigid acyl chain structure compared to that of the saturated acyl chain. It is inferred that these two factors cause smaller collision cross-sections and thus faster mobility than unsaturated PC cations.

# 6.3.3 Sodiated Phosphatidylcholine Cations

Figure 6.1c shows the plot of drift time versus mass for protonated and sodiated PC cations. The sodiated PC cations investigated in this study exhibit a good mass-mobility correlation ( $R^2 = 0.996$ ) with protonated PC ions. A recent investigation by Kim *et al.* reported that short range interactions are most important for the collision cross-sections of molecular ions larger than 150 Da [20]. The PC cations (400 - 1000 Da) investigated in this study are larger than ions that Kim *et al.* [20] investigated (60 - 250 Da). Thus, the importance of short range interactions



**Fig. 6.1** (a) Plot of drift time of saturated phosphatidylcholine (PC) cations in traveling wave ion mobility spectrometer versus ion mass. Experimentally determined data for symmetric PC and asymmetric PC cations are shown as *solid squares* and *empty circles*, respectively. The *black dash* and *red solid lines* are the linear fit to the symmetric PC cation data set and to both symmetric and asymmetric PC cation data set, respectively. (b) Plot of drift time of PC cations spanning mass range 700 – 800 Da in traveling wave ion mobility spectrometer versus ion mass. Experimentally determined data for saturated PC and unsaturated PC cations are shown as *solid squares* and *empty circles*, respectively. The *black dash* and *red solid lines* are the linear fit to the saturated PC cation data set and to both saturated and unsaturated PC cation data set, respectively. (c) Plot of drift time of protonated and sodiated PC cations in traveling wave ion mobility spectrometer versus ion mass. Experimentally determined data for protonated PC and sodiated PC cations are shown as *solid squares* and *empty circles*, respectively. The *black dash* and *red solid lines* are the linear fit to the protonated PC cation data set and to both protonated and sodiated PC cation data set, respectively

6.3 Results 93

is emphasized for collision cross-sections of PC cations. In numerous cases, metal cations have been shown to cause specific peptide structures in the gas phase through Columbic interactions with backbone amide, carboxyl, amine, and functional groups [35, 36]. In contrast, PC is composed of two esterified acyl chains and one phosphorylcholine attached to glycerol [1]. In the sodiated PC cations, sodium cation interacts solely with the phosphate group without inducing a noticeable conformation change of PC. Thus, a good correlation between mass and mobility is observed from PC cations regardless of whether they are protonated or sodiated.

# 6.3.4 Estimated Collision Cross-Sections of Ions Using T-Wave Calibration

A number of studies have employed empiric calibration methods to estimate collision cross-sections of ions using a set of calibrant ions [17, 21, 22, 25, 26]. To understand the structural characteristics related to collision cross-sections of PC cations, the calibration method was applied to estimate collision cross-sections. Figure 6.2a shows the calibration plots of  $\Omega'_D$  versus  $t''_d$  for 14 singly charged peptides and 6 PC cations (Table 6.1).

Due to the different natures of peptide and PC ions in the gas phase, we fit only the peptide calibrants first. Then we compared the fit of peptide calibrants to the fit result from the combined peptide and PC calibrants. Both linear fit and power fit to the calibrants were performed, and both fittings exhibit a high correlation coefficient ( $R^2 = 0.98$  and 0.99, respectively). Thalassinos *et al.* reported that linear fit is appropriate for calibration with small peptides. However, a slightly higher correlation was observed for power fitting in the present study. Nearly identical calibration curves were obtained from both fits for peptide and combined peptide and PC calibrants. The nature of ions in the gas phase influenced the different mass-mobility correlations. However, the empiric calibration considered only the relationship between  $\Omega'_D$  and  $t''_d$ . Thus, utilizing appropriate  $\Omega_D$  for calibration is more important than the chemical category of the calibrant. Figure 6.2b summarizes the estimated collision cross-sections of protonated PC cations. The estimated collision cross-section values of PC cations are found in Table 6.3.

# 6.3.5 Determination of Collision Cross-Sections of Ions

Shavartsburg and Smith derived equations to describe the quantitative relationship between drift time and ion mobility in TWIMS [27]. Under the condition that  $KE_{\text{max}} < s$ , where K is ion mobility,  $E_{\text{max}}$  is maximum electric field (E), and s is wave velocity, the mobility of an ion is related to the average ion velocity in TWIMS as [27]

$$\bar{v} = \frac{K^2}{bs} \int_0^b E^2(x) \, ds,$$
 (6.1)

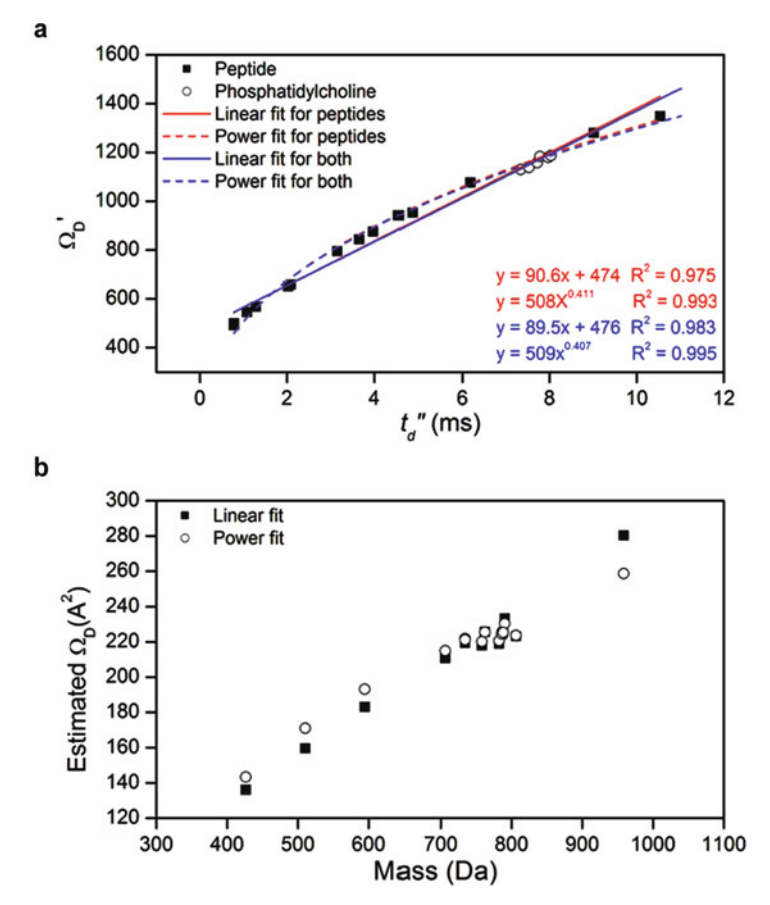


**Fig. 6.2** (a) Plot of corrected empiric cross-sections versus effective drift times for 14 peptides and 4 phosphatidylcholines (PC). For each peptide and PC the singly charged cation is used. Linear trend and power trend lines are shown as *solid* and *dash lines*, respectively. (b) A plot of the estimated cross-sections versus the ion mass for PC cations investigated in this study. The estimated collision cross-sections from linear trend and power trend are shown as *solid squares* and *empty circles*, respectively

where E(x) is a half-sinusoidal traveling wave function and b is the waveform baseline width. Note that the equation ignores the focusing field and restricts the dynamics to axial coordinates of the SRIG. The rearrangement of Equation 6.1 with drift length L and the corrected drift time  $t_d'$  yields

$$K = \sqrt{\frac{Lbs}{t_d' \int_0^b E^2(x) dx}}.$$
 (6.2)

Once K is determined, the reduced mobility  $K_0$  can be determined according to

6.3 Results 95

**Table 6.3** Collision cross-sections of phosphatidylcholine cations in N<sub>2</sub> drift gas estimated and evaluated using empiric calibration method and equations from Shavartsburg and Smith [27], respectively. Theoretically determined collision cross-sections in N<sub>2</sub> and He are also listed

		$\Omega_D  (\mathring{ ext{A}}^2)$				
PC	mass	Estimated (linear fit)	Estimated (power fit)	Evaluated	<sup>a</sup> Theoretical (in N <sub>2</sub> )	<sup>a</sup> Theoretical (in He)
5:0-5:0	426	143.4	136.1	244.8	255.3	162.5
8:0-8:0	510	171.0	159.5	289.2	301.3	197.3
11:0-11:0	594	193.1	183.0	327.3	335.0	223.8
14:0-16:0	706	214.9	210.7	367.0	361.1	248.2
16:0-16:0	734	221.9	220.4	379.9	400.7	277.1
18:0-14:0	734	221.1	219.3	378.4	363.7	254.4
16:0-18:2	758	220.1	218.0	376.7	388.2	265.8
18:0-16:0	762	225.5	225.7	386.7	364.1	254.2
16:0-20:4	782	220.7	218.9	377.8	357.0	250.6
18:0-18:2	786	224.5	224.4	385.0	387.1	270.3
18:0-18:1	788	225.3	225.5	386.4	396.2	274.4
18:0-18:0	790	230.5	233.2	396.2	395.3	275.3
16:0-22:6	806	223.6	223.2	383.3	366.8	258.0
24:0-24:0	958	258.7	280.4	451.2	423.4	305.1

<sup>&</sup>lt;sup>a</sup>Averaged over 200 conformations.

$$K_0 = \left(\frac{273 \text{ K}}{T}\right) \left(\frac{P}{760 \text{ Torr}}\right) K,\tag{6.3}$$

where *P* and *T* are the experimental pressure and temperature, respectively. Finally, the collision cross-section of an ion is evaluated by the relation [37, 38]

$$\Omega_D = \frac{3q}{16N_0} \left(\frac{2\pi}{\mu_{N_2} k_B T}\right)^{1/2} \frac{1}{K_0},\tag{6.4}$$

where  $N_0$  is the number density at standard state (273 K and 760 Torr), q is the charge on the ion,  $\mu$  is the reduced mass of ion and  $N_2$ ,  $k_B$  is the Boltzmann constant, T is the temperature in the drift region, and  $\Omega_D$  is the collision cross-section. The evaluated collision cross-sections of the examined PC cations are listed in Table 6.3. Note that a significant difference is found between the estimated  $\Omega_D$  and the evaluated  $\Omega_D$ . The evaluated  $\Omega_D$  values are on average  $\sim$  42% larger than the estimated  $\Omega_D$  values from both power and linear fit. It is of note that the collision cross-sections of calibrants are determined in He [9, 16] while the drift gas used in TWIMS is  $N_2$ . A strong contribution of short range interaction between ion and neutral is expected for  $\Omega_D$  of an ion at the mass range of PC [20]. Yet, a considerable contribution is still considered from long range interactions of ion-neutral, linear shape, and larger mass in  $N_2$  for the determination of  $\Omega_D$  of an ion. It is inferred that the observed difference of  $\Omega_D$  values are caused by lack of these terms in the calibration procedure.

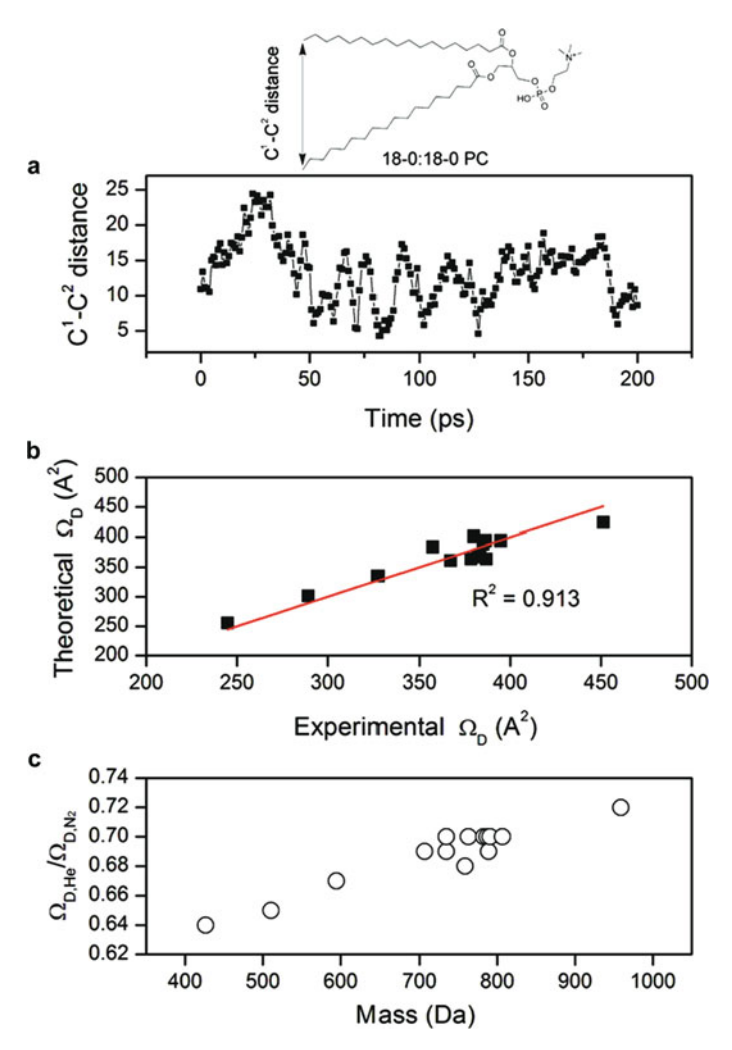


Fig. 6.3 (a) Time profile of the distance between the carbon atoms at the end of each acyl chain of 18:0–18:0 phophatidylcholine during 200 ps of the molecular dynamics simulation. The fluctuation is ranging from  $\sim 5$  Å to  $\sim 25$  Å with the time period of 5–20 ps. Approximately 17 times of fluctuation is observed from this trajectory. (b) Plot of experimentally determined collision cross-sections ( $\Omega_D$ ) of phosphatidylcholine (PC) cations in N<sub>2</sub> against theoretically determined  $\Omega_D$  using the modified TJ method for N<sub>2</sub> drift gas. The theoretical  $\Omega_D$  is obtained by averaging  $\Omega_D$  for 200 structures from MD simulations. The *solid line* is y = x. (c) Plot of theoretical  $\Omega_D$  in He over theoretical  $\Omega_D$  in N<sub>2</sub> versus mass of PC cations

# 6.3.6 Calculated Collision Cross-Sections of Ions Using the Trajectory Method

The  $\Omega_D$  of the PC cations investigated in this study were calculated using the TJ method in N<sub>2</sub> [20] and He (Table 6.3) [28]. The MD simulation trajectories of the PC

6.4 Discussion 97

cation for 200 ps reveal that the two acyl chains undergo large structural fluctuation due to the thermal energy at 300 K. Figure 6.3a shows the time profile of the C-C distance between the carbon atoms at the end of each chain of the 18:0-18:0 PC during 200 ps of dynamics. The distance between two carbon atoms fluctuates in the range of 5 to 25 Å within a 5 to 20 ps time period. In order to account for the sufficient amount of conformational change required for  $\Omega_D$  calculation, we need to sample the conformations at every 1 ps. Then, the average  $\Omega_D$  can be determined using the TJ method in N<sub>2</sub> and He for the 200 structures on the MD simulation trajectories [20, 28].

Figure 6.3b shows the plot of  $\Omega_D$  for PC cations evaluated using the Shavartsburg and Smith [27] equations versus the theoretical  $\Omega_D$  in N<sub>2</sub> calculated using the modified TJ method. The theoretical  $\Omega_D$  values of PC cations exhibit good agreement with the experimentally evaluated values. The agreement is within 6.2 % in the worst-case deviation with 3.2 % deviation on average. This shows that the experimental collision cross-sections of analyte ions can be determined using Synapt HDMS and the relationship between SRIG drift time and mobility derived by Shavartsburg and Smith [27]. In contrast, poor agreement was observed from the estimated  $\Omega_D$  of PC cations from the linear fit and power fit calibration curves with deviations of 71.2 % and 73 % on average, respectively.

#### 6.4 Discussion

### 6.4.1 Effect of Drift Gas on Ion Mobility

The difference between the estimated  $\Omega_D$  of the PC cation using empiric calibration and the evaluated  $\Omega_D$  using Equations 6.2 to 6.4 can be explained by the different polarizabilities, sizes, and shapes of He and N<sub>2</sub> molecules. In drift tube ion mobility spectrometry (DTIMS), the drift time, which corresponds to the effective drift time in TWIMS,  $t_d''$ , is inversely proportional to the ion mobility, K:

$$K = L^2 / V t_d'', (6.5)$$

where V is voltage across the drift tube. The relationship between K and  $\Omega_D$  is described as [39]

$$K = \frac{3q}{16N} \left(\frac{2\pi}{\mu k_B T}\right)^{1/2} \frac{1}{\Omega_D}.$$
 (6.6)

The corrected collision cross-section,  $\Omega'_D$ , for the empiric calibration is defined as [17, 26]

$$\Omega_D' = \frac{\Omega_D \mu^{1/2}}{q}. (6.7)$$

From Equations 6.5 through 6.7, we obtain the proportional relationship between  $t_d''$  and  $\Omega_D'$ . As discussed earlier, the default drift gas of TWIMS of Synapt HDMS is  $N_2$  [17, 30, 40]. Calibration methods commonly employ the empirical  $\Omega_D$  determined in He [16]. Thus, the corrected collision cross-section,  $\Omega_{D,N_2}'$ , using the reduced mass in  $N_2$ ,  $\mu_{N_2}$ , is related to the  $\Omega_D$  in He as

$$\Omega'_{D,N_2} = \frac{\Omega_{D,N_2} \mu_{N_2}^{1/2}}{q} = \frac{\Omega_{D,H_e} \mu_{N_2}^{1/2}}{q}.$$
 (6.8)

This relationship works if  $\Omega_{D,He} \approx \Omega_{D,N_2}$ . Hill and co-workers have demonstrated the high dependence of  $\Omega_D$  of ions on drift gas [41, 42]. Beegle et~al. demonstrated the different polarizability effects of the drift gas molecule on the  $\Omega_D$  of the ion molecule using a series of homologous Gly peptides [41]. As the size of the Gly peptide increases, the difference between  $\Omega_D$  in  $N_2$  and in He decreases. The short range interaction for  $\Omega_D$  becomes more important as the ion size increases [20]. Thus, the pre-assumption for the empiric calibration is valid when the size of the ion is very large; geometric factors of neutral and long range ion-neutral interactions are completely negligible for the determination of  $\Omega_D$  [26]. Theoretically calculated  $\Omega_D$  in  $N_2$  and He further support this argument. Figure 6.3c shows the plot of the theoretical  $\Omega_D$  in He divided by  $\Omega_D$  in  $N_2$  versus the mass of PC cations. As the size of the cation increases from 426 Da to 959 Da, the agreement between the two theoretical  $\Omega_D$  values increases from 64 % to 72 %. As a result, for the mass range of the PC cations (400 – 1000 Da), estimating  $\Omega_D$  using the empiric calibration method is not valid.

# 6.4.2 Geometrical Effect on the Collision Cross-Sections of Phosphatidyl- choline Cations

Figure 6.4a shows the plot of theoretical characteristic  $\Omega_D$  of PC cations versus ion mass compared with the corresponding surface area of PC cations in N<sub>2</sub> at 300 K using the Maximal Speed Molecular Surface (MSMS) program [43, 44]. Note that high similarity is observed from the characteristics of relative  $\Omega_D$  from theoretical calculation and the relative surface areas of PC cations. This implies that the  $\Omega_D$  for each PC cation is largely influenced by the short range van der Waals interaction between the ion and the neutral N<sub>2</sub> molecule. The molecular weight and specific geometry of the ions dominate the short range van der Waals interaction, which affects the collision cross-section of the ion [20].

The mobility of ion K becomes field-dependent at a high electric field [45]. The field dependence of K depends on the nature properties of ion-neutral interactions. In general, high field behavior of an ion is observed when the ion acquires enough energy from E to change the nature of the ion-neutral collisions [45]. The total average energy of the ions can be determined from the Wannier energy formula as follows:

6.4 Discussion 99

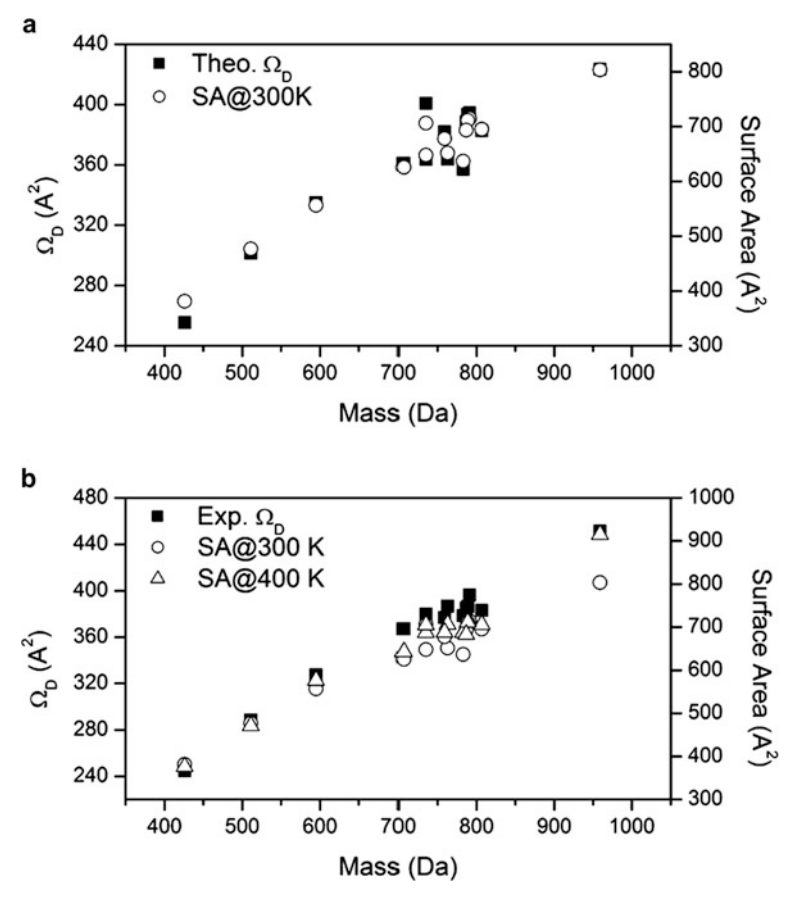


Fig. 6.4 (a) Plots of theoretically determined collision cross-sections ( $\Omega_D$ ) and surface areas of phosphatidylcholine (PC) cations in N<sub>2</sub> versus ion mass. The calculated average  $\Omega_D$  of the 200 ion conformations are shown as *solid squares* (left *y*-axis). The calculated surface areas of PC cations in N<sub>2</sub> at 300 K are shown as *empty circles* (right *y*-axis). (b) Plots of experimentally evaluated  $\Omega_D$  and surface areas of phosphatidylcholine (PC) cations in N<sub>2</sub> versus ion mass. The  $\Omega_D$  of PC cations are shown as *solid squares* (left *y*-axis). The calculated surface areas of PC cations in N<sub>2</sub> at 300 and 400 K are shown as *empty circles* and *empty triangle*, respectively (right *y*-axis)

$$\frac{3}{2}k_B T_{eff} = \frac{3}{2}k_B T + \frac{1}{2}Mv_d^2,\tag{6.9}$$

where  $T_{eff}$  is an effective temperature of ion, M is the mass of a drift gas molecule, and  $v_d$  is the drift velocity of an ion [46]. The thermal kinetic energy is  $3/2k_BT$ , and the field energy is  $1/2Mv_d^2$ . The low field behavior of an ion is achieved when

$$\frac{3}{2}k_B T \gg \frac{1}{2}Mv_d^2. {(6.10)}$$

Ion mobility spectrometers typically operate at low electric fields. The typical E/N range for the low field is a few Townsend (Td =  $10^{-17}$  Vcm<sup>2</sup>) [18, 45]. Although the applied voltage in the TWIMS is as low as 8 V in this study, due to the low pressure of the SRIG (0.39 Torr in this study), the average E/N is  $\sim$  80 Td. This is an order of magnitude larger than common IMS operating field. In addition, E/N increases to as much as  $\sim$  230 Td at  $E_{\rm max}$  of traveling wave.

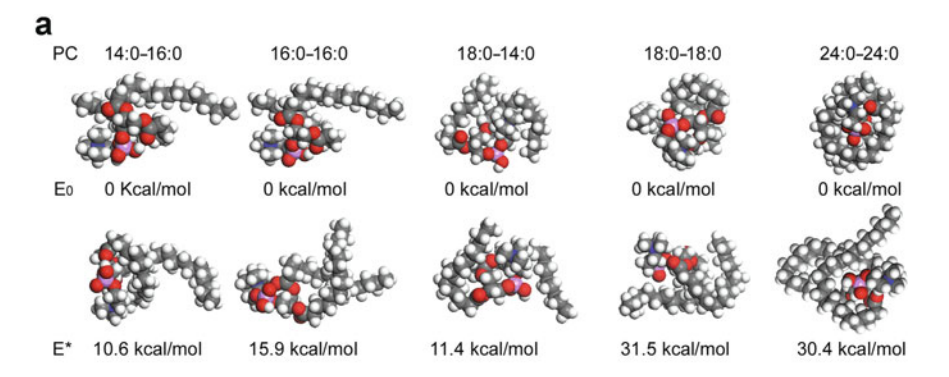
The primary effect of a high electric field is to heat the ions [45], which increases their internal energy through ion-neutral collisions. This collisional activation can result in conformation changes of the ions. Figure 6.4b shows the plots of the  $\Omega_D$  of PC cations evaluated using the Shavartsburg and Smith [27] equations versus ion mass compared with the corresponding surface area of PC cations in N<sub>2</sub> at 300 K and 400 K. Greater similarity is observed from the characteristic relative  $\Omega_D$  and the relative surface areas of PC cations at 400 K compared to the relative surface areas at 300 K. Although the experiment was performed at  $\sim$  300 K, field heating induced a shift in ion conformation distribution to slightly higher energy state. This results in a greater similarity of the characteristic between relative  $\Omega_D$  at 300 K and relative surface area at higher temperature, 400 K.

### 6.4.3 Mass-Mobility Correlations of Phophatidylcholine Cations

Saturated PC cations investigated in this study exhibit a good correlation between mass and mobility (Fig. 6.1a). However, deviations from the correlation are observed in unsaturated PC cations (Fig. 6.1b). In the previous study, we discussed the importance of van der Waals potential for determining the collision cross-section of an ion as the ion size increases [20]. This implies that strong mass-mobility correlation is highly affected by the geometry of the ion. In order to understand the mass-mobility correlation of saturated PC cations and deviations of unsaturated PC cations from the correlation plot, we investigate structures of PC cations with corresponding  $\Omega_D$ .

The minimum energy  $(E_0)$  structures of some of the saturated PC cations examined in this study are shown in Fig. 6.5a. The structures with the closest  $\Omega_D$  to the experimental values are also shown along with their corresponding relative energy values  $(E^*)$ . The plot of  $\Omega_D$  for the PC cations experimentally evaluated using the Shavartsburg and Smith [27] equations versus the theoretical  $\Omega_D$  values of  $E_0$  and  $E^*$  is shown in Fig. 6.5b. Slightly larger  $\Omega_D$  values are observed from PC cations with longer acyl chains ( $\geq$  18 carbon) compared to the  $\Omega_D$  values calculated from minimum energy structures. In contrast, smaller  $\Omega_D$  values are observed from PC cations with short acyl chains ( $\leq$  16 carbon). Note that PC cations with an acyl chain longer than 16 carbons form globular structures that are energetically favored. It is inferred that intramolecular van der Walls interactions of acyl chains drives the globular conformation to be preferred for large PC cations. However, extended structures are energetically favored for those with a shorter acyl chain (fewer than 16 carbons), whose steric effects prevent them from forming globular conformations in the gas phase. In contrast to peptide or protein ions, PC cations do not have strong

6.4 Discussion 101



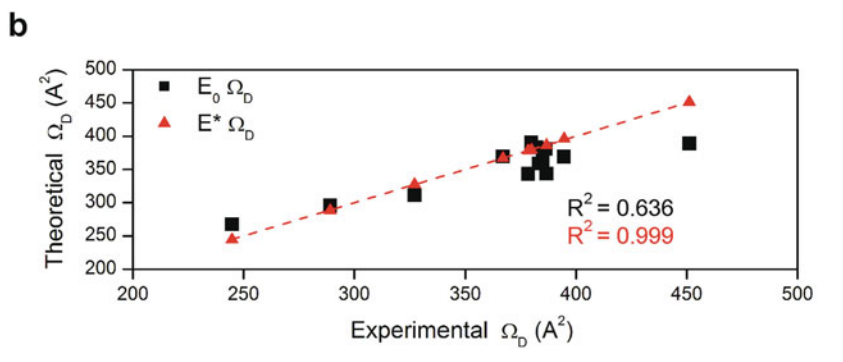


Fig. 6.5 (a) MD simulated structures of saturated phosphatidylcholine cations at minimum energy state  $(E_0)$  are shown. The structures of the closest  $\Omega_D$  to the experimental values are also shown along with corresponding relative energy values  $(E^*)$ . (b) Plot of experimentally determined collision cross-sections  $(\Omega_D)$  of phosphatidylcholine (PC) cations in  $N_2$  against theoretically determined  $\Omega_D$  at  $E_0$  and  $E^*$  using the modified TJ method for  $N_2$  drift gas. The *solid line* is y=x

intramolecular interactions to stabilize certain conformations. The energy difference between the  $E_0$  structure and the  $E^*$  structure is only 19 kcal/mol on average. Thus, the conformations of these ions may fluctuate while traveling in the SRIG. As discussed earlier, the internal energy of an ion increases with collisional activations from the traveling wave electric field, which results in continual excitation of the ion [27]. The shift in ion conformations occurs toward slightly excited  $(E^*)$  state. Especially for larger molecules (18 or more carbon acyl chains), a significant increase in  $\Omega_D$  occurs, since the increase in internal energy of these large molecules increases the importance of the entropy. As a result, the structural similarity of the saturated PC cations is maintained with moderately extended structures regardless of the length and symmetry of the PC acyl chains (Fig. 6.5a); this promotes a good correlation between mass and mobility.

# 6.4.4 Characterizing Unsaturated Phosphatidylcholines from Mass-Mobility Correlation

Unsaturated PC cations exhibit significantly deviated mobility values from the mass-mobility correlation plot of saturated PC cations (Fig. 6.1b). The drift time is reduced by  $\sim 5\%$  for the unsaturated PC cation with one double bond; the drift time reduces further at a rate of  $\sim 1\%$  for the additional double bond. Jackson et al. recently reported a  $\sim 0.5\%$  reduction in drift time for each additional double bond of phospholipids in DTIMS. In the present study, the larger difference in the mobility of unsaturated PC cations compared to saturated PC cations results from the different rate of conformation changes in TWIMS. Figure 6.6 shows structures of selected unsaturated PC cations at  $E_0$  along with the conformations at  $E^*$ . For unsaturated PC cations, a smaller shift in  $\Omega_D$  is observed from the  $\Omega_D$  of the most stable conformation compared to saturated PCs of similar mass. For those PC cations with more than 16 carbon acyl chains, saturated PC cations exhibit a  $\sim$  10% difference in  $\Omega_D$  on average, while unsaturated PC cations show only  $\sim 5\%$  difference on average (Table 6.4). As observed in Fig. 6.6, the major change in conformation occurs at the saturated acyl chain, while the conformation of the unsaturated acyl chain (yellow) maintains a bent structure. The presence of cis-double bonds in an acyl chain prevents the unsaturated acyl chain from extending by activation. As a result, less fluctuation in the ion structure occurred among unsaturated PC cations in the TWIMS. Unsaturated PC cations show smaller  $\Omega_D$  values than saturated PC cations, which can form more extended conformations. This is logical given that globular structures of unsaturated PC cations are more compact and therefore have smaller collision cross-sections. This allows us to characterize unsaturated PC cations based on their mobility, and thus collision cross-sections, using TWIMS.

**Table 6.4** Theoretically determined collision cross-sections  $(\Omega_D)$  of phosphatidylcholine cations at minimum energy state  $(E_0)$ . The differences of  $\Omega_D$   $(\Delta\Omega_D)$  and potential energy  $(\Delta E)$  from the PC structure at  $E_0$  to experimentally determined  $\Omega_D$ 

PC	$\Omega_{D,E_0} (\mathring{\text{A}}^2)$	$\Delta\Omega_D\left(\%\right)$	$\Delta E$ (kcal/mol)
5:0-5:0	267.08	9.1	15.2
8:0-8:0	295.44	2.1	10.6
11:0-11:0	311.24	-4.9	34.7
14:0-16:0	369.21	0.6	10.3
16:0-16:0	390.55	2.8	15.9
18:0-14:0	343.25	-9.3	11.4
16:0-18:2	382.85	1.6	10.4
18:0-16:0	343.38	-11.2	28.7
16:0-20:4	333.7	-11.7	26.8
18:0-18:2	362.37	-5.9	10.6
18:0-18:1	380.32	-1.6	2.21
18:0-18:0	368.93	-6.9	31.5
16:0-22:6	358.53	-6.5	30.2
24:0-24:0	388.94	-13.8	30.4

6.5 Conclusions 103

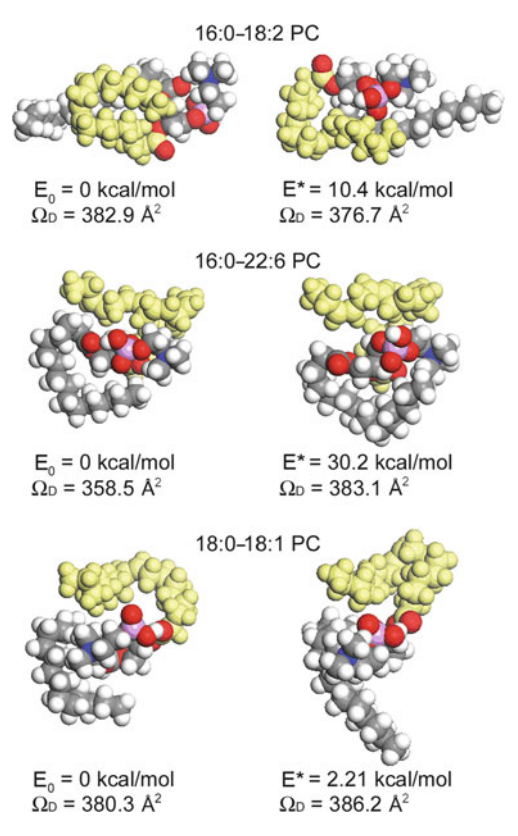


Fig. 6.6 MD simulated structures of unsaturated phosphatidylcholine cations at minimum energy state  $(E_0)$  are shown. The structures of the closest  $\Omega_D$  to the experimental values are also shown along with corresponding relative energy values  $(E^*)$ . Unsaturated acyl chain is colored in *yellow* 

#### 6.5 Conclusions

A high correlation between mass and mobility in  $N_2$  is observed from a number of saturated PC cations in TWIMS. A significant deviation from this mass-mobility correlation is observed with unsaturated PC cations. Theoretical investigation using a modified TJ method indicates that the empiric calibration method is not suitable to estimate collision cross-sections for PC cations. Instead, we evaluate collision cross-sections using a quantitative relationship between drift time and mobility derived by Shavartsburg and Smith [27]. In addition to the lack of intramolecular interactions among PC cations, collisional excitation of the ions in the SRIG induces a shift in ion conformational distribution. The unsaturated acyl chain remains bent, while the saturated acyl chain extends under the electric field, which causes larger collision cross-sections for saturated PCs and smaller ones for unsaturated PCs. The initial double bond in the acyl chain yields an approximately 5 % reduction in drift time, with further drift time reduction at the rate of  $\sim 1\%$  for each additional double bond.

As a result, greater separation and characterization of unsaturated PC cations can be achieved using TWIMS.

Acknowledgments This research was carried out at the Jet Propulsion Laboratory, California Institute of Technology, under a contract with the National Aeronautics and Space Administration (NASA), the University of California Los Angeles Mass Spectrometry and Proteomics Technology Center, and the Material and Process Simulation Center, Beckman Institute, California Institute of Technology. Financial support through NASA's Astrobiology Science and Technology Instrument Development, Planetary Instrument Definition and Development, and Mars Instrument Development programs is gratefully acknowledged. JAL acknowledges support from the NIH (RR20004).

### **Bibliography**

- 1. Gurr, M. I.; Hardwood, J. L. Lipid Biochemistry; 4th ed.; Chapman and Hall: New York, 1991.
- 2. Simoneit, B. R. T.; Summons, R. E.; Jahnke, L. L. Orig, Life Evol. Biosph. 1998, 28, 475–483.
- 3. Mossoba, M. M.; Kramer, J. K. G.; Brenna, J. T.; McDonald, R. E. *Lipid Analysis and Lipidomics* AOCS Publishing 2006.
- Woods, A. S.; Ugarov, M.; Egan, T.; Koomen, J.; Gillig, K. J.; Fuhrer, K.; Gonin, M.; Schultz, J. A. Anal. Chem. 2004, 76, 2187–2195.
- Jackson, S. N.; Ugarov, M.; Egan, T.; Post, J. D.; Langlais, D.; Schultz, J. A.; Woods, A. S. J. Mass Spectrom. 2007, 42, 1093–1098.
- Jackson, S. N.; Ugarov, M.; Post, J. D.; Egan, T.; Langlais, D.; Schultz, J. A.; Woods, A. S. J. Am. Soc. Mass Spectrom. 2008, 19, 1655–1662.
- 7. McLean, J. A.; Ridenour, W. B.; Caprioli, R. M. J. Mass Spectrom. 2007, 42, 1099–1105.
- 8. Fenn, L. S.; McLean, J. A.; Springer Heidelberg: 2008, p 905–909.
- 9. Fenn, L. S.; Kliman, M.; Mahsut, A.; Zhao, S. R.; McLean, J. A. 2009, In Press.
- 10. Gidden, J.; Bowers, M. T. J. Am. Soc. Mass Spectrom. 2003, 14, 161–170.
- 11. Fenn, L. S.; McLean, J. A. Chem. Commun. 2008, 5505-5507.
- 12. Jarrold, M. F. Annu. Rev. Phys. Chem. 2000, 51, 179-207.
- Griffin, G. W.; Dzidic, I.; Carroll, D. I.; Stillwel, R. N.; Horning, E. C. Anal. Chem. 1973, 45, 1204–1209.
- 14. Berant, Z.; Karpas, Z. J. Am. Chem. Soc. 1989, 111, 3819-3824.
- 15. Karpas, Z.; Berant, Z. J. Phys. Chem. 1989, 93, 3021–3025.
- Valentine, S. J.; Counterman, A. E.; Clemmer, D. E. J. Am. Soc. Mass Spectrom. 1999, 10, 1188–1211.
- 17. Thalassinos, K.; Grabenauer, M.; Slade, S. E.; Hilton, G. R.; Bowers, M. T.; Scrivens, J. H. *Anal. Chem.* **2009**, 81, 248–254.
- 18. Johnson, P. V.; Kim, H. I.; Beegle, L. W.; Kanik, I. J. Phys. Chem. A 2004, 108, 5785–5792.
- Kim, H. I.; Johnson, P. V.; Beegle, L. W.; Beauchamp, J. L.; Kanik, I. J. Phys. Chem. A 2005, 109, 7888–7895.
- Kim, H.; Kim, H. I.; Johnson, P. V.; Beegle, L. W.; Beauchamp, J. L.; Goddard, W. A.; Kanik, I. Anal. Chem. 2008, 80, 1928–1936.
- Ruotolo, B. T.; Giles, K.; Campuzano, I.; Sandercock, A. M.; Bateman, R. H.; Robinson, C. V. Science 2005, 310, 1658–1661.
- Ruotolo, B. T.; Hyung, S. J.; Robinson, P. M.; Giles, K.; Bateman, R. H.; Robinson, C. V. Angew. Chem.-Int. Edit. 2007, 46, 8001–8004.
- Smith, D. P.; Giles, K.; Bateman, R. H.; Radford, S. E.; Ashcroft, A. E. J. Am. Soc. Mass Spectrom. 2007, 18, 2180–2190.
- 24. Bagal, D.; Zhang, H.; Schnier, P. D. Anal. Chem. 2008, 80, 2408–2418.
- 25. Williams, J. P.; Scrivens, J. H. Rapid Commun. Mass Spectrom. 2008, 22, 187-196.

Bibliography 105

 Ruotolo, B. T.; Benesch, J. L. P.; Sandercock, A. M.; Hyung, S. J.; Robinson, C. V. *Nat. Protoc.* 2008, 3, 1139–1152.

- 27. Shvartsburg, A. A.; Smith, R. D. Anal. Chem. 2008, 80, 9689–9699.
- Mesleh, M. F.; Hunter, J. M.; Shvartsburg, A. A.; Schatz, G. C.; Jarrold, M. F. J. Phys. Chem. 1996, 100, 16082–16086.
- 29. Giles, K.; Pringle, S. D.; Worthington, K. R.; Little, D.; Wildgoose, J. L.; Bateman, R. H. Rapid Commun. Mass Spectrom. 2004, 18, 2401–2414.
- 30. Pringle, S. D.; Giles, K.; Wildgoose, J. L.; Williams, J. P.; Slade, S. E.; Thalassinos, K.; Bateman, R. H.; Bowers, M. T.; Scrivens, J. H. *Int. J. Mass Spectrom.* **2007**, 261, 1–12.
- MacKerell, A. D.; Bashford, D.; Bellott, M.; Dunbrack, R. L.; Evanseck, J. D.; Field, M. J.; Fischer, S.; Gao, J.; Guo, H.; Ha, S.; Joseph-McCarthy, D.; Kuchnir, L.; Kuczera, K.; Lau, F. T. K.; Mattos, C.; Michnick, S.; Ngo, T.; Nguyen, D. T.; Prodhom, B.; Reiher, W. E.; Roux, B.; Schlenkrich, M.; Smith, J. C.; Stote, R.; Straub, J.; Watanabe, M.; Wiorkiewicz-Kuczera, J.; Yin, D.; Karplus, M. J. Phys. Chem. B 1998, 102, 3586–3616.
- 32. Plimpton, S. J. Comput. Phys. 1995, 117, 1-19.
- 33. Feller, S. E.; Gawrisch, K.; MacKerell, A. D. J. Am. Chem. Soc. 2002, 124, 318–326.
- 34. Alberts, B.; Bray, D.; Hopkin, K.; Johnson, A.; Lewis, J.; Raff, M.; Roberts, K.; Walter, P. *Essential Cell Biology*; Second ed.; Garland Science: New York, 2004.
- 35. Kohtani, M.; Kinnear, B. S.; Jarrold, M. F. J. Am. Chem. Soc. 2000, 122, 12377–12378.
- 36. Wyttenbach, T.; Liu, D. F.; Bowers, M. T. J. Am. Chem. Soc. 2008, 130, 5993-6000.
- 37. Revercomb, H. E.; Mason, E. A. Anal. Chem. 1975, 47, 970–983.
- 38. Eiceman, G. A.; Karpas, Z. Ion Mobility Spectrometry; CRC Press: Boca Raton, FL, 1994.
- 39. Mason, E. A.; O'hara, H.; Smith, F. J. J. Phys. B 1972, 5, 169-176.
- 40. Scarff, C. A.; Thalassinos, K.; Hilton, G. R.; Scrivens, J. H. Rapid Commun. Mass Spectrom. 2008, 22, 3297–3304.
- 41. Beegle, L. W.; Kanik, I.; Matz, L.; Hill, H. H. Int. J. Mass Spectrom. 2002, 216, 257-268.
- Matz, L. M.; Hill, H. H.; Beegle, L. W.; Kanik, I. J. Am. Soc. Mass Spectrom. 2002, 13, 300–307.
- 43. Connolly, M. L. J. Am. Chem. Soc. 1985, 107, 1118-1124.
- 44. Sanner, M. F.; Olson, A. J.; Spehner, J. C. Biopolymers 1996, 38, 305–320.
- 45. Carr, T. W.; Baim, M. A.; Cohen, M. J.; Dam, R. J.; Hagen, D. F.; Hill, H. H.; Mason, E. A.; Siegel, M. W.; Spangler, G. E.; Wernlund, R. F. *Plasma Chromatography*; Plenum Press: New York, 1984.
- 46. Wannier, G. H. Bell Syst. Tech. J. 1953, 32, 170-254.

# Chapter 7 Interfacial Reactions of Ozone with Lipids and Proteins in a Model Lung Surfactant System

In part with permission from Kim, H. I.; Kim, H; Shin, Y. S.; Beegle, L. W.; Jang, S. S.; Neidholdt, E. L.; Goddard, W. A.; Heath, J. R.; Kanik, I.; Beauchamp, J. L. J. Am. Chem. Soc. 2010, 132 (7), 2254–2263. Copyright 2010 American Chemical Society.

In part with permission from Kim, H. I.; Kim, H; Shin, Y. S.; Beegle, L. W.; Goddard, W. A.; Heath, J. R.; Kanik, I.; Beauchamp, J. L. J. Phys. Chem. B 2010, 114 (29), 9496–9503. Copyright 2010 American Chemical Society.

Abstract Oxidative stresses from irritants such as hydrogen peroxide and ozone (O<sub>3</sub>) can cause dysfunction of the pulmonary surfactant (PS) in the human lung, resulting in chronic diseases of the respiratory tract. For identification of structural changes of major components of PS due to the heterogeneous reaction with O<sub>3</sub>, field induced droplet ionization (FIDI) mass spectrometry is utilized to probe the surfactant layer system. FIDI is a soft ionization method in which ions are extracted from the surface of micro liter volume droplets. We report the structurally specific oxidative changes of SP-B<sub>1-25</sub> (a shortened version of human surfactant protein B) and 1-palmitoyl-2-oleoyl-sn-phosphatidylglycerol (POPG) due to reaction with O<sub>3</sub> at the air-liquid interface. We also present studies of the interfacial oxidation of SP- $B_{1-25}$  in a non-ionizable 1-palmitoyl-2-oleoyl-sn-glycerol monolayer as a model lung surfactant system, where the competitive oxidation of the two components is observed. Our results indicate that the heterogeneous reaction at the interface is different from that in the bulk phase. For example, we observe the hydroxyhydroperoxide and the secondary ozonide as major products of the heterogeneous ozonolysis of POPG. These products are metastable and difficult to observe in the bulk-phase. In addition, compared to the nearly complete homogeneous oxidation of SP- $B_{1-25}$ , only a subset of the amino acids known to react with ozone is oxidized in the hydrophobic interfacial environment. Combining these experimental observations with the results of molecular dynamics simulations provides an improved understanding of the interfacial structure and chemistry of a model lung surfactant system when subject to oxidative stress.

### 7.1 Introduction

The human lung is constantly exposed to airborne environmental insults. Long-term and immediate exposure of lungs to pathogens, air pollutants, and other irritants can be a major cause of acute and chronic injuries such as cardiopulmonary mortality and lung cancer [1, 2, 3]. Lung disease is the third leading cause of death in the United States and ~\$154 billion is spent for direct and indirect lung disease-related health care every year [3]. Lung disease death rates are still increasing and more efforts to understand the chemical as well as the physical characteristics of lung system are required.

Pulmonary surfactant (PS) is a complex mixture of lipids and proteins [4] found in the lungs that reduces the surface tension of the alveolar sacs during the breath cycle. Phospholipids form oriented monolayers at the air-liquid interface. The principal phospholipid component of the layer, 1, 2-dipalmitoyl-sn-phosphatidylcholine (DPPC), can achieve a very low surface tension (~0 mN/m) [5, 6] while the higher fluidity of unsaturated phospholipids such as 1-palmitoyl-2-oleoyl-sn-phosphatidylglycerol (POPG) improves the adsorption and spreading properties of surfactant at the air-liquid interface [6]. Surfactant protein B (SP-B) enhances phospholipid adsorption and spreading from the sub-phase to the interface [7], and inherited deficiencies in SP-B are lethal at birth [8]. Despite its vital importance, little is known about the interactions of the protein with phospholipids to form final lipid-protein complexes in the PS [9] as well as the manner in which this complex environment modifies the interaction of reative oxygen species (ROS) with individual components.

A number of studies have reported the chemical changes of major components of PS under various oxidative stresses [10, 11, 12], as well as changes in physical properties, which cause acute lung injury and respiratory failure [1, 13, 14]. For example, Uppu et al. used human red-blood cell membranes as a model lung system and demonstrated their oxidation via a bulk-phase O<sub>3</sub> application [11]. The alteration of structure and physical properties of SP-B by ROS has been reported by Possmayer and co-workers [12, 14]. Yet, understanding detailed mechanisms of chemical and physical changes in the complex PS system is still an active and challenging field of research. In particular, the oxidative change of major PS components by a heterogeneous air-liquid reaction with an external oxidative source (i.e. O<sub>3</sub>) has not been studied thoroughly at the molecular level. An increasing number of studies have focused on the heterogeneous chemistry of small molecules at the air-liquid interface, mainly using mass spectrometric [15] and spectroscopic [16] techniques, as well as theoretical methods [17]. Fewer studies have considered the air-liquid interfacial chemistry of biologically relevant systems. Exemplifying the latter, Colussi and co-workers recently reported heterogeneous reactions with O<sub>3</sub> of ascorbic acid [18] and uric acid [19], which are components of the pulmonary epithelial lining fluid, using mass spectrometry.

Field induced droplet ionization mass spectrometry (FIDI-MS) comprises a soft ionization method to sample ions from the surface of microliter droplets [15, 20, 21]. It is ideally suited to monitor time dependent heterogeneous reactions

7.1 Introduction 109

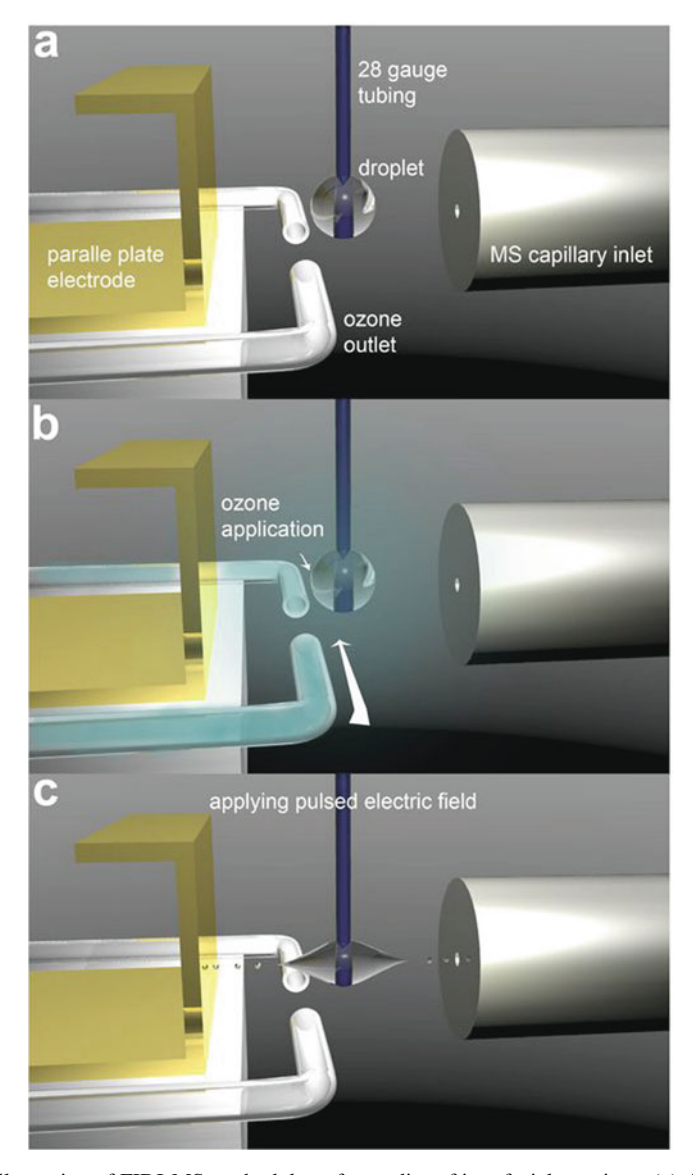


**Fig. 7.1** Illustration of FIDI-MS methodology for studies of interfacial reactions. (a) A quiescent hanging droplet of analyte-containing solution is formed on the end of a capillary. All electrical components remain at ground as the droplet is formed and reacts in a field-free environment. (b) The droplet is exposed to gas-phase reactants for a variable period of time to allow for heterogeneous reactions between gas-phase and solution-phase species. (c) After a reaciton period, a pulsed electric field stretches the neutral droplet until it emits stream of positively and negatively charged submicron droplets in opposite directions. Ionized reactants and products from heterogeneous reactions enter the capillary inlet of the mass analyzer. Either positive or negative ions can be sampled

at the air-liquid interface. A pulsed electric field stretches neutral droplets until they develop dual Taylor cones, emitting streams of positively and negatively charged submicron droplets in opposite directions. In practice, a quiescent hanging droplet is formed on the end of a capillary and then exposed to gas-phase reactants for a variable period of time, followed by FIDI-MS sampling of molecular species present in the interfacial layer (Fig. 7.1).

In this study, we utilize FIDI-MS for probing air-liquid interfacial oxidation of POPG, representative of the major unsaturated anionic lipids in lung surfactant, and SP-B<sub>1-25</sub> (FPIPLPYCWLCRALIKRIQAMIPKG) by O<sub>3</sub>. Synthetic  $\alpha$ -helical SP-B<sub>1-25</sub> is reported to produce the same effect as the entire 79 amino acid SP-B [22, 23, 24]. Sampling droplets with an interfacial layer of POPG or SP-B<sub>1-25</sub> exposed to O<sub>3</sub> gas over a range of reaction times reveals distinct air-liquid interfacial chemistry. In addition, we examine the heterogeneous reaction of a model PS system comprising SP-B<sub>1-25</sub> and 1-palmitoyl-2-oleoyl-sn-glycerol (POG) with O<sub>3</sub>. POG is non-ionizable lipid with properties at the air-liquid interface similar to POPG. It is employed to avoid undesired competition of ionization with SP-B<sub>1-25</sub> at the surface of the droplet during the FIDI experiment. For comparison to the observed heterogeneous chemistry, we also report homogeneous reactions of SP-B<sub>1-25</sub> with dissolved ozone. Structures of POPG, POG, and SP-B<sub>1-25</sub> are shown in Fig. 7.2. The observed interfacial reactions are correlated with positioning of SP-B<sub>1-25</sub> in a lipid monolayer as determined by means of molecular dynamic (MD) simulations.

$$\begin{split} \text{Phe}_{1}\text{-Pro}_{2}\text{-Ile}_{3}\text{-Pro}_{4}\text{-Leu}_{5}\text{-Pro}_{6}\text{-Tyr}_{7}\text{-Cys}_{8}\text{-Trp}_{9}\text{-Leu}_{10}\text{-Cys}_{11}\text{-Arg}_{12}\text{-Ala}_{13}\text{-Leu}_{14}\\ \text{Gly}_{25}\text{-Lys}_{24}\text{-Pro}_{23}\text{-Ileu}_{22}\text{-Met}_{21}\text{-Ala}_{20}\text{-Gln}_{19}\text{-Ile}_{18}\text{-Arg}_{17}\text{-Lys}_{16}\text{-Ile}_{15}\\ \text{SP-B}_{1.25} \end{split}$$

Fig. 7.2 Structures of POPG, POG, and SP-B<sub>1-25</sub> investigated in this study

7.2 Methods 111

#### 7.2 Methods

### 7.2.1 Chemicals and Reagents

Sodium salts of POPG and POG were purchased from Avanti Polar Lipid (Alabaster, AL).  $SP-B_{1-25}$  was purchased from Biomer Technology (Hayward, CA). All solvents were purchased from EMD Chemicals Inc. (Gibbstown, NJ).

# 7.2.2 Online FIDI-MS Technique and Heterogeneous Oxidation by O<sub>3</sub>

The FIDI-MS instrument used in this investigation were based on designs previously described by Grimm *et al.* [15]. A  $\sim$ 2 mm o.d. droplet of analyte solution is suspended from the end of a 28-gauge stainless steel capillary (Small Parts Inc.). The droplet is located on center in the region between the plate electrode and the MS inlet; the plate and inlet were separated by 6 mm. A high-voltage pulse ( $\pm$ 7 × 10<sup>5</sup> V m<sup>-1</sup>, 20 ms) is applied on the parallel plate electrode and sampling capillary to achieve FIDI. Ozonolysis reactions occur between 0 and 30 s after a quiescent droplet is achieved ( $\sim$ 1–2 s). A pencil-style UV calibration lamp (model 6035, Oriel) generates  $\sim$ 20 ppm O<sub>3</sub>. 100  $\mu$ M POPG, 50  $\mu$ M SP-B<sub>1-25</sub>, or mixtures of 100  $\mu$ M POG and 50  $\mu$ M SP-B<sub>1-25</sub> in 1:1 (by volume) water and methanol feed the droplet source. The FIDI-MS spectra reported in this study were obtained by averaging five to ten individually acquired spectra from separately prepared droplets. The m/z of each ion was determined from the locations of the peak maxima identified in the mass spectra. The experimental details for the bulk-phase O<sub>3</sub> application and the Fenton reaction of SP-B<sub>1-25</sub> are described in Section 8.8.

# 7.2.3 Molecular Dynamic Simulations

The MD simulations were performed with the all-atom CHARMM PARAM27 [25] force field using the LAMMPS (large-scale atomic/molecular massively parallel simulator) code [26]. To describe the water, we used a flexible TIP3P potential, which needs additional Hooke's constants, K of 900 kcal/mol/Å $^2$  for OH bond and K of 110 kcal/mol/rad $^2$  for HOH angle to the 3-site-rigid TIP3P model [25]. The initial conformation of SP-B<sub>1-25</sub> was taken from the Protein Data Bank structure (1DFW). The particle-particle particle-mesh (PPPM) method [27] was employed to compute the electrostatic using an accuracy criterion of  $10^{-5}$ .

The initial structures for the lipid monolayer-water systems were prepared with 48 hexagonally-packed lipids on the 3168, 3264, 3744, and 4464 water molecules for the 55, 60, 65, and 70 Å<sup>2</sup>/lipid surface densities, respectively. A pure-repulsive wall potential,  $E = \epsilon \left[ \frac{2}{15} \left( \frac{\sigma}{r} \right)^9 - \left( \frac{\sigma}{r} \right)^3 \right]$ , where  $\epsilon = 0.1521$  kcal/mol and

 $\sigma=3.1538$  Å with cut-off distance of 2.7071 Å, was applied at z=0 to prevent the water from diffusing in the negative z-direction. The dimensions of the simulation cells used were (55.21 Å × 47.82 Å × 200.0 Å) for the 55 Ų/lipid, (57.67 Å × 49.94 Å × 200.0 Å) for the 60 Ų/lipid, (60.02 Å × 51.98 Å × 200.0 Å), for the 65 Ų/lipid, and (62.28 Å × 53.94 Å × 200.0 Å) for the 70 Ų/lipid surface densities. The systems were equilibrated for 0.5 ns using 300 K NVT MD simulations by applying Nosé-Hoover thermostat with a temperature damping relaxation time of 0.1 ps. Then, 2.0 ns NVT MD simulations were performed, and these trajectories are employed for the analysis of the atomic profiles.

The initial structure for the SP-B $_{1-25}$  in the POG or POPG monolayer was constructed using the final structure after the simulation of the lipid monolayer-water system with the surface density of 60 Å $^2$ . After removing six neighboring lipids, the SP-B $_{1-25}$  is inserted into the resultant cavity with an  $\alpha$ -helical axis orientation angle of 34° to the interfacial plane. Then the dimensions of the simulation cells were slightly adjusted to (57.88 Å × 50.12 Å × 200.0 Å). Similar to the lipid monolayer simulations, 0.5 ns equilibration followed by 2.0 ns NVT MD simulation was performed at 300 K. To analyze the trajectories, we averaged the population over the last 0.5 ns of the 2.0 ns trajectories.

### 7.3 Results and Discussion

### 7.3.1 Interfacial Reaction of POPG with $O_3$

The *cis*-double bond of an unsaturated phospholipid reacts with  $O_3$  yielding aldehyde and carboxylic acid products directly from primary ozonide (POZ) or through energetic Crigee intermediates (CI), while saturated phospholipids such as DPPC remain intact. In this study we have investigated the heterogeneous reaction of  $O_3$  with POPG as a representative unsaturated phospholipid in PS system. The negative ion FIDI-MS spectra for ozonolysis of POPG in a water/methanol (1:1 by volume) droplet are shown in Fig. 7.3a along with the proposed reaction mechanisms (Fig. 7.3b). Singly deprotonated POPG, observed at m/z 748, is seen as a dominant species in the FIDI-MS spectrum before  $O_3$  application (Fig. 7.3a). Products resulting from ozonolysis of POPG appear at least as early as 5 s after exposing the droplet to  $O_3$ . The relative abundance of the reactant POPG decreases dramatically after 15 s of exposure, and then the FIDI-MS spectrum is dominated by ozonolysis products after 30 s. The time for consuming 90-99% of POPG to form the primary ozonide (POZ) at the air-liquid interface is calculated to be  $\sim 10-20$  s (see Section 8.7). This agrees well with the experimental observation of this study.

It is noteworthy that hydroxyhydroperoxide (HHP), methoxyhydroperoxide (MHP), and the SOZ, which are known to be metastable species in the bulk-phase, are observed as major products of POPG ozonolysis in the FIDI-MS spectra (Fig. 7.3a) [28]. In order to yield HHP, a Criegee intermediate (CI) or a POZ is

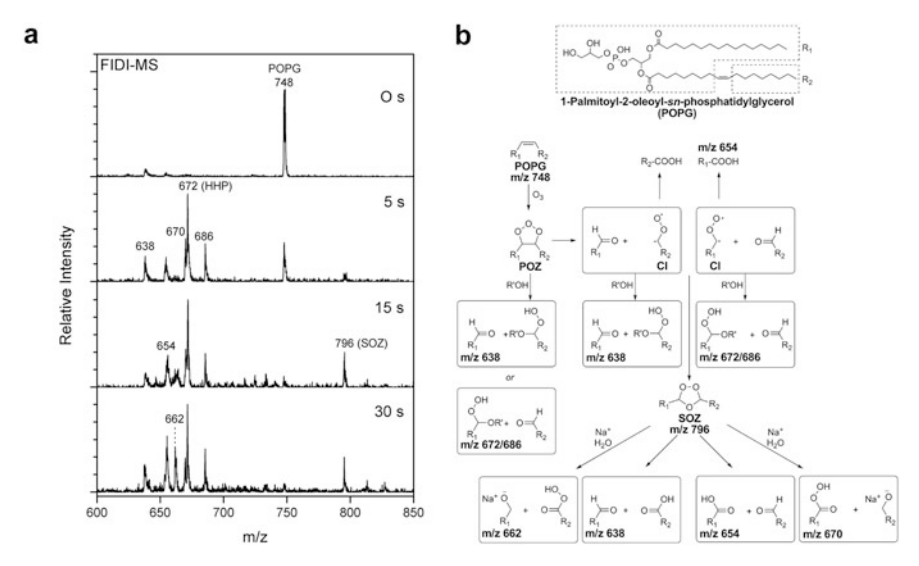


**Fig. 7.3** (a) Heterogeneous reaction of POPG with O<sub>3</sub> as a function of time. In the absence of ozone, the negative ion FIDI-MS spectrum of POPG is dominated by the singly deprotonated POPG peak at m/z 748. POPG is depleted after 15 s of the exposure and oxidation products are dominated by deprotonated hydroxyhydroperoxide (HHP) at m/z 672. The aldehyde, carboxylic acid, and methoxyhydroperoxide products are observed at m/z 638, m/z 654, and m/z 686, respectively. The secondary ozonide (SOZ) and sodiated alcohol products show up in the spectra at m/z 796 and m/z 662, respectively. (b) Summary of heterogeneous oxidation of POPG with O<sub>3</sub> at the air-liquid interface. R' is H for water and CH<sub>3</sub> for methanol

required to react with a water molecule [28, 29]. Rapid decomposition of HHP through proton transfers from water molecules yields ROS [29], which makes it difficult to observe HHP directly in the bulk-phase. The water density at the airliquid interfacial region is significantly lower than in the bulk-phase [30]. In addition, water molecules in a lipid monolayer are observed to be localized within the lipid head group region due to the strong interactions with polar head groups [31]. These conditions allow HHP to be abundant in the lipid monolayer at the air-liquid interface, which is a characteristic of the heterogeneous reaction of POPG compared to the homogeneous reaction [29]. The observed MHP originates from the reaction of a CI or POZ with a methanol molecule in the droplet.

A significant abundance of SOZ is observed in the FIDI-MS spectra after exposing the droplet to O<sub>3</sub> for 15 s. The structure of SOZ (m/z 796) is confirmed by low energy collision induced dissociation (CID), which yields the aldehyde (m/z 638) and carboxylic acid (m/z 654) fragments. The peak corresponding to SOZ continues to build up in the spectrum as the POPG lipid is depleted. We infer that the observed SOZ is not formed by direct rearrangement of POZ but rather by recombination of the CI with aldehydes (Fig. 7.3b) [28, 32]. In the bulk-phase, however, faster reaction with water molecules prevents the CI from reacting with aldehyde to form SOZ [33]. A significant amount of the sodiated alcohol product (m/z 662)

is observed after exposing the droplet to O<sub>3</sub> for 30 s. This product is due to the dissociation of SOZ followed by the association with sodium cation. This suggests that after SOZ is produced under an anhydrous environment, the newly formed hydrophilic molecule interacts with sodium cation in the liquid-phase to yield the sodiated alcohol product. These SOZ and sodiated alcohol products are characteristic of specific air-liquid interface chemistry during POPG ozonolysis.

### 7.3.2 Interfacial Oxidation of SP- $B_{1-25}$

The positive ion FIDI-MS spectra for the oxidation of  $SP-B_{1-25}$  by  $O_3$  are shown in Fig. 7.4a. The doubly protonated  $SP-B_{1-25}$  is observed as the dominant species in the FIDI-MS spectrum before  $O_3$  application. Products resulting from the oxidation of  $SP-B_{1-25}$  by  $O_3$  appear after the droplet is exposed to  $O_3$  for 5 s. The products at m/z 1481 and m/z 1489 correspond to doubly protonated  $SP-B_{1-25}$  with two oxygen atoms and with three oxygen atoms, respectively. The FIDI-MS spectrum of the droplet with  $SP-B_{1-25}$  is dominated by the triply oxygenated product at m/z 1489 after exposing the droplet to  $O_3$  for 10 s. No further oxidation of the peptide

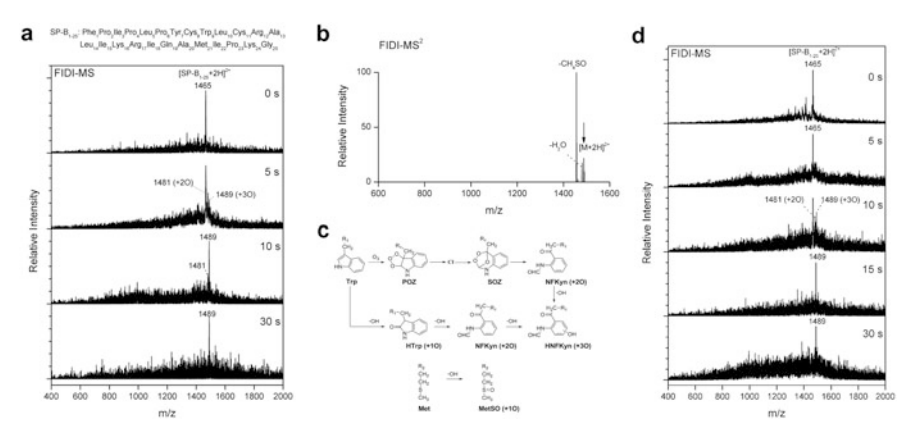


**Fig. 7.4** (a) Air-liquid interfacial oxidation of SP-B $_{1-25}$  by O $_3$  as a function of time. In the absence of ozone, the positive ion FIDI-MS spectrum of SP-B $_{1-25}$  is dominated by the doubly protonated SP-B $_{1-25}$  peak at m/z 1,465. The products at m/z 1,481 and m/z 1,489 correspond to doubly protonated SP-B $_{1-25}$  with two oxygen atoms and with three oxygen atoms, respectively, appear after the droplet is exposed to O $_3$  for 5 s. The triply oxygenated product at m/z 1,489 dominates the FIDI-MS spectrum after exposing the droplet to O $_3$  for 10 s. No further oxidation of the peptide is observed up to 30 s of exposure. (b) FIDI-MS $^2$  of doubly charged triply oxygenated SP-B $_{1-25}$  product from heterogeneous oxidation yields an exclusive fragment at m/z 1,457 resulting from the elimination of hydrosulfinylmethane (CH $_4$ SO). (c) The oxidation mechanisms of Trp by ozonolysis and hydrolysis with hydrolysis mechanism of Met in peptide. (d) Air-liquid interfacial oxidation of SP-B $_{1-25}$  by O $_3$  in the POG monolayer as a function of time. Doubly protonated SP-B $_{1-25}$  products with two oxygen atoms and with three oxygen atoms appear after the droplet is exposed to O $_3$  for 10 s. The triply oxygenated product dominates the FIDI-MS spectrum after exposing the droplet to O $_3$  for 15 s and no further oxidation of the peptide is observed up to 30 s of exposure

is observed up to 30 s of exposure. The FIDI-MS spectra show that the doubly oxygenated product immediately undergoes further oxidation to form the stable product with three oxygen atoms.

The FIDI collision induced dissociation (CID) spectrum (FIDI-MS<sup>2</sup>) of the product at m/z 1489 is shown in Fig. 7.4b. The CID of triply oxygenated SP-B<sub>1-25</sub> from heterogeneous oxidation yields an exclusive fragment at m/z 1457 resulting from the elimination of hydrosulfinylmethane (CH<sub>4</sub>SO), which is the characteristic CID fragment of methionine sulfoxide (MetSO) [34]. This indicates that the oxidation of the methionine residue (Met<sub>21</sub>) in SP-B<sub>1-25</sub> results from the heterogeneous ozonolysis. The other two oxygen atoms are added to the tryptophan residue (Trp<sub>9</sub>) forming N-formylkynrenine (NFKyn) (see Section 8.8).

In order to investigate the difference between the interfacial and bulk-phase reactions of  $O_3$  with  $SP-B_{1-25}$ ,  $O_3$  was bubbled into a solution containing  $SP-B_{1-25}$ . Oxidation using the Fenton reaction is also performed to compare the bulk-phase ozonolysis to bulk-phase oxidation by OH radical (see Section 8.8 for detailed analysis). The Fenton reaction yields a series of oxidized  $SP-B_{1-25}$  products with up to 10 oxygen atoms while the bulk-phase  $O_3$  reaction yields dominating products of 3- and 9-oxygenated  $SP-B_{1-25}$ . For the comparison to heterogeneous ozonolysis of  $SP-B_{1-25}$ , the products with three additional oxygen atoms from both reactions are analyzed. Bulk-phase  $O_3$  application yields two triply oxygenated  $SP-B_{1-25}$  products, one with NFKyn (+ 2O) and MetSO (+ 1O), and the other with hydroxy-N-formylkynrenine (HNFKyn, + 3O). The Fenton reaction yields only the product with HNFKyn.

Ozone has limited solubility in water. For a gas-phase concentration of 20 ppm O<sub>3</sub>, the equilibrium concentration of O<sub>3</sub> dissolved in aqueous solution is calculated as 22.6 nM by Henry's law [35]. In addition, O<sub>3</sub> is unstable in water, and rapidly forms secondary oxidants [36]. The major secondary oxidant formed by O<sub>3</sub> in water is OH radical [37]. This implies that two major O<sub>3</sub> oxidation pathways, ozonolysis and hydroxylation, can be observed at the air-liquid interface. The triply oxygenated SP-B<sub>1-25</sub> is formed concomitantly with the formation of the doubly oxygenated SP-B<sub>1-25</sub> after exposing the droplet to  $O_3$  for 5-10 s (Fig. 7.4a). The oxidation mechanisms of Trp and Met in peptide are shown in Fig. 7.4c. The NFKyn can be formed via direct ozonolysis of Trp [38] or hydrolysis of hydroxytryptophan (HTrp) [12]. However, the formation of MetSO from Met occurs primarily by secondary oxidants [39]. The NFKyn of the heterogeneous reaction results from the direct ozonolysis of Trp9, which is located at the hydrophobic N-terminal side of SP-B<sub>1-25</sub>. Met<sub>21</sub>, which likely forms MetSO, is located at the hydrophilic C-terminal site. Intact Cys<sub>8</sub> and Cys<sub>11</sub> support this observed O<sub>3</sub> oxidation of SP-B<sub>1-25</sub>. The rate constant for reaction of Cys with ozone is three orders of magnitude larger than that of Trp and Met [40]. However, the oxidation of Cys to yield sulfonic acid occurs primarily by reactions with secondary oxidants [41], which are not present in significant concentration in the vicinity of the hydrophobic segment of the peptide where Cys<sub>8</sub> and Cys<sub>11</sub> are located. The formation of HNFKyn requires at least one secondary oxidation step (Fig. 7.4c). After NFKyn is formed by either direct ozonolysis or reaction with secondary oxidants, the Met and NFKyn undergo

competitive oxidation to yield MetSO ( $k=1.4\times10^{-11}~{\rm cm^3~molecule^{-1}~s^{-1}}$ ) and HNFKyn ( $k=1.3\times10^{-11}~{\rm cm^3~molecule^{-1}~s^{-1}}$ ) by ROS in the bulk-phase [42]. The heterogeneous ozonolysis of Trp9 induces a change in peptide orientation at the interface. This results in Cys8 and Cys11 being exposed to ROS for oxidation in the bulk phase, which yields total 9-oxygenated SP-B<sub>1-25</sub>.

### 7.3.3 Oxidation of SP- $B_{1-25}$ in POG Monolayer by $O_3$

The interfacial reaction of SP-B<sub>1-25</sub> with ozone was also examined in a monolayer of the non-ionizable lipid POG. Almost identical FIDI-MS spectra are observed compared to the spectra obtained for ozonolysis of SP-B<sub>1-25</sub> without POG except for an  $\sim$ 5 s time delay for initiation of the reaction (Fig. 7.4d). The FIDI-MS spectrum of the SP-B<sub>1-25</sub>/POG droplet is dominated by the triply oxygenated product after 15 s of exposure. No further oxidation of the peptide is observed up to 30 s exposure.

The observed time delay of the reaction provides a critical clue regarding the location of SP-B $_{1-25}$  in the monolayer. From the FIDI-MS spectra, it takes  $\sim$ 10–20 s for POPG at the air-liquid interface to be consumed by O $_3$  (Fig. 7.3a). Both POG and POPG possess a palmitic acid chain and an oleic acid chain, the latter of which reacts with O $_3$ . Under the assumption that the reactivity of POG is similar to that of POPG, the initiation of the SP-B $_{1-25}$  ozonolysis is expected after the droplet is exposed to O $_3$  for 10 – 20 s, if the peptide is completely shielded by lipid acyl chains. However, the observed short time delay of the initiation of SP-B $_{1-25}$  ozonolysis suggests that the peptide competes directly with POG for reaction with O $_3$ . This is consistent with a picture in which the peptide is colocated at the air-liquid interface with POG at the surface of the droplet.

# 7.3.4 Interactions of SP- $B_{1-25}$ in a Lipid Monolayer

We carried out MD simulations for the POPG monolayer and POG monolayer in a water box for 2.0 ns with four different surface densities (55, 60, 65, and  $70 \text{ Å}^2/\text{lipid}$ ), which are reported as a proper density range for pulmonary surfactant function from previous theoretical studies [43, 44, 45]. Figure 7.5 shows the atomic density profiles of oxygen atoms of water molecules, saturated carbon atoms, and unsaturated carbon atoms of lipid acyl chains along  $\pm \Delta z$ , which is z-direction relative to the averaged phosphorous atom of POPG or hydroxyl hydrogen of POG. The POPG monolayer and POG monolayer exhibit almost identical atomic density profiles. Slightly stronger interaction between POPG and water is observed from their larger area of overlapping density ( $\sim$ 1.6 times). This is due to the strong ion-dipole interactions between POPG phosphate group and water molecules, which is absent from the POG monolayer. The water density at the double bond of POPG (5–20 Å) is  $\sim$ 0.0005 atom/Å<sup>3</sup>, which is  $\sim$ 70 times less dense than in the bulk-phase

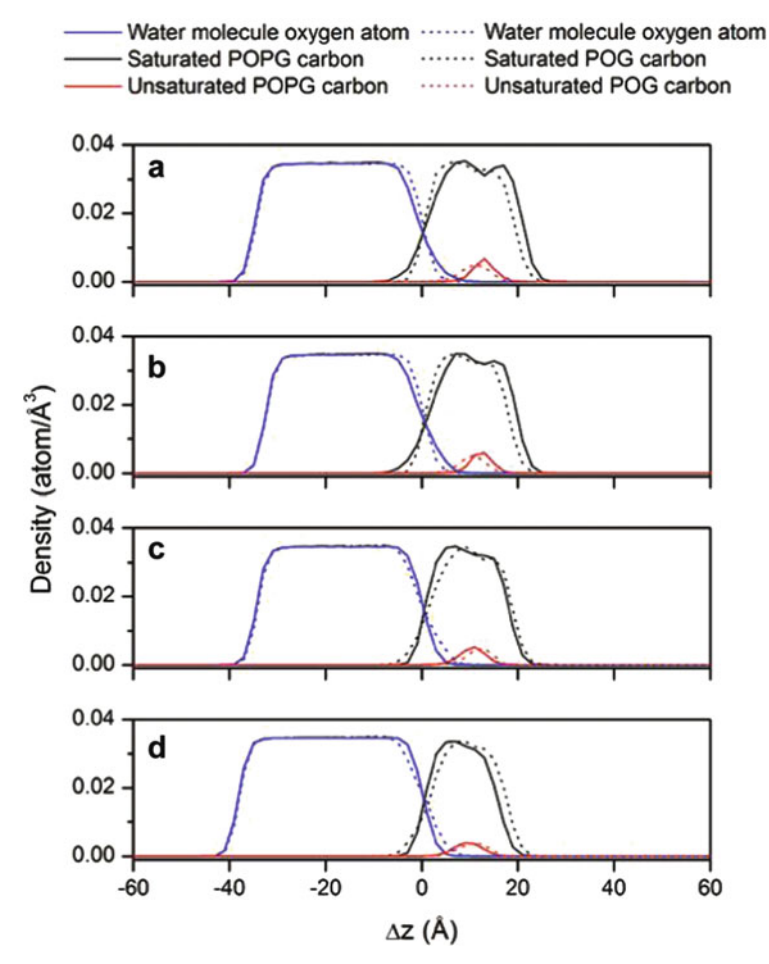


**Fig. 7.5** Atomic density profiles of POPG monolayer systems (*solid lines*) and POG monolayer systems (*dotted lines*) as a function of  $\Delta z$ , where the air/liquid interface is 0, and proceeding *left* to *right* from the water to the lipid layer. The lipid surface densities are (**a**) 55 Å<sup>2</sup>/lipid, (**b**) 60 Å<sup>2</sup>/lipid, (**c**) 65 Å<sup>2</sup>/lipid, and (**d**) 70 Å<sup>2</sup>/lipid. *Blue lines* denote the density profiles of oxygen atoms of water molecules, *black lines* denote that of saturated carbons of lipid acyl chains, and *red lines* denote that of unsaturated carbons of lipid acyl chains

( $\sim$ 0.035 atom/Å<sup>3</sup>). The low water concentrations around the double bond explains the experimental observation of the intermediates and metastable products from heterogeneous ozonolysis, including SOZ, HHP, and MHP (Fig. 7.3a), which are difficult to observe in water-rich environments [28, 29, 33].

We performed 2.0 ns duration MD simulations of the POG/SP- $B_{1-25}$ /water monolayer with 60 Å $^2$ /lipid surface density as a representative case. The final snapshot in Fig. 7.6a shows that the SP- $B_{1-25}$  is located at the air-liquid interface. The hydrophobicity index of each amino acid (AA) residue in the peptide is shown in

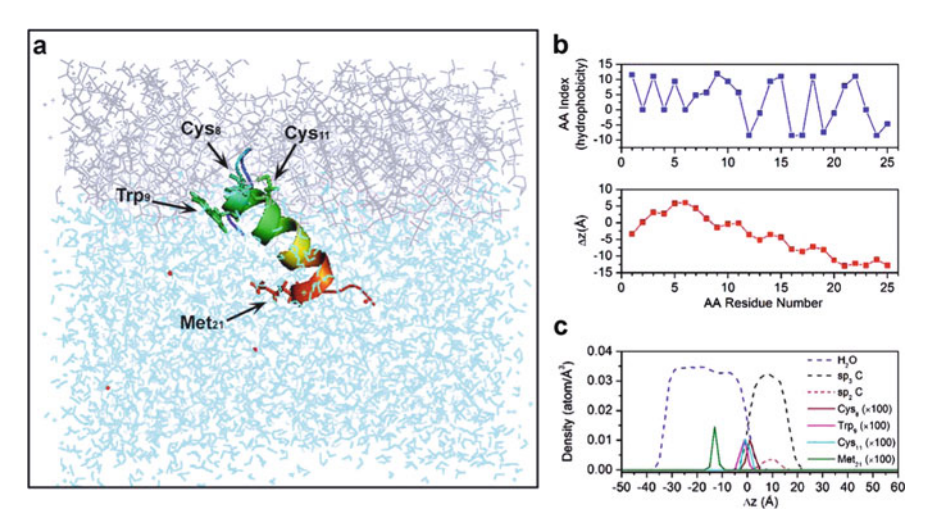


Fig. 7.6 (a) Final snapshot after 2.0 ns of MD simulation of SP-B<sub>1-25</sub> in a POG monolayer at 60 Ų/lipid. The peptide is shown in *rainbow* color (C-terminal: *red*, N-terminal: *blue*). Lipids, water molecules, and chloride are shown in *purple*, *cyan*, and *red*, respectively. (b) AA hydrophobicities [46] (*top*) and  $\Delta z$  of  $C_{\alpha}$  of each residue averaged during the last 0.5 ns of a 2.0 ns duration MD simulation (*bottom*) are plotted as a function of amino acid residue number. The air/water interface is located near  $\Delta z = 0$ . (c) Atomic density profiles of SP-B<sub>1-25</sub> in POG monolayer at 60 Ų/lipid as a function of  $\Delta z$  during the last 0.5 ns of the 2.0 ns MD simulation. *Blue dash line* denotes the density profiles of oxygen atoms of water molecules. *Black* and *red dash lines* denote those of separately summed saturated and unsaturated carbons of lipid acyl chains, respectively. *Wine*, *magenta*, *cyan*, and *olive solid lines* denote the 100 times scaled density profiles of the  $C_{\alpha}$  carbon of Cys<sub>8</sub>, Trp<sub>9</sub>, Cys<sub>11</sub>, Met<sub>21</sub> residues, respectively

Fig. 7.6b (top) [46]. Relatively strong hydrophobicity is found for the N-terminal side of the peptide with Leu, Ile, and Pro residues. In contrast, hydrophilicity is expected from C-terminal side due to Arg, Lys, and Gln residues. The MD simulated  $\Delta z$  of  $C_{\alpha}$  of each residue exhibits a good correlation with the hydrophobicity index. The hydrophobic N-terminal side of the peptide is located above the air-liquid interface, while the hydrophilic C-terminal side is located under the interface (Fig. 7.6b bottom). Figure 7.6c shows the atomic density profiles of oxygen atoms of water molecules as well as saturated and unsaturated carbon atoms of POG acyl chains along  $\Delta z$ . The 100 times scaled atomic density profiles of the  $C_{\alpha}$  carbon of Cys<sub>8</sub>, Trp<sub>9</sub>, Cys<sub>11</sub>, and Met<sub>21</sub> residues are also shown in Fig. 7.6c. The density profiles show a good agreement with the hydrophobicity index. In practice, a low water density is found around Trp<sub>9</sub>, which leads to the formation of NFKyn via direct ozonolysis. The water density around Met<sub>21</sub> is observed to be sufficiently high to expect ROS formation and subsequent reaction to yield MetSO. In contrast, the low water density near Cys<sub>8</sub> and Cys<sub>11</sub> inhibits their oxidation by ROS.

Based on the competitive reactivity of POG and SP- $B_{1-25}$  with  $O_3$  we suggest above that they are colocated at the interface. The MD simulations of SP- $B_{1-25}$  in a lipid monolayer support our interpretation. Trp<sub>9</sub> and Met<sub>21</sub> of SP- $B_{1-25}$  lie below

7.4 Conclusions 119

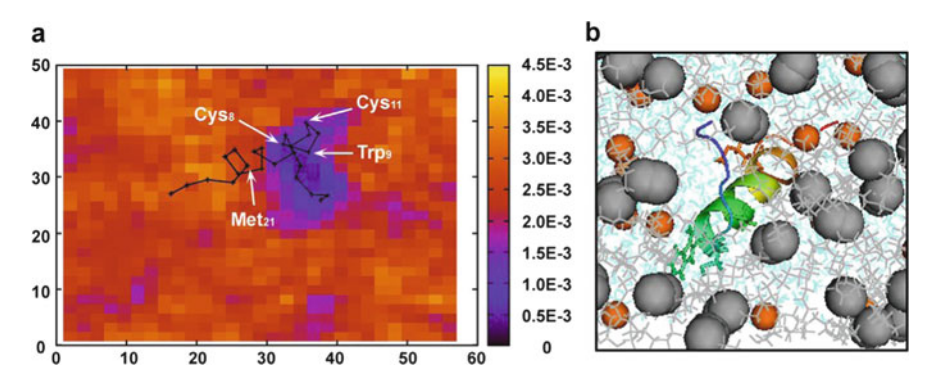


Fig. 7.7 (a) The xy-projected density profiles of saturated carbon atoms of lipid acyl chains from MD simulations is shown with colors and the averaged positions of  $C_{\alpha}$  carbons of  $SP-B_{1-25}$  in the POG monolayer is shown with a *black line* (each residue is shown with cross). (b) Top view of final snapshot after 2.0 ns of MD simulation of  $SP-B_{1-25}$  in a POG monolayer at 60 Å<sup>2</sup>/lipid. The peptide is shown in *rainbow color* (C-terminal: *red*, N-terminal: *blue*). Lipids and water molecules are shown in *gray* and *cyan*, respectively. *Black spheres* denote unsaturated carbon atoms of lipid acyl chains, and *orange spheres* denote hydroxyl oxygen atoms

(in the z-direction) the location of the lipid double bonds (Fig. 7.6c). Figure 7.7a shows the xy-projected density profiles of saturated carbon atoms of lipid acyl chains with the averaged positions of  $C_{\alpha}$  of AA residues of SP-B<sub>1-25</sub>. It is noteworthy that lipid acyl chains do not shelter the peptide at the air-liquid interface. The top view of the MD simulation final snapshot in Fig. 7.7b illustrates that SP- $B_{1-25}$  is not shielded by unsaturated carbons (black spheres) of lipids. The strong amphiphilic characteristic and the large surface area of SP-B<sub>1-25</sub> cause the peptide to position itself at the air-liquid interface where it displaces lipids. As a result, SP-B<sub>1-25</sub> forms an island in a lipid monolayer that causes the hydrophobic portion of the peptide to be exposed to O<sub>3</sub> despite its location below the position of lipid double bonds. We also simulated SP-B<sub>1-25</sub> in the POPG monolayer. The peptide penetrates deeper into the POPG monolayer due to the strong electrostatic interaction between the cationic AA residues (Arg<sub>12</sub>, Arg<sub>17</sub>, and Lys<sub>16</sub>) and the anionic phosphate group of POPG (Figs. 7.8a, b), which agrees with previous simulations in anionic lipid monolayers [43, 47]. SP- $B_{1-25}$  forms an island in the POPG monolayer and the anhydrous environments in the lipid monolayer may lead SP-B<sub>1-25</sub> to be more susceptible to direct ozonolysis than to modification by ROS (Figs. 7.8c and 7.9).

#### 7.4 Conclusions

Summarizing, to understand the unique chemistry at a model lung surfactant/air interface under  $O_3$  exposure, we utilized the FIDI-MS technique to analyze chemical reactions at this interface. In the FIDI-MS spectra, oxidized products distinct from those formed in the bulk-phase were observed from SP-B<sub>1-25</sub> alone and imbedded in the POG monolayer. We also carried out MD simulations that

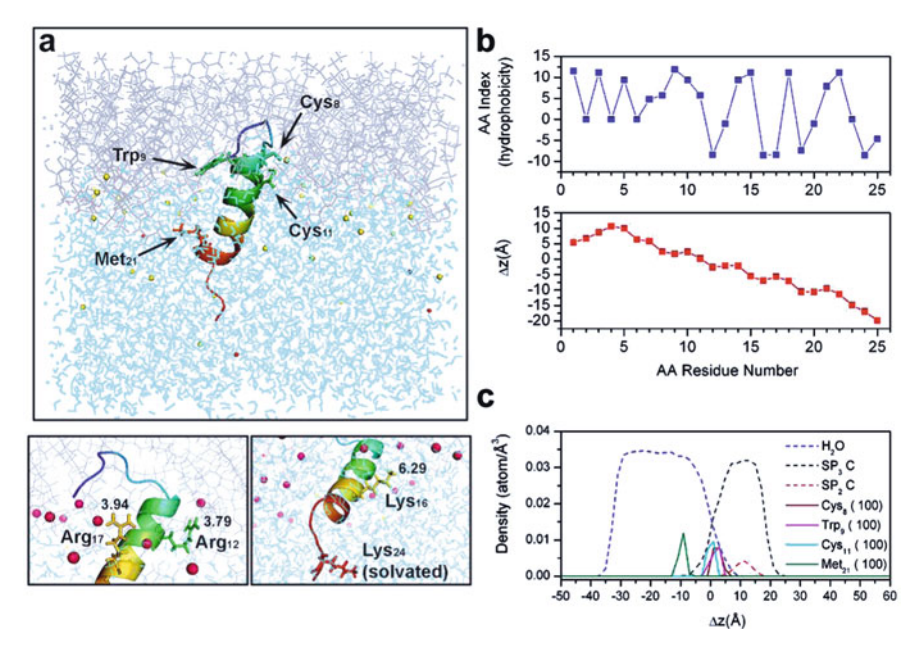
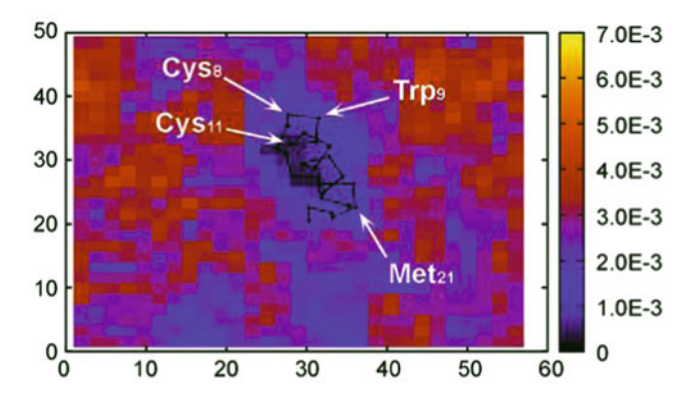


Fig. 7.8 (a) Final snapshot after 2.0 ns MD simulation of SP-B<sub>1-25</sub> in POPG monolayer at 60 Å<sup>2</sup>/lipid is shown at *top panel*. The peptide is shown in *rainbow color* (C-terminal: *red*, N-terminal: *blue*), lipids in *gray*, water molecules in *cyan*, and chloride ions in *red*. Lower *left* and *right* show that Arg residues and Lys residues (displayed with *sticks*) are interacting with phosphate groups of lipids, respectively. (Phosphorous atoms are in *magenta*.) (b) AA index for hydrophobicity scale [46] (*top*) and  $\Delta z$  of  $C\alpha$  of each residue averaged during the last 0.5 ns trajectory of 2.0 ns duration MD simulations (*bottom*) are plotted as a function of amino acid residue number. The air/water interface is located near  $\Delta z = 0$ . (c) Atomic density profiles of SP-B<sub>1-25</sub> in POG monolayer at 60 Å<sup>2</sup>/lipid as a function of  $\Delta z$  during the last 0.5 ns of the 2.0 ns MD simulation. *Blue dash line* denotes the density profiles of oxygen atoms of water molecules. *Black and red dash lines* denote those of saturated and unsaturated carbons of lipid acyl chains, respectively. *Wine*, *magenta*, *cyan*, and *olive solid lines* denote the 100 times scaled density profiles of the  $C_{\alpha}$  carbon of Cys<sub>8</sub>, Trp<sub>9</sub>, Cys<sub>11</sub>, and Met<sub>21</sub> residues, respectively

provide additional insights into the interactions between lipids,  $SP-B_{1-25}$ , and water molecules in the interfacial region. In these simulations the location of  $SP-B_{1-25}$  relative to the lipids provides a rationalization for the experimental observation that the peptides compete with the lipids for reaction with  $O_3$ .

The oxidation of PS causes surface dysfunction in adsorption, respreading, and reduction of surface tension [14, 48]. Once the O<sub>3</sub> traverses the air-liquid interface, it decays rapidly concomitant with the formation of ROS in regions with high water densities [36]. However, due to the high reactivity with PS at the interface, it has been thought that little or none of the O<sub>3</sub> can penetrate the PS monolayer to attack the epithelium cells below [49]. Instead of direct attack by O<sub>3</sub> and its ROS derivates, secondary oxidized products of PS, such as HHP, have been expected to yield cellular damage [49]. We have found that more than 60 % of the heterogeneous

7.4 Conclusions 121



**Fig. 7.9** The *xy*-projected density profiles of saturated carbon atoms of lipid acyl chains is shown with colors and the averaged positions of  $C_{\alpha}$  carbons of SP-B<sub>1-25</sub> in the POPG monolayer is shown with a *black line* (each residue is shown with *cross*)

oxidation products of POPG by O<sub>3</sub> are peroxides. These products, which are more water soluble than others, eventually dissolve into the water droplet. Then, rapid decomposition of products yields reactive oxygen species (ROS) [29] which causes cellular damage below the monolayer.

Possible protection of SP-B from homogeneous oxidation by PS lipids has been suggested in an earlier study [12]. However, we have shown that  $SP-B_{1-25}$  is oxidized directly by heterogeneous reaction with  $O_3$  since it is located at the air-liquid interface with significant exposure to  $O_3$ . The homogeneous oxidation of SP-B by ROS is known to reduce its surface activity and function [12, 14]. We have observed fast formation of NFKyn from the direct ozonolysis of  $Trp_9$  at the hydrophobic N-terminal side of  $SP-B_{1-25}$ . The oxidized residue reduces the hydrophobicity of the N-terminal side of the peptide. This induces a change in peptide orientation in the monolayer that results in NFKyn,  $Cys_8$ , and  $Cys_{11}$  being exposed to ROS for further oxidation. As a result, further oxidation of  $SP-B_{1-25}$  by a heterogeneous reaction with  $O_3$  produces effects similar to those seen in homogeneous oxidation.

Our findings present a detailed explanation for the mechanisms of the possible damage to the pulmonary system by ROS or direct ozone exposure. Further studies with a more elaborate model system comprising SP-B, SP-C, and various lipids could further clarify the effect of other environmental exposures, such as smoking and airborne particles, on the lung surfactant system.

Acknowledgments The research described in this paper was carried out at the Beckman Institute and the Noyes Laboratory of Chemical Physics at the California Institute of Technology, the Computational NanoBioTechnology Laboratory at Georgia Institute of Technology and Jet Propulsion Laboratory under a contract with the National Aeronautics and Space Administration and funded through the Director's Research and Development Fund. We appreciate the support provided by the Beckman Institute Mass Spectrometry Resource Center. Partial support was also provided by the National Science Foundation (NSF) under grant No. CHE-0416381 (JLB, PI) and the National Cancer Institute under grant No. 5U54 CA119347 (JRH, PI).

### **Bibliography**

- Anseth, J.; Goffin, A.; Fuller, G.; Ghio, A.; Kao, P. Am. J. Respir. Cell Mol. Biol. 2005, 33, 161–168.
- 2. Halliwell, B.; Gutteridge, J. Biochem. J. 1984, 219, 1-14.
- 3. Stansfield, A.; Jump, Z.; Sodlosky, S.; Rappaport, S.; Edelman, N.; Haldorsen, J.; Javed, T.; Martin, C.; Margulies, E. *ed. Maple, D*; American Lung Association National Headquarters: New York, 2008.
- 4. Vangolde, L.; Batenburg, J.; Robertson, B. Physiol. Rev. 1988, 68, 374–455.
- 5. Schram, V.; Hall, S. Biophys. J. 2004, 86, 3734–3743.
- 6. Hawco, M.; Davis, P.; Keough, K. J. Appl. Physiol. 1981, 51, 509-515.
- 7. Perez-Gil J.; Keough K. Biochim. Biophys. Acta-Mol. Basis Dis. 1998, 1408, 203–217.
- Clark J.; Wert S.; Bachurski C.; Stahlman M.; Stripp B.; Weaver T.; Whitsett J. Proc. Natl. Acad. Sci. U. S. A. 1995, 92, 7794–7798.
- 9. Perez-Gil, J. Biophys. J. 2008, 94, 1542–1543.
- 10. Pryor, W.; Das, B.; Church, D. Chem. Res. Toxicol. 1991, 4, 341-348.
- Uppu, R. M.; Cueto, R.; Squadrito, G. L.; Pryor, W. A. Arch. Biochem. Biophys. 1995, 319, 257–266.
- 12. Manzanares, D.; Rodriguez-Capote, K.; Liu, S. Y.; Haines, T.; Ramos, Y.; Zhao, L.; Doherty-Kirby, A.; Lajoie, G.; Possmayer, F. *Biochemistry* **2007**, 46, 5604–5615.
- 13. Andersson, S.; Kheiter, A.; Merritt, T. A. Lung 1999, 177, 179-189.
- Rodriguez-Capote, K.; Manzanares, D.; Haines, T.; Possmayer, F. *Biophys. J.* 2006, 90, 2808–2821.
- 15. Grimm, R. L.; Hodyss, R.; Beauchamp, J. L. Anal. Chem. 2006, 78, 3800–3806.
- 16. Voss, L. F.; Hadad, C. M.; Allen, H. C. J. Phys. Chem. B 2006, 110, 19487–19490.
- 17. Mundy, C. J.; Kuo, I. F. W. Chem. Rev. 2006, 106, 1282-1304.
- Enami, S.; Hoffmann, M. R.; Colussi, A. J. Proc. Natl. Acad. Sci. U. S. A. 2008, 105, 7365–7369.
- 19. Enami, S.; Hoffmann, M. R.; Colussi, A. J. J. Phys. Chem. B 2008, 112, 4153–4156.
- 20. Grimm, R. L.; Beauchamp, J. L. J. Phys. Chem. B 2003, 107, 14161–14163.
- 21. Grimm, R. L.; Beauchamp, J. L. J. Phys. Chem. B 2005, 109, 8244-8250.
- Takamoto, D. Y.; Lipp, M. M.; von Nahmen, A.; Lee, K. Y. C.; Waring, A. J.;
   Zasadzinski, J. A. *Biophys. J.* 2001, 81, 153–169.
- 23. Bruni, R.; Taeusch, H. W.; Waring, A. J. Proc. Natl. Acad. Sci. U. S. A. 1991, 88, 7451–7455.
- Longo, M. L.; Bisagno, A. M.; Zasadzinski, J. A. N.; Bruni, R.; Waring, A. J. Science 1993, 261, 453–456.
- 25. MacKerell, A.D.; Bashford, D.; Bellott, M.; Dunbrack, R. L.; Evanseck, J. D.; Field, M. J.; Fischer, S.; Gao, J.; Guo, H.; Ha, S.; Joseph-McCarthy, D.; Kuchnir, L.; Kuczera, K.; Lau, F. T. K.; Mattos, C.; Michnick, S.; Ngo, T.; Nguyen, D. T.; Prodhom, B.; Reiher, W. E.; Roux, B.; Schlenkrich, M.; Smith, J. C.; Stote, R.; Straub, J.; Watanabe, M.; Wiorkiewicz-Kuczera, J.; Yin, D.; Karplus, M. J. Phys. Chem. B 1998, 102, 3586–3616.
- 26. Plimpton, S. J. Comput. Phys. 1995, 117, 1-19.
- Hockney, R. W.; Eastwood, J. W. Computer simulation using particles; McGraw-Hill: New York, 1981.
- Karagulian, F.; Lea, A. S.; Dilbeck, C. W.; Finlayson-Pitts, B. J. *Phys. Chem. Chem. Phys.* 2008, 10, 528–541.
- 29. Santrock, J.; Gorski, R. A.; Ogara, J. F. Chem. Res. Toxicol. 1992, 5, 134–141.
- 30. Rivera, J. L.; Starr, F. W.; Paricaud, P.; Cummings, P. T. J. Chem. Phys. 2006, 125, 8.
- 31. Ghosh, A.; Smits, M.; Bredenbeck, J.; Bonn, M. J. Am. Chem. Soc. 2007, 129, 9608.
- 32. Lai, C. C.; Yang, S. H.; Finlayson-Pitts, B. J. Langmuir 1994, 10, 4637–4644.
- 33. Pryor, W. A. Am. J. Clin. Nutr. 1991, 53, 702-722.
- Clauser, K. R.; Hall, S. C.; Smith, D. M.; Webb, J. W.; Andrews, L. E.; Tran, H. M.;
   Epstein, L. B.; Burlingame, A. L. Proc. Natl. Acad. Sci. U. S. A. 1995, 92, 5072–5076.

Bibliography 123

35. Seinfeld, J. H.; Pandis, S. N. Atmospheric chemistry and physics: From air pollution to climate change; John Wiley & Sons: New York, 1998.

- 36. von Gunten, U. Water Res. 2003, 37, 1443-1467.
- 37. Pryor, W. A. Free Radic. Biol. Med. 1994, 17, 451-465.
- 38. Pryor, W. A.; Uppu, R. M. J. Biol. Chem. 1993, 268, 3120-3126.
- 39. Schoneich, C. BBA-Proteins Proteomics 2005, 1703, 111-119.
- 40. Pryor, W. A.; Giamalva, D. H.; Church, D. F. J. Am. Chem. Soc. 1984, 106, 7094-7100.
- 41. Berlett, B. S.; Stadtman, E. R. J. Biol. Chem. 1997, 272, 20313–20316.
- Buxton, G. V.; Greenstock, C. L.; Helman, W. P.; Ross, A. B. J. Phys. Chem. Ref. Data 1988, 17, 513–886.
- 43. Kaznessis, Y. N.; Kim, S.; Larson, R. G. J. Mol. Biol. 2002, 322, 569-582.
- Baoukina, S.; Monticelli, L.; Risselada, H. J.; Marrink, S. J.; Tieleman, D. P. Proc. Natl. Acad. Sci. U. S. A. 2008, 105, 10803–10808.
- 45. Kaznessis, Y. N.; Kim, S. T.; Larson, R. G. Biophys. J. 2002, 82, 1731–1742.
- 46. Kawashima, S.; Ogata, H.; Kanehisa, M. Nucleic Acids Research 1999, 27, 368-369.
- 47. Freites, J. A.; Choi, Y.; Tobias, D. J. Biophys. J. 2003, 84, 2169–2180.
- 48. Gilliard, N.; Heldt, G. P.; Loredo, J.; Gasser, H.; Redl, H.; Merritt, T. A.; Spragg, R. G. J. Clin. Invest. 1994, 93, 2608–2615.
- 49. Pryor, W. A. Free Radic. Biol. Med. 1992, 12, 83-88.

# Chapter 8 Appendices

**Abstract** This chapter provides appendices to support the understanding of readers. Appendices A to D contain supporting information of Chapter 2; appendices E and F contain supporting information of Chapter 3; and appendices G and H contain supporting information of Chapter 7.

# 8.1 Appendix A: Discussions on Coarse-Graining of Time- and Length-Scale in Monte Carlo Simulations for AN-OPE SAM

In order to connect from the atomistic quantum level to macroscopic level, it is necessary to coarse grain the system. We discuss below some of the consequences of the coarse graining on time- and length-scale.

### 8.1.1 Time-Scale

From the NN model, the energies required to initiate the P-to-T transition under 1.2 V/Å and T-to-P transition without external field are  $\Delta E^{\ddagger}=11.58\,\mathrm{kcal/mol}$  and  $\Delta E^{\ddagger}=12.52\,\mathrm{kcal/mol}$ , respectively. Assuming  $\Delta S^{\ddagger}=k_B\ln(2500)$ , from Eyring equation,  $k=k_BT/h\exp\left(\Delta S^{\ddagger}/k_B\right)\exp\left(-\Delta E^{\ddagger}/k_BT\right)$ , we obtain  $\tau_0=1/k=1.9\times10^{-8}\,\mathrm{s}$  and  $\tau_0=9.3\times10^{-8}\,\mathrm{s}$  for P-to-T case and T-to-P case, respectively. By comparing these values with MC results of  $\tau_0=274$ , 193 MCS and  $\tau_0=357$ , 135 MCS, we can estimate 1 MCS as an order of  $\sim10^{-13}\,\mathrm{s}$ . Thus, in actual unit, the sweep rates of  $1\times10^{-8}\,\mathrm{V/MCS}$ ,  $4\times10^{-8}\,\mathrm{V/MCS}$ , and  $2\times10^{-7}\,\mathrm{V/MCS}$  are around  $1\times10^5\,\mathrm{V/s}$ ,  $4\times10^5\,\mathrm{V/s}$ , and  $2\times10^6\,\mathrm{V/s}$ , which are  $\sim10^6\,\mathrm{times}$  faster than the experimental conditions.

### 8.1.2 Length-Scale

We found that in our simulations, the total time taken for the complete P-to-T transition under the constant external field of F,  $t_{P-to-T}(F)$  is highly overestimated when

F is near  $F_c$  due to the periodic boundary condition. It is a well known fact that the finite-size effect in simulations becomes serious near the critical point of phase transition [1]. This artifact makes the transition occur at once after the bias voltage is increased sufficiently, and finally yields a narrower range of NDR (Fig. 8.1).

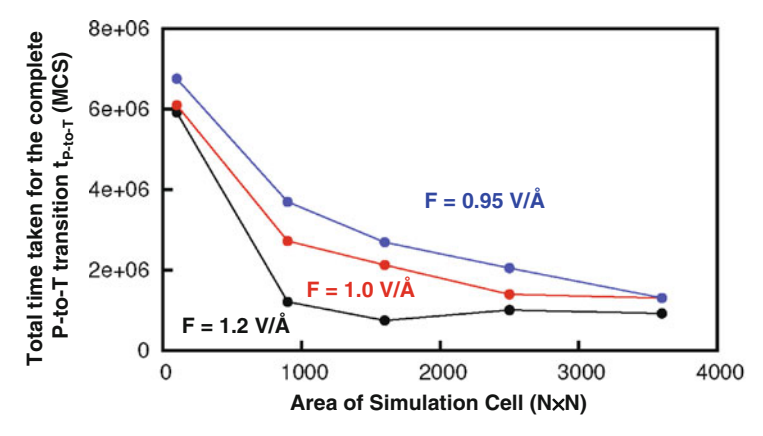


**Fig. 8.1** Total time taken for the complete P-to-T transition,  $t_{\text{P-to-T}}$  by varying the area of the periodic simulation cell as  $10 \times 10 = 100$ ,  $30 \times 30 = 900$ ,  $40 \times 40 = 1600$ ,  $50 \times 50 = 2500$ , and  $60 \times 60 = 3600$ . Black line denotes the change of  $t_{\text{P-to-T}}$  under the external field of F = 1.2 V/Å, red line denotes the change of  $t_{\text{P-to-T}}$  scaled by 10 under the external field of F = 1.0 V/Å, and blue line denotes the change of  $t_{\text{P-to-T}}$  scaled by 15 under the external field of F = 0.95 V/Å. The  $t_{\text{P-to-T}}$  value is converged at the area of 900–1600 and 2500–3600 when F = 1.2 V/Å and 1.0 V/Å, respectively. When F = 0.95 V/Å, the  $t_{\text{P-to-T}}$  value is not converged until the area of 3600. This infers that we need much larger simulation cell to get the right converged value of  $t_{\text{P-to-T}}$  as the F approaches to the critical field,  $F_c = 0.56 \text{ V/Å}$ . Otherwise, we will get the overestimated value of  $t_{\text{P-to-T}}$  near  $F_c$ 

## 8.2 Appendix B: Effect of Molecular Fluctuations on the Electrical Conductivity of AN-OPE SAM

Electrical conductivity through the AN-OPE is estimated using the fitting equation of Fig. 2.8 based on the twisting angles,  $\chi_1$  and  $\chi_2$ , from MD simulations with  $(10 \times 10)$  unit cell. We mimicked two sets of voltage sweep cycle by following MD procedures:

- (a) QM optimized P structure is employed for the initial structure, then, annealed in the absence of external field. The conformations are almost co-planar as predicted from QM calculation with a well-developed HB network. Estimated conductivity is large with the averaged value of 0.035.
- (b) External field of 1.2 V/Å is turned on to the final structure of (a). The SAM structure is partially disordered and  $\chi_1$  has largest probability at 90°. Estimated conductivity 3.21 times decreases to 0.011.

8.2 Appendix B 127

(c) QM optimized T structure is employed for the initial structure, then, annealed under the external field of 1.2 V/Å. Structural fluctuation allows AN-OPEs to have ~90° twisted conformations, resulting the loss of HB network. SAM is well-ordered. Estimated conductivity remains same to (b) with the value of 0.011.

- (d) External field is turned down from the final structure of (a). SAM forms a pretty disordered structure and  $\chi_1$  has no strongly preferring angle. Estimated conductivity 1.23 times increases to 0.013.
- (e) The final structure from step (d) is annealed in the absence of external field. SAM still has disordered structure, however, probability at  $\chi_1 = 90^{\circ}$  slightly decreases. Estimated conductivity is slightly increases to 0.014.
- (f) External field of 1.2 V/Å is re-turned on to the final structure of (e). Structure and twisting angle is similar to (b), however, it is a bit more disordered. Thus, estimated conductivity is a bit smaller than (b) with the value of 0.010.
- (g) The final structure from step (d) is annealed under the external field of 1.2 V/Å, and the SAM has still similar structure to (f). Estimated conductivity remains same to (f) with the value of 0.010.
- (h) External field is re-turned down from the final structure of (g). SAM forms a more disordered structure to (d). Thus, estimated conductivity smaller than (d) with the value of 0.012.
- (i) The final structure from step (h) is annealed in the absence of external field. SAM still has a disordered structure, however, probability at  $\chi_1 = 90^{\circ}$  slightly decreases. Estimated conductivity is 1.05 times increases to 0.013.

The conductivities during the second cycle (f–i) shows  $\sim$ 6% smaller values compared to the conductivities during the first cycle (b–e). These results are shown at Fig. 8.2.

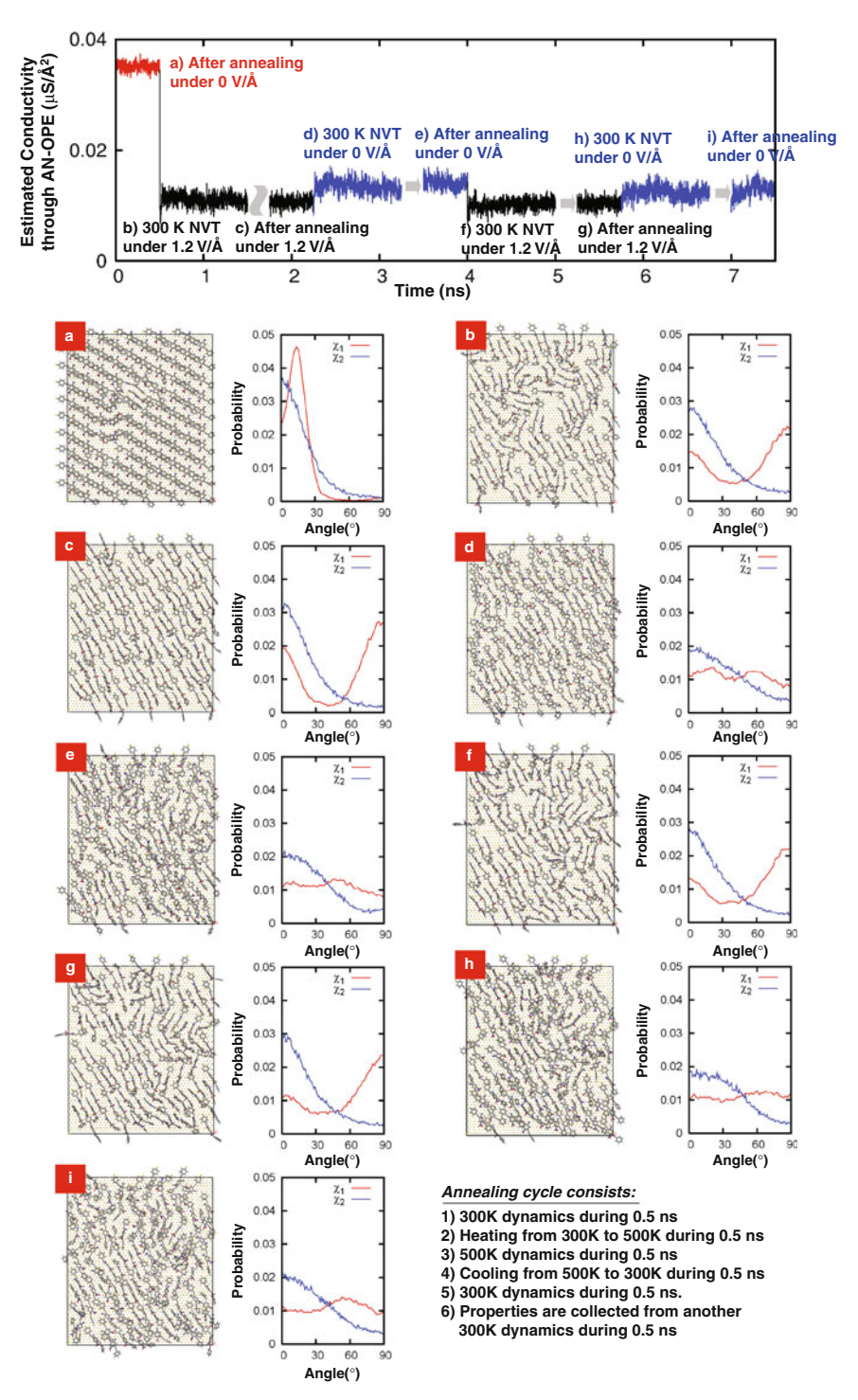


Fig. 8.2 (top panel) Electrical conductivity through the AN-OPE is estimated based on the twisting angles from MD simulations with  $(10 \times 10)$  unit cell. (bottom panels) The final snapshot after each step is shown with the populations of  $\chi_1$  and  $\chi_2$ , which are averaged during the last 0.5 ns dynamics

8.3 Appendix C 129

### 8.3 Appendix C: NDR in Other OPE-derivative Systems

We investigated that how our mechanism predicts the possibility of NDR in other systems containing other OPE derivatives.

#### 8.3.1 Bare OPE

For bare OPE (B-OPE) with no functional groups our mechanism would suggest that there is no NDR effect, since the lack of functional groups leads to only a small molecular dipole moment to interact with the external field and there is no mechanism for the increased applied field to convert from the high conductance P phase to the low conductance T phase. Reference [2] shows the experimental data on B-OPE, which shows no NDR effect.

### 8.3.2 Nitro OPE

We calculated that the SAM of 5'-nitro monosubstituted OPE system (N-OPE) on Au (111) surface. We figured out that N-OPE also can have two conformations of P and T on the SAM by forming weak HB networks along  $\begin{bmatrix} 11\bar{2}0 \end{bmatrix}$  direction and  $\begin{bmatrix} 10\bar{1}0 \end{bmatrix}$  direction, respectively. The lack of amino group makes NO<sub>2</sub> form a weak HB with the positive aromatic H atoms of the adjacent molecules (Fig. 8.3).

The twist angles are  $\chi=4^\circ$  and  $\chi=163^\circ$  and the heights of the terminal ring of are 8.73 Å and 7.63 Å for P and T, respectively. These are almost identical to the values in AN-OPE case. Therefore, we expect the conductance ratio for N-OPE to be very similar to AN-OPE.

From PBE DFT calculations, P is more stable than T by 6.57 kcal/mol when no external field is applied. The dipole moment component in the [0001] direction are 3.83 (2.01) debye for P and 6.61 (3.86) debye for T from the analysis of Mulliken charges, while the parenthetical values are from quantum mechanical wave-function. Thus, the favorable state is changed from P to T as the external field is applied (Fig. 8.4). This suggests that the N-OPE also undergoed conformational change from P to T as the bias voltage increases. The critical field  $F_c$  is calculated as 0.49 V/Å and 0.74 V/Å when using dipole moments from Mulliken charge and QM wave-function, respectively. Since these are in the range of the Fc in AN-OPE system (0.56 V/Å), the critical bias voltage where NDR occurs to be similar to the critical bias voltage of AN-OPE system of  $\sim$ 0.6 V. Reference [2] also shows the experimental data on N-OPE, which shows a well-defined hysteretic NDR at  $\sim$ 0.6 V as predicted from our calculations.

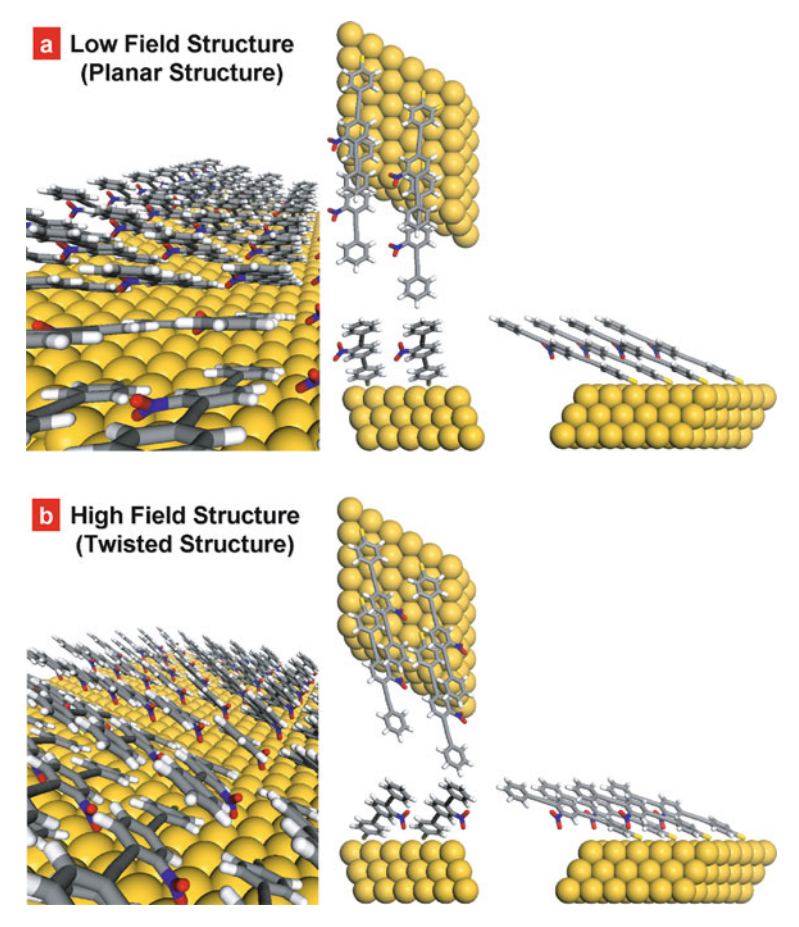


**Fig. 8.3** (a) Optimized geometry for the low field structure (P) of N-OPE SAM. Here [0001] is the surface normal and the views are along z-axis ( $upper\ middle$ ), y-axis ( $lower\ middle$ ), and x-axis ( $lower\ right$ ). The left picture is a perspective along the axis of one plane of molecules. The weak hydrogen bonding network is aligned along the  $\begin{bmatrix} 11\bar{2}0 \end{bmatrix}$  direction. (b) Optimized geometry for the high field structure (T) of N-OPE SAM. Here  $\begin{bmatrix} 0001 \end{bmatrix}$  is the surface normal and the views are along z-axis ( $upper\ middle$ ), y-axis ( $lower\ middle$ ), and x-axis ( $lower\ right$ ). The left picture is a perspective along the axis of one plane of molecules. The weak hydrogen bonding network is aligned along the  $\begin{bmatrix} 10\bar{1}0 \end{bmatrix}$  direction

8.5 Appendix E 131

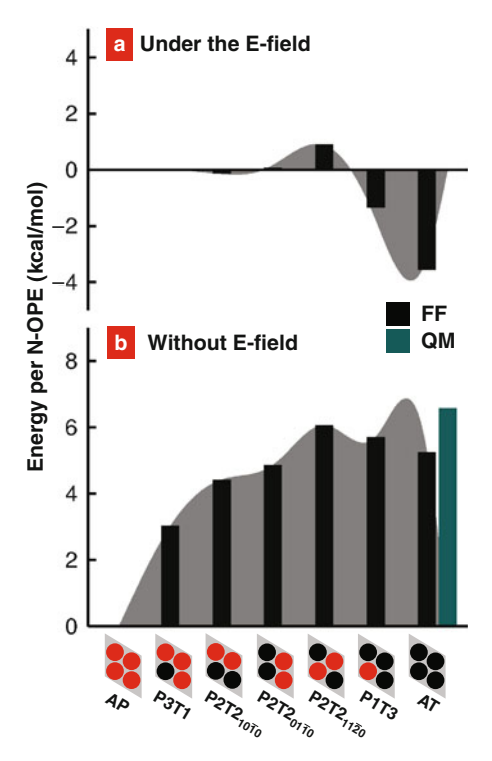


**Fig. 8.4** (a) Energies of various conformations of N-OPE relative to the AP conformation computed with a 0.6 V/Å external field from FF calculations (*black histograms*). (b) Energies of various conformations of N-OPE relative to the AP conformation computed with no external field from FF calculations (*black histograms*), and OM calculations (*green histograms*)

## **8.4** Appendix D: Conversion Factor Between External Electric Field and Bias Voltage

To connect the NEGF results and MC simulations, we need to convert the magnitude of external field, F, into the bias voltage, V. Since the critical bias voltage  $V_c$  is observed as  $\sim$ 0.6 V from the experiment and the critical field  $F_c$  is 0.56 V/Å in our NN model, we set the linear coefficient c as 0.93 Å<sup>-1</sup>, which is defined by F/V.

# 8.5 Appendix E: Mulliken Charge Distributions of Bistable [2]Rotaxane Molecular Switch Depending on CBPQT<sup>4+</sup> Ring's Position

The shuttling motion of charge accepting cyclobis-(paraquat-*p*-phenylene) (CBPQT<sup>4+</sup>) between the charge donating stations such as tetrathiafulvalene (TTF) and 1,5-dioxynaphthalene (DNP) moieties is governed by the charge transfer

### a) Backbone

Fig. 8.5 Structures of (a) backbone part and (b) CBPQT $^{4+}$  ring part with numbered atoms. The assigned numbers on the atoms are associated with the partial charge distribution data shown in Table 8.1, 8.2, and 8.3

amount between the ring and the backbone. Since the potential energy surface that the CBPQT $^{4+}$  ring suffers while traveling along the backbone has a large dependency on the local charge distribution of the rotaxane molecule, we performed DFT calculations for 9 different ring's positions by varying the oxidation states, 0, +1, and +2. Computed Mulliken charge distributions are tabulated in this section.

**Table 8.1** Partial charge distribution of neutral rotaxane when the center of mass of the CBPQT<sup>4+</sup> ring moves from z = 10.92 Å (TTF side) to z = 44.83 Å

2 = 10.92 Å         1 = 10.92 Å         2 = 10.92 Å         2 = 10.92 Å         1 = 10.92 Å	(DNP side)	side)	)							,	)			,		
-0.5382         C25         -0.3287         C49         -0.1555         H73         0.1454         C97         -0.1001         C121         -0.1305         H145         0.1753         C169           0.0386         S26         0.2329         C50         -0.0665         H74         0.1450         H98         0.1234         C122         0.1089         H146         0.1392         C170           0.0860         S26         -0.2391         C51         -0.0662         H76         0.1136         C101         -0.1694         H149         0.1390         H171           0.0809         S29         0.2279         C53         -0.0660         H77         0.1135         C101         -0.1075         N125         -0.1694         H179         0.132         C101         -0.1075         N125         H179         0.1303         H174         0.1304         H179         0.132         0.0460         D100         H171         0.1132         H102         0.1251         C124         0.1169         H179         0.1132         H102         0.1251         C124         0.1169         H117         0.1132         H117         0.1132         H117         0.1132         H117         0.1132         H117         0.1130	= 1(	).92 Å														
0.0386         S26         0.2392         C50         -0.0643         H74         0.1450         H98         0.1234         C122         0.1089         H146         0.1392         C170           0.0644         C27         -0.0631         C51         -0.0645         H75         0.1138         C99         0.0338         C123         -0.1530         H147         0.1390         H171           0.0809         S29         -0.2731         C52         -0.0664         H76         0.1136         C10         -0.0490         H149         0.1309         H171           0.0809         S29         0.2279         C53         -0.0664         H78         0.1136         C10         -0.1054         C126         -0.1694         H189         0.1251         C126         -0.1694         H189         0.1251         H189         0.1251         C126         -0.1694         H199         0.1038         H190         0.1039         H191         0.1169         H199         0.1039         H191         0.1261         H199         0.1261         H190         0.1261         H191         0.1261         H191         0.1262         C177         C178         C178         C16094         H191         0.1276         C179	_	-0.5382	C25	-0.3287	C49	-0.1555	H73	0.1454	C97	-0.1001	C121	-0.1305	H145	0.1753	C169	-0.0964
0.0644         CZ7         -0.2631         CS1         -0.0545         H75         0.1133         C99         0.0338         C123         -0.1530         H147         0.1309         H171           -0.8061         CZ2         -0.0662         H76         0.1136         C100         0.0458         C124         0.1503         H149         0.1206         H172           0.0800         S29         0.0279         C53         -0.0660         H77         0.1135         C101         -0.1075         H149         0.1203         C173           0.0910         C32         0.0469         C56         -0.1512         H80         0.1034         C105         0.0409         C17         0.0499         H149         0.123         C17         0.0499         C17         0.0499         C17         0.0499         C17         0.0499         C17         0.0499         C17         0.01094         H149         0.173         H144         0.1747         C175         0.0499         H144         0.173         H144         0.1747         C175         0.0499         H149         0.173         H144         0.1749         H174         0.179         H144         0.1749         H174         0.179         H144         0.17	2	0.0386	S26	0.2392	C50	-0.0636	H74	0.1450	86H	0.1234	C122	0.1089	H146	0.1392	C170	-0.0997
-0.5061         C28         -0.1531         C52         -0.0662         H76         0.1136         C100         0.0458         C124         0.1503         H148         0.1203         CH73           0.0800         \$29         0.2279         C53         -0.0660         H77         0.1135         C101         -0.1075         N125         -0.1690         H149         0.1203         C173           0.0800         C30         -0.0511         C53         -0.0641         H79         0.1037         H104         0.129         C126         -0.1690         H150         0.1758         N174           -0.1521         C30         -0.0469         C55         -0.1512         H80         0.1037         H104         0.129         C126         -0.1790         H117         0.1195         H118         0.129         C175         0.1784         H117         0.1196         H15         0.1196         H118         0.129         C175         0.178         H118         0.129         C175         0.1196         H118         0.129         C175         0.1196         H18         0.125         C106         0.0199         H118         0.1196         H18         0.1129         C106         0.1199         C126 <t< td=""><td><u>5</u></td><td>0.0644</td><td>C27</td><td>-0.2631</td><td>C51</td><td>-0.0545</td><td>H75</td><td>0.1133</td><td>C39</td><td>0.0338</td><td>C123</td><td>-0.1530</td><td>H147</td><td>0.1390</td><td>H171</td><td>0.1167</td></t<>	<u>5</u>	0.0644	C27	-0.2631	C51	-0.0545	H75	0.1133	C39	0.0338	C123	-0.1530	H147	0.1390	H171	0.1167
0.0809         S29         0.2279         C53         -0.0660         H77         0.1135         C101         -0.1075         N125         -0.4090         H149         0.1203         C173           0.0400         C30         0.0921         C54         -0.0541         H78         0.1132         H102         0.1251         C126         -0.1694         H150         0.1747         C173           -0.0516         C31         -0.0511         C55         -0.0641         H79         0.1034         C103         -0.1024         H150         0.1747         C175           -0.1521         C33         0.0546         C57         0.4161         H81         0.1037         C105         0.01094         C173         0.0122         H152         0.1676         C176           -0.2770         C33         0.0546         C57         0.4161         H81         0.1327         C105         0.01024         H153         0.1167         C177         0.1167         C176         0.1279         H153         0.1167         C178         0.1027         H154         0.1167         C178         0.0122         C176         0.1167         C178         0.0127         C179         0.1167         C178         0.0127	4	-0.5061	C28	-0.1531	C52	-0.0662	9/H	0.1136	C100	0.0458	C124	0.1503	H148	0.1206	H172	0.1187
0.0400         C30         0.0921         C54         -0.0541         H78         0.1132         H102         0.1251         C126         -0.1694         H150         0.1758         N174         -0.5162         0.031         0.0400         C30         -0.5162         0.03         H151         0.1758         N174         C175           -0.5162         0.31         -0.5111         C55         -0.0641         H79         0.1037         H104         0.1234         C127         0.0979         H151         0.1747         C175           -0.1521         C33         -0.0546         C55         -0.4161         H81         0.1257         C106         -0.1097         C129         -0.1221         H152         0.1467         C176           -0.2770         O34         -0.5323         H58         0.1165         H82         0.1755         C106         -0.1097         C13         -0.1022         H154         0.1467         C178           -0.2401         H37         0.1166         H61         0.1123         H82         0.1541         H109         0.1246         C13         -0.1024         H18         0.174         H18           0.2401         H37         0.1166         H61         0	5	0.0809	S29	0.2279	C53	-0.0660	H77	0.1135	C101	-0.1075	N125	-0.4090	H149	0.1203	C173	-0.1699
-0.5162         O.31         -0.5111         C.55         -0.0641         H79         0.1038         C103         -0.1094         C127         0.0979         H151         0.1747         C175           0.0910         C.32         0.0469         C.56         -0.1512         H80         0.1037         H104         0.1219         C128         -0.1228         H152         0.1676         C176           -0.1721         C.33         0.0546         C.57         0.4161         H81         0.1725         C106         -0.1097         C129         -0.1228         H152         0.1676         C177           -0.2770         0.34         H35         0.1162         H82         0.1725         C106         -0.1097         C139         0.0293         H167         0.1173         C106         C1107         C132         -0.025         H187         C179	9	0.0400	C30	0.0921	C54	-0.0541	H78	0.1132	H102	0.1251	C126	-0.1694	H150	0.1758	N174	-0.4127
0.0910         C32         0.0469         C56         -0.1512         H80         0.1037         H104         0.1219         C122         -0.1228         H152         0.1676         C176           -0.1521         C33         0.0546         C57         0.4161         H81         0.3257         C105         0.0442         C129         -0.1221         H153         0.1396         C177           -0.2770         O34         -0.5323         H58         0.1162         H82         0.1755         C106         -0.1097         C139         -0.025         H153         0.1467         C178           -0.2314         H36         0.0195         H69         0.1121         H84         0.1514         C106         -0.1027         C132         -0.025         H153         0.173         C178         -0.026         C178         C178         -0.026         C178         C179         C179         C178         C179         C178         C179	7	-0.5162	031	-0.5111	C55	-0.0641	H79	0.1038	C103	-0.1094	C127	0.0979	H151	0.1747	C175	0.1642
-0.1521         C33         0.0546         C57         0.4161         H81         0.3257         C105         0.0442         C129         -0.1221         H153         0.1396         C177           -0.2770         034         -0.5323         H58         0.1162         H82         0.1725         C106         -0.1097         C130         -0.0930         H154         0.1467         C178           -0.2770         034         -0.5323         H58         0.1165         H83         0.1534         H107         0.1160         C131         -0.1025         H155         0.173         C179           -0.3314         H36         0.0165         H84         0.1514         C108         -0.1073         C132         -0.0962         C156         0.1030         H180           0.2401         H37         0.1160         H46         0.1132         H86         0.1546         C133         -0.1670         C157         -0.1264         H181           0.1002         H40         0.1133         H87         0.1616         C113         -0.1060         C136         0.1679         C156         0.1094         C156         0.1094         C157         0.1264         H181           0.1002         H	<u>%</u>	0.0910	C32	0.0469	C56	-0.1512	H80	0.1037	H104	0.1219	C128	-0.1228	H152	0.1676	C176	-0.1350
-0.2770         O34         -0.5323         H58         0.1162         H82         0.1725         C106         -0.1097         C130         0.0930         H154         0.1467         C178           0.2519         H35         0.1195         H89         0.1165         H83         0.1836         H107         0.1160         C131         -0.1025         H155         0.1713         C179           -0.3314         H36         0.01993         H60         0.1121         H84         0.1541         C108         -0.1073         C132         -0.0962         C156         0.1030         H180           0.2401         H37         0.1066         H61         0.1121         H84         0.1541         C110         0.0278         C132         -0.0670         C157         -0.1264         H180           0.2401         H37         0.1132         H86         0.1648         0.1246         C13         -0.1670         C157         C159         C157         H181           0.0985         H39         0.1132         H87         0.1615         C111         -0.1077         C135         C158         0.1579         H183           0.1048         O.1108         H89         0.1526         C113 <td>6,</td> <td>-0.1521</td> <td>C33</td> <td>0.0546</td> <td>C57</td> <td>0.4161</td> <td>H81</td> <td>0.3257</td> <td>C105</td> <td>0.0442</td> <td>C129</td> <td>-0.1221</td> <td>H153</td> <td>0.1396</td> <td>C177</td> <td>0.1107</td>	6,	-0.1521	C33	0.0546	C57	0.4161	H81	0.3257	C105	0.0442	C129	-0.1221	H153	0.1396	C177	0.1107
0.2519         H35         0.1195         H89         0.1165         H83         0.1836         H107         0.1160         C131         -0.1025         H155         0.1193         H30           -0.3314         H36         0.0993         H60         0.1121         H84         0.1514         C108         -0.1073         C132         -0.0962         C156         0.1030         H180           0.2401         H37         0.1066         H61         0.1123         H85         0.1541         H109         0.1246         C133         -0.1670         C157         -0.1264         H181           0.0985         H38         0.1120         H86         0.1634         C110         0.0278         N134         -0.4094         C157         -0.1264         H181           0.0985         H39         0.1132         H87         0.1615         C111         -0.1077         C135         0.1581         N159         -0.4091         H181           0.1002         H40         0.1108         H89         0.1656         C113         -0.1275         C160         0.1409         H183           0.1048         O4108         H89         0.1656         C113         -0.1275         C167         -0.14	110	-0.2770	034	-0.5323	H58	0.1162	H82	0.1725	C106	-0.1097	C130	0.0930	H154	0.1467	C178	-0.1538
-0.3314         H36         0.0993         H60         0.1121         H84         0.1514         C108         -0.1073         C132         -0.0962         C156         0.1030         H180           0.2401         H37         0.1066         H61         0.1123         H85         0.1541         H109         0.1246         C133         -0.1670         C157         -0.1264         H181           0.2351         H38         0.1120         H86         0.1132         H86         0.1645         C110         0.0278         N134         -0.4094         C157         -0.1264         H181           0.0985         H39         0.1130         H87         0.1615         C111         -0.1017         C135         0.1581         N159         -0.4091         H182           0.1024         O.198         H40         0.1408         H89         0.1656         C113         -0.1275         C160         0.1409         H183         0.1579         H184         0.1577         H184         0.1577         H184         0.1577         C136         0.1571         H184         0.1571         C136         C137         C136         C137         C136         C141         H184         H184         C134         C14	11	0.2519	H35	0.1195	H59	0.1165	H83	0.1836	H107	0.1160	C131	-0.1025	H155	0.1713	C179	0.1485
0.2401         H37         0.1066         H61         0.1123         H85         0.1541         H109         0.1246         C133         -0.1670         C157         -0.1264         H181           0.3251         H38         0.1120         H62         0.1132         H86         0.1684         C110         0.0278         N134         -0.4094         C158         0.1579         H182           0.0985         H39         0.1190         H63         0.1133         H87         0.1615         C111         -0.1017         C135         0.1581         N159         -0.4091         H183           0.1002         H40         0.1108         H64         0.1406         H88         0.1557         H112         0.1217         C136         0.1575         C160         0.1409         H183           0.1048         O.1108         H64         0.1406         H89         0.1626         C113         -0.1275         C160         0.1409         H184           0.1048         O.4409         O.66         -0.4800         C90         -0.1024         H114         0.1130         C138         C116         0.157         C139         0.1509         H189         0.1509         C139         0.1509         H1	112	-0.3314	H36	0.0993	09H	0.1121	H84	0.1514	C108	-0.1073	C132	-0.0962	C156	0.1030	H180	0.1752
0.3251         H38         0.1120         H62         0.1132         H86         0.1684         C110         0.0278         N134         -0.4094         C158         0.1579         H182           0.0985         H39         0.1190         H63         0.1133         H87         0.1615         C111         -0.1017         C135         0.1581         N159         -0.4091         H183           0.1002         H40         0.1108         H64         0.1406         H88         0.1557         H112         0.1217         C136         -0.1275         C160         0.1412         H184           0.1048         O41         -0.5246         H65         0.1408         H89         0.1626         C113         -0.1274         C136         0.1457         C116         -0.1474         C136         C137         C136         C161         -0.1499         H184         H184         0.137         C136         C131         C136         C137         C136         C161         D.1499         H185         D.1499         H184         D.1499         C136         D.1499         H184         D.1490         D.1499         H184         D.1490         D.1499         H184         D.1414         D.1141         D.1414         <	13	0.2401	H37	0.1066	H61	0.1123	H85	0.1541	H109	0.1246	C133	-0.1670	C157	-0.1264	H181	0.1518
0.0985         H39         0.1190         H63         0.1133         H87         0.1615         C111         -0.1017         C135         0.1581         N159         -0.4091         H183           0.1002         H40         0.1108         H64         0.1406         H88         0.1557         H112         0.1217         C136         -0.1275         C160         0.1412         H184           0.1048         O41         -0.1408         H89         0.1626         C113         -0.1275         C160         0.1419         H184           0.1024         C42         0.0409         O66         -0.4800         C90         -0.1002         H114         0.1130         C138         -0.1411         H162         0.1514         H185           0.0961         C43         0.0594         C67         0.0066         H91         0.1229         C115         0.130         C138         0.150         H187         H187           0.0861         C43         0.0661         C92         -0.1185         C116         -0.1241         H140         0.1670         C164         -0.1660         H188           0.1065         C45         0.0661         C92         -0.1185         C116         -0.1241 </td <td>114</td> <td>0.3251</td> <td>H38</td> <td>0.1120</td> <td>H62</td> <td>0.1132</td> <td>98H</td> <td>0.1684</td> <td>C110</td> <td>0.0278</td> <td>N134</td> <td>-0.4094</td> <td>C158</td> <td>0.1579</td> <td>H182</td> <td>0.1386</td>	114	0.3251	H38	0.1120	H62	0.1132	98H	0.1684	C110	0.0278	N134	-0.4094	C158	0.1579	H182	0.1386
0.1002         H40         0.1108         H64         0.1406         H88         0.1557         H112         0.1217         C136         -0.1275         C160         0.1412         H184           0.1048         O41         -0.5246         H65         0.1408         H89         0.1626         C113         -0.1234         C137         0.1055         C161         -0.1499         H185           0.1024         C42         0.0409         O66         -0.4800         C90         -0.1002         H114         0.1130         C138         -0.1411         H162         0.1514         H186           0.0961         C43         0.0554         C67         0.0066         H91         0.1229         C115         0.136         C139         0.1509         H163         0.1743         H187           0.0861         C44         -0.7664         C92         -0.1185         C116         -0.1241         H140         0.1670         C164         -0.1660         H188           0.1065         C45         0.0661         C92         -0.1185         C116         -0.1241         H140         0.1670         C164         -0.1660         H188           0.1065         C45         0.0669         C94	115	0.0985	H39	0.1190	H63	0.1133	H87	0.1615	C1111	-0.1017	C135	0.1581	N159	-0.4091	H183	0.1589
0.1048         O41         -0.5246         H65         0.1408         H89         0.1626         C113         -0.1234         C137         0.1055         C161         -0.1499         H185           0.1024         C42         0.0409         O66         -0.4800         C90         -0.1002         H114         0.1130         C138         -0.1411         H162         0.1514         H186           0.0961         C43         0.0594         C67         0.0066         H91         0.1229         C115         0.1305         C139         0.1509         H163         0.1743         H187           0.0861         O44         -0.5104         C68         0.0661         C92         -0.1185         C116         -0.1241         H140         0.1670         C164         -0.1660         H188           0.1065         C45         0.0615         O69         -0.4963         H93         0.1330         H117         0.1181         H141         0.1414         C165         0.0905         H189           0.1183         C46         0.0157         C70         0.0609         C94         0.3278         C118         -0.1012         H142         0.1502         C164         -0.1151         H190	911	0.1002	H40	0.1108	H64	0.1406	H88	0.1557	H112	0.1217	C136	-0.1275	C160	0.1412	H184	0.1691
0.1024         C42         0.0409         O66         -0.4800         C90         -0.1002         H114         0.1130         C138         -0.1411         H162         0.1514         H186           0.0961         C43         0.0594         C67         0.0066         H91         0.1229         C115         0.3105         C139         0.1509         H163         0.1743         H187           0.0861         C94         -0.6185         C116         -0.1241         H140         0.1670         C164         -0.1660         H188           0.1065         C45         0.0615         O69         -0.4963         H93         0.1330         H117         0.1181         H141         0.1414         C165         0.0905         H189           0.1183         C46         0.0157         C70         0.0609         C94         0.3278         C118         -0.1012         H142         0.1502         C166         -0.1151         H190           0.0908         C94         0.3278         C118         -0.1043         H143         0.1742         C167         -0.1154         H191           0.0908         C97         -0.183         H119         0.1243         H144         0.1770         C16	17	0.1048	041	-0.5246	H65	0.1408	68H	0.1626	C113	-0.1234	C137	0.1055	C161	-0.1499	H185	0.1802
0.0961         C43         0.0594         C67         0.0066         H91         0.1229         C115         0.3105         C139         0.1509         H163         0.1743         H187           0.0861         O44         -0.5104         C68         0.0661         C92         -0.1185         C116         -0.1241         H140         0.1670         C164         -0.1660         H188           0.1065         C45         0.0615         O69         -0.4963         H93         0.1330         H117         0.1181         H141         0.1414         C165         0.0905         H189           0.1183         C46         0.0157         C70         0.0609         C94         0.3278         C118         -0.1012         H142         0.1502         C166         -0.1151         H190           0.0908         O47         -0.4889         C71         0.0341         C95         -0.1183         H119         0.1243         H144         0.1742         C167         -0.1154         H191           0.0908         C48         0.4122         O72         -0.5288         H96         0.1323         C120         0.1554         H144         0.1770         C168         0.0977         Total <td>18</td> <td>0.1024</td> <td>C42</td> <td>0.0409</td> <td>990</td> <td>-0.4800</td> <td>C90</td> <td>-0.1002</td> <td>H114</td> <td>0.1130</td> <td>C138</td> <td>-0.1411</td> <td>H162</td> <td>0.1514</td> <td>H186</td> <td>0.1291</td>	18	0.1024	C42	0.0409	990	-0.4800	C90	-0.1002	H114	0.1130	C138	-0.1411	H162	0.1514	H186	0.1291
0.0861         O44         -0.5104         C68         0.0661         C92         -0.1185         C116         -0.1241         H140         0.1670         C164         -0.1660         H188           0.1065         C45         0.0615         O69         -0.4963         H93         0.1330         H117         0.1181         H141         0.1414         C165         0.0905         H189           0.1183         C46         0.0157         C70         0.0609         C94         0.3278         C118         -0.1012         H142         0.1502         C166         -0.1151         H190           0.0908         O47         -0.4889         C71         0.0341         C95         -0.1183         H119         0.1243         H143         0.1742         C167         -0.1154         H191           0.1188         C48         0.4122         O72         -0.5288         H96         0.1323         C120         0.1554         H144         0.1770         C168         0.0977         Total	[19	0.0961	C43	0.0594	C67	9900.0	H91	0.1229	C115	0.3105	C139	0.1509	H163	0.1743	H187	0.1321
0.1065 C45 0.0615 O69 -0.4963 H93 0.1330 H117 0.1181 H141 0.1414 C165 0.0905 H189 0.1183 C46 0.0157 C70 0.0609 C94 0.3278 C118 -0.1012 H142 0.1502 C166 -0.1151 H190 0.0908 O47 -0.4889 C71 0.0341 C95 -0.1183 H119 0.1243 H143 0.1742 C167 -0.1154 H191 0.1188 C48 0.4122 O72 -0.5288 H96 0.1323 C120 0.1554 H144 0.1770 C168 0.0977 Total	120	0.0861	94	-0.5104	892	0.0661	C92	-0.1185	C116	-0.1241	H140	0.1670	C164	-0.1660	H188	0.1761
0.1183 C46 0.0157 C70 0.0609 C94 0.3278 C118 -0.1012 H142 0.1502 C166 -0.1151 H190 0.0908 O47 -0.4889 C71 0.0341 C95 -0.1183 H119 0.1243 H143 0.1742 C167 -0.1154 H191 0.1188 C48 0.4122 O72 -0.5288 H96 0.1323 C120 0.1554 H144 0.1770 C168 0.0977 Total	21	0.1065	C45	0.0615	690	-0.4963	H93	0.1330	H117	0.1181	H141	0.1414	C165	0.0905	H189	0.1751
0.0908 O47 -0.4889 C71 0.0341 C95 -0.1183 H119 0.1243 H143 0.1742 C167 -0.1154 H191 0.1188 C48 0.4122 O72 -0.5288 H96 0.1323 C120 0.1554 H144 0.1770 C168 0.0977 Total	22	0.1183	C46	0.0157	C70	0.0609	C94	0.3278	C118	-0.1012	H142	0.1502	C166	-0.1151	H190	0.1627
0.1188 C48 0.4122 O72 -0.5288 H96 0.1323 C120 0.1554 H144 0.1770 C168 0.0977 Total	[23	0.0908	047	-0.4889	C71	0.0341	C95	-0.1183	H119	0.1243	H143	0.1742	C167	-0.1154	H191	0.1373
	124	0.1188	C48	0.4122	072	-0.5288	96H	0.1323	C120	0.1554	H144	0.1770	C168	0.0977	Total	4.0000

$\overline{}$	
õ	i
⋾	i
П	
-=	
$\overline{}$	ï
ಾ	ı
	1
_	
_	
3.1	
~ -	
e	i
e	i
	i

	0.77														
z = 1	5.66 A														
01	-0.5354	C25	-0.3661	C49	-0.1546	H73	0.1468	C97	-0.1017	C121	-0.1304	H145	0.1792	C169	-0.1051
C2	0.0359	S26	0.2715	C50	-0.0629	H74	0.1463	H98	0.1198	C122	0.0989	H146	0.1450	C170	-0.1064
C3	0.0682	C27	-0.2746	C51	-0.0530	H75	0.1147	C39	0.0329	C123	-0.1558	H147	0.1434	H171	0.1284
90	-0.5076	C28	-0.1462	C52	-0.0660	9/H	0.1150	C100	0.0439	C124	0.1486	H148	0.1146	H172	0.1268
C2	0.0749	S29	0.2325	C53	-0.0659	H77	0.1150	C101	-0.1090	N125	-0.4095	H149	0.1142	C173	-0.1644
92	0.0423	C30	0.0856	C54	-0.0525	H78	0.1147	H102	0.1232	C126	-0.1559	H150	0.1758	N174	-0.4130
07	07 -0.5133	031	-0.5186	C55	-0.0634	H79	0.1052	C103	-0.1117	C127	0.0860	H151	0.1745	C175	0.1411
C8	0.0915	C32	0.0514	C56	-0.1501	H80	0.1052	H104	0.1156	C128	-0.1116	H152	0.1764	C176	-0.1341
60	-0.1370	C33	0.0644	C57	0.4175	H81	0.3271	C105	0.0401	C129	-0.1133	H153	0.1486	C177	0.1040
C10	-0.2477	034	-0.5377	H58	0.1154	H82	0.1991	C106	-0.1119	C130	0.0935	H154	0.1513	C178	-0.1543
S11	0.2436	H35	0.0999	H59	0.1155	H83	0.1581	H107	0.1071	C131	-0.1146	H155	0.1754	C179	0.1551
C12	-0.3058	H36	0.1066	09H	0.1123	H84	0.1531	C108	-0.1087	C132	-0.1144	C156	0.0879	H180	0.1804
S13	0.2640	H37	0.1000	H61	0.1123	H85	0.1562	H109	0.1218	C133	-0.1607	C157	-0.1168	H181	0.1553
H14	0.3230	H38	0.1023	H62	0.1136	98H	0.1702	C110	0.0280	N134	-0.4175	C158	0.1067	H182	0.1366
H15	0.0995	H39	0.0950	H63	0.1137	H87	0.1636	C1111	-0.1035	C135	0.1631	N159	-0.4037	H183	0.1650
H16	0.0994	H40	0.0979	H64	0.1415	H88	0.1582	H1112	0.1217	C136	-0.1311	C160	0.1531	H184	0.1748
H17	0.1030	041	-0.5256	H65	0.1416	68H	0.1648	C113	-0.1255	C137	0.0930	C161	-0.1407	H185	0.1796
H18	0.1033	C42	0.0421	990	-0.4785	C30	-0.1019	H114	0.0988	C138	-0.1571	H162	0.1581	H186	0.1417
H19	0.0962	C43	0.0589	C67	0.0052	H91	0.1192	C115	0.3010	C139	0.1475	H163	0.1819	H187	0.1407
H20	0.0964	044	-0.5101	89D	0.0654	C92	-0.1191	C116	-0.1266	H140	0.1764	C164	-0.1597	H188	0.1802
H21	0.1134	C45	0.0616	690	-0.4937	H93	0.1309	H1117	0.1045	H141	0.1533	C165	0.0778	H189	0.1741
H22	0.1142	C46	0.0145	C70	0.0596	C94	0.3255	C118	-0.1029	H142	0.1507	C166	-0.1225	H190	0.1709
H23	0.1231	047	-0.4874	C71	0.0336	C95	-0.1190	H1119	0.1247	H143	0.1779	C167	-0.1207	H191	0.1437
H24	0.1247	C48	0.4136	072	-0.5257	96H	0.1302	C120	0.1602	H144	0.1764	C168	0.0821	Total	4.0000

	_	_
•	Continuino /	
	٩	٠.
,		4
,	×	4
	×	

	'	'			'	'	0.1519	'		'														
	C169	C170	H171	H172	C173	N174	C175	C176	C177	C178	C179	H180	H181	H182	H183	H184	H185	H186	H187	H188	H189	H190	H191	Total
	0.1794	0.1468	0.1486	0.1172	0.1170	0.1800	0.1800	0.1734	0.1379	0.1528	0.1830	0.0841	-0.1294	0.1561	-0.4072	0.1460	-0.1474	0.1563	0.1841	-0.1716	0.0753	-0.1068	-0.1067	0.0784
	H145	H146	H147	H148	H149	H150	H151	H152	H153	H154	H155	C156	C157	C158	N159	C160	C161	H162	H163	C164	C165	C166	C167	C168
	-0.1257	0.0874	-0.1464	0.1496	-0.4116	-0.1591	0.0627	-0.1156	-0.1181	0.0637	-0.1034	-0.1026	-0.1607	-0.4152	0.1586	-0.1229	0.0931	-0.1515	0.1520	0.1781	0.1399	0.1530	0.1822	0.1819
	C121	C122	C123	C124	N125	C126	C127	C128	C129	C130	C131	C132	C133	N134	C135	C136	C137	C138	C139	H140	H141	H142	H143	H144
	-0.1044	0.1124	0.0293	0.0429	-0.1114	0.1216	-0.1140	0.1048	0.0307	-0.1140	0.0939	-0.1110	0.1198	0.0338	-0.1041	0.1252	-0.1390	0.0777	0.3001	-0.1395	0.0780	-0.1031	0.1263	0.1532
	C97	H98	C39	C100	C101	H102	C103	H104	C105	C106	H107	C108	H109	C110	C1111	H1112	C113	H114	C115	C116	H1117	C118	H1119	C120
	0.1479	0.1474	0.1102	0.1105	0.1105	0.1103	0.1001	0.1000	0.3230	0.2039	0.1603	0.1541	0.1579	0.1736	0.1652	0.1605	0.1681	-0.1047	0.1124	-0.1206	0.1272	0.3214	-0.1206	0.1261
	H73	H74	H75	9/H	H77	H78	H79	H80	H81	H82	H83	H84	H85	98H	H87	H88	68H	C30	H91	C92	H93	C94	C95	96H
	-0.1537	-0.0622	-0.0510	-0.0662	-0.0659	-0.0507	-0.0625	-0.1484	0.4201	0.1132	0.1134	0.1121	0.1120	0.1138	0.1138	0.1418	0.1421	-0.4753	0.0019	0.0699	-0.5035	0.0620	0.0369	-0.5375
	C49	C50	C51	C52	C53	C54	C55	C56	C57	H58	H59	09H	H61	H62	H63	H64	H65	990	C67	89D	690	C70	C71	072
	-0.3276	0.2626	-0.2950	-0.1555	0.2815	0.0756	-0.5159	0.0604	0.0561	-0.5499	0.1088	0.1023	0.0927	0.0929	0.0951	0.0956	-0.5280	0.0441	0.0584	-0.5104	0.0619	0.0136	-0.4860	0.4151
	C25	S26	C27	C28	S29	C30	031	C32	C33	034	H35	H36	H37	H38	H39	H40	041	C42	C43	94	C45	C46	047	C48
= 18.75 Å	-0.5336	0.0349	0.0686	-0.5057	0.0723	0.0434	-0.5136	0.0891	-0.1367	-0.2433	0.3179	-0.2980	0.3122	0.3227	0.0999	0.1000	0.1039	0.1041	0.0987	0.0989	0.1137	0.1146	0.1281	0.1291
z = 1	01	C2	C3	04	C2	92	07	8 C8	60	C10	S11	C12	S13	H14	H15	H16	H17	H18	H19	H20	H21	H22	H23	H24

۰	C	7
	ã	5
	Ē	3
	2	=
•	Ξ	3
	Ē	Ξ
	C	5
	C	١
	_	_
		_
•		•
,	×	1.0
,		
,	×	10021
	٥	1
	٥	1
	٥	

= 2	3.27 Å														
_	-0.5279	C25	-0.3086	C49	-0.1582	H73	0.1443	C97	-0.1072	C121	-0.1336	H145	0.1741	C169	-0.1167
2	0.0329	S26	0.3543	C50	-0.0650	H74	0.1439	86H	0.1019	C122	0.0917	H146	0.1418	C170	-0.1121
ξί	0.0686	C27	-0.2483	C51	-0.0574	H75	0.1106	C39	0.0222	C123	-0.1462	H147	0.1403	H171	0.1147
4	-0.5049	C28	-0.1425	C52	-0.0664	9/H	0.1108	C100	0.0446	C124	0.1463	H148	0.1170	H172	0.1171
35	0.0712	S29	0.3447	C53	-0.0660	H77	0.1112	C101	-0.1131	N125	-0.4239	H149	0.1248	C173	-0.1604
92	0.0422	C30	0.0685	C54	-0.0571	H78	0.1109	H102	0.1231	C126	-0.1481	H150	0.1767	N174	-0.4187
21 21	-0.5141	031	-0.5163	C55	-0.0652	H79	0.1008	C103	-0.1230	C127	0.0648	H151	0.1780	C175	0.1537
<u>%</u>	0.0877	C32	0.0676	C56	-0.1524	H80	0.1008	H104	0.0839	C128	-0.1201	H152	0.1617	C176	-0.1241
60	-0.1360	C33	0.0476	C57	0.4143	H81	0.3234	C105	0.0307	C129	-0.1195	H153	0.1407	C177	0.0941
C10	-0.2406	034	-0.5518	H58	0.11111	H82	0.2112	C106	-0.1282	C130	0.0670	H154	0.1543	C178	-0.1423
S11	0.3762	H35	0.1321	H59	0.1109	H83	0.1521	H107	0.0635	C131	-0.1020	H155	0.1797	C179	0.1488
C12	-0.3078	H36	0.1294	09H	0.1107	H84	0.1439	C108	-0.1150	C132	-0.1022	C156	0.0788	H180	0.1737
S13	0.3603	H37	0.0980	H61	0.1110	H85	0.1487	H109	0.1213	C133	-0.1533	C157	-0.1126	H181	0.1489
H14	0.3242	H38	0.1011	H62	0.1130	98H	0.1662	C110	0.0159	N134	-0.4168	C158	0.1456	H182	0.1451
H15	0.1026	H39	0.1051	H63	0.1132	H87	0.1568	C1111	-0.1167	C135	0.1442	N159	-0.4189	H183	0.1687
H16	0.1025	H40	0.1004	H64	0.1367	H88	0.1526	H112	0.0892	C136	-0.1185	C160	0.1430	H184	0.1770
H17	0.1048	041	-0.5293	H65	0.1368	68H	0.1612	C113	-0.1346	C137	9060.0	C161	-0.1573	H185	0.1787
H18	0.1053	C42	0.0434	990	-0.4814	C90	-0.1076	H114	0.0981	C138	-0.1525	H162	0.1414	H186	0.1414
H19	0.1001	C43	0.0614	C67	0.0072	H91	0.0998	C115	0.2978	C139	0.1483	H163	0.1713	H187	0.1392
H20	0.1007	94	-0.5120	89D	0.0681	C92	-0.1219	C116	-0.1389	H140	0.1590	C164	-0.1596	H188	0.1775
H21	0.1158	C45	0.0601	690	-0.4995	H93	0.1270	H117	0.1061	H141	0.1242	C165	0.0909	H189	0.1745
H22	0.1164	C46	0.0206	C70	0.0622	C94	0.3204	C118	-0.1235	H142	0.1558	C166	-0.1188	H190	0.1586
H23	0.1342	047	-0.4929	C71	0.0362	C95	-0.1215	H119	0.1059	H143	0.1781	C167	-0.1157	H191	0.1389
H24	t 0.1349 C	C48	0.4084	072	-0.5357	96H	0.1268	C120	0.1535	H144	0.1783	C168	0.0885	Total	4.0000

÷	τ.	3
	ã	5
	ספווע	3
	5	3
•	Ξ	3
	Contin	₹
	ç	₹
	٩	,
	_	_
•	_	
		•
	×	
٥	X	1.0
٥	X	1.0
٥	X	1.0
٥	×	1.0

	'	'					0.1652	'		'														
	C169	C170	H171	H172	C173	N174	C175	C176	C177	C178	C179	H180	H181	H182	H183	H184	H185	H186	H187	H188	H189	H190	H191	Total
	0.1859	0.1403	0.1347	0.1268	0.1277	0.1751	0.1877	0.1696	0.1413	0.1621	0.1885	0.0998	-0.1168	0.1546	-0.4006	0.1550	-0.1441	0.1600	0.1897	-0.1759	0.0742	-0.1125	-0.1173	0.0697
	H145	H146	H147	H148	H149	H150	H151	H152	H153	H154	H155	C156	C157	C158	N159	C160	C161	H162	H163	C164	C165	C166	C167	C168
	-0.1208	0.1032	-0.1394	0.1505	-0.4077	-0.1678	0.0696	-0.1174	-0.1136	0.0801	-0.1037	-0.1027	-0.1756	-0.4041	0.1486	-0.1203	0.0971	-0.1463	0.1520	0.1695	0.1472	0.1656	0.1915	0.1884
	C121	C122	C123	C124	N125	C126	C127	C128	C129	C130	C131	C132	C133	N134	C135	C136	C137	C138	C139	H140	H141	H142	H143	H144
	-0.1307	0.0822	0.0113	0.0256	-0.1375	0.1047	-0.1342	0.1000	0.0210	-0.1352	0.1008	-0.1374	0.1023	0.0149	-0.1266	0.0905	-0.1250	0.1350	0.3213	-0.1267	0.1326	-0.1282	0.0858	0.1648
	C97	86H	C39	C100	C101	H102	C103	H104	C105	C106	H107	C108	H109	C110	C1111	H112	C113	H1114	C115	C116	H1117	C118	H1119	C120
	0.1186	0.1186	0.0976	0.0977	0.0989	0.0985	0.0953	0.0954	0.3163	0.2260	0.1864	0.0799	0.0904	0.1230	0.0956	0.0966	0.1142	-0.1319	0.0784	-0.1264	0.1392	0.3322	-0.1244	0.1421
	H73	H74	H75	9/H	H77	H78	H79	H80	H81	H82	H83	H84	H85	98H	H87	H88	68H	C30	H91	C92	H93	C94	C95	96H
	-0.1814	-0.0854	-0.0911	-0.0708	-0.0635	-0.1008	-0.0796	-0.1795	0.3787	0.1055	0.1010	0.1089	0.1103	0.1115	0.1122	0.1088	0.1074	-0.5197	0.0387	0.0682	-0.5108	0.0763	0.0350	-0.5416
	C49	C50	C51	C52	C53	C54	C55	C56	C57	H58	H59	09H	H61	H62	H63	H64	H65	990	C67	89D	690	C70	C71	072
	-0.3052	0.4090	-0.2440	-0.1406	0.4042	0.0737	-0.5186	0.0555	0.0403	-0.5223	0.1449	0.1428	0.1076	0.1057	0.1262	0.1250	-0.5175	0.0313	0.0775	-0.5162	0.0451	0.0596	-0.5225	0.3625
	C25	S26	C27	C28	S29	C30	031	C32	C33	034	H35	H36	H37	H38	H39	H40	041	C42	C43	94	C45	C46	047	C48
= 28.17 Å	-0.5279	0.0336	0.0642	-0.4978	0.0698	0.0368	-0.5149	0.0870	-0.1348	-0.2362	0.4294	-0.3105	0.4158	0.3259	0.1039	0.1038	0.1086	0.1090	0.1038	0.1045	0.1215	0.1221	0.1439	0.1448
z = 2	01	C5	C3	90	CS	92	07	% C8	60	C10	S11	C12	S13	H14	H15	H16	H17	H18	H19	H20	H21	H22	H23	H24

	nilec	
	(Cont	
,	_	4
•	_	4
,	_	4
۲	_	4
,	×	4
,	×	5
•	×	5
•	_	5
•	×	1.0
•	×	1.0
•	×	1.0
•	×	1.0
•	×	1.0
•	×	1.0
•	×	1.0

	0														
z = 3	2.22 A														
01	-0.5161	C25	-0.3055	C49	-0.1725	H73	0.1357	C97	-0.1262	C121	-0.1251	H145	0.1745	C169	-0.1091
C2	0.0282	S26	0.4047	C50	-0.0767	H74	0.1350	86H	0.0980	C122	0.0894	H146	0.1440	C170	-0.1080
C3	0.0666	C27	-0.2433	C51	-0.0753	H75	0.1040	C99	0.0160	C123	-0.1407	H147	0.1420	H171	0.1173
9	-0.4995	C28	-0.1396	C52	-0.0682	9/H	0.1045	C100	0.0354	C124	0.1447	H148	0.1305	H172	0.1207
C2	C5 0.0678	S29	0.3949	C53	-0.0640	H77	0.1053	C101	-0.1447	N125	-0.4183	H149	0.1399	C173	-0.1633
92	0.0406	C30	0.0786	C54	-0.0816	H78	0.1053	H102	0.0451	C126	-0.1515	H150	0.1733	N174	-0.4158
07	-0.5148	031	-0.5159	C55	-0.0736	H79	0.0980	C103	-0.1122	C127	0.0801	H151	0.1778	C175	0.1536
C8	0.0862	C32	0.0525	C56	-0.1652	H80	0.0978	H104	0.1207	C128	-0.1184	H152	0.1813	C176	-0.1322
60	-0.1360	C33	0.0441	C57	0.3991	H81	0.3209	C105	0.0481	C129	-0.1211	H153	0.1505	C177	0.0938
C10	-0.2385	034	-0.5289	H58	0.0984	H82	0.2178	C106	-0.1156	C130	0.0788	H154	0.1502	C178	-0.1458
S11	0.4169	H35	0.1408	H59	0.0976	H83	0.1966	H107	0.1196	C131	-0.1258	H155	0.1780	C179	0.1469
C12	-0.3088	H36	0.1388	09H	0.1013	H84	0.1093	C108	-0.1253	C132	-0.1260	C156	0.0906	H180	0.1777
S13	0.4024	H37	0.1123	H61	9660.0	H85	0.1272	H109	0.0851	C133	-0.1541	C157	-0.1265	H181	0.1549
H14	0.3290	H38	0.1120	H62	0.1145	98H	0.1531	C110	0.0170	N134	-0.4439	C158	0.1447	H182	0.1367
H15	0.1095	H39	0.1213	H63	0.1132	H87	0.1252	C1111	-0.1064	C135	0.1598	N159	-0.4128	H183	0.1681
H16	0.1093	H40	0.1201	H64	0.1203	H88	0.1311	H112	0.1043	C136	-0.1196	C160	0.1442	H184	0.1750
H17	0.1086	041	-0.5425	H65	0.1215	68H	0.1473	C113	-0.1209	C137	0.0851	C161	-0.1504	H185	0.1762
H18	0.1090	C42	0.0439	990	-0.4966	C30	-0.1211	H114	0.1273	C138	-0.1548	H162	0.1499	H186	0.1408
H19	0.1043	C43	0.0756	C67	0.0159	H91	0.0996	C115	0.3169	C139	0.1430	H163	0.1747	H187	0.1407
H20	0.1049	044	-0.5151	89D	0.0707	C92	-0.0891	C116	-0.1220	H140	0.1665	C164	-0.1609	H188	0.1777
H21	0.1192	C45	0.0478	690	-0.5089	H93	0.0664	H117	0.1270	H141	0.1388	C165	0.0777	H189	0.1741
H22	0.1198	C46	0.0446	C70	0.0674	C94	0.2924	C118	-0.1066	H142	0.1528	C166	-0.1205	H190	0.1665
H23	0.1404	047	-0.5135	C71	0.0366	C95	-0.1345	H119	0.0998	H143	0.1788	C167	-0.1185	H191	0.1461
H24	0.1412	C48	0.3821	072	-0.5391	96H	0.0991	C120	0.1553	H144	0.1788	C168	0.0792	Total	4.0000

÷	τ.	3
	ã	5
	ספווע	3
	5	3
•	Ξ	3
	Contin	₹
	ç	₹
	٩	,
	_	_
•	_	
		•
	×	
٥	X	1.0
٥	X	1.0
٥	X	1.0
٥	×	1.0

= 3	= 36.84 Å														
	-0.5259	C25	-0.3059	C49	-0.1820	H73	0.1240	C97	-0.1144	C121	-0.1372	H145	0.1807	C169	-0.1108
~1	0.0323	S26	0.4327	C50	-0.0869	H74	0.1231	86H	0.1205	C122	0.0815	H146	0.1424	C170	-0.1091
3	0.0659	C27	-0.2407	C51	-0.0839	H75	0.0996	C39	0.0365	C123	-0.1454	H147	0.1427	H171	0.1262
4	-0.5007	C28	-0.1385	C52	-0.0727	9/H	0.1003	C100	0.0308	C124	0.1515	H148	0.1253	H172	0.1276
35	0.0700	S29	0.4198	C53	-0.0569	H77	0.1025	C101	-0.1142	N125	-0.4075	H149	0.1276	C173	-0.1593
92	0.0375	C30	0.0813	C54	-0.1058	H78	0.1025	H102	0.0814	C126	-0.1642	H150	0.1799	N174	-0.4069
27	-0.5148	031	-0.5156	C55	-0.0757	H79	0.0962	C103	-0.1122	C127	0.0767	H151	0.1839	C175	0.1585
C8	0.0867	C32	0.0471	C56	-0.1772	H80	0.0960	H104	0.1176	C128	-0.1154	H152	0.1779	C176	-0.1230
60	-0.1354	C33	0.0490	C57	0.3883	H81	0.3197	C105	0.0409	C129	-0.1149	H153	0.1526	C177	0.0831
C10	-0.2366	034	-0.5321	H58	0.0928	H82	0.2261	C106	-0.1129	C130	0.0805	H154	0.1653	C178	-0.1460
S11	0.4426	H35	0.1446	H59	0.0914	H83	0.2109	H107	0.1191	C131	-0.1101	H155	0.1893	C179	0.1575
C12	-0.3096	H36	0.1424	09H	0.0863	H84	0.0702	C108	-0.1163	C132	-0.1092	C156	0.0815	H180	0.1815
S13	0.4262	H37	0.11114	H61	0.0882	H85	0.1056	H109	0.1021	C133	-0.1681	C157	-0.1198	H181	0.1602
H14	0.3257	H38	0.1115	H62	0.0897	98H	0.1420	C110	0.0234	N134	-0.4067	C158	0.1592	H182	0.1481
H15	0.1046	H39	0.1225	H63	0.0874	H87	0.0611	C1111	-0.1060	C135	0.1594	N159	-0.4103	H183	0.1745
H16	0.1044	H40	0.1210	H64	0.0967	H88	0.0977	H1112	0.1081	C136	-0.1348	C160	0.1536	H184	0.1823
H17	0.1074	041	-0.5477	H65	0.1013	68H	0.1290	C113	-0.1234	C137	0.0778	C161	-0.1467	H185	0.1749
H18	0.1079	C42	0.0541	990	-0.5145	C30	-0.1145	H114	0.1189	C138	-0.1459	H162	0.1589	H186	0.1429
H19	0.1030	C43	0.0649	C67	0.0296	H91	0.1232	C115	0.3113	C139	0.1519	H163	0.1835	H187	0.1428
H20	0.1037	94	-0.5206	C68	0.0709	C92	-0.1426	C116	-0.1241	H140	0.1765	C164	-0.1576	H188	0.1767
H21	0.1210	C45	0.0525	690	-0.5108	H93	0.0764	H1117	0.1201	H141	0.1508	C165	0.0704	H189	0.1818
H22	0.1216	C46	0.0640	C70	0.0707	C94	0.3055	C118	-0.1059	H142	0.1658	C166	-0.1177	H190	0.1738
H23	0.1443	047	-0.5284	C71	0.0368	C95	-0.1391	H1119	0.1077	H143	0.1912	C167	-0.1177	H191	0.1484
H24	0.1451	C48	0.3469	072	-0.5395	96H	0.0788	C120	0.1592	H144	0.1839	C168	0.0713	Total	4.0000

	(continued
,	<u>ಶ</u>
	ó
ς	×
	<u>د</u>
7	Tap
•	=
,	Œ
ŀ	_

z = 4	0.99 Å														
01	-0.5159	C25	-0.3067	C49	-0.2057	H73	0.1285	C97	-0.1074	C121	-0.1407	H145	0.1784	C169	-0.1095
C2	0.0293	S26	0.4372	C50	-0.1201	H74	0.1299	86H	0.1154	C122	0.1034	H146	0.1440	C170	-0.1101
C3	0.0656	C27	-0.2398	C51	-0.0974	H75	0.0984	C39	0.0306	C123	-0.1451	H147	0.1421	H171	0.1204
9	-0.4982	C28	-0.1378	C52	-0.0737	9/H	0.0972	C100	0.0343	C124	0.1507	H148	0.1211	H172	0.1186
C2	0.0681	S29	0.4222	C53	-0.0859	H77	0.1048	C101	-0.1161	N125	-0.4068	H149	0.1236	C173	-0.1667
Ce	0.0382	C30	0.0830	C54	-0.1223	H78	0.1039	H102	0.0952	C126	-0.1588	H150	0.1776	N174	-0.4123
07	-0.5149	031	-0.5150	C55	-0.0841	H79	0.0983	C103	-0.1145	C127	0.0678	H151	0.1795	C175	0.1620
C8	0.0862	C32	0.0449	C56	-0.1764	H80	0.0986	H104	0.1093	C128	-0.1213	H152	0.1755	C176	-0.1338
60	-0.1359	C33	0.0527	C57	0.3881	H81	0.3235	C105	0.0378	C129	-0.1142	H153	0.1455	C177	0.0897
C10	-0.2370	034	-0.5347	H58	0.0980	H82	0.2251	C106	-0.1147	C130	0.0560	H154	0.1612	C178	-0.1567
S11	0.4443	H35	0.1443	H59	0.1029	H83	0.2156	H107	0.1088	C131	-0.0953	H155	0.1857	C179	0.1517
C12	-0.3093	H36	0.1422	09H	0.0919	H84	0.0971	C108	-0.1159	C132	-0.0939	C156	0.0751	H180	0.1839
S13	0.4266	H37	0.1101	H61	0.0905	H85	0.0844	H109	0.1023	C133	-0.1551	C157	-0.1250	H181	0.1558
H14	0.3285	H38	0.1100	H62	0.0818	98H	0.1464	C110	0.0249	N134	-0.4097	C158	0.1635	H182	0.1555
H15	0.1087	H39	0.1215	H63	0.0878	H87	0.0796	C1111	-0.1069	C135	0.1526	N159	-0.4120	H183	0.1814
H16	0.1086	H40	0.1201	H64	0.0986	H88	0.1095	H1112	0.1088	C136	-0.1444	C160	0.1484	H184	0.1799
H17	0.1092	041	-0.5413	H65	0.1036	68H	0.1429	C113	-0.1250	C137	0.1113	C161	-0.1473	H185	0.1782
H18	0.1097	C42	0.0691	990	-0.5147	C30	-0.1074	H114	0.1113	C138	-0.1486	H162	0.1564	H186	0.1428
H19	0.1051	C43	0.0524	C67	0.0211	H91	0.1173	C115	0.3060	C139	0.1524	H163	0.1830	H187	0.1434
H20	0.1057	94	-0.5140	S92	0.0755	C92	-0.1276	C116	-0.1258	H140	0.1737	C164	-0.1629	H188	0.1813
H21	0.1211	C45	0.0620	690	-0.5085	H93	0.0948	H1117	0.1125	H141	0.1477	C165	0.0803	H189	0.1788
H22	0.1217	C46	0.0478	C70	0.0660	C94	0.2948	C118	-0.1068	H142	0.1610	C166	-0.1216	H190	0.1755
H23	0.1443	047	-0.5228	C71	0.0380	C95	-0.1273	H1119	0.1087	H143	0.1858	C167	-0.1119	H191	0.1561
H24	0.1451 (	C48	0.3500	072	-0.5385	96H	0.0913	C120	0.1526	H144	0.1826	C168	0.0896	Total	4.0000

ļ	_	
۰	ਲ	
	nne	
	ᆵ	
	coni	
	_	
	2.7	
	e 8.1	
	ق	
	e	

$\frac{2}{4} = \frac{5}{4}$	4.83 Å														
01	-0.5296	C25	-0.3069	C49	-0.1992	H73	0.1190	C97		C121	-0.1320	H145	0.1826	C169	-0.0994
C2	0.0335	S26	0.4410	C50	-0.0908	H74	0.1297	86H		C122	0.1098	H146	0.1255	C170	-0.1127
C3	0.0666	C27	-0.2394	C51	-0.1154	H75	0.0725	C39		C123	-0.1509	H147	0.1247	H171	0.1292
04	-0.5019	C28	-0.1376	C52	-0.0789	9/H	0.0790	C100		C124	0.1546	H148	0.1343	H172	0.1299
C2	0.0705	S29	0.4254	C53	-0.0754	H77	0.1015	C101		N125	-0.4184	H149	0.1336	C173	-0.1640
92	0.0376	C30	0.0834	C54	-0.1167	H78	0.1005	H102		C126	-0.1620	H150	0.1766	N174	-0.4194
07	-0.5147	031	-0.5149	C55	-0.0857	H79	0.1032	C103	-0.1137	C127	0.0903	H151	0.1762	C175	0.1631
83 C8	0.0867	C32	0.0439	C56	-0.2003	H80	0.1046	H104		C128	-0.1069	H152	0.1653	C176	-0.1351
60	-0.1358	C33	0.0534	C57	0.3667	H81	0.3303	C105		C129	-0.1129	H153	0.1377	C177	0.1139
C10	-0.2369	034	-0.5346	H58	0.1090	H82	0.2265	C106		C130	0.0864	H154	0.1493	C178	-0.1508
S11	0.4468	H35	0.1449	H59	0.1099	H83	0.2178	H107		C131	-0.1154	H155	0.1721	C179	0.1538
C12	-0.3092	H36	0.1428	09H	0.1027	H84	0.1290	C108		C132	-0.1010	C156	0.1067	H180	0.1757
S13	0.4292	H37	0.1103	H61	0.1022	H85	0.0905	H109		C133	-0.1634	C157	-0.1263	H181	0.1493
H14	0.3239	H38	0.1099	H62	0.0802	98H	0.1196	C110		N134	-0.4077	C158	0.1539	H182	0.1343
H15	0.1026	H39	0.1218	H63	0.0799	H87	0.1169	C1111		C135	0.1470	N159	-0.4089	H183	0.1643
H16	0.1025	H40	0.1205	H64	0.1206	H88	0.0888	H112		C136	-0.1273	C160	0.1478	H184	0.1832
H17	0.1065	041	-0.5400	H65	0.1318	68H	0.1270	C113		C137	0.1112	C161	-0.1356	H185	0.1714
H18	0.1070	C42	0.0608	990	-0.5288	C30	-0.1068	H114		C138	-0.1376	H162	0.1505	H186	0.1324
H19	0.1024	C43	0.0493	C67	0.0243	H91	0.1138	C115		C139	0.1432	H163	0.1734	H187	0.1302
H20	0.1030	044	-0.5028	C68	0.0856	C92	-0.1262	C116		H140	0.1624	C164	-0.1640	H188	0.1758
H21	0.1206	C45	0.0826	690	-0.5018	H93	0.1019	H117		H141	0.1362	C165	0.0799	H189	0.1804
H22	0.1212	C46	0.0252	C70	0.0601	C94	0.3007	C118		H142	0.1550	C166	-0.1072	H190	0.1686
H23	0.1443	047	-0.5302	C71	0.0404	C95	-0.1259	H119		H143	0.1799	C167	-0.1069	H191	0.1425
H24	4 0.1451 C	C48	0.3608	072	-0.5371	96H	0.1003	C120		H144	0.1720	C168	0.0867	Total	4.0000

**Table 8.2** Partial charge distribution of +1 oxidized rotaxane when the center of mass of the CBPQT<sup>4+</sup> ring moves from z = 10.92 Å (TTF side) to z = 44.83 Å (DNP side)

z = 1	0.92 Å														
01	-0.5374	C25	-0.3310	C49	-0.1512	H73	0.1519	C97	-0.0909	C121	-0.1317	H145	0.1823	C169	-0.0971
C5	0.0394	S26	0.2497	C50	-0.0588	H74	0.1514	86H	0.1431	C122	0.1110	H146	0.1469	C170	-0.1002
C	0.0616	C27	-0.2626	C51	-0.0466	H75	0.1168	C39	0.0421	C123	-0.1532	H147	0.1452	H171	0.1218
9	-0.5052	C28	-0.1540	C52	-0.0661	9/H	0.1171	C100	0.0541	C124	0.1519	H148	0.1186	H172	0.1212
C2	0.0829	S29	0.2401	C53	-0.0671	H77	0.1193	C101	-0.0975	N125	-0.4077	H149	0.1218	C173	-0.1747
92	0.0353	C30	0.0903	C54	-0.0439	H78	0.1191	H102	0.1466	C126	-0.1712	H150	0.1853	N174	-0.4084
07	-0.5164	031	-0.5120	C55	-0.0603	H79	0.1230	C103	-0.1017	C127	0.0969	H151	0.1816	C175	0.1714
c%	0.0927	C32	0.0465	C56	-0.1435	H80	0.1230	H104	0.1446	C128	-0.1219	H152	0.1803	C176	-0.1317
60	-0.1515	C33	0.0470	C57	0.4246	H81	0.3399	C105	0.0567	C129	-0.1218	H153	0.1503	C177	0.1167
C10	-0.2775	034	-0.5247	H58	0.1252	H82	0.1811	C106	-0.1020	C130	0.0899	H154	0.1542	C178	-0.1522
S11	0.2587	H35	0.1257	H59	0.1257	H83	0.1865	H107	0.1386	C131	-0.1031	H155	0.1818	C179	0.1564
C12	-0.3311	H36	0.1027	09H	0.1181	H84	0.1578	C108	-0.0973	C132	-0.0964	C156	0.1058	H180	0.1891
S13	0.2507	H37	0.11114	H61	0.1182	H85	0.1651	H109	0.1461	C133	-0.1727	C157	-0.1276	H181	0.1639
H14	0.3272	H38	0.1184	H62	0.1180	98H	0.1778	C110	0.0290	N134	-0.4048	C158	0.1595	H182	0.1434
H15	0.0995	H39	0.1252	H63	0.1182	H87	0.1695	C1111	-0.0947	C135	0.1653	N159	-0.4078	H183	0.1669
H16	0.1011	H40	0.1155	H64	0.1440	H88	0.1680	H112	0.1344	C136	-0.1252	C160	0.1422	H184	0.1751
H17	0.1060	041	-0.5109	H65	0.1442	68H	0.1741	C113	-0.1187	C137	0.1114	C161	-0.1505	H185	0.1891
H18	0.1040	C42	0.0286	990	-0.4718	C30	-0.0908	H114	0.1312	C138	-0.1392	H162	0.1584	H186	0.1308
H19	0.0955	C43	0.0606	C67	-0.0012	H91	0.1425	C115	0.3246	C139	0.1589	H163	0.1816	H187	0.1362
H20	0.0862	94	-0.5109	C68	0.0653	C92	-0.1101	C116	-0.1194	H140	0.1723	C164	-0.1681	H188	0.1831
H21	0.1097	C45	0.0575	690	-0.4994	H93	0.1579	H117	0.1370	H141	0.1453	C165	0.0897	H189	0.1804
H22	0.1212	C46	0.0132	C70	0.0593	C94	0.3479	C118	-0.0939	H142	0.1544	C166	-0.1148	H190	0.1638
H23	0.0940	047	-0.4878	C71	0.0207	C95	-0.1098	H119	0.1375	H143	0.1790	C167	-0.1156	H191	0.1374
H24	4 0.1214 C	C48	0.4187	072	-0.4878	96H	0.1573	C120	0.1569	H144	0.1823	C168	0.0949	Total	5.0000

	continued
	7.0
•	ě
,	<u> </u>
E	Tap

z = 1	5.66 Å														
01	-0.4907	C25	-0.3683	C49	-0.1507	H73	0.1522	C97	-0.0941	C121	-0.1283	H145	0.1870	C169	-0.1049
C2	0.0201	S26	0.2822	C50	-0.0585	H74	0.1517	86H	0.1382	C122	0.1036	H146	0.1508	C170	-0.1067
C3	0.0653	C27	-0.2754	C51	-0.0459	H75	0.1175	C99	0.0413	C123	-0.1539	H147	0.1494	H171	0.1294
90	-0.5034	C28	-0.1483	C52	-0.0663	9/H	0.1178	C100	0.0483	C124	0.1542	H148	0.1144	H172	0.1288
C2	0.0709	S29	0.2428	C53	-0.0669	H77	0.1199	C101	-0.1009	N125	-0.4064	H149	0.1135	C173	-0.1673
92	0.0396	C30	0.0855	C54	-0.0433	H78	0.1197	H102	0.1407	C126	-0.1591	H150	0.1828	N174	-0.4099
07	-0.5136	031	-0.5192	C55	-0.0598	H79	0.1253	C103	-0.1071	C127	0.0841	H151	0.1801	C175	0.1459
C8	0.0912	C32	0.0505	C56	-0.1434	H80	0.1253	H104	0.1346	C128	-0.1115	H152	0.1802	C176	-0.1335
C)	-0.1368	C33	0.0603	C57	0.4247	H81	0.3417	C105	0.0505	C129	-0.1132	H153	0.1510	C177	0.1083
C10	-0.2459	034	-0.5334	H58	0.1238	H82	0.2073	C106	-0.1073	C130	0.0919	H154	0.1561	C178	-0.1531
S11	0.2609	H35	0.0995	H59	0.1242	H83	0.1612	H107	0.1255	C131	-0.1145	H155	0.1812	C179	0.1590
C12	-0.3060	H36	0.1100	09H	0.1177	H84	0.1585	C108	-0.1007	C132	-0.1147	C156	0.0940	H180	0.1886
S13	0.2820	H37	0.1037	H61	0.1177	H85	0.1657	H109	0.1392	C133	-0.1630	C157	-0.1150	H181	0.1625
H14	0.3395	H38	0.1057	H62	0.1179	98H	0.1782	C110	0.0269	N134	-0.4148	C158	0.1129	H182	0.1374
H15	0.1215	H39	0.0978	H63	0.1180	H87	0.1702	C1111	-0.0989	C135	0.1671	N159	-0.3998	H183	0.1679
H16	0.1214	H40	0.1019	H64	0.1443	H88	0.1687	H112	0.1306	C136	-0.1308	C160	0.1590	H184	0.1808
H17	0.1113	041	-0.5132	H65	0.1445	68H	0.1746	C113	-0.1230	C137	0.0977	C161	-0.1393	H185	0.1869
H18	0.1115	C42	0.0305	990	-0.4718	C30	-0.0941	H114	0.1114	C138	-0.1556	H162	0.1668	H186	0.1457
H19	0.1018	C43	0.0601	C67	-0.0012	H91	0.1377	C115	0.3097	C139	0.1516	H163	0.1925	H187	0.1445
H20	0.1019	94	-0.5107	S92	0.0647	C92	-0.1118	C116	-0.1240	H140	0.1826	C164	-0.1637	H188	0.1881
H21	0.1178	C45	0.0579	690	-0.4978	H93	0.1539	H117	0.1170	H141	0.1572	C165	0.0764	H189	0.1810
H22	0.1187	C46	0.0125	C70	0.0592	C94	0.3429	C118	-0.0981	H142	0.1576	C166	-0.1223	H190	0.1766
H23	0.1280	047	-0.4862	C71	0.0194	C95	-0.1116	H119	0.1337	H143	0.1865	C167	-0.1204	H191	0.1470
H24	H24 0.1299	C48	0.4194	072	-0.4806	96H	0.1531	C120	0.1656	H144	0.1827	C168	0.0817	Total	5.0000

continued)
8.2
$\infty$
<u>e</u>
9
[z]

z = 18.75 Å														
C25 -0.3207	-0.3207	Ü	49		H73	0.1538	C97	-0.1005	C121	-0.1249	H145	0.1867	C169	-0.1077
S26 0.2837	0.2837	S	0	'	H74	0.1532	86H	0.1221	C122	0.0927	H146	0.1506	C170	-0.1063
C27 -0.2968	-0.2968	CS			H75	0.1222	C99	0.0352	C123	-0.1435	H147	0.1515	H171	0.1130
C28 -0.1570	-0.1570	CS	2	'	9/H	0.1226	C100	0.0440	C124	0.1561	H148	0.1190	H172	0.1126
S29 0.3045	0.3045	CS	~	'	H77	0.1233	C101	-0.1071	N125	-0.4085	H149	0.1185	C173	-0.1774
C30 0.0754	0.0754	ζ2	4		H78	0.1230	H102	0.1302	C126	-0.1631	H150	0.1864	N174	-0.4027
031 -0.5167	-0.5167	C55		-0.0597	H79	0.1121	C103	-0.1124	C127	0.0607	H151	0.1878	C175	0.1594
C32 0.0590	0.0590	C56			H80	0.1119	H104	0.1125	C128	-0.1159	H152	0.1739	C176	-0.1306
C33 0.0573	0.0573	C57			H81	0.3337	C105	0.0350	C129	-0.1188	H153	0.1381	C177	0.0921
034 -0.5496	-0.5496	H58			H82	0.2145	C106	-0.1123	C130	0.0630	H154	0.1610	C178	-0.1481
H35 0.1119	0.1119	H59			H83	0.1659	H107	0.1002	C131	-0.1028	H155	0.1920	C179	0.1515
H36 0.1059	0.1059	09H			H84	0.1603	C108	-0.1067	C132	-0.1020	C156	0.0886	H180	0.1924
H37 0.0924	0.0924	H61			H85	0.1664	H109	0.1279	C133	-0.1647	C157	-0.1274	H181	0.1622
H38 0.0924	0.0924	H62			98H	0.1787	C110	0.0336	N134	-0.4124	C158	0.1640	H182	0.1392
H39	0.0947	H63		0.1167	H87	0.1724	C1111	-0.1020	C135	0.1654	N159	-0.4032	H183	0.1845
H40 0.0963	0.0963	H64			H88	0.1703	H112	0.1303	C136	-0.1209	C160	0.1527	H184	0.1863
041 -0.5207	-0.5207	H65			68H	0.1758	C113	-0.1384	C137	0.0972	C161	-0.1458	H185	0.1893
C42 0.0381	0.0381	990			C90	-0.1007	H114	0.0788	C138	-0.1494	H162	0.1632	H186	0.1456
C43 0.0585	0.0585	C67		'	H91	0.1223	C115	0.3010	C139	0.1568	H163	0.1936	H187	0.1454
044 -0.5109	-0.5109	892			C92	-0.1159	C116	-0.1392	H140	0.1808	C164	-0.1765	H188	0.1917
C45 0.0602	0.0602	590	_	'	H93	0.1399	H117	0.0782	H141	0.1413	C165	0.0740	H189	0.1860
C46 0.0108	0.0108	C2	0		C94	0.3315	C118	-0.1010	H142	0.1621	C166	-0.1055	H190	0.1858
047 -0.4847	-0.4847	C2	_		C95	-0.1158	H119	0.1314	H143	0.1920	C167	-0.1056	H191	0.1405
C48 0.4206	0.4206	072		'	96H	0.1387	C120	0.1613	H144	0.1899	C168	0.0767	Total	5.0000
l			1											

Table 8.2 (continued)

C49         -0.1512         H73         0.1523         C97         -0.1066         C121         -0.130         H145         0.1785         C169         -0.1157           C50         -0.0596         H74         0.1519         H98         0.1029         C122         0.1013         H146         0.149         C170         -0.1109           C51         -0.0474         H75         0.1178         C99         0.0216         C124         0.1529         H149         0.1478         H171         0.1108           C52         -0.0662         H76         0.1181         C100         0.0461         C124         0.1529         H149         0.1264         C177         0.0159           C53         -0.0663         H79         0.1212         H102         0.1229         C127         0.0544         H151         0.1264         C171         0.0159           C55         -0.0665         H79         0.1327         H104         0.0294         C129         0.0184         H152         0.1664         C173         0.0184         H153         0.1664         C173         0.0184         H153         0.1649         C179         0.0184           C55         -0.0444         H79         0.1327 <th>72 77 Å</th> <th></th> <th></th> <th></th> <th></th> <th>Table 8.</th> <th>able 8.2 (continued</th> <th>ned)</th> <th></th> <th></th> <th></th> <th></th> <th></th> <th></th>	72 77 Å					Table 8.	able 8.2 (continued	ned)						
-0.0596         H74         0.1519         H98         0.1029         C122         0.1013         H146         0.1449         C170           -0.0474         H75         0.1178         C99         0.0216         C123         -0.1426         H147         0.1437         H171           -0.0662         H76         0.1181         C100         0.0461         C124         0.1529         H148         0.1178         H171           -0.0644         H77         0.1215         C101         -0.1229         C127         -0.4594         H189         0.1264         C173           -0.0644         H78         0.1212         H102         0.1261         C127         -0.0444         H179         0.1264         C173           -0.0444         H78         0.1227         C103         -0.1229         C127         -0.1694         H172         0.1264         C173           0.1431         H81         0.1327         H104         0.0294         C129         -0.1184         H152         C176           0.1121         H83         0.1657         H107         0.0615         C13         -0.1064         H152         0.1665         C176           0.1132         H84         0.1583<	-0.3072	_	C49	-0.1512	H73	0.1523	C97	-0.1066	C121	-0.1309	H145	0.1785	C169	-0.1157
-0.0474         H75         0.1178         C99         0.0216         C123         -0.1426         H147         0.1437         H171           -0.0662         H76         0.1181         C100         0.0461         C124         0.1529         H148         0.1178         H172           -0.0674         H77         0.1215         C101         -0.1123         N125         -0.4153         H149         0.1264         C173           -0.0444         H78         0.1212         H102         0.1261         C126         -0.1504         H150         0.1829         N174           -0.0443         H78         0.1217         H104         0.0832         C127         0.0644         H151         0.1841         C175           -0.0443         H80         0.1327         H104         0.0832         C128         -0.1194         H152         0.1665         C176           0.1431         H81         0.1327         H104         0.0832         C128         -0.1194         H152         0.1665         C176           0.1134         H83         0.1657         H107         0.0615         C138         C156         0.1689         H181           0.1155         H84         0.1584<	S26 0.3874		C50	-0.0596	H74	0.1519	86H	0.1029	C122	0.1013	H146	0.1449	C170	-0.1109
-0.0662         H76         0.1181         C100         0.0461         C124         0.1529         H148         0.1178         H172           -0.0674         H77         0.1215         C101         -0.1123         N125         -0.4153         H149         0.1264         C173           -0.0444         H78         0.1212         H102         0.1261         C126         -0.1504         H150         0.1864         C173           -0.0443         H78         0.1327         C103         -0.1229         C127         0.0644         H151         0.1849         C175           -0.0443         H80         0.1327         H104         0.0832         C128         -0.1194         H152         0.1665         C176           0.1121         H81         0.1327         H104         0.0832         C128         -0.1194         H152         0.1665         C176           0.1121         H82         0.1657         H107         0.0615         C131         -0.1106         H182         C176           0.1135         H84         0.1583         C108         -0.1143         C132         -0.1064         H182         0.1665         C178           0.1155         H88         0.16	-0.2490		C51	-0.0474	H75	0.1178	C99	0.0216	C123	-0.1426	H147	0.1437	H171	0.1128
-0.0674         H77         0.1215         C101         -0.1123         N125         -0.4153         H149         0.1264         C173           -0.0444         H78         0.1212         H102         0.1261         C126         -0.1504         H150         0.1829         N174           -0.0444         H78         0.1212         H102         0.1261         C126         -0.1504         H151         0.1829         N174           -0.0443         H89         0.1327         H104         0.0832         C128         -0.1194         H152         0.1665         C176           0.4241         H81         0.32481         C105         0.0294         C129         -0.1184         H152         0.1665         C176           0.1121         H82         0.2267         C106         -0.1286         C129         -0.1188         H152         0.1620         C177           0.1135         H84         0.1583         C108         -0.1143         C132         -0.1006         H184         C179           0.1136         H85         0.1644         H109         0.1244         C133         -0.1568         C15         -0.1099         H181           0.1137         H88         0.	-0.1455	_	C52	-0.0662	9/H	0.1181	C100	0.0461	C124	0.1529	H148	0.1178	H172	0.1159
-0.0444         H78         0.1212         H102         0.1261         C126         -0.1504         H150         0.1829         N174         -0.0665         H78         0.1212         H102         0.01229         C127         0.0644         H151         0.1841         C175           -0.1443         H80         0.1327         H104         0.0832         C128         -0.1194         H152         0.1665         C176           0.4241         H81         0.3481         C105         0.0294         C129         -0.1184         H152         0.1665         C176           0.1121         H82         0.2267         C106         -0.1286         C129         -0.1184         H152         0.1662         C177           0.1135         H84         0.1583         C106         -0.1286         C130         0.0661         H154         0.1620         C178           0.1136         H83         0.1644         H109         0.1244         C132         -0.1020         C156         0.1884         C179           0.1137         H86         0.1773         C110         0.0159         N134         -0.4089         C189         H181           0.1430         H88         0.1694         H	0.3775	_	253	-0.0674	H77	0.1215	C101	-0.1123	N125	-0.4153	H149	0.1264	C173	-0.1641
-0.0665         H79         0.1327         C103         -0.1229         C127         0.0644         H151         0.1841         C175           -0.1443         H80         0.1327         H104         0.0832         C128         -0.1194         H152         0.1665         C176           -0.1443         H81         0.1327         H104         0.0832         C128         -0.1194         H152         0.1665         C176           0.1121         H82         0.2267         C106         -0.1286         C130         0.0661         H154         0.1620         C177           0.1115         H83         0.1657         H107         0.0615         C131         -0.1016         H154         0.1620         C178           0.1138         H84         0.1583         C108         -0.1143         C132         -0.1020         C178         C179           0.1138         H85         0.1644         H109         0.1244         C133         -0.1568         C159         -0.1909         H181           0.1157         H86         0.1773         C110         0.0159         N134         -0.4089         C159         -0.1099         H181           0.1430         H88         0.16	0.0695	$\overline{}$	254	-0.0444	H78	0.1212	H102	0.1261	C126	-0.1504	H150	0.1829	N174	-0.4101
-0.1443         H80         0.1327         H104         0.0832         C128         -0.1194         H152         0.1665         C176           0.4241         H81         0.3481         C105         0.0294         C129         -0.1188         H153         0.1428         C177           0.1121         H82         0.2267         C106         -0.1286         C130         0.0661         H154         0.1620         C178           0.1135         H84         0.1583         C108         -0.1143         C132         -0.1006         H155         0.1884         C179           0.1138         H85         0.1644         H109         0.1244         C132         -0.1020         C156         0.0892         H180           0.1157         H86         0.1773         C110         0.0159         N134         -0.4089         C159         -0.1099         H181           0.1159         H87         0.1716         C111         -0.1181         C135         0.158         H182         0.1599         H181           0.1150         H88         0.1694         H112         0.0159         C135         0.1599         H183           0.1430         H88         0.1694         H114 <td>-0.5174</td> <td><math>\circ</math></td> <td>355</td> <td>-0.0605</td> <td>H79</td> <td>0.1327</td> <td>C103</td> <td>-0.1229</td> <td>C127</td> <td>0.0644</td> <td>H151</td> <td>0.1841</td> <td>C175</td> <td>0.1624</td>	-0.5174	$\circ$	355	-0.0605	H79	0.1327	C103	-0.1229	C127	0.0644	H151	0.1841	C175	0.1624
0.4241         H81         0.3481         C105         0.0294         C129         -0.1188         H153         0.1428         C177           0.1121         H82         0.2267         C106         -0.1286         C130         0.0661         H154         0.1620         C178           0.1119         H83         0.1657         H107         0.0615         C131         -0.1016         H155         0.1884         C179           0.1138         H84         0.1583         C108         -0.1143         C132         -0.1020         C156         0.0892         H180           0.1157         H86         0.1773         C110         0.0159         N134         -0.4089         C157         -0.1099         H181           0.1159         H87         0.1716         C111         -0.1181         C135         0.158         C159         -0.1099         H181           0.1430         H88         0.1694         H112         0.0194         C136         -0.153         C160         0.1498         H184           0.1430         H89         0.1741         C113         -0.1373         C137         0.1097         C161         -0.1549         H184           0.0603         C92 </td <td>0.0639</td> <td><math>\circ</math></td> <td>99</td> <td>-0.1443</td> <td>H80</td> <td>0.1327</td> <td>H104</td> <td>0.0832</td> <td>C128</td> <td>-0.1194</td> <td>H152</td> <td>0.1665</td> <td>C176</td> <td>-0.1213</td>	0.0639	$\circ$	99	-0.1443	H80	0.1327	H104	0.0832	C128	-0.1194	H152	0.1665	C176	-0.1213
0.1121         H82         0.2267         C106         -0.1286         C130         0.0661         H154         0.1620         C178         -           0.1119         H83         0.1657         H107         0.0615         C131         -0.1016         H155         0.1884         C179           0.1138         H84         0.1583         C108         -0.1143         C132         -0.1020         C156         0.0892         H180           0.1157         H86         0.1773         C110         0.0159         N134         -0.4089         C157         -0.1099         H181           0.1159         H87         0.1716         C111         -0.1181         C135         0.158         C157         -0.1099         H181           0.1150         H88         0.1694         H112         0.0159         C135         0.153         N159         -0.4097         H183           0.1430         H88         0.1694         H112         0.0914         C136         -0.1153         C161         -0.1549         H184           0.1430         H89         0.1741         H114         0.0975         C138         -0.1484         H162         0.1540         H188           -0.0007 <td>0.0484</td> <td><math>\mathcal{O}</math></td> <td>57</td> <td>0.4241</td> <td>H81</td> <td>0.3481</td> <td>C105</td> <td>0.0294</td> <td>C129</td> <td>-0.1188</td> <td>H153</td> <td>0.1428</td> <td>C177</td> <td>0.1037</td>	0.0484	$\mathcal{O}$	57	0.4241	H81	0.3481	C105	0.0294	C129	-0.1188	H153	0.1428	C177	0.1037
0.1119         H83         0.1657         H107         0.0615         C131         -0.1016         H155         0.1884         C179           0.1135         H84         0.1583         C108         -0.1143         C132         -0.1020         C156         0.0892         H180           0.1138         H85         0.1644         H109         0.1244         C133         -0.1568         C157         -0.1099         H181           0.1157         H86         0.1773         C110         0.0159         N134         -0.4089         C158         0.1530         H182           0.1159         H87         0.1716         C111         -0.1181         C135         0.159         N159         -0.4097         H182           0.1430         H88         0.1694         H112         0.0914         C136         -0.153         C160         0.1498         H184           0.1430         H89         0.1741         C113         -0.1373         C137         0.1007         C161         -0.1549         H184           0.0075         H91         0.1009         C115         0.2941         C139         0.1561         H187         H187           0.0638         C92         -0.1212 </td <td>-0.5525</td> <td>Η</td> <td>28</td> <td>0.1121</td> <td>H82</td> <td>0.2267</td> <td>C106</td> <td>-0.1286</td> <td>C130</td> <td>0.0661</td> <td>H154</td> <td>0.1620</td> <td>C178</td> <td>-0.1390</td>	-0.5525	Η	28	0.1121	H82	0.2267	C106	-0.1286	C130	0.0661	H154	0.1620	C178	-0.1390
0.1135         H84         0.1583         C108         -0.1143         C132         -0.1020         C156         0.0892         H180           0.1138         H85         0.1644         H109         0.1244         C133         -0.1568         C157         -0.1099         H181           0.1157         H86         0.1773         C110         0.0159         N134         -0.4089         C158         0.1530         H182           0.1159         H87         0.1716         C111         -0.1181         C135         0.1539         N159         -0.4097         H182           0.1430         H88         0.1694         H112         0.0914         C136         -0.1153         C160         0.1498         H184           0.1430         H89         0.1741         C113         -0.1373         C137         0.1007         C161         -0.1549         H184           -0.0007         H91         0.1009         C115         0.2941         C139         0.164         H162         0.1424         H184           -0.003         C92         -0.1212         C116         -0.1409         H140         0.1606         C164         -0.1625         H188           -0.5000         H	0.1391	Η	59	0.1119	H83	0.1657	H107	0.0615	C131	-0.1016	H155	0.1884	C179	0.1564
0.1138         H85         0.1644         H109         0.1244         C133         -0.1568         C157         -0.1099         H181           0.1157         H86         0.1773         C110         0.0159         N134         -0.4089         C158         0.1530         H182           0.1159         H87         0.1716         C111         -0.1181         C135         0.1539         N159         -0.4097         H182           0.1430         H88         0.1694         H112         0.0914         C136         -0.1153         C160         0.1498         H184           0.1430         H89         0.1741         C113         -0.1373         C137         0.1007         C161         -0.1540         H184           -0.4732         C90         -0.1071         H114         0.0975         C138         -0.1484         H162         0.1422         H186           -0.0007         H91         0.1009         C115         0.2941         C139         0.1561         H187         H187           0.0638         C92         -0.1212         C116         -0.1409         H140         0.1606         C164         -0.1625         H188           -0.5000         H93         0.	0.1361	Η	09	0.1135	H84	0.1583	C108	-0.1143	C132	-0.1020	C156	0.0892	H180	0.1806
0.1157         H86         0.1773         C110         0.0159         N134         -0.4089         C158         0.1530         H182           0.1159         H87         0.1716         C111         -0.1181         C135         0.1539         N159         -0.4097         H183           0.1430         H88         0.1694         H112         0.0914         C136         -0.1153         C160         0.1498         H184           0.1430         H89         0.1741         C113         -0.1373         C137         0.1007         C161         -0.1540         H184           -0.4732         C90         -0.1071         H114         0.0975         C138         -0.1484         H162         0.1422         H186           -0.0007         H91         0.1009         C115         0.2941         C139         0.1561         H187         H187           0.0638         C92         -0.1212         C116         -0.1409         H140         0.1606         C164         -0.1625         H188           -0.5000         H93         0.1295         H117         0.1058         H141         0.1223         C166         -0.1177         H190           0.0069         C94         0.2	0.0987	Ξ	.61	0.1138	H85	0.1644	H109	0.1244	C133	-0.1568	C157	-0.1099	H181	0.1545
0.1159         H87         0.1716         C1111         -0.1181         C135         0.1539         N159         -0.4097         H183           0.1430         H88         0.1694         H112         0.0914         C136         -0.1153         C160         0.1498         H184           0.1430         H89         0.1741         C113         -0.1373         C137         0.1007         C161         -0.1540         H184           -0.0007         H91         0.1009         C115         0.2941         C138         -0.1484         H162         0.1422         H186           -0.0007         H91         0.1009         C115         0.2941         C139         0.1561         H162         0.1422         H186           -0.0038         C92         -0.1212         C116         -0.1409         H140         0.1606         C164         -0.1625         H188           -0.5000         H93         0.1295         H117         0.1058         H141         0.1223         C165         0.0908         H189           0.0065         C94         0.3217         C118         -0.1256         H142         0.1615         C166         -0.1177         H190           0.0099 <td< td=""><td>0.1019</td><td>Ξ</td><td>62</td><td>0.1157</td><td>98H</td><td>0.1773</td><td>C110</td><td>0.0159</td><td>N134</td><td>-0.4089</td><td>C158</td><td>0.1530</td><td>H182</td><td>0.1509</td></td<>	0.1019	Ξ	62	0.1157	98H	0.1773	C110	0.0159	N134	-0.4089	C158	0.1530	H182	0.1509
0.1430         H88         0.1694         H112         0.0914         C136         -0.1153         C160         0.1498         H184           0.1430         H89         0.1741         C113         -0.1373         C137         0.1007         C161         -0.1540         H185           -0.4732         C90         -0.1071         H114         0.0975         C138         -0.1484         H162         0.1422         H186           -0.0007         H91         0.1009         C115         0.2941         C139         0.1561         H163         0.1747         H187           0.0638         C92         -0.1212         C116         -0.1409         H140         0.1606         C164         -0.1625         H188           -0.5000         H93         0.1295         H117         0.1058         H141         0.1223         C165         0.0908         H189           0.0605         C94         0.3217         C118         -0.1256         H142         0.1615         C166         -0.1177         H190           0.0099         C95         -0.1208         H119         0.1084         H143         0.1848         C167         -0.1147         H191           -0.4819 <td< td=""><td>0.1090</td><td>Ĭ</td><td>53</td><td>0.1159</td><td>H87</td><td>0.1716</td><td>C1111</td><td>-0.1181</td><td>C135</td><td>0.1539</td><td>N159</td><td>-0.4097</td><td>H183</td><td>0.1758</td></td<>	0.1090	Ĭ	53	0.1159	H87	0.1716	C1111	-0.1181	C135	0.1539	N159	-0.4097	H183	0.1758
0.1430         H89         0.1741         C113         -0.1373         C137         0.1007         C161         -0.1540         H185           -0.4732         C90         -0.1071         H114         0.0975         C138         -0.1484         H162         0.1422         H186           -0.0007         H91         0.1009         C115         0.2941         C139         0.1561         H163         0.1747         H187           0.0638         C92         -0.1212         C116         -0.1409         H140         0.1606         C164         -0.1625         H188           -0.5000         H93         0.1295         H117         0.1058         H141         0.1223         C165         0.0908         H189           0.0605         C94         0.3217         C118         -0.1256         H142         0.1615         C166         -0.1177         H190           0.0099         C95         -0.1208         H119         0.1084         H143         0.1848         C167         -0.1147         H191           -0.4819         H96         0.1291         C120         0.1612         H144         0.1835         C168         0.0879         Total	0.1037	H	74	0.1430	H88	0.1694	H112	0.0914	C136	-0.1153	C160	0.1498	H184	0.1839
-0.4732         C90         -0.1071         H114         0.0975         C138         -0.1484         H162         0.1422         H186           -0.0007         H91         0.1009         C115         0.2941         C139         0.1561         H163         0.1747         H187           0.0638         C92         -0.1212         C116         -0.1409         H140         0.1606         C164         -0.1625         H188           -0.5000         H93         0.1295         H117         0.1058         H141         0.1223         C165         0.0908         H189           0.0605         C94         0.3217         C118         -0.1256         H142         0.1615         C166         -0.1177         H190           0.0099         C95         -0.1208         H119         0.1084         H143         0.1848         C167         -0.1147         H191           -0.4819         H96         0.1291         C120         0.1612         H144         0.1835         C168         0.0879         Total	-0.5282	Ξ	92	0.1430	68H	0.1741	C113	-0.1373	C137	0.1007	C161	-0.1540	H185	0.1841
-0.0007         H91         0.1009         C115         0.2941         C139         0.1561         H163         0.1747         H187           0.0638         C92         -0.1212         C116         -0.1409         H140         0.1606         C164         -0.1625         H188           -0.5000         H93         0.1295         H117         0.1058         H141         0.1223         C165         0.0908         H189           0.0605         C94         0.3217         C118         -0.1256         H142         0.1615         C166         -0.1177         H190           0.0099         C95         -0.1208         H119         0.1084         H143         0.1848         C167         -0.1147         H191           -0.4819         H96         0.1291         C120         0.1612         H144         0.1835         C168         0.0879         Total	0.0433	0	99	-0.4732	C30	-0.1071	H114	0.0975	C138	-0.1484	H162	0.1422	H186	0.1463
0.0638         C92         -0.1212         C116         -0.1409         H140         0.1606         C164         -0.1625         H188           -0.5000         H93         0.1295         H117         0.1058         H141         0.1223         C165         0.0908         H189           0.0605         C94         0.3217         C118         -0.1256         H142         0.1615         C166         -0.1177         H190           0.0099         C95         -0.1208         H119         0.1084         H143         0.1848         C167         -0.1147         H191           -0.4819         H96         0.1291         C120         0.1612         H144         0.1835         C168         0.0879         Total	0.0586	$\circ$	297	-0.0007	H91	0.1009	C115	0.2941	C139	0.1561	H163	0.1747	H187	0.1442
-0.5000         H93         0.1295         H117         0.1058         H141         0.1223         C165         0.0908         H189           0.0665         C94         0.3217         C118         -0.1256         H142         0.1615         C166         -0.1177         H190           0.0099         C95         -0.1208         H119         0.1084         H143         0.1848         C167         -0.1147         H191           -0.4819         H96         0.1291         C120         0.1612         H144         0.1835         C168         0.0879         Total	-0.5118	$\circ$	89	0.0638	C92	-0.1212	C116	-0.1409	H140	0.1606	C164	-0.1625	H188	0.1815
0.0605         C94         0.3217         C118         -0.1256         H142         0.1615         C166         -0.1177         H190           0.0099         C95         -0.1208         H119         0.1084         H143         0.1848         C167         -0.1147         H191           -0.4819         H96         0.1291         C120         0.1612         H144         0.1835         C168         0.0879         Total	0.0609	$\circ$	69(	-0.5000	H93	0.1295	H117	0.1058	H141	0.1223	C165	0.0908	H189	0.1806
0.0099 C95 -0.1208 H119 0.1084 H143 0.1848 C167 -0.1147 H191 -0.4819 H96 0.1291 C120 0.1612 H144 0.1835 C168 0.0879 Total	0.0118	$\circ$	270	0.0605	C94	0.3217	C118	-0.1256	H142	0.1615	C166	-0.1177	H190	0.1642
-0.4819 H96 0.1291 C120 0.1612 H144 0.1835 C168 0.0879 Total	-0.4865	$\overline{}$	271	0.0099	C95	-0.1208	H119	0.1084	H143	0.1848	C167	-0.1147	H191	0.1429
	0.4187	$\circ$	372	-0.4819	96H	0.1291	C120	0.1612	H144	0.1835	C168	0.0879	Total	5.0000

continued)
8.2
$\infty$
<u>e</u>
9
[z]

	1009	1037	1237	1212	1658	4128	1636	1239	1022	1448	1494	1838	1511	1447	1668	1852	1821	1414	1374	1880	1782	1710	1443	5.0000
		'			'																			
	C169	C170	H171	H172	C173	N174	C175	C176	C177	C178	C179	H180	H181	H182	H183	H184	H185	H186	H187	H188	H189	H190	H191	Total
	0.1850	0.1400	0.1348	0.1240	0.1230	0.1750	0.1866	0.1679	0.1395	0.1579	0.1848	0.0961	-0.1184	0.1498	-0.4024	0.1512	-0.1455	0.1578	0.1864	-0.1733	0.0757	-0.1127	-0.1171	0.0705
	H145	H146	H147	H148	H149	H150	H151	H152	H153	H154	H155	C156	C157	C158	N159	C160	C161	H162	H163	C164	C165	C166	C167	C168
	-0.1220	0.1014	-0.1415	0.1478	-0.4094	-0.1666	0.0705	-0.1168	-0.1133	0.0800	-0.1032	-0.1022	-0.1749	-0.4049	0.1483	-0.1216	0.0953	-0.1466	0.1509	0.1669	0.1448	0.1545	0.1841	0.1849
	C121	C122	C123	C124	N125	C126	C127	C128	C129	C130	C131	C132	C133	N134	C135	C136	C137	C138	C139	H140	H141	H142	H143	H144
	-0.1288	0.0887	0.0142	0.0258	-0.1343	0.1045	-0.1331	0.1012	0.0236	-0.1334	0.1035	-0.1352	0.1016	0.0147	-0.1260	0.0908	-0.1250	0.1357	0.3218	-0.1265	0.1336	-0.1270	9980.0	0.1617
	C97	86H	C39	C100	C101	H102	C103	H104	C105	C106	H107	C108	H109	C110	C1111	H112	C113	H114	C115	C116	H117	C118	H1119	C120
	0.1543	0.1539	0.1127	0.1129	0.1139	0.1136	0.1016	0.1015	0.3260	0.2266	0.1881	0.1474	0.1624	0.1809	0.1669	0.1700	0.1804	-0.1297	0.0843	-0.1272	0.1343	0.3257	-0.1257	0.1366
	H73	H74	H75	9/H	H77	H78	H79	H80	H81	H82	H83	H84	H85	98H	H87	H88	68H	C30	H91	C92	H93	C94	C95	96H
	-0.1541	-0.0587	-0.0484	-0.0655	-0.0675	-0.0430	-0.0610	-0.1402	0.4263	0.1073	0.1030	0.1173	0.1186	0.1194	0.1201	0.1384	0.1373	-0.4639	-0.0075	0.0711	-0.4999	0.0572	0.0379	-0.5359
	C49	C50	C51	C52	C53	C54	C55	C56	C57	H58	H59	09H	H61	H62	H63	H64	H65	990	C67	C68	690	C70	C71	072
	-0.3046	0.4139	-0.2438	-0.1407	0.4096	0.0736	-0.5188	0.0549	0.0401	-0.5219	0.1461	0.1439	0.1078	0.1059	0.1271	0.1257	-0.5212	0.0389	0.0634	-0.5154	0.0541	0.0205	-0.4931	0.4154
	C25	S26	C27	C28	S29	C30	031	C32	C33	034	H35	H36	H37	H38	H39	H40	041	C42	C43	944	C45	C46	047	C48
: 28.17 Å	-0.4928	0.0234	0.0599	-0.4841	0.0624	0.0370	-0.5153	0.0854	-0.1351	-0.2356	0.4361	-0.3111	0.4220	0.3384	0.1202	0.1200	0.1174	0.1179	0.1128	0.1134	0.1246	0.1252	0.1465	0.1473
z = 2	01	C2	C3	90	C2	9) Ce	07	% C3	60	C10	S11	C12	S13	H14	H15	H16	H17	H18	H19	H20	H21	H22	H23	H24

Table 8.2 (continued)

01         -0.4888         C25         -0.3055         C49           C2         0.0209         S26         0.4325         C50           C3         0.0612         C27         -0.2413         C51           O4         -0.4864         C28         -0.1392         C52           C5         0.0626         S29         0.4228         C53           C6         0.0371         C30         0.0786         C54           O7         -0.5154         O31         -0.5166         C55           C8         0.0833         C32         0.0495         C56           C9         -0.1355         C32         0.0495         C56           C10         -0.2355         O34         -0.5276         H58           S11         0.4472         H35         0.1464         H69           H14         0.3394         H38         0.1131         H61           H15         0.1225         H39         0.1134         H63           H16         0.1223         H40         0.1234         H64           H18         0.1123         C42         0.0453         O6453         O6453         O6453	-0.1591 -0.0615 -0.0541 -0.0651 -0.0661 -0.0505 -0.0444 0.4206 0.0989 0.0988	H73 H74 H75 H76 H77	0.1520	C97	-0.1275	C121	-0.1238	H145	0.1815	0160	-0.1070
0.4325 -0.2413 -0.1392 0.4228 0.0786 -0.5166 0.0437 -0.5276 0.1442 0.1131 0.1134 0.1248										C107	0.01.0
-0.2413 -0.1392 0.4228 0.0786 -0.5166 0.0437 -0.5276 0.1442 0.1131 0.1134 0.1248			0.1511	H98	0.0994	C122	0.0918	H146	0.1477	C170	-0.1063
C28 -0.1392 S29 0.4228 C30 0.0786 O31 -0.5166 C32 0.0495 C33 0.0437 O34 -0.5276 H35 0.1464 H36 0.1442 H37 0.1131 H39 0.1248 H40 0.1234 O41 -0.5431			0.1187	C39	0.0162	C123	-0.1400	H147	0.1457	H171	0.1174
S29 0.4228 C30 0.0786 O31 -0.5166 C32 0.0495 C33 0.0437 O34 -0.5276 H35 0.1464 H36 0.1442 H37 0.1131 H38 0.1130 H40 0.1234 O41 -0.5431			0.1194	C100	0.0346	C124	0.1501	H148	0.1262	H172	0.1212
C30 0.0786 O31 -0.5166 C32 0.0495 C33 0.0437 O34 -0.5276 H35 0.1464 H36 0.1442 H37 0.1131 H38 0.1130 H39 0.1248 H40 0.1234 O41 -0.5431			0.1210	C101	-0.1438	N125	-0.4156	H149	0.1336	C173	-0.1661
O31 -0.5166 C32 0.0495 C33 0.0437 O34 -0.5276 H35 0.1464 H36 0.1442 H37 0.1131 H38 0.1130 H39 0.1248 H40 0.1234 O41 -0.5431			0.1210	H102	0.0426	C126	-0.1551	H150	0.1796	N174	-0.4137
C32 0.0495 C33 0.0437 O34 -0.5276 H35 0.1464 H36 0.1442 H37 0.1131 H38 0.1130 H39 0.1248 H40 0.1234 O41 -0.5431	•		0.1235	C103	-0.1115	C127	0.0779	H151	0.1805	C175	0.1586
C33 0.0437 O34 -0.5276 H35 0.1464 H36 0.1442 H37 0.1131 H38 0.1130 H39 0.1248 H40 0.1234 O41 -0.5431			0.1232	H104	0.1242	C128	-0.1164	H152	0.1832	C176	-0.1316
O34 -0.5276 H35 0.1464 H36 0.1442 H37 0.1131 H38 0.1130 H39 0.1248 H40 0.1234 O41 -0.5431			0.3422	C105	0.0484	C129	-0.1181	H153	0.1505	C177	0.0963
H35 0.1464 H36 0.1442 H37 0.1131 H38 0.1130 H39 0.1248 H40 0.1234 O41 -0.5431			0.2275	C106	-0.1146	C130	0.0784	H154	0.1504	C178	-0.1443
H36 0.1442 H37 0.1131 H38 0.1130 H39 0.1248 H40 0.1234 O41 -0.5431			0.2056	H107	0.1231	C131	-0.1234	H155	0.1791	C179	0.1514
H37 0.1131 H38 0.1130 H39 0.1248 H40 0.1234 O41 -0.5431			0.1360	C108	-0.1252	C132	-0.1205	C156	0.0930	H180	0.1823
H38 0.1130 H39 0.1248 H40 0.1234 O41 -0.5431			0.1570	H109	0.0837	C133	-0.1566	C157	-0.1251	H181	0.1597
H39 0.1248 H40 0.1234 O41 -0.5431 C42 0.0453			0.1749	C110	0.0170	N134	-0.4416	C158	0.1505	H182	0.1343
H40 0.1234 O41 -0.5431 C42 0.0453			0.1543	C1111	-0.1060	C135	0.1656	N159	-0.4109	H183	0.1678
O41 -0.5431 C42 0.0453			0.1622	H112	0.1050	C136	-0.1168	C160	0.1495	H184	0.1790
C42 0.0453			0.1736	C113	-0.1203	C137	0.0869	C161	-0.1488	H185	0.1821
1		'	0.1240	H114	0.1299	C138	-0.1544	H162	0.1559	H186	0.1412
C43 0.0711			0.1012	C115	0.3175	C139	0.1468	H163	0.1816	H187	0.1412
044 -0.5149		'	0.0937	C116	-0.1215	H140	0.1717	C164	-0.1648	H188	0.1839
C45 0.0499			0.0693	H117	0.1298	H141	0.1432	C165	0.0763	H189	0.1797
C46 0.0298			0.2897	C118	-0.1063	H142	0.1565	C166	-0.1187	H190	0.1686
047 -0.5010		C95 –	0.1365	H119	0.1007	H143	0.1827	C167	-0.1169	H191	0.1470
C48 0.4068			0.0984	C120	0.1604	H144	0.1832	C168	0.0781	Total	5.0000

tinue
(con
8.2
$\frac{8}{2}$

z=3	6.84 Å														
01	-0.4780	C25	-0.3059	C49	- 1	H73	0.1457	C97	-0.1141	C121	-0.1377	H145	0.1861	C169	-0.11115
C2	0.0175	S26	0.4552	C50	1	H74	0.1447	86H	0.1227	C122	0.0804	H146	0.1496	C170	-0.1092
C3	0.0589	C27	-0.2386	C51		H75	0.1199	C39	0.0371	C123	-0.1468	H147	0.1497	H171	0.1291
04	-0.4819	C28	-0.1377	C52	- 1	9/H	0.1207	C100	0.0304	C124	0.1499	H148	0.1126	H172	0.1299
C2	0.0596	S29	0.4418	C53	'	H77	0.1233	C101	-0.1140	N125	-0.4076	H149	0.1137	C173	-0.1610
92	0.0362	C30	0.0814	C54		H78	0.1233	H102	0.0808	C126	-0.1646	H150	0.1855	N174	-0.4067
07	-0.5155	031	-0.5159	C55	-0.0691	H79	0.1265	C103	-0.1116	C127	0.0770	H151	0.1835	C175	0.1615
83 C8	0.0846	C32	0.0445	C56		H80	0.1262	H104	0.1197	C128	-0.1148	H152	0.1824	C176	-0.1219
60	-0.1353	C33	0.0490	C57		H81	0.3451	C105	0.0416	C129	-0.1141	H153	0.1570	C177	0.0846
C10	-0.2343	034	-0.5312	H58		H82	0.2313	C106	-0.1124	C130	0.0807	H154	0.1618	C178	-0.1451
S11	0.4658	H35	0.1491	H59		H83	0.2184	H107	0.1214	C131	-0.1084	H155	0.1857	C179	0.1586
C12	-0.3100	H36	0.1467	H60		H84	0.1078	C108	-0.1160	C132	-0.1080	C156	0.0831	H180	0.1874
S13	0.4476	H37	0.1121	H61		H85	0.1442	H109	0.1027	C133	-0.1689	C157	-0.1190	H181	0.1657
H14	0.3433	H38	0.1122	H62		98H	0.1674	C110	0.0234	N134	-0.4066	C158	0.1610	H182	0.1364
H15	0.1279	H39	0.1253	H63		H87	0.1083	C1111	-0.1057	C135	0.1597	N159	-0.4106	H183	0.1700
H16	0.1276	H40	0.1237	H64		H88	0.1394	H1112	0.1091	C136	-0.1349	C160	0.1547	H184	0.1841
H17	0.1205	041	-0.5481	H65		68H	0.1627	C113	-0.1230	C137	0.0777	C161	-0.1469	H185	0.1794
H18	0.1210	C42	0.0559	990	'	C90	-0.1141	H114	0.1205	C138	-0.1475	H162	0.1640	H186	0.1426
H19	0.1160	C43	0.0590	C67		H91	0.1261	C115	0.3116	C139	0.1513	H163	0.1891	H187	0.1423
H20	0.1167	044	-0.5199	S92		C92	-0.1430	C116	-0.1237	H140	0.1805	C164	-0.1589	H188	0.1812
H21	0.1267	C45	0.0565	690	1	H93	0.0746	H1117	0.1218	H141	0.1545	C165	0.0704	H189	0.1830
H22	0.1272	C46	0.0451	C70		C94	0.3033	C118	-0.1055	H142	0.1606	C166	-0.1188	H190	0.1685
H23	0.1502	047	-0.5189	C71		C95	-0.1395	H1119	0.1087	H143	0.1857	C167	-0.1193	H191	0.1350
H24	t 0.1511 C	C48	0.3783	072	۱ '	96H	0.0770	C120	0.1590	H144	0.1823	C168	0.0710	Total	5.0000

Table 8.2 (continued)

2 = 2	0.99 Å														
01	-0.4992 C	C25	-0.3052	C49	-0.2062	H73	0.1302	C97	-0.0937	C121	-0.1396	H145	0.1771	C169	-0.1085
C2	0.0230	S26	0.4336	C50	-0.1216	H74	0.1316	H98	0.1388	C122	0.1037	H146	0.1400	C170	-0.1091
C3	0.0623	C27	-0.2415	C51	-0.0954	H75	0.0984	C39	0.0306	C123	-0.1447	H147	0.1386	H171	0.1123
9	-0.4923	C28	-0.1401	C52	-0.0744	9/H	0.0972	C100	0.0635	C124	0.1508	H148	0.1248	H172	0.1116
C2	0.0644	S29	0.4192	C53	-0.0847	H77	0.1055	C101	-0.1005	N125	-0.4065	H149	0.1268	C173	-0.1672
92	0.0370	C30	0.0748	C54	-0.1236	H78	0.1047	H102	0.1441	C126	-0.1595	H150	0.1769	N174	-0.4123
07	-0.5151	031	-0.5161	C55	-0.0831	H79	0.0988	C103	-0.0929	C127	0.0680	H151	0.1839	C175	0.1629
8 C8	0.0858	C32	0.0531	C56	-0.1755	H80	0.0991	H104	0.1535	C128	-0.1229	H152	0.1668	C176	-0.1334
C3	-0.1350	C33	0.0254	C57	0.3903	H81	0.3248	C105	0.0547	C129	-0.1157	H153	0.1349	C177	0.0901
C10	-0.2353	034	-0.5065	H58	0.1096	H82	0.2279	C106	-0.0931	C130	0.0555	H154	0.1655	C178	-0.1570
S11	0.4466	H35	0.1482	H59	0.1145	H83	0.2015	H107	0.1532	C131	-0.0949	H155	0.1898	C179	0.1527
C12	-0.3107	H36	0.1457	09H	0.0992	H84	0.0939	C108	-0.1002	C132	-0.0938	C156	0.0757	H180	0.1804
S13	0.4285	H37	0.1284	H61	0.0979	H85	0.0850	H109	0.1506	C133	-0.1555	C157	-0.1247	H181	0.1503
H14	0.3362	H38	0.1296	H62	0.0878	98H	0.1508	C110	0.0440	N134	-0.4102	C158	0.1650	H182	0.1579
H15	0.1181	H39	0.1305	H63	0.0936	H87	0.0754	C1111	-0.0867	C135	0.1532	N159	-0.4120	H183	0.1842
H16	0.1180	H40	0.1284	H64	0.0988	H88	0.1119	H112	0.1508	C136	-0.1427	C160	0.1494	H184	0.1839
H17	0.1145	041	-0.5271	H65	0.1039	68H	0.1475	C113	-0.1067	C137	0.1120	C161	-0.1477	H185	0.1776
H18	0.1149	C42	0.0499	990	-0.5136	C30	-0.0934	H114	0.1653	C138	-0.1479	H162	0.1495	H186	0.1473
H19	0.1097	C43	0.0587	C67	0.0182	H91	0.1407	C115	0.3524	C139	0.1527	H163	0.1791	H187	0.1477
H20	0.1104	044	-0.5158	C68	0.0765	C92	-0.1192	C116	-0.1075	H140	0.1651	C164	-0.1639	H188	0.1805
H21	0.1237	C45	0.0544	690	-0.5080	H93	0.1348	H117	0.1665	H141	0.1364	C165	0.0805	H189	0.1829
H22	0.1243	C46	0.0506	C70	0.0643	C94	0.3263	C118	-0.0862	H142	0.1657	C166	-0.1211	H190	0.1792
H23	0.1465	047	-0.5233	C71	0.0386	C95	-0.1188	H119	0.1508	H143	0.1905	C167	-0.1112	H191	0.1594
H24	0.1473	C48	0.3478	072	-0.5380	96H	0.1314	C120	0.1535	H144	0.1872	C168	0.0898	Total	5.0000

(continued)
8.2
Table

z = 4	= 44.83 Å														
01	-0.4636	C25	-0.2904	C49	-0.1990	H73	0.1223	C97	-0.0948	C121	-0.1319	H145	0.1880	C169	-0.0988
C2	0.0124	S26	0.4261	C50	-0.0934	H74	0.1326	86H	0.1313	C122	0.1041	H146	0.1238	C170	-0.1125
C3	0.0579	C27	-0.2396	C51	-0.1192	H75	0.0692	C39	0.0345	C123	-0.1509	H147	0.1226	H171	0.1317
04	-0.4846	C28	-0.1349	C52	-0.0826	9/H	0.0779	C100	0.0589	C124	0.1581	H148	0.1412	H172	0.1327
CS	0.0538	S29	0.4100	C53	-0.0780	H77	0.1025	C101	-0.1036	N125	-0.4267	H149	0.1397	C173	-0.1673
92	0.0414	C30	0.0771	C54	-0.1208	H78	0.1021	H102	0.1321	C126	-0.1657	H150	0.1805	N174	-0.4234
07	-0.5150	031	-0.5155	C55	-0.0885	H79	0.1047	C103	-0.0992	C127	0.0880	H151	0.1841	C175	0.1675
C8	0.0830	C32	0.0512	C56	-0.2005	H80	0.1057	H104	0.1396	C128	-0.1059	H152	0.1679	C176	-0.1352
60	-0.1320	C33	0.0356	C57	0.3654	H81	0.3330	C105	0.0546	C129	-0.11111	H153	0.1411	C177	0.1129
C10	-0.2355	034	-0.5181	H58	0.1172	H82	0.2157	C106	-0.0993	C130	0.0847	H154	0.1586	C178	-0.1504
S11	0.4373	H35	0.1435	H59	0.1186	H83	0.2003	H107	0.1383	C131	-0.1145	H155	0.1815	C179	0.1584
C12	-0.2964	H36	0.1413	H60	0.1086	H84	0.1308	C108	-0.1033	C132	-0.1001	C156	0.1016	H180	0.1835
S13	0.4175	H37	0.1212	H61	0.1078	H85	0.0945	H109	0.1361	C133	-0.1656	C157	-0.1273	H181	0.1549
H14	0.3483	H38	0.1219	H62	0.0840	98H	0.1219	C110	0.0370	N134	-0.4121	C158	0.1589	H182	0.1408
H15	0.1349	H39	0.1256	H63	0.0830	H87	0.1165	C1111	-0.0929	C135	0.1512	N159	-0.4164	H183	0.1729
H16	0.1346	H40	0.1239	H64	0.1211	H88	0.0935	H112	0.1355	C136	-0.1263	C160	0.1525	H184	0.1918
H17	0.1242	041	-0.5292	H65	0.1339	68H	0.1350	C113	-0.1141	C137	0.1089	C161	-0.1361	H185	0.1777
H18	0.1247	C42	0.0492	990	-0.5292	C90	-0.0947	H114	0.1455	C138	-0.1370	H162	0.1583	H186	0.1386
H19	0.1199	C43	0.0512	C67	0.0195	H91	0.1325	C115	0.3377	C139	0.1461	H163	0.1840	H187	0.1358
H20	0.1204	94	-0.5034	S92	0.0889	C92	-0.1198	C116	-0.1149	H140	0.1673	C164	-0.1687	H188	0.1837
H21	0.1240	C45	0.0793	690	-0.4997	H93	0.1289	H117	0.1467	H141	0.1412	C165	0.0775	H189	0.1897
H22	0.1246	C46	0.0252	C70	0.0566	C94	0.3262	C118	-0.0925	H142	0.1672	C166	-0.1065	H190	0.1814
H23	0.1432	047	-0.5309	C71	0.0416	C95	-0.1194	H119	0.1356	H143	0.1925	C167	-0.1065	H191	0.1532
H24	0.1440	C48	0.3580	072	-0.5359	96H	0.1270	C120	0.1700	H144	0.1806	C168	0.0845	Total	5.0000

**Table 8.3** Partial charge distribution of +2 oxidized rotaxane when the center of mass of the CBPQT<sup>4+</sup> ring moves from  $z = 10.92 \,\text{Å}$  (TTF side) to  $z = 44.83 \,\text{Å}$  (DNP side)

†   	2 - ++.03 A (DINE SIDE)	(and )													
z = 1	10.92 Å														
01	-0.4596	C25	-0.3297	C49	-0.1448	H73	0.1605	C97	-0.0890	C121	-0.1310	H145	0.1870	C169	-0.0978
C2	0.0112	S26	0.2671	C50	-0.0570	H74	0.1600	86H	0.1477	C122	0.1127	H146	0.1497	C170	-0.1009
C3	0.0601	C27	-0.2613	C51	-0.0393	H75	0.1526	C39	0.0436	C123	-0.1525	H147	0.1491	H171	0.1214
04	-0.5032	C28	-0.1534	C52	-0.0648	H76	0.1532	C100	0.0567	C124	0.1549	H148	0.1198	H172	0.1226
C2	0.0762	S29	0.2547	C53	-0.0642	H77	0.1534	C101	-0.0954	N125	-0.4061	H149	0.1228	C173	-0.1764
9) Ce	0.0345	C30	0.0905	C54	-0.0415	H78	0.1531	H102	0.1515	C126	-0.1737	H150	0.1899	N174	-0.4069
07	-0.5166	031	-0.5123	C55	-0.0562	H79	0.1677	C103	-0.0997	C127	0.0954	H151	0.1862	C175	0.1722
% C3	0.0915	C32	0.0442	C56	-0.1448	H80	0.1678	H104	0.1501	C128	-0.1221	H152	0.1827	C176	-0.1327
60	-0.1514	C33	0.0456	C57	0.4249	H81	0.3747	C105	0.0591	C129	-0.1217	H153	0.1514	C177	0.1176
C10	-0.2763	034	-0.5221	H58	0.1280	H82	0.1856	C106	-0.1000	C130	0.0888	H154	0.1580	C178	-0.1521
S11	0.2751	H35	0.1293	H59	0.1286	H83	0.1931	H107	0.1437	C131	-0.1042	H155	0.1862	C179	0.1577
C12	-0.3321	H36	0.1063	09H	0.1244	H84	0.1679	C108	-0.0952	C132	-0.0977	C156	0.1078	H180	0.1938
S13	0.2665	H37	0.1132	H61	0.1245	H85	0.1747	H109	0.1514	C133	-0.1743	C157	-0.1274	H181	0.1680
H14	0.3545	H38	0.1204	H62	0.1238	98H	0.1779	C110	0.0305	N134	-0.4037	C158	0.1623	H182	0.1435
H15	0.1376	H39	0.1284	H63	0.1239	H87	0.1767	C1111	-0.0926	C135	0.1664	N159	-0.4063	H183	0.1691
H16	0.1391	H40	0.1186	H64	0.1506	H88	0.1773	H112	0.1390	C136	-0.1257	C160	0.1454	H184	0.1794
H17	0.1185	041	-0.5087	H65	0.1508	68H	0.1737	C113	-0.1172	C137	0.1125	C161	-0.1501	H185	0.1940
H18	0.1161	C42	0.0274	990	-0.4813	C30	-0.0889	H114	0.1361	C138	-0.1401	H162	0.1623	H186	0.1345
H19	0.1033	C43	0.0556	C67	0.0039	H91	0.1472	C115	0.3280	C139	0.1597	H163	0.1873	H187	0.1400
H20	0.0933	94	-0.5029	892	0.0341	C92	-0.1086	C116	-0.1179	H140	0.1757	C164	-0.1709	H188	0.1880
H21	0.1135	C45	0.0554	690	-0.4294	H93	0.1625	H117	0.1421	H141	0.1460	C165	0.0882	H189	0.1862
H22	0.1258	C46	0.0061	C70	0.0396	C94	0.3505	C118	-0.0918	H142	0.1607	C166	-0.1152	H190	0.1690
H23	0.0969	047	-0.4769	C71	-0.0059	C95	-0.1083	H119	0.1421	H143	0.1861	C167	-0.1159	H191	0.1410
H24	0.1266	C48	0.4245	072	-0.3868	96H	0.1617	C120	0.1602	H144	0.1879	C168	0.0939	Total	000009

Fable 8.3 (continued

	-0.1049	-0.1068	0.1288	0.1285	-0.1689	-0.4098	0.1471	-0.1336	0.1091	-0.1533	0.1599	0.1917	0.1645	0.1376	0.1691	0.1837	0.1901	0.1478	0.1465	0.1913	0.1841	0.1783	0.1474	000009
	C169	C170	H171	H172	C173	N174	C175	C176	C177	C178	C179	H180	H181	H182	H183	H184	H185	H186	H187	H188	H189	H190	H191	Total
	0.1896	0.1525	0.1511	0.1144	0.1136	0.1854	0.1830	0.1806	0.1505	0.1585	0.1841	0.0951	-0.1149	0.1142	-0.3991	0.1602	-0.1393	0.1687	0.1956	-0.1654	0.0761	-0.1223	-0.1204	0.0815
	H145	H146	H147	H148	H149	H150	H151	H152	H153	H154	H155	C156	C157	C158	N159	C160	C161	H162	H163	C164	C165	C166	C167	C168
	-0.1283	0.1048	-0.1534	0.1553	-0.4058	-0.1604	0.0836	-0.1117	-0.1134	0.0914	-0.1145	-0.1148	-0.1643	-0.4148	0.1679	-0.1310	0.0987	-0.1556	0.1524	0.1830	0.1564	0.1604	0.1900	0.1857
	C121	C122	C123	C124	N125	C126	C127	C128	C129	C130	C131	C132	C133	N134	C135	C136	C137	C138	C139	H140	H141	H142	H143	H144
	-0.0898	0.1472	0.0460	0.0523	-0.0960	0.1493	-0.1033	0.1443	0.0568	-0.1036	0.1350	-0.0957	0.1481	0.0275	-0.0957	0.1360	-0.1210	0.1188	0.3156	-0.1221	0.1245	-0.0948	0.1392	0.1670
	C97	86H	C39	C100	C101	H102	C103	H104	C105	C106	H107	C108	H109	C110	C1111	H112	C113	H114	C115	C116	H117	C118	H119	C120
	0.1600	0.1594	0.1521	0.1527	0.1523	0.1520	0.1701	0.1703	0.3757	0.2056	0.1630	0.1655	0.1726	0.1762	0.1755	0.1758	0.1723	-0.0896	0.1468	-0.1073	0.1643	0.3521	-0.1071	0.1634
	H73	H74	H75	9/H	H77	H78	H79	H80	H81	H82	H83	H84	H85	98H	H87	H88	68H	C30	H91	C92	H93	C94	C95	96H
	-0.1464	-0.0571	-0.0409	-0.0654	-0.0652	-0.0423	-0.0564	-0.1465	0.4244	0.1278	0.1285	0.1213	0.1214	0.1211	0.1211	0.1485	0.1487	-0.4837	0.0046	0.0344	-0.4322	0.0408	-0.0071	-0.3773
	C49	C50	C51	C52	C53	C54	C55	C56	C57	H58	H59	H60	H61	H62	H63	H64	H65	990	C67	C68	690	C70	C71	072
	-0.3665	0.2876	-0.2751	-0.1483	0.2488	0.0854	-0.5195	0.0501	0.0576	-0.5305	0.1005	0.1114	0.1058	0.1080	0.0998	0.1040	-0.5065	0.0258	0.0591	-0.5105	0.0568	0.0079	-0.4802	0.4241
	C25	S26	C27	C28	S29	C30	031	C32	C33	034	H35	H36	H37	H38	H39	H40	041	C42	C43	94	C45	C46	047	C48
5.66 Å	-0.4118	-0.0008	0.0505	-0.4609	0.0477	0.0412	-0.5142	0.0866	-0.1374	-0.2447	0.2712	-0.3073	0.2908	0.3667	0.1570	0.1568	0.1359	0.1362	0.1282	0.1282	0.1259	0.1269	0.1331	4 0.1350 C
z = 1	01	C5	C3	9	C2	92	07	C8	60	C10	S11	C12	S13	H14	H15	H16	H17	H18	H19	H20	H21	H22	H23	H24

p
Ø.
⋾
-=
Ħ
=
$\sim$
٠,
$\overline{}$
~
ų.
8.3
e 8.
le 8.
e 8.
ble 8.

z = 1	= 18.75 Å														
01	-0.4309	C25	-0.3153	C49	-0.1456	H73	0.1594	C97	-0.0949	C121	-0.1244	H145	0.1908	C169	-0.1077
C2	0.0058	S26	0.3018	C50	-0.0552	H74	0.1588	H98	0.1370	C122	0.0941	H146	0.1534	C170	-0.1065
C3	0.0513	C27	-0.2962	C51	-0.0406	H75	0.1402	C39	0.0473	C123	-0.1429	H147	0.1535	H171	0.1134
04	-0.4589	C28	-0.1575	C52	-0.0649	9/H	0.1407	C100	0.0461	C124	0.1581	H148	0.1180	H172	0.1124
C2	0.0506	S29	0.3241	C53	-0.0661	H77	0.1424	C101	-0.1007	N125	-0.4080	H149	0.1177	C173	-0.1802
92	0.0371	C30	0.0752	C54	-0.0381	H78	0.1422	H102	0.1408	C126	-0.1649	H150	0.1901	N174	-0.4006
07	-0.5151	031	-0.5172	C55	-0.0555	H79	0.1626	C103	-0.1100	C127	0.0604	H151	0.1918	C175	0.1628
8 C8	0.0845	C32	0.0582	C56	-0.1422	H80	0.1627	H104	0.1252	C128	-0.1167	H152	0.1735	C176	-0.1304
60	-0.1335	C33	0.0553	C57	0.4293	H81	0.3718	C105	0.0445	C129	-0.1200	H153	0.1370	C177	0.0951
C10	-0.2348	034	-0.5475	H58	0.1247	H82	0.2233	C106	-0.1099	C130	0.0627	H154	0.1643	C178	-0.1477
S11	0.3872	H35	0.1154	H59	0.1254	H83	0.1706	H107	0.1126	C131	-0.1025	H155	0.1960	C179	0.1541
C12	-0.3088	H36	0.1090	09H	0.1207	H84	0.1671	C108	-0.1003	C132	-0.1017	C156	0.0902	H180	0.1976
S13	0.3748	H37	0.0939	H61	0.1205	H85	0.1748	H109	0.1387	C133	-0.1670	C157	-0.1275	H181	0.1655
H14	0.3590	H38	0.0943	H62	0.1210	98H	0.1816	C110	0.0331	N134	-0.4107	C158	0.1669	H182	0.1384
H15	0.1468	H39	0.0970	H63	0.1210	H87	0.1781	C1111	-0.0991	C135	0.1678	N159	-0.4024	H183	0.1861
H16	0.1467	H40	0.0981	H64	0.1488	H88	0.1786	H1112	0.1350	C136	-0.1199	C160	0.1551	H184	0.1904
H17	0.1322	041	-0.5092	H65	0.1491	68H	0.1776	C113	-0.1372	C137	0.0997	C161	-0.1454	H185	0.1941
H18	0.1324	C42	0.0293	990	-0.4767	C90	-0.0947	H1114	0.0855	C138	-0.1486	H162	0.1670	H186	0.1479
H19	0.1263	C43	0.0583	C67	0.0002	H91	0.1373	C115	0.3056	C139	0.1590	H163	0.1988	H187	0.1479
H20	0.1265	044	-0.5105	C68	0.0462	C92	-0.1090	C116	-0.1382	H140	0.1806	C164	-0.1788	H188	0.1967
H21	0.1281	C45	0.0577	690	-0.4574	H93	0.1569	H1117	0.0853	H141	0.1409	C165	0.0735	H189	0.1900
H22	0.1291	C46	0.0079	C70	0.0473	C94	0.3490	C118	-0.0981	H142	0.1652	C166	-0.1056	H190	0.1873
H23	0.1449	047	-0.4814	C71	-0.0048	C95	-0.1087	H119	0.1362	H143	0.1956	C167	-0.1057	H191	0.1394
H24	0.1462	C48	0.4242	072	-0.4108	96H	0.1557	C120	0.1636	H144	0.1937	C168	0.0762	Total	000009

$\overline{}$
Ø.
~
=
.=
+
$\Box$
0
ō
$\overline{}$
_
m
ų.
8.3
8.3
e 8.3
le 8.
∞.
le 8.
le 8.

CC25         -0.2988         C49         -0.1472         H73         0.1583         C97         -0.1063         C121         -0.1317         H145         0.1846         C169         -0.1153           S26         0.4117         C53         -0.0678         H74         0.1578         H98         0.1039         C122         0.0991         H146         0.1486         C170         -0.1153           C28         -0.0431         C53         -0.0663         H76         0.1469         C100         0.0402         C123         -0.0492         H147         0.1486         H177         0.1160           C28         -0.0431         C53         -0.0663         H77         0.1460         C101         -0.1114         N125         -0.1429         H147         0.1189         H177         0.1160         0.1114         N125         -0.1428         H177         0.1160         0.1114         N125         -0.1429         H147         0.1189         H177         0.1189         0.1280         C122         -0.0429         H147         0.1189         H177         0.1160         N111         N112         0.1180         H118         0.1180         H118         0.1189         H118         0.1189         H118         0.118<		= 23.27 Å													
C50         -0.0578         H74         0.1578         H98         0.1039         C122         0.0991         H146         0.1496         C170           C51         -0.0423         H75         0.1444         C99         0.0221         C123         -0.1428         H147         0.1485         H711           C52         -0.0665         H76         0.1459         C100         0.0462         C124         0.1552         H148         0.1189         H717           C53         -0.0660         H77         0.1460         C101         -0.1114         N125         -0.4192         H149         0.1281         C173           C53         -0.0660         H77         0.1460         C101         -0.1140         N152         0.1990         N174           C54         -0.0571         H79         0.1689         H104         0.0821         C124         0.1180         H152         0.1190         N174           C55         -0.0443         H81         0.3742         C105         0.0299         C129         0.01183         H152         C176         C177           C57         0.132         H82         0.1635         H104         0.0820         C13         0.0118 <t< td=""><td>.25</td><td>I</td><td>0.2988</td><td>C49</td><td>-0.1472</td><td>H73</td><td>0.1583</td><td>C97</td><td>-0.1063</td><td>C121</td><td>-0.1317</td><td>H145</td><td>0.1846</td><td>C169</td><td>-0.1150</td></t<>	.25	I	0.2988	C49	-0.1472	H73	0.1583	C97	-0.1063	C121	-0.1317	H145	0.1846	C169	-0.1150
C51         -0.0423         H75         0.1454         C99         0.0221         C123         -0.1428         H147         0.1485         H171           C52         -0.0655         H76         0.1459         C100         0.0462         C124         0.1552         H148         0.1189         H172           C53         -0.0660         H77         0.1460         C101         -0.1114         N125         -0.4192         H149         0.1281         C173           C54         -0.0671         H79         0.1687         C103         -0.1290         C127         0.0630         H151         0.1991         C175           C55         -0.0443         H80         0.1689         H104         0.0821         C128         -0.1193         H152         0.1742         C176           C55         -0.1463         H80         0.1689         H104         0.0821         C128         -0.1193         H154         0.1742         C176           C55         -0.1463         H82         0.2281         C106         -0.1290         C139         -0.1081         H153         0.1742         C176           H84         0.1636         H107         0.0580         C131         -0.1011	26		0.4117	C50	-0.0578	H74	0.1578	86H	0.1039	C122	0.0991	H146	0.1496	C170	-0.1103
C52         -0.0655         H76         0.1459         C100         0.0462         C124         0.1552         H148         0.1189         H172           C53         -0.0660         H77         0.1460         C101         -0.1114         N125         -0.4192         H149         0.1281         C173           C54         -0.0428         H78         0.1457         H102         0.1301         C126         -0.1540         H150         0.1990         N174           C55         -0.0428         H79         0.1687         C103         -0.1229         C127         0.0630         H151         0.1912         C175           C55         -0.0463         H80         0.1689         H104         0.0821         C128         -0.1190         H152         0.1742         C176           C57         0.4249         H81         0.3742         C105         -0.1290         C138         H153         0.1492         C176           H58         0.1132         H82         0.1693         H107         0.0580         C131         H153         H181         H181           H60         0.1159         H83         0.1693         H109         0.1231         C135         C156 <td< td=""><td>- 723</td><td>ı</td><td>-0.2473</td><td>C51</td><td>-0.0423</td><td>H75</td><td>0.1454</td><td>C39</td><td>0.0221</td><td>C123</td><td>-0.1428</td><td>H147</td><td>0.1485</td><td>H171</td><td>0.1129</td></td<>	- 723	ı	-0.2473	C51	-0.0423	H75	0.1454	C39	0.0221	C123	-0.1428	H147	0.1485	H171	0.1129
C53         -0.0660         H77         0.1460         C101         -0.1114         N125         -0.4192         H149         0.1281         C173           C54         -0.0428         H78         0.1457         H102         0.1301         C126         -0.1540         H150         0.1900         N174           C55         -0.0428         H78         0.1457         H102         0.1301         C126         -0.1540         H150         0.1900         N174           C55         -0.0463         H80         0.1689         H104         0.0829         C127         -0.1901         H152         0.1742         C176           C57         0.4249         H81         0.3742         C105         0.0299         C129         -0.1183         H152         0.1742         C176           H58         0.1130         H83         0.1663         H107         0.0580         C131         -0.1011         H155         0.1742         C176           H60         0.1150         H83         0.1663         H109         0.1281         C132         -0.1011         H185         C177           H61         0.1158         H84         0.1665         H109         0.1323         C133	C28	'	-0.1435	C52	-0.0655	9/H	0.1459	C100	0.0462	C124	0.1552	H148	0.1189	H172	0.1161
C54         -0.0428         H78         0.1457         H102         0.1301         C126         -0.1540         H150         0.1900         N174         -0.255         -0.0428         H78         0.1457         H102         0.1301         C122         0.01540         H151         0.1912         C175         C75         -0.0571         H79         0.1687         C103         -0.1229         C127         0.0630         H151         0.1912         C175         C77           C55         -0.1463         H81         0.1689         H104         0.0299         C129         -0.1183         H153         0.1482         C176           H58         0.1324         H82         0.2281         C106         -0.1290         C139         0.0643         H154         0.1742         C176           H59         0.1130         H83         0.1693         H107         0.0580         C131         -0.1011         H155         0.1991         C179           H60         0.1156         H84         0.1636         H109         0.1281         C132         -0.1018         H154         0.1791         C179         C179         C170         C170         C132         C131         C180         C132         C131 <td>S29</td> <td></td> <td>0.4010</td> <td>C53</td> <td>-0.0660</td> <td>H77</td> <td>0.1460</td> <td>C101</td> <td>-0.1114</td> <td>N125</td> <td>-0.4192</td> <td>H149</td> <td>0.1281</td> <td>C173</td> <td>-0.1685</td>	S29		0.4010	C53	-0.0660	H77	0.1460	C101	-0.1114	N125	-0.4192	H149	0.1281	C173	-0.1685
C55         -0.0571         H79         0.1687         C103         -0.1229         C127         0.0630         H151         0.1912         C175           C56         -0.1463         H80         0.1689         H104         0.0821         C128         -0.1190         H152         0.1742         C176           C57         0.4249         H81         0.3742         C105         0.0299         C129         -0.1183         H153         0.1482         C177           H58         0.1132         H82         0.2281         C106         -0.1290         C139         0.0643         H154         0.1742         C176           H69         0.1130         H83         0.1693         H107         0.0580         C131         -0.1011         H155         0.1991         C179           H60         0.1156         H84         0.1636         C108         -0.1133         C132         -0.1011         H155         0.1991         C179           H61         0.1156         H85         0.1695         H109         0.1281         C132         -0.1018         C156         0.0873         H181           H62         0.1180         H87         0.1755         C111         -0.1202	C30		0.0685	C54	-0.0428	H78	0.1457	H102	0.1301	C126	-0.1540	H150	0.1900	N174	-0.4119
C56         -0.1463         H80         0.1689         H104         0.0821         C128         -0.1190         H152         0.1742         C176         -0.183         H53         0.1482         C176         C177           K57         0.4249         H81         0.3742         C105         0.0299         C129         -0.1183         H153         0.1482         C177           H58         0.1132         H82         0.2281         C106         -0.1290         C130         0.0643         H154         0.1716         C178           H60         0.1130         H83         0.1693         H107         0.0580         C131         -0.1011         H155         0.1991         C179           H60         0.1156         H84         0.1636         C108         -0.1133         C132         -0.1011         H155         0.1991         C179           H61         0.1156         H88         0.1656         H109         0.1281         C132         -0.1018         C156         0.0873         H181           H64         0.1180         H87         0.1758         C111         -0.1202         C135         0.1886         C158         0.1417         H183           H64         <	031		-0.5181	C55	-0.0571	H79	0.1687	C103	-0.1229	C127	0.0630	H151	0.1912	C175	0.1672
C57         0.4249         H81         0.3742         C105         0.0299         C129         -0.1183         H153         0.1482         C177           H58         0.1132         H82         0.2281         C106         -0.1290         C130         0.0643         H154         0.1716         C178           H69         0.1130         H83         0.1693         H107         0.0580         C131         -0.1011         H155         0.1991         C179           H60         0.1156         H84         0.1636         C108         -0.1133         C132         -0.1018         C156         0.0873         H180           H61         0.1156         H85         0.1695         H109         0.1281         C132         -0.1018         C156         0.0873         H180           H62         0.1178         H86         0.1758         C110         0.0147         N134         -0.4108         C155         H181           H64         0.1467         H87         0.1755         C111         -0.1202         C135         0.1147         C160         0.1579         H183           H64         0.1463         H89         0.1746         H112         0.0939         C136 <t< td=""><td>C32</td><td></td><td>0.0633</td><td>C56</td><td>-0.1463</td><td>H80</td><td>0.1689</td><td>H104</td><td>0.0821</td><td>C128</td><td>-0.1190</td><td>H152</td><td>0.1742</td><td>C176</td><td>-0.1211</td></t<>	C32		0.0633	C56	-0.1463	H80	0.1689	H104	0.0821	C128	-0.1190	H152	0.1742	C176	-0.1211
H58         0.1132         H82         0.2281         C106         -0.1290         C130         0.0643         H154         0.1716         C178           H59         0.1130         H83         0.1693         H107         0.0580         C131         -0.1011         H155         0.1991         C179           H60         0.1156         H84         0.1636         C108         -0.1133         C132         -0.1018         C156         0.0873         H180           H61         0.1159         H85         0.1695         H109         0.1281         C132         -0.1012         C157         -0.1103         H181           H62         0.1178         H86         0.1758         C110         0.0147         N134         -0.4108         C155         0.1103         H181           H64         0.1180         H87         0.1755         C111         -0.1202         C135         0.1386         N159         -0.4137         H183           H64         0.1467         H88         0.1746         H112         0.0939         C136         -0.1477         C160         0.1519         H184           H65         0.1463         H89         0.1721         C113         -0.1477	C33		0.0482	C57	0.4249	H81	0.3742	C105	0.0299	C129	-0.1183	H153	0.1482	C177	0.1040
H59         0.1130         H83         0.1693         H107         0.0580         C131         -0.1011         H155         0.1991         C179           H60         0.1156         H84         0.1636         C108         -0.1133         C132         -0.1018         C156         0.0873         H180           H61         0.1156         H85         0.1636         C108         -0.1133         C132         -0.1018         C156         0.0873         H180           H62         0.1178         H86         0.1758         C110         0.0147         N134         -0.4108         C157         -0.1103         H181           H64         0.1180         H87         0.1755         C111         -0.1202         C135         0.1386         N159         -0.4137         H181           H64         0.1467         H88         0.1746         H112         0.0939         C136         -0.147         C160         0.1519         H184           H65         0.1463         H89         0.1721         C113         -0.1409         C137         0.1011         C161         -0.147         H184         H184           C67         0.0044         H91         0.1017         C115	034		-0.5534	H58	0.1132	H82	0.2281	C106	-0.1290	C130	0.0643	H154	0.1716	C178	-0.1386
H60         0.1156         H84         0.1636         C108         -0.1133         C132         -0.1018         C156         0.0873         H180           H61         0.1159         H85         0.1695         H109         0.1281         C132         -0.1612         C157         -0.1103         H181           H62         0.1178         H86         0.1758         C110         0.0147         N134         -0.4108         C158         0.1555         H182           H64         0.1180         H87         0.1755         C111         -0.1202         C135         0.1386         N159         -0.4137         H183           H64         0.1462         H88         0.1746         H112         0.0939         C135         0.1147         C160         0.1519         H184           H65         0.1463         H89         0.1721         C113         -0.1409         C137         0.1011         C161         -0.1549         H184           C67         0.0044         H91         0.1017         C115         0.2911         C139         0.1662         H183         H184           C70         0.04467         H93         0.1331         H117         0.1060         H141	H35		0.1434	H59	0.1130	H83	0.1693	H107	0.0580	C131	-0.1011	H155	0.1991	C179	0.1602
H61         0.1159         H85         0.1695         H109         0.1281         C133         -0.1612         C157         -0.1103         H181           H62         0.1178         H86         0.1758         C110         0.0147         N134         -0.1612         C157         -0.1103         H181           H63         0.1180         H87         0.1755         C111         -0.1202         C135         0.1386         N159         -0.4137         H183           H64         0.1462         H88         0.1746         H112         0.0939         C136         -0.1147         C160         0.1519         H184           H65         0.1463         H89         0.1721         C113         -0.1409         C137         0.1011         C161         -0.1549         H184           C64         0.04834         C90         -0.1068         H114         0.0968         C138         -0.1477         H162         0.1481         H186           C67         0.0044         H91         0.1017         C115         0.2911         C139         0.1662         H183         H187           C70         0.04467         H93         0.1331         H117         0.1060         H141	H36		0.1400	09H	0.1156	H84	0.1636	C108	-0.1133	C132	-0.1018	C156	0.0873	H180	0.1901
H62         0.1178         H86         0.1758         C110         0.0147         N134         -0.4108         C158         0.1555         H182           H63         0.1180         H87         0.1755         C111         -0.1202         C135         0.1586         N159         -0.4137         H183           H64         0.1462         H88         0.1746         H112         0.0939         C136         -0.1147         C160         0.1519         H184           H65         0.1463         H89         0.1721         C113         -0.1409         C137         0.1011         C161         -0.1546         H184           C64         -0.04834         C90         -0.1068         H114         0.0968         C138         -0.1477         H162         0.1481         H186           C67         0.0044         H91         0.1017         C115         0.2911         C139         0.1662         H163         0.1823         H187           C68         0.04467         H93         0.1331         H117         0.1060         H141         0.1261         C165         0.0895         H189           C70         0.0452         C94         0.3330         C118         -0.1288	H37		0.0981	H61	0.1159	H85	0.1695	H109	0.1281	C133	-0.1612	C157	-0.1103	H181	0.1629
H63         0.1180         H87         0.1755         C111         -0.1202         C135         0.1586         N159         -0.4137         H183           H64         0.1462         H88         0.1746         H112         0.0939         C136         -0.1147         C160         0.1519         H184           H65         0.1463         H89         0.1721         C113         -0.1409         C137         0.1011         C161         -0.1546         H184           C64         -0.4834         C90         -0.1068         H114         0.0968         C138         -0.1477         H162         0.1481         H186           C67         0.0044         H91         0.1017         C115         0.2911         C139         0.1602         H163         0.1823         H187           C68         0.0400         C92         -0.1203         C116         -0.1441         H140         0.1666         C164         -0.1662         H188           C70         0.0452         C94         0.1331         H117         0.1060         H141         0.1261         C165         0.0895         H189           C71         -0.0046         C95         -0.1199         H119         0.1111	H38		0.1018	H62	0.1178	98H	0.1758	C110	0.0147	N134	-0.4108	C158	0.1555	H182	0.1584
H64         0.1462         H88         0.1746         H112         0.0939         C136         -0.1147         C160         0.1519         H184           H65         0.1463         H89         0.1721         C113         -0.1409         C137         0.1011         C161         -0.1546         H185           O66         -0.4834         C90         -0.1068         H114         0.0968         C138         -0.1477         H162         0.1481         H186           C67         0.0044         H91         0.1017         C115         0.2911         C139         0.1662         H163         0.1823         H187           C68         0.0446         C92         -0.1203         C116         -0.1441         H140         0.1666         C164         -0.1662         H188           C70         0.0452         C94         0.1331         H117         0.1060         H141         0.1261         C165         0.0895         H189           C71         -0.0046         C95         -0.1199         H119         0.1111         H143         0.1943         C167         -0.1142         H191           C71         -0.03812         H96         0.1327         C120         0.1638	H39		0.11111	H63	0.1180	H87	0.1755	C1111	-0.1202	C135	0.1586	N159	-0.4137	H183	0.1848
H65         0.1463         H89         0.1721         C113         -0.1409         C137         0.1011         C161         -0.1546         H185           O66         -0.4834         C90         -0.1068         H114         0.0968         C138         -0.1477         H162         0.1481         H186           C67         0.0044         H91         0.1017         C115         0.2911         C139         0.1602         H163         0.1823         H187           C68         0.04467         H93         0.1331         H117         0.1060         H141         0.1261         C164         -0.1662         H188           C70         0.0452         C94         0.3330         C118         -0.1288         H142         0.1701         C166         -0.1171         H190           C71         -0.0046         C95         -0.1199         H119         0.1111         H143         0.1943         C167         -0.1142         H191           O72         -0.3812         H96         0.1327         C120         0.1638         H144         0.1901         C168         -0.1142         H191	H40		0.1049	H64	0.1462	H88	0.1746	H112	0.0939	C136	-0.1147	C160	0.1519	H184	0.1914
O66         -0.4834         C90         -0.1068         H114         0.0968         C138         -0.1477         H162         0.1481         H186           C67         0.0044         H91         0.1017         C115         0.2911         C139         0.1602         H163         0.1823         H187           C68         0.04467         H93         0.1331         H117         0.1060         H141         0.1261         C165         0.0895         H189           C70         0.0452         C94         0.3230         C118         -0.1288         H142         0.1701         C166         -0.1171         H190           C71         -0.0046         C95         -0.1199         H119         0.1111         H143         0.1943         C167         -0.1142         H191           O72         -0.3812         H96         0.1327         C120         0.1638         H144         0.1901         C168         0.0862         Total	041		-0.5266	H65	0.1463	68H	0.1721	C113	-0.1409	C137	0.1011	C161	-0.1546	H185	0.1908
C67         0.0044         H91         0.1017         C115         0.2911         C139         0.1602         H163         0.1823         H187           C68         0.0400         C92         -0.1203         C116         -0.1441         H140         0.1666         C164         -0.1662         H188           O69         -0.4467         H93         0.1331         H117         0.1060         H141         0.1261         C165         0.0895         H189           C70         0.0452         C94         0.3230         C118         -0.1288         H142         0.1701         C166         -0.1171         H190           C71         -0.0046         C95         -0.1199         H119         0.1111         H143         0.1943         C167         -0.1142         H191           O72         -0.3812         H96         0.1327         C120         0.1638         H144         0.1901         C168         0.0862         Total	C42		0.0419	990	-0.4834	C90	-0.1068	H114	0.0968	C138	-0.1477	H162	0.1481	H186	0.1518
C68         0.0400         C92         -0.1203         C116         -0.1441         H140         0.1666         C164         -0.1662         H188           O69         -0.4467         H93         0.1331         H117         0.1060         H141         0.1261         C165         0.0895         H189           C70         0.0452         C94         0.3230         C118         -0.1288         H142         0.1701         C166         -0.1171         H190           C71         -0.0046         C95         -0.1199         H119         0.1111         H143         0.1943         C167         -0.1142         H191           O72         -0.3812         H96         0.1327         C120         0.1638         H144         0.1901         C168         0.0862         Total	C43		0.0576	C67	0.0044	H91	0.1017	C115	0.2911	C139	0.1602	H163	0.1823	H187	0.1496
O69         -0.4467         H93         0.1331         H117         0.1060         H141         0.1261         C165         0.0895         H189           C70         0.0452         C94         0.3230         C118         -0.1288         H142         0.1701         C166         -0.1171         H190           C71         -0.0046         C95         -0.1199         H119         0.1111         H143         0.1943         C167         -0.1142         H191           O72         -0.3812         H96         0.1327         C120         0.1638         H144         0.1901         C168         0.0862         Total	94		-0.5116	S92	0.0400	C92	-0.1203	C116	-0.1441	H140	0.1666	C164	-0.1662	H188	0.1874
C70 0.0452 C94 0.3230 C118 -0.1288 H142 0.1701 C166 -0.1171 H190 C71 -0.0046 C95 -0.1199 H119 0.1111 H143 0.1943 C167 -0.1142 H191 O72 -0.3812 H96 0.1327 C120 0.1638 H144 0.1901 C168 0.0862 Total	C45		0.0605	690	-0.4467	H93	0.1331	H117	0.1060	H141	0.1261	C165	0.0895	H189	0.1875
C71 -0.0046 C95 -0.1199 H119 0.1111 H143 0.1943 C167 -0.1142 H191 O72 -0.3812 H96 0.1327 C120 0.1638 H144 0.1901 C168 0.0862 Total	C46		0.0079	C70	0.0452	C94	0.3230	C118	-0.1288	H142	0.1701	C166	-0.1171	H190	0.1724
O72 -0.3812 H96 0.1327 C120 0.1638 H144 0.1901 C168 0.0862 Total	047		-0.4797	C71	-0.0046	C95	-0.1199	H119	0.1111	H143	0.1943	C167	-0.1142	H191	0.1490
	C48		0.4231	072	-0.3812	96H	0.1327	C120	0.1638	H144	0.1901	C168	0.0862	Total	000009

Table 8.3 (continued)

= 28.17 Å													
5	0.3044	. C49	-0.1518	H73	0.1575	C97	-0.1302	C121	-0.1201	H145	0.1926	C169	-0.1004
9	0.4414	. C50	-0.0575	H74	0.1571	86H	0.0862	C122	0.1070	H146	0.1443	C170	-0.1035
	0.2417	C51	-0.0451	H75	0.1261	C39	0.0133	C123	-0.1386	H147	0.1380	H171	0.1256
∞ .	-0.1402	_	-0.0653	9/H	0.1264	C100	0.0237	C124	0.1549	H148	0.1268	H172	0.1230
6	0.4370	C53	-0.0666	H77	0.1297	C101	-0.1385	N125	-0.4059	H149	0.1255	C173	-0.1701
0	0.0735	_	-0.0417	H78	0.1294	H102	0.1047	C126	-0.1714	H150	0.1803	N174	-0.4100
<u>-</u>	-0.5197		-0.0586	H79	0.1474	C103	-0.1353	C127	0.0690	H151	0.1934	C175	0.1698
2	0.0521		-0.1415	H80	0.1475	H104	0.1035	C128	-0.1161	H152	0.1734	C176	-0.1230
3	0.0394		0.4276	H81	0.3590	C105	0.0215	C129	-0.1124	H153	0.1438	C177	0.1068
4	-0.5200		0.1076	H82	0.2323	C106	-0.1371	C130	0.0794	H154	0.1658	C178	-0.1430
Š	0.1519		0.1033	H83	0.1968	H107	0.1037	C131	-0.1027	H155	0.1936	C179	0.1549
9	0.1495		0.1195	H84	0.1507	C108	-0.1379	C132	-0.1020	C156	0.1012	H180	0.1919
7	0.1083		0.1209	H85	0.1667	H109	0.1040	C133	-0.1788	C157	-0.1158	H181	0.1572
∞	0.1065		0.1216	98H	0.1810	C110	0.0145	N134	-0.4020	C158	0.1575	H182	0.1502
6	0.1310		0.1223	H87	0.1700	C1111	-0.1267	C135	0.1539	N159	-0.3987	H183	0.1737
0	0.1296		0.1403	H88	0.1748	H112	0.0899	C136	-0.1202	C160	0.1581	H184	0.1925
-	-0.5186		0.1392	68H	0.1798	C113	-0.1243	C137	0.0995	C161	-0.1429	H185	0.1883
2	0.0370		-0.4704	C30	-0.1309	H114	0.1392	C138	-0.1449	H162	0.1663	H186	0.1464
3	0.0631		-0.0041	H91	0.0828	C115	0.3226	C139	0.1559	H163	0.1963	H187	0.1418
4	-0.5159		0.0583	C92	-0.1266	C116	-0.1260	H140	0.1745	C164	-0.1780	H188	0.1953
5	0.0530	690	-0.4865	H93	0.1388	H117	0.1371	H141	0.1511	C165	0.0743	H189	0.1853
9	0.0183		0.0546	C94	0.3277	C118	-0.1278	H142	0.1630	C166	-0.1119	H190	0.1792
11	-0.4897		0.0055	C95	-0.1249	H119	0.0851	H143	0.1940	C167	-0.1162	H191	0.1508
∞	0.4184		-0.4303	96H	0.1410	C120	0.1697	H144	0.1921	C168	0.0696	Total	0000.9

utinued
3 (6
ထံ
apl
_

1	.25		0.3054	C49	-0.1606	H73	0.1530	C97	-0.1312	C121	-0.1218	H145	0.1901	C169	-0.1064
036 S26	\$26		0.4775	C50	-0.0619	H74	0.1520	H98	0.1004	C122	0.0983	H146	0.1535	C170	-0.1059
410 C27 -	227 -	- 1	-0.2371	C51	-0.0552	H75	0.1212	C99	0.0139	C123	-0.1366	H147	0.1514	H171	0.1181
305 C28 -	. 228		-0.1378	C52	-0.0648	9/H	0.1219	C100	0.0341	C124	0.1581	H148	0.1289	H172	0.1219
350 S29	\$29		0.4663	C53	-0.0656	H77	0.1241	C101	-0.1447	N125	-0.4110	H149	0.1364	C173	-0.1715
356 C30	230		0.0791	C54	-0.0516	H78	0.1241	H102	0.0384	C126	-0.1602	H150	0.1881	N174	-0.4089
164 031	. 15C		-0.5174	C55	-0.0640	H79	0.1284	C103	-0.1106	C127	0.0760	H151	0.1895	C175	0.1675
801 C32	232		0.0438	C56	-0.1442	H80	0.1282	H104	0.1281	C128	-0.1153	H152	0.1923	C176	-0.1300
355 C33	233		0.0444	C57	0.4200	H81	0.3463	C105	0.0490	C129	-0.1167	H153	0.1559	C177	0.1033
316 034	. J34		-0.5262	H58	0.0979	H82	0.2354	C106	-0.1136	C130	0.0770	H154	0.1626	C178	-0.1408
917 H35	H35		0.1553	H59	0.0982	H83	0.2215	H107	0.1265	C131	-0.1227	H155	0.1924	C179	0.1594
105 H36	H36		0.1530	09H	0.1059	H84	0.1306	C108	-0.1254	C132	-0.1198	C156	0.1003	H180	0.1931
727 H37	H37		0.1141	H61	0.1026	H85	0.1558	H109	0.0825	C133	-0.1619	C157	-0.1232	H181	0.1689
719 H38	H38		0.1141	H62	0.1208	98H	0.1749	C110	0.0169	N134	-0.4368	C158	0.1597	H182	0.1447
545 H39	H39		0.1303	H63	0.1190	H87	0.1506	C1111	-0.1056	C135	0.1749	N159	-0.4061	H183	0.1795
542 H40	H40		0.1289	H64	0.1301	H88	0.1619	H1112	0.1069	C136	-0.1145	C160	0.1576	H184	0.1890
486 041	741		-0.5426	H65	0.1317	68H	0.1745	C113	-0.1195	C137	0.0939	C161	-0.1455	H185	0.1898
491 C42	242		0.0426	990	-0.4707	C30	-0.1296	H114	0.1325	C138	-0.1511	H162	0.1655	H186	0.1489
453 C43	243		0.0742	C67	-0.0012	H91	0.1028	C115	0.3176	C139	0.1545	H163	0.1926	H187	0.1488
458 044	44		-0.5155	C68	0.0623	C92	-0.0977	C116	-0.1208	H140	0.1808	C164	-0.1701	H188	0.1918
375 C45	245		0.0462	690	-0.4876	H93	0.0721	H1117	0.1326	H141	0.1502	C165	0.0743	H189	0.1895
380 C46	246		0.0337	C70	0.0546	C94	0.2893	C118	-0.1058	H142	0.1686	C166	-0.1174	H190	0.1805
590 047	<b>247</b>		-0.5037	C71	0.0188	C95	-0.1412	H1119	0.1023	H143	0.1962	C167	-0.1156	H191	0.1571
599 C48	748		0.4038	072	-0.4743	96H	0.1001	C120	0.1697	H144	0.1924	C168	0.0763	Total	0000.9
	١														

p
Ø.
⋾
-=
Ħ
=
$\sim$
٠,
$\overline{}$
~
ų.
8.3
e 8.
le 8.
e 8.
ble 8.

O1 -0.4047 C2 -0.0006 C3 -0.4281 O4 -0.4281 C5 0.0343 C6 0.0397 O7 -0.5154 C8 0.0802 C9 -0.1366	C25 S26 C27 C28 S29 S29 C30	-0.3037 $0.4528$ $-0.2397$	C49	-0.1695	H73	0.1516	C97	-0.1109	C121	-0.1370	H145	0.1938	C169	-0.11116
CC2 -0.0006 CC3 0.0421 OO4 -0.4281 CC5 0.034; CC6 0.039; OO7 -0.5156 CC8 0.080; CC9 -0.1366		0.4528 $-0.2397$	-						(1)					
C3 0.0421 O4 -0.4281 C5 0.0345 C6 0.0397 O7 -0.515x C8 0.0805 C9 -0.1364		-0.2397	C50	-0.0675	H74	0.1506	86H	0.1291	C122	0.0856	H146	0.1561	C170	-0.1090
O4 -0.4281 C5 0.034; C6 0.0397 O7 -0.515¢ C8 0.080; C9 -0.1361			C51	-0.0619	H75	0.1285	C39	0.0365	C123	-0.1449	H147	0.1557	H171	0.1261
C5 0.0343 C6 0.0397 O7 -0.5154 C8 0.0807 C9 -0.1360		-0.1384	C52	-0.0653	9/H	0.1293	C100	0.0373	C124	0.1550	H148	0.1126	H172	0.1255
C6 0.0397 O7 -0.5152 C8 0.0802 C9 -0.1364		0.4388	C53	-0.0607	H77	0.1327	C101	-0.1113	N125	-0.4040	H149	0.1147	C173	-0.1650
O7 -0.5154 C8 0.0805 C9 -0.1360		0.0780	C54	-0.0691	H78	0.1327	H102	0.0946	C126	-0.1681	H150	0.1941	N174	-0.4031
C8 0.0802 C9 -0.1360		-0.5165	C55	-0.0678	H79	0.1427	C103	-0.1048	C127	0.0758	H151	0.1913	C175	0.1686
C9 -0.136		0.0481	C56	-0.1493	H80	0.1425	H104	0.1333	C128	-0.1140	H152	0.1914	C176	-0.1202
		0.0367	C57	0.4137	H81	0.3579	C105	0.0420	C129	-0.1134	H153	0.1610	C177	0.0892
C10 -0.236		-0.5186	H58	0.0956	H82	0.2245	C106	-0.1055	C130	0.0790	H154	0.1716	C178	-0.1430
S11 0.464(		0.1505	H59	9060.0	H83	0.2121	H107	0.1354	C131	-0.1089	H155	0.1967	C179	0.1644
C12 -0.307		0.1480	09H	0.0877	H84	0.1096	C108	-0.1132	C132	-0.1080	C156	0.0873	H180	0.1945
S13 0.445		0.1205	H61	0.0942	H85	0.1519	H109	0.1178	C133	-0.1739	C157	-0.1181	H181	0.1742
H14 0.3682		0.1213	H62	0.0939	98H	0.1731	C110	0.0320	N134	-0.4028	C158	0.1658	H182	0.1433
H15 0.1602		0.1294	H63	0.0952	H87	0.1109	C1111	-0.0991	C135	0.1685	N159	-0.4073	H183	0.1785
H16 0.1598		0.1274	H64	0.1139	H88	0.1475	H112	0.1283	C136	-0.1334	C160	0.1582	H184	0.1932
H17 0.147		-0.5463	H65	0.1162	68H	0.1705	C113	-0.1149	C137	0.0839	C161	-0.1453	H185	0.1840
H18 0.1478		0.0549	990	-0.4767	C30	-0.1108	H114	0.1444	C138	-0.1450	H162	0.1708	H186	0.1498
H19 0.144		0.0603	C67	0.0026	H91	0.1321	C115	0.3285	C139	0.1584	H163	0.1946	H187	0.1500
H20 0.1445		-0.5202	S92	0.0563	C92	-0.1414	C116	-0.1156	H140	0.1869	C164	-0.1616	H188	0.1854
H21 0.1339		0.0546	690	-0.4753	H93	0.0782	H117	0.1458	H141	0.1565	C165	0.0695	H189	0.1910
H22 0.134		0.0456	C70	0.0502	C94	0.3086	C118	-0.0989	H142	0.1682	C166	-0.1181	H190	0.1744
H23 0.152		-0.5189	C71	9600.0	C95	-0.1378	H119	0.1280	H143	0.1943	C167	-0.1187	H191	0.1395
H24 0.153		0.3799	072	-0.4415	96H	0.0834	C120	0.1653	H144	0.1891	C168	0.0696	Total	000009

ned
contir
8.3
le
E

	)84	060	155	148	729	385	725	312	157	537	262	)37	527	543	127	930	371	530	533	302	916	384	599	000
	-0.10	-0.10	0.11	0.11	-0.1729	-0.4(	0.17	-0.13	0.0	-0.15	0.15	0.15	0.16	0.16	0.15	0.15	0.18	0.15	0.15	0.15	0.15	0.18	0.16	9.00
	C169	C170	H171	H172	C173	N174	C175	C176	C177	C178	C179	H180	H181	H182	H183	H184	H185	H186	H187	H188	H189	H190	H191	Total
	0.1877	0.1482	0.1466	0.1245	0.1267	0.1871	0.1921	0.1783	0.1445	0.1757	0.2015	0.0818	-0.1220	0.1745	-0.4080	0.1571	-0.1443	0.1621	0.1929	-0.1694	0.0786	-0.1202	-0.1102	0.0884
	H145	H146	H147	H148	H149	H150	H151	H152	H153	H154	H155	C156	C157	C158	N159	C160	C161	H162	H163	C164	C165	C166	C167	C168
	-0.1382	0.1099	-0.1412	0.1589	-0.4022	-0.1650	0.0661	-0.1213	-0.1141	0.0536	-0.0937	-0.0937	-0.1610	-0.4062	0.1621	-0.1412	0.1184	-0.1446	0.1606	0.1767	0.1461	0.1765	0.2030	0.1957
	C121	C122	C123	C124	N125	C126	C127	C128	C129	C130	C131	C132	C133	N134	C135	C136	C137	C138	C139	H140	H141	H142	H143	H144
	-0.0927	0.1407	0.0312	0.0630	-0.1008	0.1437	-0.0926	0.1551	0.0546	-0.0928	0.1548	-0.1004	0.1512	0.0436	-0.0868	0.1519	-0.1065	0.1666	0.3521	-0.1073	0.1679	-0.0863	0.1519	0.1624
	C97	86H	C39	C100	C101	H102	C103	H104	C105	C106	H107	C108	H109	C110	C1111	H112	C113	H114	C115	C116	H117	C118	H119	C120
	0.1354	0.1369	0.1091	0.1078	0.1187	0.1179	0.1301	0.1305	0.3486	0.2290	0.2092	0.0942	0.0890	0.1551	0.0745	0.1194	0.1534	-0.0924	0.1429	-0.1190	0.1329	0.3248	-0.1187	0.1291
	H73	H74	H75	9/H	H77	H78	H79	H80	H81	H82	H83	H84	H85	98H	H87	H88	68H	C30	H91	C92	H93	C94	C95	96H
	-0.2109	-0.1242	-0.0933	-0.0743	-0.0846	-0.1240	-0.0823	-0.1732	0.3922	0.1088	0.1145	0.0996	0.0980	0.0847	0.0911	0.0956	0.1034	-0.5123	0.0160	0.0685	-0.4955	0.0594	0.0172	-0.4682
	C49	C50	C51	C52	C53	C54	C55	C56	C57	H58	H59	09H	H61	H62	H63	H64	H65	990	C67	89D	690	C70	C71	072
	-0.3040	0.4539	-0.2403	-0.1400	0.4385	0.0753	-0.5165	0.0505	0.0256	-0.5059	0.1522	0.1497	0.1289	0.1302	0.1332	0.1310	-0.5276	0.0536	0.0548	-0.5148	0.0583	0.0507	-0.5229	0.3445
	C25	S26	C27	C28	S29	C30	031	C32	C33	034	H35	H36	H37	H38	H39	H40	041	C42	C43	440	C45	C46	047	C48
= 40.99 Å	-0.4191	0.0021	0.0476	-0.4442	0.0424	0.0379	-0.5156	0.0817	-0.1360	-0.2350	0.4681	-0.3100	0.4479	0.3635	0.1537	0.1534	0.1398	0.1403	0.1357	0.1362	0.1322	0.1328	0.1527	0.1536
z = 4	01	C2	C3	9	C2	Ce	07	C8	60	C10	S11	C12	S13	H14	H15	H16	H17	H18	H19	H20	H21	H22	H23	H24

inued	
cont	
$\overline{}$	
$\overline{}$	
ت	
_	
$\overline{}$	
<b>8.3</b>	
8.3	
8.3	
8.3	
8.3	
8.3	
8.3	
8.3	
8.3	
8.3	
8.3	
8.3	
8.3	
8.3	
8.3	
8.3	
8.3	
8.3	
8.3	
8.3	
$\overline{}$	

z = 4	4.83 Å														
01	-0.4013	C25	-0.3058	C49	-0.2005	H73	0.1234	C97	-0.0914	C121	-0.1271	H145	0.1942	C169	-0.0987
C2	0.0005	S26	0.4296	C50	-0.0957	H74	0.1360	86H	0.1417	C122	0.1194	H146	0.1255	C170	-0.1122
C3	0.0300	C27	-0.2430	C51	-0.1217	H75	0.0672	C39	0.0338	C123	-0.1455	H147	0.1234	H171	0.1354
90	-0.3817	C28	-0.1404	C52	-0.0845	9/H	0.0757	C100	0.0618	C124	0.1663	H148	0.1467	H172	0.1357
CS	0.0182	S29	0.4136	C53	-0.0794	H77	0.1041	C101	-0.0997	N125	-0.4130	H149	0.1456	C173	-0.1737
92	0.0434	C30	0.0761	C54	-0.1246	H78	0.1033	H102	0.1455	C126	-0.1702	H150	0.1871	N174	-0.4134
07	-0.5101	031	-0.5160	C55	-0.0919	H79	0.1058	C103	-0.0943	C127	0.0881	H151	0.1926	C175	0.1774
C8	0.0749	C32	0.0518	C56	-0.2023	H80	0.1073	H104	0.1535	C128	-0.1056	H152	0.1764	C176	-0.1316
60	-0.1407	C33	0.0290	C57	0.3642	H81	0.3356	C105	0.0560	C129	-0.1107	H153	0.1487	C177	0.1240
C10	-0.2406	034	-0.5105	H58	0.1219	H82	0.2103	C106	-0.0945	C130	0.0849	H154	0.1697	C178	-0.1467
S11	0.4336	H35	0.1474	H59	0.1233	H83	0.2033	H107	0.1521	C131	-0.1141	H155	0.1936	C179	0.1666
C12	-0.3053	H36	0.1451	H60	0.1116	H84	0.1345	C108	-0.0993	C132	-0.0994	C156	0.1171	H180	0.1945
S13	0.4126	H37	0.1258	H61	0.1113	H85	0.0982	H109	0.1499	C133	-0.1715	C157	-0.1226	H181	0.1639
H14	0.3707	H38	0.1269	H62	0.0834	98H	0.1232	C110	0.0395	N134	-0.4017	C158	0.1689	H182	0.1493
H15	0.1626	H39	0.1297	H63	0.0843	H87	0.1156	C1111	-0.0888	C135	0.1603	N159	-0.4023	H183	0.1838
H16	0.1623	H40	0.1277	H64	0.1230	H88	0.0963	H1112	0.1463	C136	-0.1224	C160	0.1611	H184	0.2012
H17	0.1619	041	-0.5241	H65	0.1355	68H	0.1414	C113	-0.1093	C137	0.1208	C161	-0.1314	H185	0.1849
H18	0.1624	C42	0.0437	990	-0.5287	C30	-0.0912	H1114	0.1595	C138	-0.1332	H162	0.1647	H186	0.1437
H19	0.1620	C43	0.0507	C67	0.0149	H91	0.1429	C115	0.3468	C139	0.1545	H163	0.1924	H187	0.1414
H20	0.1621	944	-0.5030	C68	0.0923	C92	-0.1164	C116	-0.1101	H140	0.1718	C164	-0.1737	H188	0.1904
H21	0.1364	C45	0.0797	690	-0.4980	H93	0.1415	H1117	0.1609	H141	0.1451	C165	0.0776	H189	0.1977
H22	0.1370	C46	0.0230	C70	0.0531	C94	0.3320	C118	-0.0882	H142	0.1765	C166	-0.1058	H190	0.1904
H23	0.1507	047	-0.5312	C71	0.0425	C95	-0.1161	H119	0.1466	H143	0.2023	C167	-0.1067	H191	0.1605
H24	4 0.1514 C	C48	0.3563	072	-0.5348	96H	0.1397	C120	0.1799	H144	0.1877	C168	0.0839	Total	000009

# 8.6 Appendix F: Consideration of Metric Effect on the Bistable [2]Rotaxane Molecule During the Constant MD Simulations Using Fixman's Theorem

When we consider a system with N generalized coordinates  $q_i$ , associated conjugated momenta  $p_i$ , and masses  $m_i$ , the Hamiltonian of this system H is given by

$$H\left(p,q\right) = \frac{1}{2}\mathbf{p}^{T}\mathbf{M}^{-1}\mathbf{p} + V\left(\mathbf{q}\right), \tag{8.1}$$

where M is the "symmetric metric tensor" or "mass-metric tensor" that is defined as

$$M_{kl} = \sum_{i}^{N} m_i \frac{\partial \mathbf{r}_i}{\partial q_k} \cdot \frac{\partial \mathbf{r}_i}{\partial q_l}.$$
 (8.2)

Among N generalized coordinates, we consider that  $\nu$  generalized coordinates  $q_i''$  are constrained, and rests of them  $q_i'$  are not. Then, according to the Fixman's theorem [3], the ratio of the original partition function Q and the partition function from the constraint dynamics  $Q_c$  is

$$\frac{Q}{Q_c} = (\det \mathbf{Z})^{-1/2}, \tag{8.3}$$

where

$$Z_{kl} = \sum_{i}^{\nu} \frac{1}{m_i} \frac{\partial q_k''}{\partial \mathbf{r}_i} \cdot \frac{\partial q_l''}{\partial \mathbf{r}_i}.$$
 (8.4)

In our simulation, the (det **Z**) is determined as the inverse of the CBPQT<sup>4+</sup> ring's mass,  $1/M_{\rm ring}$ . From Eq. 8.3, the difference between the original free energy  $F = -k_BT \ln Q$  and the free energy from the constraint dynamics  $F_c = -k_BT \ln Q$  is determined by

$$F - F_c = -k_B T \ln(\det \mathbf{Z})^{-1/2} = -\frac{1}{2} k_B T \ln M_{\text{ring}} = \text{const.}$$
 (8.5)

Therefore, the metric effect only adds a constant scalar value to the absolute free energy values, which has no influence on the relative energetics.

### 8.7 Appendix G: Time for Consumption of POPG

The formation of primary ozonide (POZ), which is the first step in the ozonolysis of 1-palmitoyl-2-oleoyl-*sn*-phosphatidylglycerol (POPG) at the air-liquid interface, is described as

8.8 Appendix H 161

$$O_3 + POPG \xrightarrow{k_1} POZ.$$
 (8.6)

The ozone concentration is assumed to be constant during the reaction, which allows calculating the reaction rate using the pseudo-first order rate constant  $k_2 = k_1$  [O<sub>3</sub>], where  $k_1 = 4.5 \times 10^{-16}$  cm<sup>3</sup> mol<sup>-1</sup> s<sup>-1</sup> adopted from the OPPC ozonolysis on NaCl [4]. The ozone concentration, measured spectrophotometrically using an absorption cell with 10 cm path length, is determined to be  $\sim 5 \times 10^{14}$  mol cm<sup>-3</sup> (20 ppm). The reaction rate is expressed as

$$-\frac{d [POPG]_{surf}}{dt} = k_2 [POPG]_{surf,0}.$$
 (8.7)

Solving Eq. 8.7 gives

$$\frac{[\text{POPG}]_{surf}}{[\text{POPG}]_{surf,0}} = e^{-k_2 t}.$$
(8.8)

For 90 and 99% depletion of POPG at the air-liquid interface, it takes  $\sim$ 10 and  $\sim$ 20 s, respectively.

### 8.8 Appendix H: Bulk-Phase Ozonolysis

### 8.8.1 Methods

### 8.8.1.1 Chemicals and Reagents

Ammonium bicarbonate (NH<sub>4</sub>HCO<sub>3</sub>), iron (II) dichloride (FeCl<sub>2</sub>), sodium ethylenediaminetetraacetic acid (EDTA), trypsin from porcine pancreas were purchased from Sigma-Aldrich (St. Louis, MO). SP-B<sub>1-25</sub> was purchased from Biomer Technology (Hayward, CA).

### 8.8.1.2 Bulk-Phase O<sub>3</sub> Reaction

A continuous flow of  $\sim$ 20 ppm  $O_3$  in air was applied to the  $100\,\mu\text{M}$  SP-B<sub>1-25</sub> solution in 1:1 (by volume) water and methanol solvent for  $30\,\text{s}$ , 1, 1.5, 2, 3, 4, and 5 min. The SP-B<sub>1-25</sub> solution was diluted to  $50\,\mu\text{M}$  for ESI with 1:1 water/methanol and 1% acetic acid by volume. Trypsin digests of SP-B<sub>1-25</sub> and  $O_3$  treated SP-B<sub>1-25</sub> were prepared by incubating  $200\,\mu\text{M}$  of SP-B<sub>1-25</sub> with  $6\,\mu\text{g}$  of trypsin from porcine pancreas in 1 mL of water containing 25 mM ammonium bicarbonate (NH<sub>4</sub>HCO<sub>3</sub>) at 37°C for 4 h. The trypsin was then removed using a Millipore Microcon centrifugal filter fitted with an Ultracel YM-10 membrane. The sample solution was diluted to an appropriate concentration for ESI with 1:1 water/methanol and 1% acetic acid by volume. Product analysis was performed on a Thermo Finnigan LCQ Deca XP ion trap mass spectrometer (ITMS) in positive and negative modes. The

nomenclature proposed by Roepstorff and Fohlman [5] was used for the parent and fragment ions.

#### 8.8.1.3 Fenton Reaction

SP-B $_{1-25}$  (500  $\mu$ M) was incubated with 600  $\mu$ M FeCl $_2$ , 600  $\mu$ M sodium EDTA, and 30 mM H $_2$ O $_2$  in 1 mL water at 37°C for 12, 18, and 24 h. The peptide was purified using a Varian C18 OMIX 100  $\mu$ L pipette tip. The sample solution was diluted to an appropriate concentration with 1:1 water/methanol and 1% acetic acid by volume. Product analysis was performed on a Micromass QTof2 quadrupole time of flight mass spectrometer in the positive ion mode.

### 8.8.2 Results and Discussion

Triply and quadruply protonated SP- $B_{1-25}$  are observed as dominating ions in the ESI-MS spectrum with a small amount of doubly protonated peptides (Fig. 8.6a, d). Figure 8.6 shows oxidized products of triply and quadruply charged SP- $B_{1-25}$  from the bulk-phase  $O_3$  reaction and the Fenton reaction with intact SP- $B_{1-25}$ . As seen

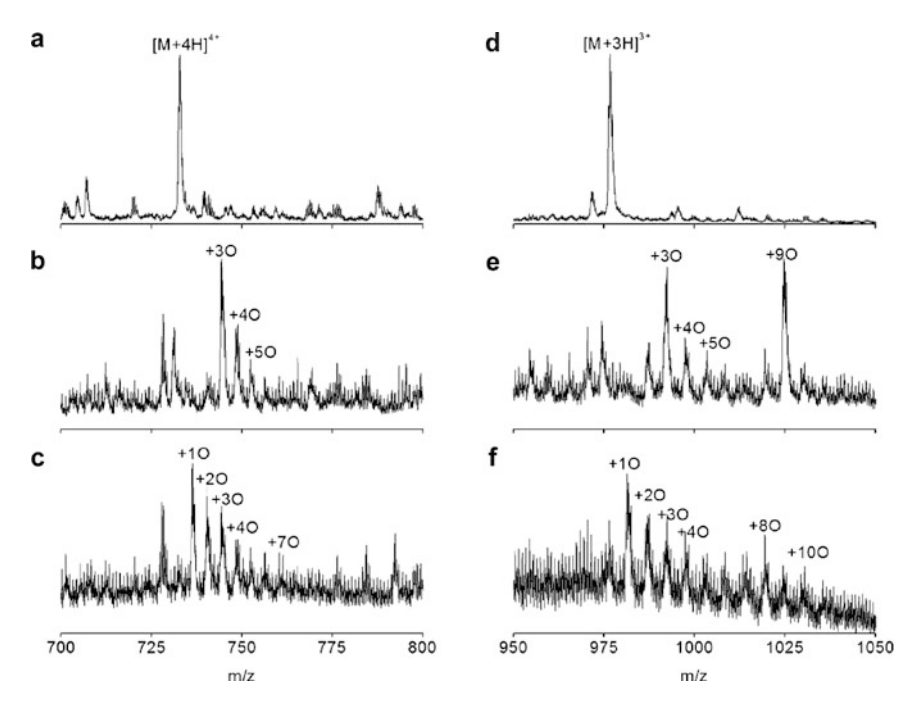


Fig. 8.6 (a) Quadruply charged SP- $B_{1-25}$  and oxidized products from (b) the bulk-phase  $O_3$  reaction and (c) the Fenton reaction with intact SP- $B_{1-25}$ . (d) Triply charged SP- $B_{1-25}$  and oxidized products from (e) the bulk-phase  $O_3$  reaction and (f) the Fenton reaction are also shown

8.8 Appendix H

in Fig. 8.6b, e, incorporation of three and nine oxygens in SP-B $_{1-25}$  are observed as major products from the bulk-phase  $O_3$  reaction with the peptide. Other oxygenated peptides (+ 4O and + 5O) are also observed as minor products in the spectrum. The Fenton reaction yields a series of oxidized SP-B $_{1-25}$  products with up to 10 oxygen atoms (Figs. 8.6c, f). It is notable that the bulk-phase  $O_3$  reaction yields dominating products of 3- and 9-oxygenated SP-B $_{1-25}$ . This suggests the high stability of SP-B $_{1-25}$  incorporating 3 and 9 oxygen atoms. In order to determine structures of the oxidized SP-B $_{1-25}$  by the bulk-phase  $O_3$  reaction, trypsin digest was performed after applying  $O_3$  for 3 min to the SP-B $_{1-25}$  solution.

The ESI mass spectrum of a trypsin digest of  $SP-B_{1-25}$  exhibits 7 major ion peaks. The masses and segments of the observed tryptic digest ions of  $SP-B_{1-25}$  are indicated in Fig. 8.7a. The ESI mass spectrum of a trypsin digest of  $SP-B_{1-25}$  oxidized by reaction with bulk-phase  $O_3$  exhibits segments with MetSO (m/z 817, m/z 874, and m/z 1,030) and the less abundant N-terminal segment of FPIPLPY-CWLCR + 8O at m/z 1636 in positive ion mode (Fig. 8.7b). The negative ion mode ESI mass spectrum also exhibits corresponding deprotonated segment ion peaks (Fig. 8.7c).

The structures of segments are confirmed by CID spectra. As seen in Fig. 8.8a, the CID of the ion at m/z 817 exhibits the elimination of hydrosulfinylmethane (CH<sub>4</sub>SO, 64 mass unit), which is the characteristic dissociation pathway of methionine sulfoxide (MetSO) [6, 7]. The structure of the segment FPIPLPYCWLCR + 80 is also investigated using CID. Fragments from the CID of the cationic FPIPLPYCWLCR + 80 at m/z 1636 yields y-type fragments ( $y_7$  and  $y_9$ ) with all eight oxygen atoms as dominant products (Fig. 8.8b). The fragment PLPYCW with six oxygen atoms indicates that Cys<sub>8</sub> and Trp<sub>9</sub> are oxidized to sulfonic acid (+30) and hydroxy-Nformylkynurenine (HNFKyn, +30), respectively. Thus, we can assume that  $Cys_{11}$  is oxidized to sulfenic acid (+ 20). The structures are further confirmed by the fragments of  $c_8 + 3O$  and PLPYC + 3O resulting from the CID of FPIPLPYCWLCR + 80 in negative ion mode (Fig. 8.8c). It is notable that Cys<sub>8</sub> and Cys<sub>11</sub> are located next to each other in the helical structure [8]. Asymmetric oxidation of closely located Cys residues is caused by the possible formation of sulfonic anhydride (R<sub>1</sub>-O<sub>2</sub>SOSO<sub>2</sub>-R<sub>2</sub>). No segment peak is observed from the triply oxygenated SP-B<sub>1-25</sub> after tryptic digest of the products from the bulk-phase O<sub>3</sub> reaction.

The observed high abundance of SP- $B_{1-25}$  where 3 and 9 oxygen atoms have been added can be explained by the distinct oxidation mechanisms of  $O_3$  in aqueous solution. Cys easily undergoes oxidation by  $O_3$  to form sulfonic acid in aqueous solution primarily by reactions with secondary oxidants [9]. Cys<sub>8</sub> and Cys<sub>11</sub>, which are located near the hydrophobic N-terminal site in SP- $B_{1-25}$ , are hardly oxidized by reactive oxygen species (ROS) at the air-liquid interface. Trp9 and Met<sub>21</sub> are oxidized to form NFKyn and MetSO by ozonolysis and ROS, respectively, by interfacial reactions. This induces a change in peptide orientation in the interface that results in NFKyn, Cys<sub>8</sub>, and Cys<sub>11</sub> being exposed to ROS for further oxidation. As a result, NFKyn occurs to form HNFKyn and, simultaneously, Cys<sub>8</sub> and Cys<sub>11</sub> are also oxidized by ROS to form sulfonic anhydride.

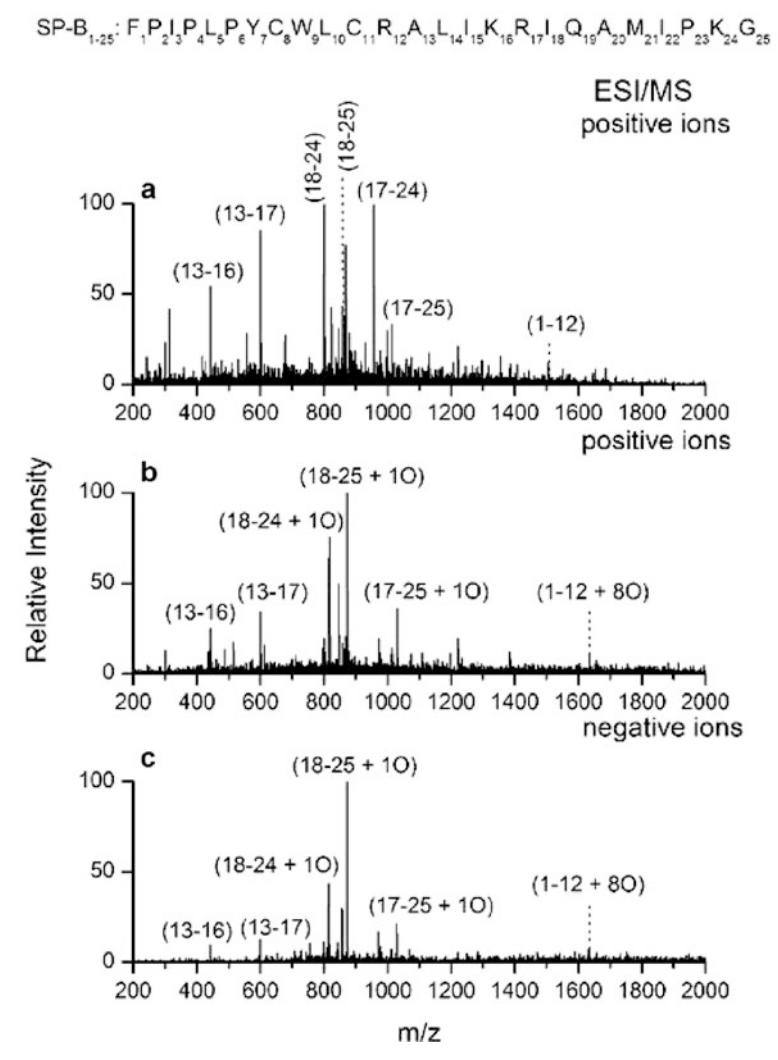
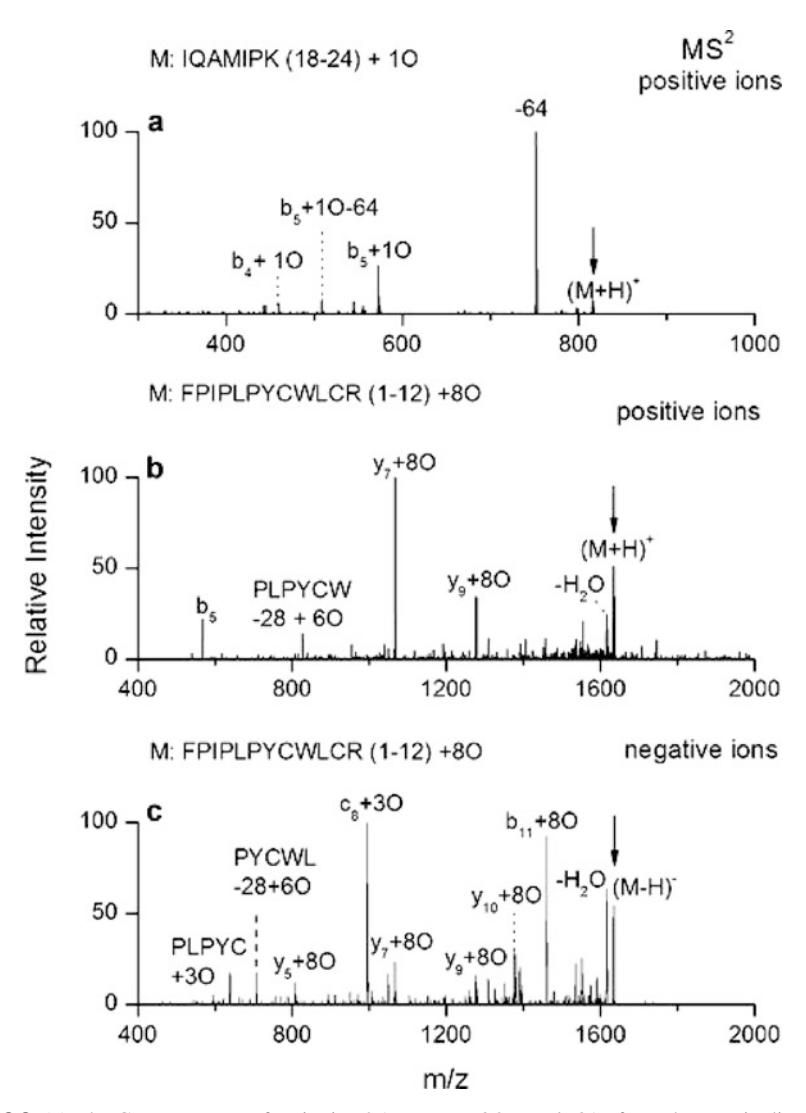


Fig. 8.7 (a) The ESI mass spectrum of the trypsin digests of  $SP-B_{1-25}$  in positive mode. (b) The ESI mass spectrum of the trypsin digests of the oxidized  $SP-B_{1-25}$  from the bulk-phase  $O_3$  reaction in positive mode. (c) The negative mode ESI mass spectrum of the trypsin digests of the oxidized  $SP-B_{1-25}$  from the bulk-phase  $O_3$  reaction

The SP-B<sub>1-25</sub> products with three additional oxygen atoms from both reactions are analyzed using CID. Figure 8.9 shows CID spectra (ESI-MS<sup>2</sup>) of triply oxygenated products of quadruply protonated SP-B<sub>1-25</sub> from bulk-phase  $O_3$  application and from the Fenton reaction. The ESI-MS<sup>2</sup> spectrum of the triply oxygenated SP-B<sub>1-25</sub> by bulk-phase  $O_3$  application implies the presence of two products, one with NFKyn (+ 2O) and MetSO (+ 1O), and the other with HNFKyn (+ 3O). Evidence of the MetSO in the oxidized SP-B<sub>1-25</sub> is found from the CID experiment

8.8 Appendix H 165



**Fig. 8.8** (a) The CID spectrum of cationic IQAMIPK + 30 at m/z 817 from the tryptic digest of the oxidized SP-B<sub>1-25</sub>. (b) The CID of cationic FPIPLPYCWLCR + 80 at m/z 1,636 from the tryptic digest of the oxidized SP-B<sub>1-25</sub>. (c) The CID of anionic FPIPLPYCWLCR + 80 at m/z 1,634 from the tryptic digest of the oxidized SP-B<sub>1-25</sub>

involving the quadruply charged SP-B<sub>1-25</sub> product from the bulk-phase O<sub>3</sub> reaction (Fig. 8.9a). For example, the paired fragments of  $y_{20}$ -CH<sub>4</sub>SO and  $y_{20}$  fragments, which are observed at m/z 782 and m/z 803 (triply charged) and at m/z 1172 and m/z 1204 (doubly charged), confirm the presence of MetSO (Fig. 8.9a). Interesting CID fragments are also observed in the ESI-MS<sup>2</sup> spectrum. The singly charged fragment at m/z 680, m/z 832, and m/z 938 are WLCRA + 30, LPYCWLCRALIKR + 30 and PLPYCWLCRALIKRI + 30, respectively. These fragments are evidence

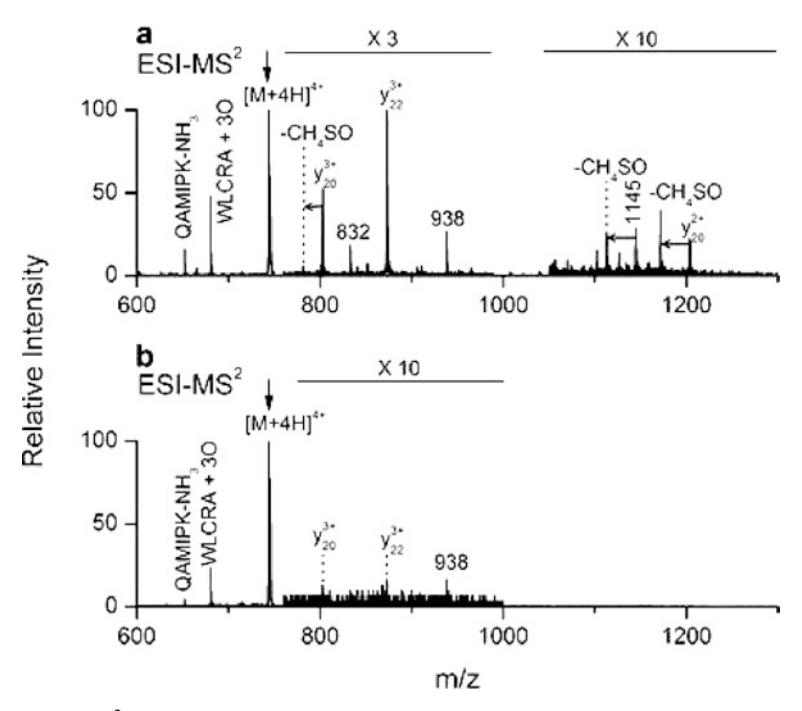


Fig. 8.9 ESI-MS $^2$  of triply oxygenated products of quadruply protonated SP-B<sub>1-25</sub> from (a) bulk-phase  $O_3$  application, and from (b) the Fenton reaction. M denotes a parent ion, which is triply oxygenated SP-B<sub>1-25</sub>

of the formation of HNFKyn through the oxidation of Trp9 from the bulk-phase  $O_3$  reaction. This is further supported by the singly charged fragment at m/z 652, QAMIPK-NH3, which indicates that no oxidation has occurred at Met<sub>21</sub>. The ESI-MS<sup>2</sup> spectrum of the triply oxygenated SP-B<sub>1-25</sub> by bulk-phase  $O_3$  reaction implies the presence of two products, one with NFKyn (+ 2O) and MetSO (+ 1O), and the other with HNFKyn (+ 3O). The CID fragment abundance implies that the bulk-phase  $O_3$  reaction with SP-B<sub>1-25</sub> yields more product peptides with HNFKyn compared to product peptides with NFKyn and MetSO. The ESI-MS<sup>2</sup> spectrum of SP-B<sub>1-25</sub> product from the Fenton reaction is shown in Fig. 8.9b. The CID of the Fenton product exhibits the presence of HNFKyn at m/z 652, m/z 680, and m/z 938, which corresponds to the singly charged fragments QAMIPK-NH<sub>3</sub>, WLCRA + 3O, and PLPYCWLCRALIKRI + 3O, respectively. However, evidence for the formation of the product with NFKyn and MetSO is not found in the spectrum.

### **Bibliography**

- 1. Binder, K. Rep. Prog. Phys. **1997**, 60, 487–559.
- 2. Candra, P. M.S. Dissertations, University of Minnesota, 2006.
- 3. Fixman, M. Proc. Natl. Acad. Sci. USA. 1974, 71, 3050–3053.

Bibliography 167

4. Karagulian, F.; Lea, A. S.; Dilbeck, C. W.; Finlayson-Pitts, B. J. *Phys. Chem. Chem. Phys.* **2008**, 10, 528–541.

- 5. Roepstorff, P.; Fohlman, J. Biomed. Mass Spectrom. 1984, 11, 601–601.
- Clauser, K. R.; Hall, S. C.; Smith, D. M.; Webb, J. W.; Andrews, L. E.; Tran, H. M.; Epstein, L. B.; Burlingame, A. L. Proc. Natl. Acad. Sci. USA. 1995, 92, 5072–5076.
- 7. Qin, J.; Chait, B. T. Anal. Chem. 1997, 69, 4002-4009.
- 8. Bruni, R.; Taeusch, H. W.; Waring, A. J. Proc. Natl. Acad. Sci. USA. 1991, 88, 7451–7455.
- 9. Berlett, B. S.; Stadtman, E. R. J. Biol. Chem. 1997, 272, 20313-20316.

## Index

A	H
Absorption isotherm, 5, 51, 54–55	Hopping mechanism, 5, 57
Adiabatic approximation, 35	
Air pollution, 6	I
Ammonium cations, 5, 65–82, 86	Interfacial reaction, 107–121
Arrhenius plot, 60	Ion-induced dipole interaction, 6, 67, 69,
Timemus prot, 00	78–80, 89
B	Ion mobility spectrum, 6, 65, 68–69, 71,
Biomolecular ions, 66	85–104
Blue moon sampling, 5, 29, 34	Ion-quadrupole interaction, 6, 69, 89
r 8, -, -, -	1 1
C	L
Coarse-graining, 1, 4	Lipid membranes, 85–86, 91
Collision cross-section, 6, 65–67, 70–71,	Langevin capture cross-section, 75–76
74–75, 86–87, 89–91, 93–97	Lattice Monte Carlo, 4
Conformational change, 3, 9–25,	Lipid precursors, 5–6, 67
97, 129	Lung, 6, 108, 110
2.,	Eurig, 0, 100, 110
D	M
Density functional theory, 69, 90	Mass-mobility correlation, 6, 67, 70–72, 86,
Diffusion, 5, 47–62	91, 93
1,5-Dioxynaphthalene, 4, 27	Memory, 5, 28
Drift gas, 6, 66–71, 74, 76, 78, 86–87, 89,	Modified trajectory method, 6, 86
95–96	Molecular dynamics, 1, 3, 29–32, 48, 50, 89,
Drift time, 68–71, 86–94, 97, 102	96, 107
	Molecular electronics, 9, 27–42
E	Molecular switch, 4–5, 28, 37–38,
Electrospray ionization, 65, 68–69,	131–159
88–89	Multiphysics, 1–6
	Multiscale computational simulation,
F	1–7
Field induced droplet ionization,	
7, 108	N
Free energy, 5, 27–42, 160	Nanoscale junctions, 1, 3, 9, 47
	Nearest neighbor model, 4, 11, 18
G	Negative differential resistance, 3,
Good solvation, 5, 57–58, 60–61	9–25
Grand canonical Monte Carlo,	Non-equilibrium Green function, 4
5, 48	Nucleation, 20–22, 24
5, 70	14ucication, 20–22, 24

170 Index

0	S
Oligo-phenylene ethynelene, 3	Self-assembled monolayer, 3,
Oxidative stress to lung, 108	9–25, 29
Ozonolysis, 6, 111–112, 114–119, 121	Surfactant protein B, 6, 108
P	Т
Phosphatidylcholine, 67, 86–87, 90–96, 99,	Tetrathiafulvalene, 4, 27
101–103, 108	Traveling wave ion mobility spectrometry, 6,
Poisson process, 20–22	85–103
Polymer electrolyte membrane fuel cells, 48	
Poor solvation, 5, 57–58, 60–61	$\mathbf{W}$
Potential of mean force, 29–31, 35–36	Water uptake, 5, 51–52, 54–55,
Pulmonary surfactant, 6, 116	57, 59
R	Z
Rotaxane, 4, 27–42	Zeolite, 5, 47–62